SMALL-SCALE MAGNETIC FEATURE EVOLUTION AS OBSERVED BY HINODE/NFI AND SOHO/MDI

L.M. Thornton

A Thesis Submitted for the Degree of PhD
at the
University of St. Andrews

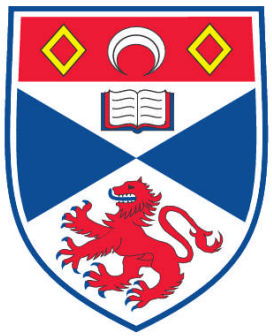

2011

Small-Scale Magnetic Feature Evolution as Observed by Hinode/NFI and SOHO/MDI

L. M. Thornton

Thesis submitted for the degree of Doctor of Philosophy

of the University of St Andrews

6th September 2010

The surface (photosphere) of the Sun is threaded throughout by magnetic fields. Groups of magnetic fields form magnetic features (of a wide range of sizes in flux and area) on the surface where the fields are directed into or out of the Sun. The aim of this thesis is to examine in detail the four key processes, emergence, cancellation, fragmentation and coalescence, which determine the behaviour of small-scale magnetic features, in the Sun's photosphere. I identify features in both Hinode/NFI and SOHO/MDI full-disk to enable for these processes to be examined at the currently smallest observable scales and over an entire solar cycle.

The emerging event frequency versus flux distribution, for intranetwork emerging regions to active regions, is found to follow a power-law distribution with index -2.50, which spans nearly 7 orders of magnitude in flux ($10^{16} - 10^{23}$ Mx) and 18 orders of magnitude in frequency. The global rate of flux emergence is found to be 3.9×10^{24} Mx day^{-1}. Since the slope of all emerged fluxes is less than -2 this implies that most of the new flux that is fed into the solar atmosphere is from small-scale emerging events. This single power-law distribution over all emerged fluxes suggests a scale-free dynamo, therefore indicating that in addition to dynamo actions in the tachocline producing sunspots, a turbulent dynamo may act throughout the convection zone.

Similarly for cancellations I find a power-law relationship between the frequency of cancellation and the peak flux lost per cancelling event (for events detected in both Hinode/NFI and SOHO/MDI full-disk), with slope -2.10. Again, the process of cancellation appears to be scale free and the slope is less than -2 indicating that numerous small-scale features are cancelling the majority of flux on the Sun.

I also estimate the frequency of all surface processes at solar maximum and find, 1.3×10^{8}, 4.5×10^{7}, 4.0×10^{7} and 3.6×10^{6} events per day over the whole solar surface for emergence, cancellation, fragmentation and coalescence events, respectively. All the surface processes are found to behave in a similar manner over all flux scales. The majority of events for all processes occur in features with flux below 10^{20} Mx, which highlights the dynamic nature of the magnetic carpet.

Using SOHO/MDI full-disk data I investigate the cyclic variation of the 4 key processes throughout cycle 23. It is found that the rate of emerging events, cancellations, fragmentations and coalescences varied in anti-phase with the solar cycle by a factors of 3.4, 3.1, 2.4 and 2.2, respectively over the cycle. Not surprisingly, therefore, the number of network features detected throughout the cycle also exhibits an anti-phase variation over the solar cycle by a factor of 1.9. The mean peak flux of tracked small-scale network, fragmenting, coalescing and cancelling features showed in-phase relationships with the solar cycle by factors of 1.4, 1.7, 2.4 and 1.2, respectfully. The total flux which is emerged and cancelled by small-scale events, varied in anti-phase with the solar cycle, by a factors of 1.9 and 3.2. This is clearly due to the variation in the number of emerging and cancelling events and the fact that the flux of individual emerging events showed no cyclic variation.

The results in this thesis show that the large-scale solar cycle plays a complex role in the surface processes features undergo. The fact that the number of ephemeral regions emerging has an anti-phase variation to the solar cycle has a knock on effect in the number of features which are available to undergo surface processes. Also decaying active regions, during more active periods, contribute more small-scale features, with high flux density, into the network which has an effect on the surface processes.

This work has revealed the significant importance of small-scale features in the flux budget through continual emergence and cancellation, plus highlighted how through dynamic surface motions, small-scale features form the fundamental components with which the network is developed.

Declarations

I, Lynsey Margaret Thornton, hereby certify that this thesis, which is approximately 51 000 words in length, has been written by me, that it is the record of work carried out by me and that it has not been submitted in any previous application for a higher degree.

I was admitted as a research student in September 2006 and as a candidate for the degree of Doctor of Philosophy in September 2007; the higher study for which this is a record was carried out in the University of St Andrews between 2006 and 2010.

Date: _____ Signature of Candidate: _____.

I hereby certify that the candidate has fulfilled the conditions of the Resolution and Regulations appropriate for the degree of Doctor of Philosophy in the University of St Andrews and that the candidate is qualified to submit this thesis in application for that degree.

Date: _____ Signature of Supervisor: _____.

In submitting this thesis to the University of St Andrews we understand that we are giving permission for it to be made available for use in accordance with the regulations of the University Library for the time being in force, subject to any copyright vested in the work not being affected thereby. We also understand that the title and the abstract will be published, and that a copy of the work may be made and supplied to any bona fide library or research worker, that my thesis will be electronically accessible for personal or research use unless exempt by award of an embargo as requested below, and that the library has the right to migrate my thesis into new electronic forms as required to ensure continued access to the thesis. We have obtained any third-party copyright permissions that may be required in order to allow such access and migration, or have requested the appropriate embargo below.

The following is an agreed request by candidate and supervisor regarding the electronic publication of this thesis:

Access to Printed copy and electronic publication of thesis through the University of St Andrews.

Date: _____ Signature of Candidate: _____ Signature of Supervisor: _____.

Acknowledgments

I don't think I would have enjoyed my PhD so much if it wasn't for the great people in the department. I'd like to say a few special mentions: firstly to all my office mates throughout my PhD, I've had so much fun and learned so much from you, to all the Angel night girls, for helping me chill out with a cup of tea and a good gossip and finally to my supervisor, Clare Parnell, who was constant source of knowledge and help.

Throughout my time doing my PhD I was lucky enough to have one of the best flat mates. Jon, I really appreciated all the times you had dinner on the table when I came in from work and how you always listened to me having a good moan.

I would also like to say a huge thanks to all my family who have provided endless support and encouragement throughout my PhD especially the write up.

Also to all my friends in both St. Andrews and Denny, who weren't in the solar group, I couldn't wish to have better people around me.

Finally I would like to thank the STFC for their financial support.

Contents

Chapter 1

Introduction

1.1 The Sun

The Sun is just an average G2V main sequence star midway through its life at 4.5 billion years of age. However, what makes the Sun so distinct from other stars is its close proximity to the Earth: the mean distance from Sun to Earth is 1.46×10^9 km, in comparison to the next closest star, Proxima Centauri, which is 0.27 million times further away. The closeness of the Sun allows for unique observations helping us to understand the Sun and other stars in considerable detail.

The Sun is made up of various layers, as seen in Figure 1.1, each of which has distinct properties. Each layer will be briefly described below.

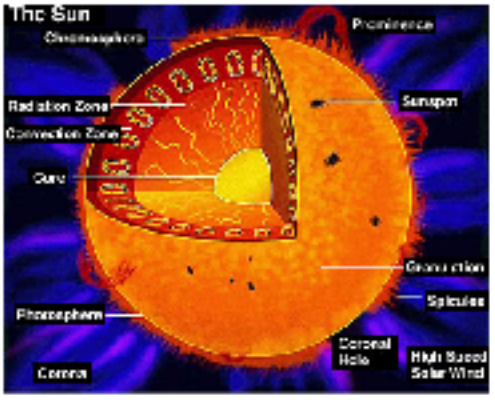

Figure 1.1: Cartoon depicting the layers of the Sun and some common solar structures. Image Courtesy of SolarScapes, Space Science Institute, http://www.spacescience.org/Education/ResourcesForEducators/CurriculumMaterials/Solarscapes/ Figure1.pdf)

1.1.1 Interior Structure

At the centre of the Sun, up to 0.25 solar radii, is its core. Temperature in the core reaches up to 1.5×10^7 K and it is the most dense region of the Sun with a density of 1.6×10^5 kg m^{-3}. The high temperature and pressure in the core provide ideal conditions to allow nuclear fusion to take place. Fusion in the Sun's core involves H ions fusing together to form He which releases vast amounts of energy in the form of photons (EUV) and neutrinos. The energy released in this vast fusion reactor is transferred from the core up to the

surface through two zones.

The first is the radiative zone where the energy is transferred without any bulk flow of material, since the region is still very dense (200 kg m^{-3}). The high temperature ($8 \times 10^6 - 5 \times 10^5$ K) in the radiative zone means all electrons are stripped from atoms. Therefore, energy is transferred in the form of photons which are constantly absorbed then re-emitted. In total it takes about 170 thousand years for photons to transfer their energy out of the radiative zone, during which time the photons lose significant amounts of energy.

The second zone is the convection zone. As the density and temperature reduce at around 0.7 solar radii, convection becomes the main mechanism which transfers energy to the surface of the Sun. The reduced temperature here ($5 \times 10^5 - 6600$ K) allows some heavier nuclei to capture electrons. Thus at the base of the convection zone radiation is absorbed without being re-emitted and so the material at the base of the convective zone heats and expands causing it to rise. It takes about 10 days for plasma to get from the bottom to the top of the convection zone. As the hot material reaches the surface it radiates its energy as sunlight into space, which then cools and sinks back to the bottom of convection zone, where the process is repeated.

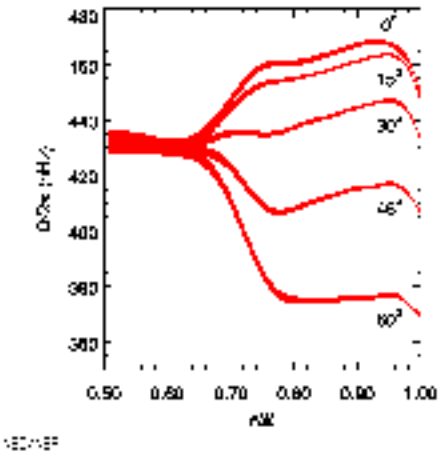

Figure 1.2: The above image shows the rotation rate of the Sun plotted against radius. Below 0.7 solar radii the solar interior rotates as a solid body after which differential rotation rapidly takes effect causing the rotation rate to vary with both latitude and depth. Image courtesy of Global Oscillation Network Group:http://gong.nso.edu/

Between the radiative zone and the convection zone is a thin layer, with a thickness of 0.04 times the solar radius, called the tachocline. Below this layer the Sun rotates as a solid body (with a rotational period of $\approx$ 28 days) and above it, in the convection zone, differential rotation takes effect as shown in Figure 1.2. The effect of differential rotation increases until at the photospheric level the rotation rate is $\approx$ 25 days at the equator and $\approx$ 35 days at the poles. The shearing of the plasma in the tachocline layer between the uniform rotation of the radiative zone and the differential rotation above is believed to play an important role in the large scale solar dynamo, which is the mechanism that generates the Sun's large-scale magnetic field.

1.1.2 Photosphere

The photosphere is the lowest layer of the solar atmosphere and is observed as the solar surface, since here gaseous material changes from being completely opaque to partially transparent. The photosphere is much thinner than the layers below it, at only about 500 km thick, and has a greatly reduced temperature of between 4500 K and 6000 K. Throughout the photosphere dynamic motions are observed on all scales, caused by the overshoot of convection flows from below. Supergranules are the largest surface manifestation of the convection cells. They have an average diameter of between 13-18 Mm (Hagenaar, 2001) and a typical lifetime of a few days (Simon and Leighton, 1964; Livingston and Orrall, 1974; De Rosa and Toomre, 2004). At the centers of these cells are upflows of hot plasma moving at a typical speed of 0.3-0.7 km s^{-1} (Plaskett, 1954). When this hot plasma reaches the surface it is pushed away from the cell center at a speed of between 0.3-0.5 km s^{-1} to the cooler down-flow regions at the edges of the supergranular cells, where it descends into the convection zone at a speed of 0.1-0.2 km s^{-1} (Simon and Leighton, 1964).

Convection in the photosphere can also be seen in smaller cells known as granules. These are about 10 times smaller than supergranules with a diameter of less than 1400 km (Lang, 2001). They are also much shorter lived and only last $\approx$ 8 minutes (Bahng and Schwarzschild, 1961). Given their size it is estimated that there are roughly 1 million granules on the Sun at any one time (Priest, 1982). Supergranules and granules can be seen by observing Doppler shifts, caused by photospheric material in motion, in spectral lines. An example of a dopplergram from SOHO/MDI is seen in Figure 1.3. The light and dark regions show material which is moving towards and away, respectively.

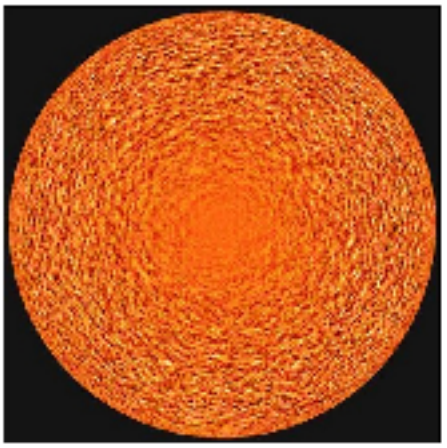

Figure 1.3: A full-disk dopplergram from SOHO/MDI in which supergranule cells can be seen. A dopplergram, such as this one from the SOHO spacecraft, shows motions on the Sun's surface with areas moving toward us appearing dark, and areas moving away, bright. Image courtesy of SOHO/MDI (ESA/NASA).

Magnetic phenomena are also highly evident in the photosphere. Magnetic flux tubes generated in the solar interior rise through the photosphere and into the atmosphere. Foot-points of these flux tubes are visible in magnetograms of the photosphere as white (positive) and black (negative) magnetic features covering a wide range of scales from active regions (a few times 10^{22} Mx) down to the smallest intranetwork (IN) features (10^{16}Mx). The magnetic features that I will be studying are visible in magnetograms such as those from Kitt Peak, the Michelson Doppler Imager (MDI) aboard SOHO (Scherrer et al., 1995) (Figure 1.4)b

and those derived from the Stokes I and V parameters from the Narrowband Filter Imager (NFI) aboard Hinode (Tsuneta et al., 2008). I will be using both SOHO/MDI and NFI data throughout this thesis and a full description of the data is given in Chapter 2.

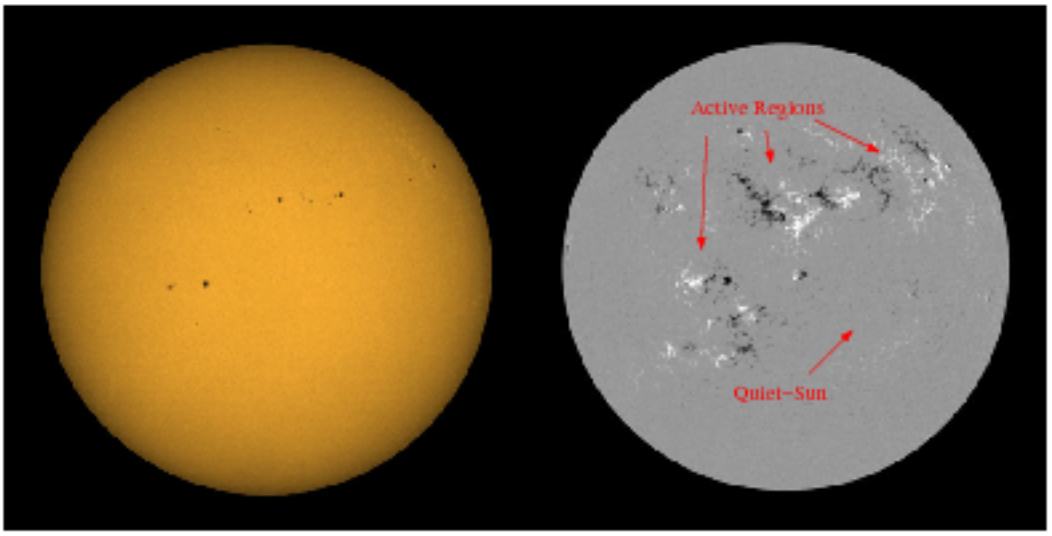

Figure 1.4: These two images of the photosphere of the Sun were observed simultaneously by SOHO/MDI in both white light (left) and a magnetogram (right). In the white light image sunspots can be seen which correspond to the active regions highlighted in the magnetogram. The regions outside active regions, containing small-scale flux are known as the quiet-Sun or magnetic carpet. Images courtesy of SOHO/MDI (ESA/NASA).

Figures 1.4left and right show full-disk white light and magnetogram images of the photosphere taken by SOHO/MDI, respectively. Whilst only the sunspots are visible in the white light image, both large-scale and small-scale features are visible in the magnetogram.

1.1.3 Chromosphere and Transition Region

Above the photosphere is the chromosphere, which is about 1500 km thick. Something rather surprising begins to happen throughout the chromosphere, which appears to go against the laws of thermodynamics: the temperature at bottom of the chromosphere matches photospheric temperatures, of just 5800 K, but at the top the temperature has increased to $\approx$ 10000 K. In the transition region above, which is only 200 km thick, this temperature increase continues, but with a much steeper gradient, reaching temperatures of up to a million K. Figure 1.5 shows the temperature gradient throughout the solar atmosphere. The density is also greatly reduced from 2.0×10^{-4} kg m^{-3} at the base of the convection zone to 1.0×10^{-11} kg m^{-3} at the bottom of the transition region. On reaching the corona the density is $\approx 1 \times 10^{-12}$ kg m^{-3}.

The presence of magnetic fields in the chromosphere and transition region, results in a highly non-uniform medium which produces many interesting features such as spicules, fibrils, chromospheric network and solar prominences, all of which can be seen in Figure 1.1 and Figure 1.6. Chromospheric and transitional region dynamics can be seen clearly through a range of spectral lines including Ca II (e.g. SOT aboard Hinode), Hα (e.g. Big Bear Solar Observatory) and He I (e.g. Mauna Loa Solar Observatory).

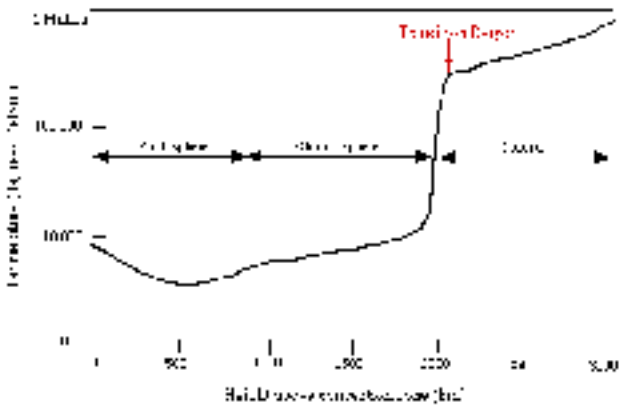

Figure 1.5: This plot shows the temperature against height in the solar atmosphere. A dramatic increase in temperature occurs between the convection zone and corona in a layer called the transition region.

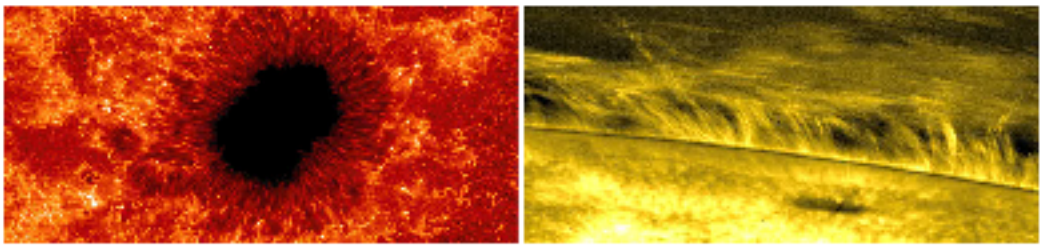

Figure 1.6: Images of the chromosphere as observed by the Solar Optical Telescope aboard Hinode. The left figure shows a sunspot on the disk and the right image shows spicules protruding from the limb of the Sun, a small sunspot (dark spot on the disk) and a prominence (horizontal filamentary structure) both observed in the Ca II H line at 39.7 Å. These images highlight the complex configurations that are created by the magnetic fields on the Sun. Both images courtesy of Hinode JAXA/NASA.

1.1.4 Corona

The corona is the outermost part of the solar atmosphere, starting at ≈ 2 Mm above the surface and extending all the way to the Earth and beyond into interplanetary space. It is also the hottest part of the atmosphere with temperatures in the inner corona ranging between 1 million K to in excess of 10 million K. The source of the heat is the Poynting flux injected by the convective motions moving the magnetic field that threads through the photosphere, with the energy being stored in the magnetic field. What is unknown is the mechanism by which this energy is released into the upper atmosphere. This is often referred to as the coronal heating problem. The problem of the hot corona is one of the most discussed topics of the Sun and two main heating mechanisms have been proposed: reconnection (e.g. Sturrock 1999; Hudson 1991; Priest and Forbes 2000) and wave heating (e.g. Athay and White 1978; Abdelatif 1987; Assis and Busnardo-Neto 1987; Davila 1987; Einaudi and Mok 1987), with the likelihood that both mechanisms contribute.

The corona shines through visible sunlight being scattered by electrons (K corona) or dust particles (F corona) in interplanetary space, but due to it being much fainter than the layers below it can only be observed in white light at eclipses or by using a coronagraph (Figure 1.7 left). The structure of the corona

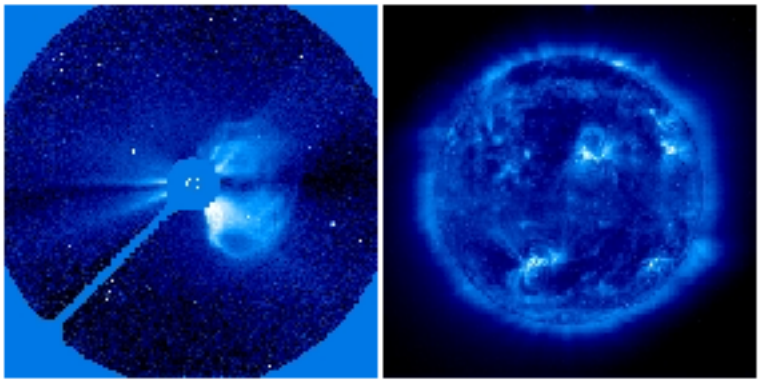

Figure 1.7: Above left is a SOHO/LASCO C3 white light image of a large coronal mass ejection (CME) and right a SOHO/EIT image at 171Å showing the solar corona at a temperature of about 1 million K. Both images courtesy of SOHO (ESA/NASA)

is highly variable throughout the solar cycle. Coronagraph images of the corona near the solar minimum reveals large radially extended structures, known as streamers, straddling the equator, whilst the poles are relatively dim. Around the solar maximum, the large-scale structure of the corona becomes much more complex with streamers extending radially in all directions.

Because of the temperature of the corona, it radiates most of its energy at X-ray and EUV wavelengths and can be viewed using instruments such as SOHO/EIT and TRACE. EUV and X-Ray observations show bright complex active regions. These highly dynamic active region fields can produce large-scale energetic events such as CME's and flares. Small-scale hot features known as X-ray bright points are also seen. These energetic events reconfigure stressed magnetic fields to lower energy states, releasing energy in the process. Outside these bright regions are dark regions. These are known as coronal holes where field extends radially. Outside coronal holes and active regions, there are also dim regions containing quiet-Sun fields. The coronal emission varies throughout the solar cycle reducing at both X-ray and EUV wavelengths by a factor of 100 and 2, respectively, between solar maximum and minimum.

1.2 Magnetic Activity on the Sun

The cyclic behaviour of the Sun was discovered in 1843 (Schwabe, 1843) but it was not until magnetic fields were first detected in sunspots in 1908 by Hale (1908), that the cyclic variation was linked to magnetic fields. The solar magnetic cycle goes through two global field maxima/minima. Between these the polarity at the poles reverses and only when the magnetic field has returned to its original polarity is the cycle complete. The 22 year magnetic cycle plays a pivotal role in the evolution of the active Sun, indeed the 11 year sunspot cycle is a consequence of it as well as the periodic variation in the number of large-scale features, such as flares, CME's and prominences. It is now known that magnetic fields, which are anchored in the photosphere and extend out to the corona and beyond, are the principal reason for the varied structure in the solar atmosphere, on both large and small scales.

The existence of the solar magnetic fields in the solar atmosphere indicates the presence of dynamo

mechanisms below the surface. The origin of large-scale fields has been studied extensively and they are most likely the product of a global dynamo active at the convection zone in the tachocline (Moffat, 1978). The origin of the magnetic carpet has still to be fully understood. It is unclear if there is just one dynamo process acting on all scales, as recently suggested from observations (Parnell et al., 2009), or whether there is a separate small-scale turbulent dynamo (Meneguzzi and Pouquet, 1989; Durney et al., 1993; Lin, 1995; Tobias, 2002), producing small-scale fields, just below the photosphere. This question is investigated further in Chapter 5.

Throughout this thesis, I will use photospheric magnetogram observations to investigate magnetic fields in the photosphere. In magnetograms, the foot-points of the fields can be seen as magnetic flux features over a wide range of fluxes from $10^{16} - 10^{23}$ Mx. They are known to undergo 4 processes: emergence, fragmentation, coalescence and cancellation (Livi et al., 1985; Schrijver et al., 1997). Emergence is the process by which new flux arrives in the photosphere from the convection zone below. In observations of the photosphere emergence is identified by the appearance of bipolar flux features, or a cluster of negative flux and a cluster of positive flux, which will increase in flux and grow in area as the flux tube emerges. There is no typical size for the emerging bipoles, rather it has been found that they are part of a continuous spectrum of fluxes from 10^{19} Mx to 10^{23} Mx (Hagenaar et al., 2003).

The other three processes can occur anytime after the emergence of the features (Livi et al., 1985). Fragmentation involves the splitting of a single, large feature into two or more smaller features (Vrabec, 1971; Smithson, 1973). The converse of this is coalescence, where two or more like-polarity features coalesce to from a single, larger feature (Vrabec, 1974; Martin, 1988). Cancellation of flux occurs when two opposite-polarity features come into close proximity, leading to flux decreasing through either submergence below the photosphere or by lifting of a closed magnetic loop into the corona (Livi et al., 1985). Depending on the initial flux of each feature, partial or full removal of the features occurs. Like emergence, the other processes occur over a continuum of fluxes. When studying the magnetic field in the photosphere the features are generally split into two categories: active regions ($> 10^{20}$ Mx) or quiet regions ($\leq 10^{20}$Mx), according to their flux. The following two sections describe both types of features paying particular attention to the quiet-Sun as these features are the main subject of this thesis.

1.2.1 Active Regions

Active regions are the largest manifestations of magnetic flux on the solar surface and the longest lived with a lifetime of days to months (Solanki, 2003). They contain a multitude of magnetic features over a range of fluxes from 10^{20} Mx and above, with the largest features, sunspots, typically having flux of 10^{22} Mx (Harvey, 1993). In white light images of the photosphere sunspots appear dark against the background (e.g. Figure 1.4). This is due to the fact they are about 2000 K cooler than their surroundings, as their concentrated strong magnetic field restricts the convection of heat from below the photosphere. Active regions have a complex magnetic structure and are very dynamic which is the reason why they are often associated with flares and CME's.

Active region flux is sustained through the emergence of sunspots which are heavily influenced by the global magnetic cycle ($\approx$22 year). The sunspot cycle is half of the global magnetic cycle at $\approx$11 years and

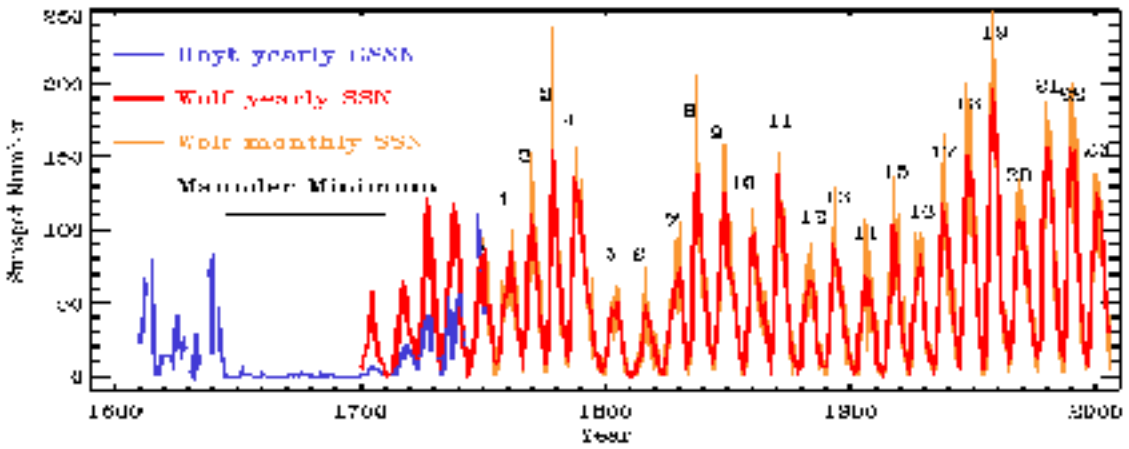

Figure 1.8: A graph of the Sunspot number index versus date. Three historical reconstructions are shown: the monthly sunspot number (orange), and yearly sunspot number (red), and the Group sunspot number (blue) (generally deemed a more reliable reconstruction between 1610 to 1750). Image courtesy of Paul Charbonneau, Physics Dept. Universite de Montreal

defined as the reversal of the polarity of the leading spot in an active region. Each sunspot cycle follows the rise and fall of large-scale activity on the Sun as shown in Figure 1.8. The 11 year sunspot cycle is clearly evident here. One feature to note is the period between 1645 and 1715 where practically no sunspots were observed, known as the Maunder Minimum which coincided with a mini ice age on Earth. Like the magnetic cycle the sunspot cycle can vary in both length and amplitude. The emergence of sunspots, on the photosphere primarily occurs in two bands, one in each hemisphere. At the beginning of the sunspot cycle (solar minimum), active regions appear at ± 45 degrees latitude but as the cycle progresses to maximum, the areas of new emergence migrate toward the equator reaching ± 15 degrees. The emergence rate of active regions is 8 times greater at the solar maximum than at the minimum (Harvey and Zwaan, 1993). The orientation of the active regions is also very systematic and the majority follow Hale's polarity law. This law states that at any given time, the leading polarity of sunspots in active regions, in the direction of rotation (east to west), will be the same in the northern/southern hemisphere, but opposite to that of the southern/northern hemisphere.

The development of a sunspot in the photosphere can take anywhere from a few hours to several days (Zwaan, 1978; Solanki, 2003). The emergence process of active regions is very dynamic and commonly coalescence and cancellation are seen to occur within the emerging region (Vrabec, 1974; Solanki, 2003; Handy and Schrijver, 2001). It is thought that the thick flux tubes associated with the sunspots are composed of a number of thin flux tubes. For some reason in the convection zone the thick tube splits into smaller bundles of tubes which rise separately but coalesce back into the large flux tubes once they are on the surface (Vrabec, 1974; Solanki, 2003).

Although cancellation and emergence are typically thought of opposite processes, they can both occur in an emerging active region due to the presence of U-loops (van Driel-Gesztelyi et al., 2000). The emergence of flux generally occurs due to Ω-loops rising from the convection zone, U-loops have essentially the opposite configuration to Ω-loops i.e. their foot-points will appear as magnetic features in the photosphere

but the flux tube will be concave below the photosphere. It is thought that U-loops occur when two Ω-loops emerge together which are connected by the same toroidal flux tube or through convection zone reconnection between opposite-polarity foot-points of neighbouring Ω-loops (Brouwer and Zwaan, 1990; van Driel-Gesztelyi et al., 1992). Eventually the concave part rises causing two foot-points of the U-loop to cancel.

The decay of the active regions can begin before they are fully emerged (McIntosh, 1981). Largely the decay of an active region occurs around the border, where small magnetic features fragment from the larger source and move radially outwards at speeds of up to 1 km s^{-1} (Sheeley, 1969; Brickhouse and Labonte, 1988; Wang and Zirin, 1992). It has been estimated that this radial flow of small scale features removes up to 5×10^{18} Mx hr^{-1} from an active region (Zwaan, 1974; Livi et al., 1985).

As they decay flux from sunspots slowly disperses into the surrounding regions and their flux is either transported pole-wards or equator-wards via meridional flows. Also during the decay phase, as well as dispersing into the surrounding field, the opposite-polarity components move apart (Zwaan, 1978). The flux which is transported pole-wards is of opposite polarity to the current polarity of the flux at the pole, thus upon reaching the polar flux it ultimately cancels it, causing a reverse in polarity. The flux which is transported equator-wards is of opposite polarity to the active region flux approaching the equator from the other hemisphere and these fluxes also cancel.

1.2.2 Quiet-Sun

Small-scale magnetic features were first observed in high-resolution magnetograms in the early 1970's (Beckers and Schröter, 1968; Harvey, 1971; Dunn and Zirker, 1973; Stenflo, 1973; Livingston and Harvey, 1975; Smithson, 1975). These observations revealed that there was a small-scale mixed-polarity component of magnetic field ubiquitously outside active regions. Over time the importance of small-scale features, in the structure and sustaining of the magnetic carpet, has become apparent. When small-scale features were first discovered it was thought that they were just the remnants of active regions, dispersed by differential rotation and convection (Bumba and Howard, 1965), but it was soon discovered that the quiet-Sun was sustained by ephemeral regions (Harvey and Martin, 1973; Harvey et al., 1975). Over the years observations of the photosphere have continued to improve and this has revealed flux features, and the emergence of flux features, on continually reducing scales. Initially it was assumed that outside large sunspots and plage regions there was practically no magnetic field. Subsequent analysis over the years has revealed this small-scale magnetic component may contain a large fraction of the Sun's magnetic flux.

Quiet-Sun magnetic features have flux in the range of a few times $10^{18} - 10^{20}$ Mx and can be divided into intranetwork (IN), network and ephemeral regions (Livingston and Harvey, 1975; Zirin, 1987; Harvey, 1993; Keller et al., 1994; Wang et al., 1995). These features and their properties are discussed fully below.

1.2.2.1 Network Features

Network features were the first features to be observed in the quiet-Sun (Simon and Leighton, 1964; Sheeley, 1966; Howard, 1967). Their field extends out into the solar atmosphere producing a 'network' of connections that (practically) interlinks all magnetic features. The flux in network features ranges between $\approx 10^{18} - 10^{20}$ Mx (Martin, 1988; Wang et al., 1995; Hagenaar et al., 1999). Spatially the features have typical diameters between $10^3 - 10^4$ km and typical areas of few tens of Mm^2 (Ramsey et al., 1977; Wang et al., 1995; Wang, 1988; Meunier, 2003). In the photosphere, the network is observed to be comprised of mixed polarity features which reside in supergranular lanes and at vertices (Schrijver et al., 1997). Thus, at any one time the network covers between 15-20% of the surface (Foukal et al., 1991), correponding to 10^{23} Mx in surface flux.

The magnetic network is sustained by ephemeral regions, decaying active regions and the coalescence of IN fields (Martin, 1988; Schrijver et al., 1997). A previous estimate of the importance of each of these components found that almost 90% of the network was the residual of emerging bipolar regions (from ephemeral regions up to active regions) with the remaining 10% coming from IN features and decaying active regions (Martin, 1990).

The network field evolves on supergranular time scales with the features continually undergoing fragmentation, coalescence and cancellation, with other network, IN and ephemeral region features (Martin, 1988). The lifetime of network features is typically about a few hours to a few days (Wang et al., 1989; Liu et al., 1994). The movement of network features is relatively slow with an average velocity of 0.06 km s^{-1} (Zirin, 1985).

1.2.2.2 Intranetwork Features

In 1975 magnetogram observations of the photosphere revealed mixed-polarity small-scale features, just above resolution and inside supergranular cells (Livingston and Harvey, 1975; Smithson, 1975). These features became known as intranetwork fields and are the smallest and weakest of the quiet-Sun features with flux in the range of a few times 10^{16}- a few times 10^{18}Mx and diameters typically less than 1 Mm (Harvey, 1977; Livi et al., 1985; Zirin, 1985, 1987; Martin, 1988; Wang, 1988; Wang et al., 1995; Title and Schrijver, 1998). With a few times 10^{15} Mx being the lower bound with current observational resolution (it is likely, with improved instrumental resolution, that there are even smaller concentrations).

Generally observations have revealed that the emergence of IN features tends to occur as clusters of mixed-polarity features moving radially from a localised emergence centre, inside a supergranular cell (Zirin, 1985; Martin, 1988; Wang et al., 1995). But there have also been observational examples showing the emergence of IN bipolar pairs which behave like ephemeral regions (Zirin, 1985; Wang et al., 1995). This has raised the question of whether or not IN features are a continuation of ephemeral regions down to smaller scales. This is one of the topics which will be investigated in this thesis and is discussed in Chapter 5.

After emergence the motions of IN fields are driven by granular and supergranular flows, which sweep

IN features to vertices and boundaries where they become part of the network (Parker, 1963; Zhang et al., 1998b). IN features move more rapidly than network features at a typical speed of $0.25-2.0$ km s^{-1} (Zirin, 1985; Keller et al., 1994; Wang et al., 1995; de Wijn et al., 2008). They are very dynamic and continuously merge and cancel with both network and other IN features (Livi et al., 1985; Wang et al., 1995). Due to their small flux content, IN concentrations tend to vary on granular timescales and thus have lifetimes of minutes to hours (Zhang et al., 1998a; de Wijn et al., 2008).

Even though IN fields are intrinsically weak, their dynamic nature and ubiquitous distribution suggest that they provide a valuable contribution to the total solar magnetic flux budget (Socas-Navarro and Sánchez Almeida, 2002). Indeed, it is thought that as much as 10^{23} Mx, which is $\approx 20\%$ of the total flux in quiet-Sun, is in form of IN elements at any given time (Wang et al., 1995). To maintain this level of flux 10^{24} Mx day^{-1} must be emerging (and cancelling) in the photosphere (Zirin, 1985; Wang et al., 1995).

With the resolution capabilities of instruments ever increasing, there is still considerable interest in understanding the origin and behaviour of magnetic fields, including determining the size of the smallest magnetic features on the Sun (Domínguez Cerdeña et al., 2003; Sánchez Almeida et al., 2003; Socas-Navarro et al., 2004; Manso Sainz et al., 2004; Khomenko et al., 2005; Domínguez Cerdeña et al., 2006b,a; Harvey et al., 2007; Sánchez Almeida, 2007; Orozco Suárez et al., 2008; Lites et al., 2008). To date there is no indication that the IN features have any sort of variation throughout the solar magnetic cycle.

1.2.2.3 Ephemeral Regions

Ephemeral regions are small bipolar regions which emerge preferentially near supergranular boundaries (Wang, 1988; Harvey, 1993). The initial separation between the opposite-polarity peaks is in the range of 2-9 Mm (Martin and Harvey, 1979; Chae et al., 2001; Hagenaar, 2001). They typically have flux in the range of $10^{18} - 10^{20}$ Mx (Harvey and Martin, 1973; Harvey et al., 1975; Harvey, 1993; Chae et al., 2001; Hagenaar, 2001; Hagenaar et al., 2003), with total areas from 10's-100's Mm^2 (Harvey and Martin, 1973).

After emergence most bipoles initially move apart rapidly in opposite directions with velocities of anywhere in the range 0.1-5 km s^{-1}, slowing down as the opposite-polarity features move apart (Harvey and Martin, 1973; Born, 1974; Zirin, 1985; Chou and Wang, 1987; Barth and Livi, 1990). It is still unclear as to what drives this separation and both the mechanisms of buoyancy and the supergranule horizontal flows driving the foot-points of the flux tube apart have been proposed (Zirin, 1985; Chou and Wang, 1987). Note, however, that not all opposite-polarity features of emerging bipoles separate. Smaller bipoles with less flux often stay at a constant separation through their life (Zirin, 1985). During the emergence phase the borders of each pole expand at a rate of 2.3 km s^{-1} (Hagenaar, 2001), whilst the flux in each pole increases at a rate of between 2-30 $\times 10^{18}$ Mx (Harvey, 1993; Chae et al., 2001; Hagenaar, 2001). As they are moving apart the flux features drift towards the boundaries and vertices of supergranular cells, often fragmenting along the way due to granular convection (Simon et al., 2001). When the features reach the network they lose their identity as ephemeral regions and begin their life as network features. The lifetime of an ephemeral region is defined as the time the opposite-polarity features can be recognised as a bipole. This is typically a few hours to a few days, larger bipoles tend to be recognised for longer (Harvey, 1993; Harvey and Martin, 1973; Harvey et al., 1975; Title, 2000b; Hagenaar, 2001).

The frequency of emergence of ephemeral regions over the entire solar surface is of the order of 10^2 - 10^4 regions per day (Harvey, 1993; Chae et al., 2001; Hagenaar, 2001; Hagenaar et al., 2003). This corresponds to a flux emergence rate of between 10^{22} - 10^{23} Mx day^{-1} (Harvey et al., 1975; Harvey, 1993; Title, 2000b; Chae et al., 2001; Hagenaar, 2001; Simon et al., 2001). From this flux emergence rate it can be estimated that the time taken to recycle all the quiet-Sun flux on the Sun must be of the order of a few hours (Hagenaar et al., 2003; Close et al., 2005). The small-scale IN flux emergence rate estimated is slightly higher than this at 1.1×10^{24} Mx day^{-1} over whole solar surface (Martínez González and Bellot Rubio, 2009). As this is for features of mean flux 9.1×10^{16} Mx, this would imply that $\approx 10^7$ small-scale emerging features appear each day (Martínez González and Bellot Rubio, 2009).

Ephemeral regions do not share sunspot's inclination to emerge with a preferred orientation or latitude (Harvey and Martin, 1973; Hagenaar, 2001). Also rather than increase in number at solar maximum the opposite effect has been found with the number of ephemeral regions decreasing between minimum and maximum by a factor of about 2 (Martin and Harvey, 1979; Martin, 1988; Hagenaar et al., 2003).

A number of investigations have been done to find the relationship between IN emerging regions, ephemeral regions and active regions (Hagenaar, 2001; Hagenaar et al., 2003). Of particular interest is the emergence frequency, flux emergence rate, orientation and variation of emergence over the solar cycle. Unlike active regions, ephemeral regions and small-scale IN emerging regions have been found to have no preferred orientation (Harvey and Martin, 1973; Hagenaar, 2001; de Wijn et al., 2008). Ephemeral regions also appear to vary in anti-phase with the solar cycle by a factor of about 2 (Martin and Harvey, 1979; Martin, 1988; Hagenaar et al., 2003), but it is unclear if the same is true for IN emerging events. Determining the relationship between flux features of all scales is one of the key aims of this thesis.

1.3 Outline of Thesis

The aim of this thesis is to investigate further the emergence and behaviour of the currently smallest observable flux features and to fully investigate the behaviour of small-scale features over an entire solar cycle. In the introduction questions have already been raised as to the origin of small-scale fields and the relationship between features of different fluxes. I aim to answer these questions plus a few more in the chapters that follow.

To develop an understanding of the processes which small-scale flux features undergo, I directly analyse observations of magnetograms on the surface of the Sun. Two types of data are used, SOHO/MDI full-disk and NFI/Hinode, which, together, cover solar cycle 23 and have varying resolutions. This allows the observation of magnetic flux features over nearly 7 orders of magnitude in flux. The data sets and their preparation are discussed in detail in Chapter 2.

Chapter 3 focuses on how to extract useful information from the magnetogram data sets. Two feature identification methods, clumping and downhill and the tracking approach are presented, which are used throughout the thesis. There are various approaches and assumptions which have to be made when separating flux features from background noise in the data and when following their evolution throughout time.

The implications that can arise from these are discussed.

As well as being able to identify flux features, I want to be able to investigate their origin and the process of emergence in the photosphere. Chapter 4 focuses on developing three methods of detecting the emergence of new flux features in magnetograms: the Bipole Comparison method, the Tracked Bipolar method and the Tracked Cluster method. Three methods are developed to help ascertain the best approach of finding small-scale emerging flux in magnetograms.

In Chapter 5, I investigate the results of magnetic feature identification, tracking and emergence detection using the Hinode/NFI data. This chapter highlights the advantages of tracking features and the difference it makes to the outcomes of the emergence detection algorithms. I also investigate the process of the emergence of IN flux, to see if it is an extension of ephemeral region behaviour down to smaller fluxes.

The evolution of features in Hinode/NFI is also considered (Chapter 6). I have developed algorithms to detect the processes of fragmentation, coalescence and cancellation. Whilst cancellation has been the focus of a few studies, there is little literature on the processes of fragmentation and coalescence especially at small scales.

Chapters 7 and 8 move on to investigating the variation of small-scale features, their emergence and evolution, over an entire solar cycle using SOHO/MDI full-disk data which covers the period from the minimum of cycle 22 up to the current minimum of cycle 23. I also compare the results I find for features observed using SOHO/MDI to those observed by Hinode/NFI in order to find if there is any relationship between IN, network and active region fields.

Finally, in Chapter 9, using the characteristics of the small-scale emerging and cancelling events detected in both the Hinode/NFI and SOHO/MDI I estimate the viability of quiet-Sun coronal heating through these processes.

Chapter 2

Magnetic Field Data and its Preparation

Throughout this thesis I will be using magnetic field data sets from both the Michelson Doppler Imager (MDI) aboard the Solar and Heliospheric Observatory (SOHO) and the Narrowband Filtergraph (NFI) from the Solar Optical Telescope (SOT) on-board Hinode. The data sets are prepared in a similar manner for each chapter so, to avoid repetition, a thorough description of the data sets and their preparation is presented here.

The instruments which provide the data, the data sets themselves and the preparation of each data set are described in § 2.1 and § 2.2, with the former focusing on the SOHO/MDI data and the latter considering the Hinode/NFI data.

The last section (§ 2.3) details finding the residual noise estimate of each data set (the final reduced noise after processing), which is an important quantity and is used in the identification of magnetic data.

The aim of this thesis is to study the evolution of small-scale magnetic features and their variation over the solar cycle. I use the Hinode/NFI data for studying the smallest observable quiet-Sun features but, since Hinode has only been operational since 2006, I use SOHO/MDI to study how the small-scale feature dynamics vary over the solar cycle. The main differences between the MDI full-disk and NFI data, are their resolutions which affect the sizes of features identified; small network and IN features are difficult to identify in full-disk magnetograms as their flux is often below the residual data noise and their areas are of the order of one MDI pixel. Higher resolution data allows for more detail to be observed in the structures of identified features i.e. a single magnetic feature in full-disk magnetogram data may appear as two or more features in higher resolution data. Before any analysis is undertaken all the data sets are preprocessed to ensure useful and accurate information about the magnetic field is obtained.

2.1 Solar and Heliospheric Observatory

The SOHO satellite (Domingo et al., 1995) is a joint National Aeronautics and Space Administration (NASA) and European Space Agency (ESA) project and was launched on December 2nd 1995, with operations beginning in April 1996. SOHO continually observes the Sun throughout its orbit of the Sun about the Sun-Earth Lagrangian 1 point (effectively the point where the gravitational and centrifugal force of the Earth and Sun are balanced) which is 1.5×10^6 km from the Earth. The three main objectives of the mission were: (1) studying the solar interior using helioseismology, (2) studying heating mechanisms of the solar corona and (3) investigating the solar wind and its acceleration process. SOHO has currently been

in operation for a complete solar cycle from the minimum of cycle 22 up to the present minimum. This is a unique occurrence for a satellite and allows an in-depth study of the variation of small-scale flux features throughout the cycle.

There are 12 instruments on board (Domingo et al., 1995):

- Solar interior and surface instruments:
  - MDI (Michelson Doppler Imager).
  - GOLF (Global Oscillations at Low Frequencies)
  - VIRGO (Variability of Solar Irradiance and Gravity Oscillations).
- Transition region and coronal instruments:
  - EIT (Extreme ultraviolet Imaging Telescope).
  - CDS (Coronal Diagnostic Spectrometer).
  - SUMER (Solar Ultraviolet Measurements of Emitted Radiation).
  - LASCO (Large Angle and Spectrometric Coronagraph).
  - UVCS (Ultraviolet Coronagraph Spectrometer).
- In-situ solar wind instruments:
  - SWAN (Solar Wind Anisotropies).
  - CELIAS (Charge, Element, and Isotope Analysis System).
  - COSTEP (Comprehensive Suprathermal and Energetic Particle Analyzer).
  - ERNE (Energetic and Relativistic Nuclei and Electron).

This thesis focuses on the evolution of flux features in the photosphere, which are the foot-points of magnetic fields. From SOHO, I use level 1.5 and 1.8 MDI data (Scherrer et al., 1995) which has been extensively used for studying magnetic fields in the photosphere (Title and Schrijver, 1998; Chae et al., 2001; Hagenaar, 2001; Hagenaar et al., 2003; Parnell et al., 2009). The instrument images the Sun through polarizing filters, centered on the Ni I 767.8 Å($\pm$190mÅ) photospheric absorption line, using a 1024$\times$1024 pixel CCD camera. MDI can observe at two spatial resolutions: (i) full-disk which has a 4 arcsecond pixel resolution (pixel size 2 arcseconds) with a 34 $\times$ 34 arcmin field of view, and (ii) high-resolution, which has a 1.25 arcsecond resolution (pixel size 0.625 arcseconds) over a 10.5 $\times$ 10.5 arcmin field of view. The difference in the Doppler shift in the right and left circularly polarized light from the Ni I 6768 Å line, is a measure of the Zeeman splitting which is proportional to the magnetic flux density. Since the magnetic flux density is just the line-of-sight component of the magnetic field averaged over a pixel, line-of-sight magnetograms can be constructed. MDI full-disk magnetograms typically have a cadence of 1 minute or 96 minutes.

2.1.1 MDI Full-Disk Preparation

The majority of the data used in this thesis is in the form of SOHO/MDI full-disk magnetogram sequences. The impetus for choosing high-cadence full-disk MDI magnetograms, over high-resolution MDI magnetograms was because, initially, I wanted to compare my results to previous results by Hagenaar (2001) and Hagenaar et al. (2003). The MDI/full-disk data also allows the identification of flux features over a larger number of orders of magnitude than the high-resolution MDI data, with full-disk MDI providing the higher end of the scale from 10^{18} Mx up to 10^{23} Mx (and Hinode extending this down to 10^{16} Mx). High-cadence data is required so that small features, which may only have lifetimes of the order of tens of minutes, can be identified and tracked. All the full-disk data sets used have an original cadence of 1 minute. The long duration of the data sets allows for the evolution of larger, longer-lived, features to also be investigated. Furthermore, high-cadence, long duration and large field of view data provides better statistics due to the large number of features identified. There are suitable SOHO/MDI full-disk magnetograms available at regular intervals over a complete solar cycle (from between the minimum of cycle 22/23 in December 1996 to the minimum of cycle 23/24 in December 2008). These allow a detailed investigation of the variation in many aspects of small-scale flux features over the large-scale solar cycle. Table 2.1 shows the year, start date, start time and duration of each of the data sets, used in this thesis.

Figure 2.1 shows an example magnetogram from each set. The data starts at the solar minimum of cycle 22/23 (December 1996) and tellingly the magnetic field in the data for this year is very quiet. The data sets continue to be fairly quiet, with only a few high latitude active regions appearing up until December 1999, where lower latitude active regions are present as well. This active period continues through to January 2003, where there is a clear reduction in activity. The activity in the northern hemisphere is greatly reduced for this year, with the southern hemisphere remaining active. Between January 2004 to February 2007 the activity continues to decrease with only a few decaying active regions in these data sets. From December 2007 to March 2008 only a few very small active regions appear. From October 2008 to the last data set taken on December 2008 there are no active regions present.

As I am interested in identifying small-scale features in magnetograms whose flux will often be just above the noise level, the noise in the data needs to be reduced as much as possible. Thus further processing was applied to these data. At the photospheric level, I wish to analyse the radial component of the magnetic field. This ensures that a direct comparison can be made between the magnetic fields of features from various positions on the surface. To extract this from the line-of-sight component observed, all pixels are multiplied by $\frac{1}{cos(\psi)}$, where ψ is the heliocentric angle. The assumption here is that the magnetic field of all photospheric features is radial. As $\frac{1}{cos(\psi)}$ tends to infinity towards the limb ($\psi = 90°$), a heliocentric cutoff $\psi_{cutoff} = 45°$ is chosen. I chose this value after trialing the cutoff values $30°, 45°, 60°$. I discounted the value $60°$ as features were difficult to track towards the limb at this cutoff value. The results for feature identification using a $30°$ or $45°$ were very similar but the $\psi_{cutoff} = 45°$ was chosen as the data sets with this cutoff contained a greater number of features, thus giving better statistics.

Projection effects (due to the curvature of the Sun) are taken into account by applying an area correction to each pixel. The corrected area of each square pixel is then given by:

$$A_{c1c2} = \int_{\phi_c=\phi_{c1}}^{\phi_{c2}} \int_{\theta_c=\theta_{c1}}^{\theta_{c2}} R^2 sin(\theta_c) d\phi_c d\theta_c,$$

where R is the radius of the Sun, θ_{ci} is the co-latitude and ϕ_{ci} is the longitude of the pixel. The magnetic field from each pixel is converted to flux by multiplying the original signal detected from each pixel by the corrected pixel area.

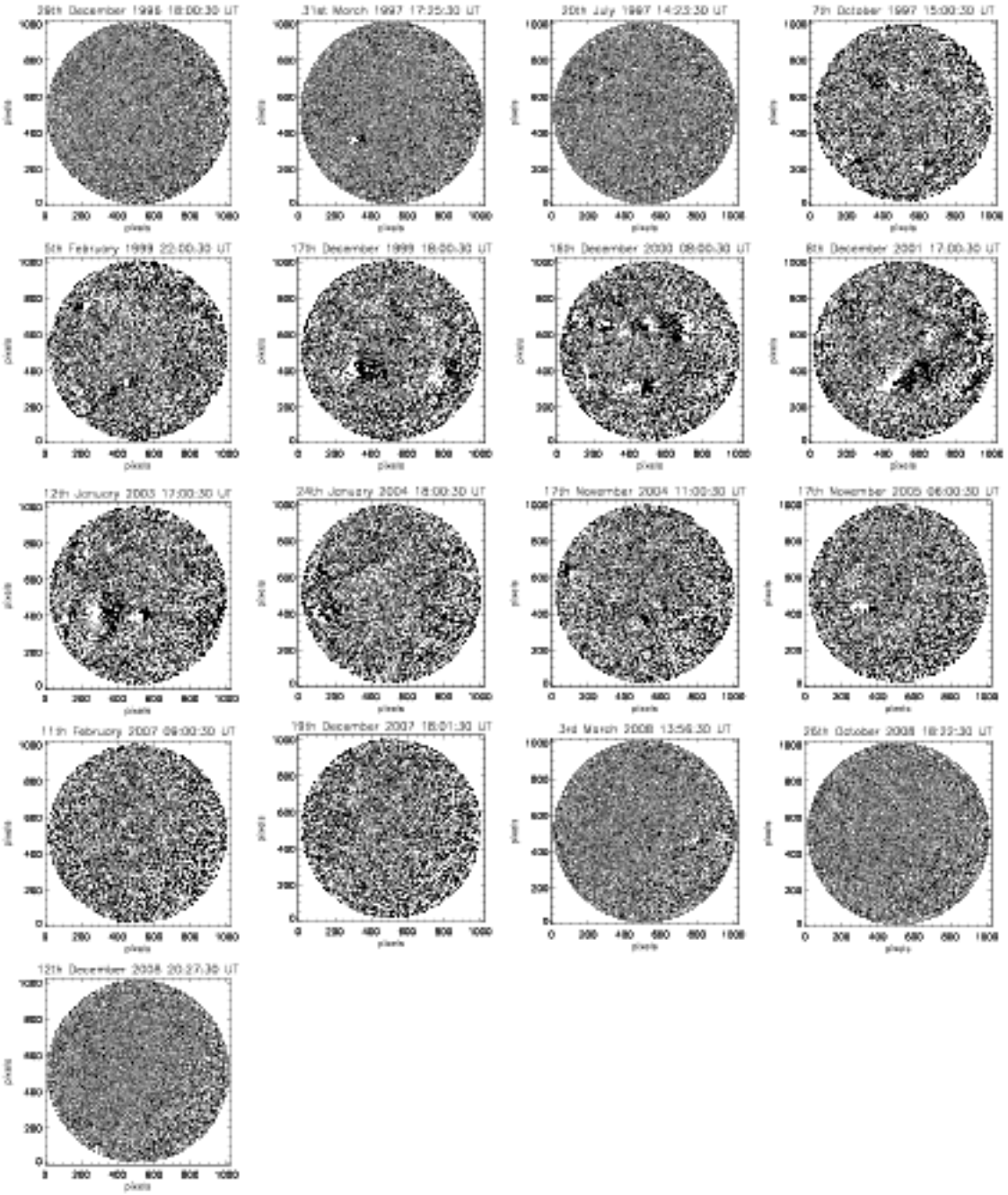

Figure 2.1: Example magnetograms of the data from each MDI full-disk data set, with pixel saturation ± 50 Mx cm^{-2}. The date of each magnetogram is given at the top of each plot.

Year	Start Date	Data Number	Prepared Data Start Time (UT)	Duration After Preparation (hours:minutes)	Number of Images After Preparation	Original σ (Mx cm^{-2})	Corrected σ (Mx cm^{-2})	Level
1996	29th Dec	35010	18:05:30	7:50	96	16.08	11.24	1.5
1997	31st March	37217	17:07:30	6:48	84	15.42	10.98	1.5
1997	20th July	39878	14:05:30	7:50	96	15.40	11.31	1.5
1997	7th Oct	41775	15:27:30	7:23	94	27.09	11.45	1.8
1999	5th Feb	53446	22:33:00	8:22	92	27.88	11.78	1.8.2
1999	17th Dec	61002	18:34:00	7:21	92	28.39	12.67	1.8.2
2000	16th Dec	69752	08:11:30	7:44	96	29.60	12.99	1.8.2
2001	8th Dec	78329	17:44:30	7:11	89	28.55	12.68	1.8.2
2003	12th Jan	87929	17:29:30	7:26	92	29.55	12.99	1.8.2
2004	24th Jan	96978	18:39:30	7:16	90	28.58	12.32	1.8.2
2004	17th Nov	104123	11:28:30	7:27	94	27.11	11.46	1.8.2
2005	17th Nov	112878	06:21:30	7:34	93	27.31	11.49	1.8.2
2007	11th Feb	123705	09:37:30	7:18	90	27.68	11.46	1.8.2
2007	19th Dec	131178	18:24:30	7:31	93	27.55	11.40	1.8.2
2008	3rd March	133717	13:06:30	7:49	96	16.51	11.39	1.5
2008	26th Oct	138666	18:05:30	7:50	96	16.21	11.16	1.5
2008	12th Dec	139796	20:05:30	7:50	96	16.69	11.31	1.5

Table 2.1: Information relating to the full-disk MDI data sets. The value σ is defined as the signal error, the corrected data σ is the value used to determine a minimum flux threshold in feature identification.

Satellite instruments are highly vulnerable to cosmic ray impacts on their detectors, so it is desirable to reduce their effect as much as possible. In particular, cosmic rays may hit more than one pixel and so spatial comparison techniques to spot these pixels do not always work. Cosmic ray effects are removed by despiking images using 'zspike' (Deforest, 2004). This identifies the pixels affected by cosmic ray hits, by comparing the pixels from the reference frame, temporally (± n frames, where here n =3), to find pixels which have a value which is either unrealistically high or low. These bad pixels are then replaced with the mean value of the surrounding good pixels, in the reference frame.

To further reduce the spatial noise, from granulation, in the SOHO/MDI full-disk data, a Gaussian type smoothing was used. The data set was split into two sets, one containing only positive pixels and the other containing only negative pixels. The polarities were considered separately, to prevent small-scale bipoles from disappearing. Each pixel was smoothed by accounting for the mask of eight pixels surrounding it. Each pixel $r(x, y, t) = r^k_{i,j}$ is smoothed spatially in the following way:

$$r^k_{i,j} = (r^k_{i,j} + 0.25(r^k_{i\pm1,j} + r^k_{i,j\pm1}) + 0.125(r^k_{i\pm1,j\pm1} + r^k_{i\pm1,j\mp1}))/2.5$$

After smoothing, the positive and negative components were recombined.

Magnetograms are also corrected for temporal noise, due to p-mode oscillations modifying the magnetic field strength along the line-of-sight and photon counting statistics, by applying a Gaussian temporal smoothing. Each pixel $r(x, y, t) = r^k_{i,j}$ then becomes

$$r^k_{i,j} = \frac{r^k_{i,j} + g(1)(r^{k\pm1}_{i,j}) + g(2)(r^{k\pm2}_{i,j}) + g(3)(r^{k\pm3}_{i,j})}{1 + 2g(1) + 2g(2) + 2g(3)},$$

where:

$$g(x) = \frac{1}{\sqrt{2\pi}} e^{-\frac{x^2}{4}}.$$

The centre of the Gaussian is the reference frame and the temporal average is over 7 frames (3 forwards, 3 backwards and the central frame). Temporal averaging and spatial smoothing allows for better association of features between frames as it has the result of enhancing each magnetic feature over area and time.

At this stage the images in each data set are at ≈ 1 minute cadence. P-modes can affect magnetic field observations as the photosphere moves towards and away from us. I average magnetograms over a 5 minute cadence to compensate for the effects of p-modes as these have been found to have a dominant frequency at 5 minutes. This is done using the header information from each image, to average over ≈ 5 minutes. Missing images can cause this to vary resulting in a cadence of 4-6 minutes. After all the corrections have been applied the resultant data sets are 8-10 hours long with a cadence of 4-6 minutes and cover an area of 445.93×10^3 Mm^2 per frame.

Despite the SOHO website stating that all the magnetogram data was calibrated to level 1.8.2 it was discovered that the data I obtained was actually of two different calibration levels: level 1.5 for the December 1996-July 1997 and March 2008-December 2008 data sets and level 1.8.2 for the intermediate data sets. Whilst the level 1.8.2 data have already had a degree of correction for plate scale, zero offset and sensitivity effects, and the most severe cosmic rays have also been removed, the level 1.5 data are uncalibrated for

these effects. On analysing both levels of data it was clear that the mean field strength of the pixels in the level 1.8.2 data was considerably higher than those in the level 1.5 data. Therefore, a correction factor had to be applied to the level 1.5 data. This correction factor was applied once all the data sets had been processed by the methods above. The correction factor was found by comparing the magnetic field values of each data set. It was found that a correction factor of 1.84 applied to all pixels gave magnetic field values for the December 1996-July 1997 and March 2008-December 2008 data sets which were consistent with those values found for the October 1997-December 2007 data sets.

2.2 Hinode

The Hinode satellite, the successor to Yohkoh, is a joint collaboration between the Japanese Aerospace Exploration Agency's Institute of Space and Aeronautical Science (ISAS/JAXA),National Aeronautics and Space Administration (NASA, United States) and the Science and Technology Facilities Council (STFC, United Kingdom) (Kosugi et al., 2007). It was launched on 22nd September 2006, with the first data being made available in April 2007. Hinode orbits the Earth in a quasi-circular sun-synchronous orbit which allows contact with a ground station in Norway in nearly every orbit to download data. Hence, observations are possible 24 hours a day for about 8 months of the year. Hinode has a mission life $\geq$ 3 years and its principal aim throughout this time is to understand the role of how energy is generated in the photosphere and how this energy affects the upper corona and inter-planetary space. It has three packages on board:

- SOT (Solar Optical Telescope), which is a white-light telescope and vector magnetograph, uses polarizing optics to measure magnetic fields in the solar photosphere.
- EIS (Extreme Ultraviolet Imaging Spectrograph) takes high-cadence, monochromatic images of the transition region and corona of the Sun.
- XRT (Solar X-Ray Telescope) is a high-resolution, grazing-incidence telescope with the primary purpose of observing the generation, transport, and emergence of solar magnetic fields, as well as the ultimate dissipation of magnetic energy in forms such as flares and pico-flares, coronal heating, and coronal mass ejections.

SOT is the telescope used for studying photospheric magnetic fields (Tsuneta et al., 2008). It consists of two instruments: the Optical Telescope Assembly (OTA) and the Focal Plane Package (FPP). OTA is a 50 cm diffraction-limited Gregorian telescope and the FPP includes the narrowband filtergraph (NFI), the broadband filtergraph (BFI) and the Stokes Spectro-Polarimeter (SP). The combined SOT system is optimized for the accurate measurement of the vector magnetic field in the photosphere and dynamics of both the photosphere and chromosphere associated with magnetic fields.

I use NFI data as opposed to SP data since the SP rasters across the Sun to produce images, so although its resolution and the sensitivity are very good, the cadence is not high enough for tracking the evolution of small-scale features. NFI data is primarily chosen due to the much higher temporal resolution. Despite NFI data having a reduction in both spatial resolution and sensitivity, compared with the SP data, features

with flux of order 10^{18} Mx can still be clearly identified. The maximum field of view for NFI is 328 $\times$ 164 arcsecs with on board pixel resolution at 0.08 arcsecs, but the data is binned 2x2 before it is sent to Earth to give a pixel resolution of 0.16 arcsecs, as this improves the signal to noise ratio.

2.2.1 NFI Data Preparation

The data sequence was obtained on the 19th September 2007 between 12:44 UT and 17:43 UT from NFI, using the Na I D1 resonance line at 5896 Å, in the Solar Optical Telescope (SOT) package aboard Hinode (Kosugi et al., 2007; Tsuneta et al., 2008). The data was originally prepared by Craig DeForest (DeForest et al., 2009). Line-of-sight high-resolution magnetograms were derived from the observed Stokes parameters I and V by first subtracting the NFI pedestal of 800 digitizer counts from each V, I pair. Then, we apply the conversion factor of (Lamb et al., 2008), who used a simultaneous MDI and Hinode data set to calibrate the Hinode data, and multiply the pixel ratios $V/I*$ by 6555 Mx cm^{-2}, where $I* = I - 2 \times 200. \times$FGNINT. FGNINT is taken from the header information and indicates how many images are integrated, in this case it is 8. Below is a description of the data processing steps.

The original field of view for NFI was reduced because of a reported glint near the left hand side (DeForest et al., 2009) and due to the presence of air bubbles in the index-matching fluid in the tunable filter in the upper right hand portion of the image (Ichimoto et al., 2008). The reduced field of view is 138 $\times$ 96 arcsecs (863 $\times$ 600 pixels). The radial component of the magnetic field was extracted from the magnetograms by applying a $\frac{1}{cos(\psi)}$ correction to each pixel, where ψ is the heliocentric angle. To despike the images, and remove cosmic ray hits 'zspike' (Deforest, 2004) is used to identify bad pixels, which are then replaced with the mean value of the surrounding good pixels. Further spatial smoothing, applied to reduce instrumental noise, was achieved by applying a 2 pixel FWHM Gaussian kernel. To reduce the effect of p-mode oscillations images were smoothed temporally by applying a 3 minute FWHM Gaussian weighting function. Finally the NFI data was deconvolved using an NFI point-spread function, which was derived by DeForest et al. (2009) using NFI observations from the July 2008 eclipse. The resulting data consisted of 200 images with a precise 90 second cadence starting at 12:44 UT and ending at 17:44 UT.

A comparison of both the magnetic field images in Figure 2.2 reveals that the high-resolution NFI data identifies much smaller features, and more of the quiet-Sun structure, than the full-disk MDI magnetograms. The white box in Figure 2.2a shows the field of view of the NFI data compared to the full-disk MDI.

2.3 Residual Data Noise Estimate

In the chapters that follow, the data which is processed here is analysed using various feature identification programs and other event detection algorithms. In order to apply the feature identification programs, an estimate of the remaining noise in the prepared data is required. Since the method for determining noise is the same in all cases, it is described in detail here.

Any observation is subject to both systematic and random errors, those which are known continual errors

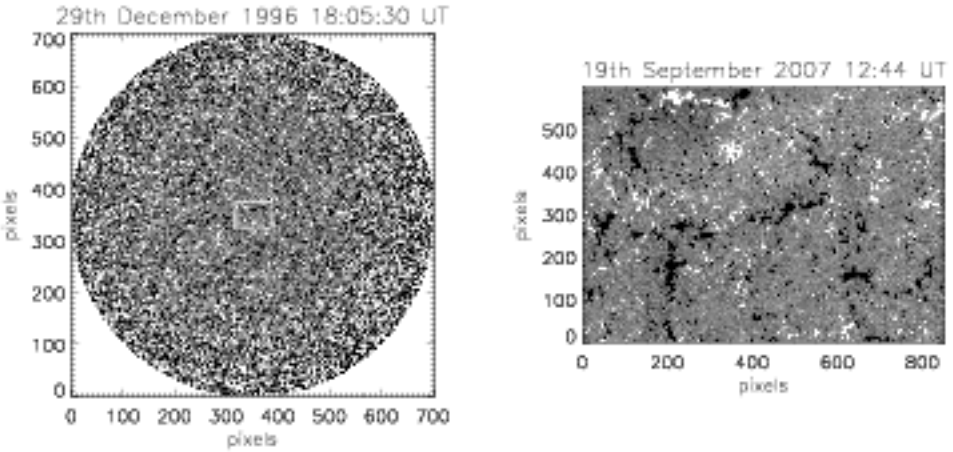

Figure 2.2: Example processed magnetograms from (a) full-disk MDI (white square is the field of view of the prepared NFI) and (b) NFI/Hinode, both with pixel saturation ±30 Mx cm^{-2}. Note these images were not taken at the same time.

in all measurements and those which are caused by unknown or unpredictable changes, respectively. In the data discussed in this chapter systematic errors can manifest themselves in ways such as field dimming due to active regions, pixel gain errors and ageing of the sensor. Random errors can become present through radiation damage of pixels, instrumental noise and unpredictable changes in environmental conditions. The methods above are designed to minimise these errors and there effects on feature identification and tracking as much as possible. However, after preparation the processed data still has some residual systematic effects and random errors due to the fact that none of the correction techniques are perfect.

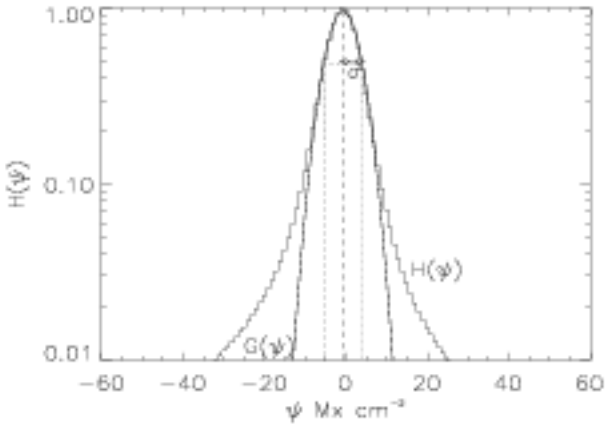

Figure 2.3: Histogram, H(Ψ), of the pixel fluxes in the prepared Hinode data. A Gaussian, G(Ψ), is fitted to the core of the histogram (solid), with the centre of the Gaussian (dashed) and FWHM (dotted) marked.

To find the residual noise in the data the first step is to plot the histogram of the distribution of pixel fluxes ($H(\psi)$). By assuming that the core of the distribution corresponds to noise and that it is Gaussian

(Hagenaar et al., 1999), a parabolic fit is then applied to the central part of the distribution

$$G(\psi) = H_{max} e^{-\psi^2/2\sigma^2}.$$

The half-width half-maximum of the Gaussian, σ, is defined as the signal error and is used to determine a minimum threshold in feature identification. An example of the histogram ($H(\psi)$) and the Gaussian fit ($G(\psi)$) from the NFI data is shown in Figure 2.3.

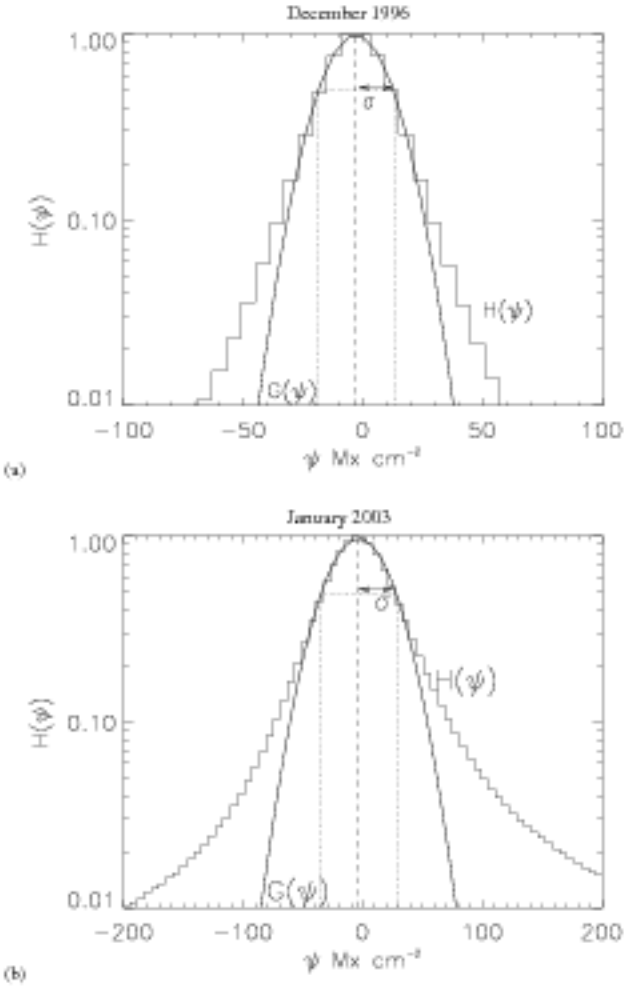

Figure 2.4: Histogram, H(Ψ), of the pixel fluxes in the prepared full-disk MDI data from (a) December 1996 and (b) January 2003 . A Gaussian, G(Ψ), is fitted to the core of the histogram (solid), with the centre of the Gaussian (dashed) and FWHM (dotted) marked.

The value of σ found for the Hinode data was 4 Mx cm^{-2}. The values of σ found for the full-disk data are listed in Table 2.1. It can be seen that the value of σ varies slightly in phase with the solar cycle. This can partly be explained by Potts and Diver (2008), who found that the sensitivity of the pixels and the uniformity of the field of view in the MDI CCD changed over the solar cycle as a result of radiation damage, optics damage and general ageing of the instrument. It can also be seen that there is an asymmetry

in Figures 2.3, 2.4 a) and b). This asymmetry is always apparent when plotting the distribution of the pixel fluxes due to the imbalance of flux on the portion of disk under observation.

Chapter 3

Feature Identification and Tracking

Magnetograms of the photosphere reveal the patchwork nature of negative and positive polarity magnetic features on all scales. Analysis of these features is used to give an insight into the dynamics of magnetic fields in the photosphere. In this thesis, I analyse magnetograms extensively, with all the analysis stemming from magnetic feature identification and magnetic feature tracking.

Feature identification in magnetograms is the process of separating out genuine concentrations of flux (known as flux features) from the background noise on a frame by frame basis. Feature tracking is the process of associating magnetic features between frames in order to follow their evolution. Neither of these processes has just one approach and, depending on the assumptions made, results can vary. This chapter describes the feature identification and tracking algorithms, which I use throughout this thesis.

Small-scale feature identification has been ongoing since the 1970's when observations revealed that the quiet-Sun contained a large amount of the Sun's surface flux (Beckers and Schröter, 1968; Harvey, 1971; Dunn and Zirker, 1973; Stenflo, 1973; Livingston and Harvey, 1975; Smithson, 1975). Original observations were magnetograph photographic plates from observatories such as Kitt Peak and Mount Wilson (Babcock, 1953; Harvey, 1971; Livingston and Harvey, 1971) and the analysis of the quiet-Sun was based around defining the small-scale features, their behaviour and discovering their origins (Martin, 1988). Initially the typical flux of features analysed was of order 10^{18} Mx on a length scale of a few hundred km (Livingston and Harvey, 1969; Harvey, 1971). As observations improved in sensitivity and resolution, the size of the features which could be observed decreased and is now down to a few times 10^{16} Mx (Wang et al., 1995).

Initially quiet-Sun, small-scale features were identified manually (Martin, 1988; Harvey, 1993; Wang et al., 1995). The process of feature identification progressed to automated methods for a number of reasons: the move from photographic plates to digital data, the increase in the amount of data, and the impetus to apply a more objective analysis to data. In particular, new satellite instruments for measuring photospheric magnetic fields, such as SOHO/MDI (launched in 1995), provided observers with a vast quantity of high-cadence magnetogram observations. The advantages of automated identification of features, as opposed to manual identification, in data like this is the speed at which a large number of features can be identified, the ability to identify structure within flux features and also identifying weak flux features which can be missed by eye.

The tracking of features has enabled better estimates of feature lifetimes to be made and also allowed the evolution of features to be followed (DeForest et al., 2007; Lamb et al., 2008). This was mostly done manually until the late 90's, but the development of automated identification methods, has led to auto-

mated tracking algorithms. Automated tracking methods allow for a more in depth study into the processes of small-scale feature evolution, dispersal of small-scale flux and how the quiet-Sun surface structure is obtained (Schrijver et al., 1997; Hagenaar et al., 1999).

Using data of magnetic features that have been identified and tracked Parnell et al. (2009) found that the distribution of all features identified in observations from Hinode/NFI, and both MDI full-disk and high-resolution, follows a power-law over 5 orders of magnitude of flux. These results suggest the presence of a scale-free element in the production of the surface flux, either in the form of a scale-free dynamo or through surface processes creating a scale-free distribution.

The feature identification and tracking methods used on all these data sets are the same and so here, to prevent repetition, I explain these methods in detail.

3.1 Feature Identification

There are 3 main automated feature identification algorithms: clumping, downhill and curvature. Each varies in their definition of a flux feature and so the results of the algorithms are sensitive to the methods used and the assumptions made (DeForest et al., 2007; Parnell et al., 2009). In this thesis I only use the clumping and downhill approaches which are described below.

The clumping and downhill methods were developed by Parnell (2002) and Welsch and Longcope (2003), respectively. Here, I describe the clumping and downhill algorithms, which I have used, to identify features. The following steps described in this paragraph are the same regardless of the method used. The original data is split into two cubes, one cube containing only positive pixels and one cube containing only negative pixels. The feature identification is applied to these cubes separately and then the cubes are re-combined after the algorithm is complete. The features are identified in each single-polarity frame in turn and Figure 3.1a shows an example frame, of size (x,y) (where x,y are the x and y sizes of the original array, respectively), containing only positive pixels. Before features can be identified, ghost-cells (of value zero) need to be added around the frame, increasing it to size (x+2,y+2) (Figure 3.1b). This allows for a mask of 8 pixels to be placed around any pixel in the original part of the frame, containing the data. Each pixel which is below the cutoff is set to zero, where the cutoff is $m\sigma$ (where $m = 2$ and σ is determined from the processed data in Chapter 2). The remaining n non-zero pixels are ranked in descending order, with each pixel being given a unique integer label according to its position in the ranked list i.e. integer array $[n,n-1,...,2,1]$, with n corresponding to the highest value pixel, $n-1$ to the second highest pixel and so on with 1 being given to the lowest ranking pixel. This is shown in Figure 3.1c. The remaining pixels are now ready to be grouped into features. Features are found by looping through each pixel in descending order and creating a mask of eight pixels around them, as seen in Figure 3.1d. The value of the central pixel is then compared to the other eight pixels in the mask. If the central pixel is the largest value then its label is untouched, however if one of the surrounding eight pixels has a larger value then the central pixel is relabeled with the larger value label (Figures 3.1e and 3.1f). Once this process has been completed for every pixel in order singly peaked features will have been identified as shown in Figures 3.2a and 3.3a.

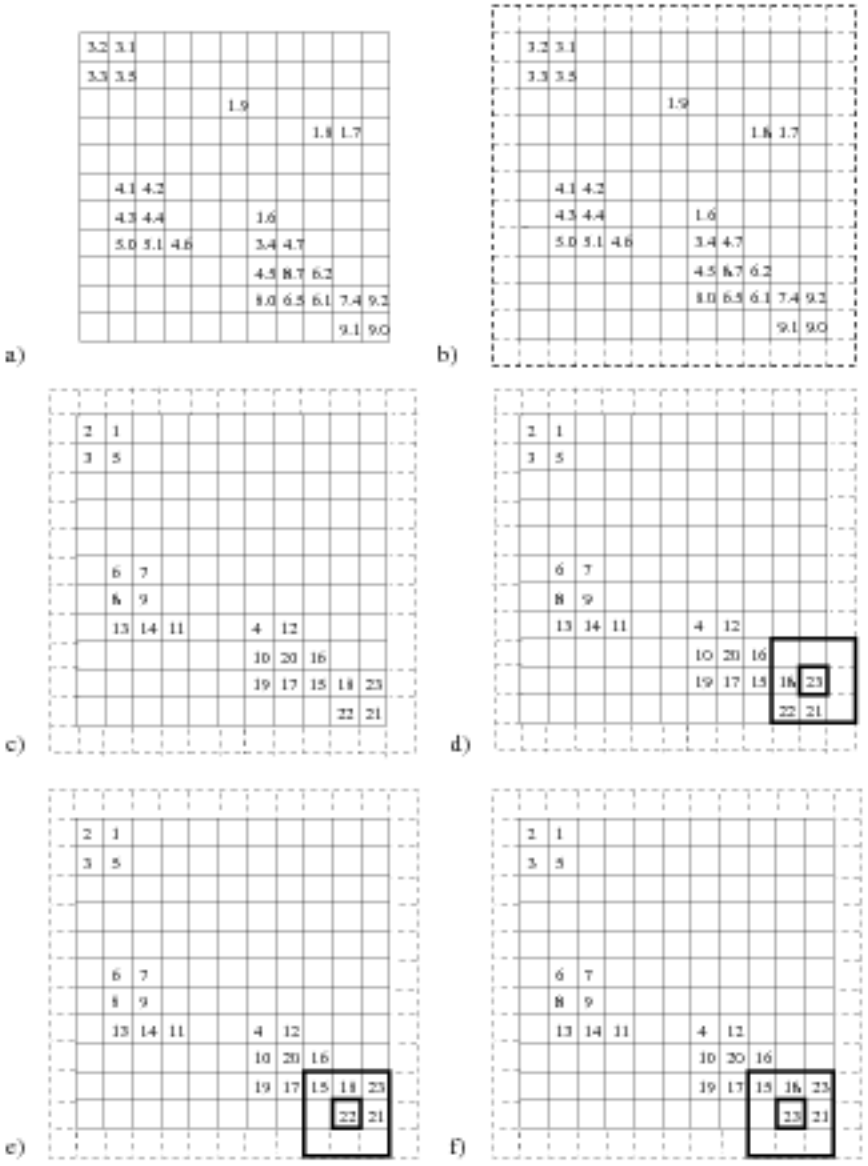

Figure 3.1: Cartoons illustrating the steps of downhill and clumping feature identification, as applied to a single frame. (a) Initially two cubes of single polarity data are created i.e to create the positive cube all the negative polarity pixels are set to zero. (b) Then ghost cells, of value zero, are placed around the original data. (c) To identify the features, each pixel is listed in descending order and given a unique integer label according to its position in the list (the higher the pixel value the bigger the integer label). Once the pixels are in descending order a mask is placed over each pixel in order (from highest to lowest), covering the pixel and the eight surrounding it. The central label is compared to those surrounding it (d-f). If it is the largest then its label remains the same (d), but if one of the surrounding pixels has a larger value then the central pixel takes that label too (e,f). This process is repeated for all non-zero pixels.

This is the stage where the two algorithms diverge. At this point the features which have been identified are contiguous same-sign pixels with flux above a lower cutoff, that are singly peaked (i.e. as Figure 3.3 shows), which is the definition of a downhill feature. This method is called 'downhill' because each feature only has a single maximum in absolute flux and all pixels decrease in absolute value (flow downhill) as you head away from a local maximum. Consequently the features identified by the downhill approach are

known as flux peaks.

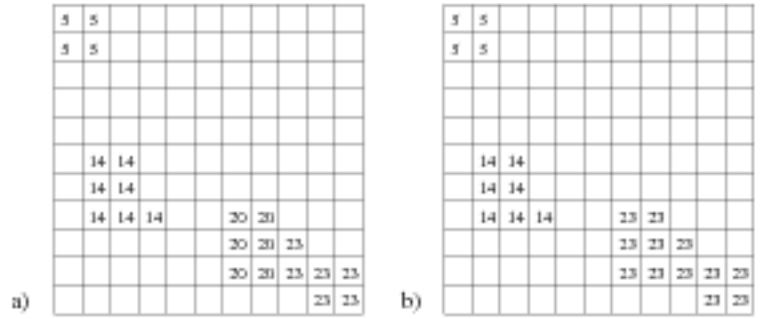

Figure 3.2: (a) Data after the steps in Figure 3.1 are completed and downhill features (flux peaks) have been identified. In order to identify the clumping features (flux massifs) the steps from Figure 3.1(d-f) must be repeated until none of the non-zero pixels change their labels when the mask is placed upon them.

In order to find the features, known as flux massifs, identified by clumping, all features which have non-zero labels adjacent to one another need to be given the same label. This is achieved by applying the eight pixel mask to all non-zero pixels again, changing the value of the pixels if there is a larger pixel value in the mask. This is repeated until no pixels change their value. The result is groups of same sign contiguous pixels, with flux above the lower cutoff, which share a unique label as shown in Figures 3.2b and 3.3b. These flux massifs may be multiply peaked, but do not have to be.

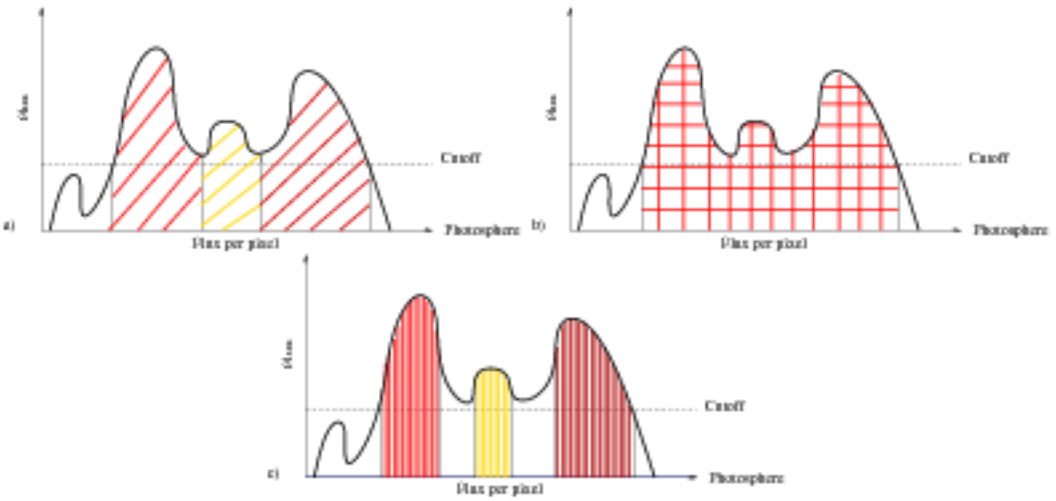

Figure 3.3: Cartoons illustrating how features are identified using each method: (a) the downhill method segments the single flux massif into three flux peaks separated at the saddle points, (b) the clumping method identifies one large flux massif above the threshold (c) the curvature method identifies the cores of the three peaks above the threshold.

Once all the features in the positive and negative data are identified, the ghost cells are removed and the positive and negative cubes are recombined. Using the same example frames as that in Figure 2.2, the features found using both the clumping and downhill methods have been coloured, in the NFI (Figure 3.4)and full-disk data (Figure 3.5). An additional example has also been provided for the full-disk data in Figure 3.5, which contains an active region to highlight the differences between the clumping and downhill

methods.

Like the downhill method, the curvature method identifies the detailed structure of photospheric magnetic features. However, the downhill approach is used here because, unlike curvature, no correction factor is required to determine the fluxes for the photospheric flux features. The difference essentially between the clumping and downhill methods is that flux peaks are flux massifs divided along their saddle-lines.

After the downhill and clumping feature identification is applied to the data sets, area filtering is applied. When working with data containing features with fluxes just above the residual data noise, it is useful to reject small-features, because the likelihood of false positives is much greater. A minimum area value of 4 pixels is defined which is equivalent to 0.05 Mm^2 for the Hinode/NFI and between 7.84-11.08 Mm^2 (depending on the position on the disk) for the MDI full-disk data at disk centre. A lifetime criteria is also applied after feature association, which is discussed in the next section.

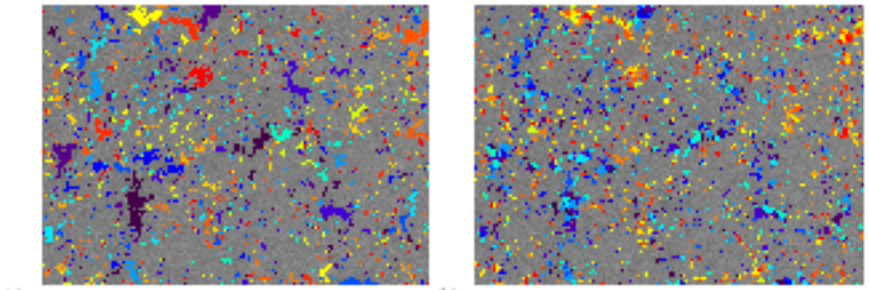

Figure 3.4: (a) Flux massifs identified using the clumping method and (b) flux peaks identified using the downhill method in the same NFI example frame as in Figure 2.2b, taken on the 19th September 2007 at 12:52:14 UT. The blues and magenta colours are the negative features, whilst the reds and yellows are the positive features. The background pixels have been saturated at $\pm$ 30 Mx cm^{-2}.

Once the features are identified their characteristics are found: flux, area and centre of flux (a flux weighted centre equivalent to the centre of mass). From Figure 3.3, it is obvious there will be a difference, between the mean area and flux of features identified in clumping and downhill data, with the values being found in downhill being smaller. Small IN and network features will often be identified as individual flux massifs and flux peaks as they are likely to only have one flux peak, but larger features, identified as a single flux massif, will tend to be segmented into multiple flux peaks by the downhill approach. This in turn will affect the flux distributions found by the different methods for a given data set, with features identified by the downhill method having a distribution which is enhanced at small fluxes and drops off faster than features identified by the clumping method.

Something that also needs to be considered is the results of the clumping and downhill approaches if they are applied to data sets from different instruments with different resolutions. Applying the downhill method to data with increased resolution has the effect of identifying more structure (flux peaks) within larger flux features (i.e there will be a reduction in the number of larger features identified). This is ideal if the aim of the feature identification is to gain insight into the complex structure of large flux features, such as sunspots. However, if the aim is to compare features from different instruments with different resolution, then the clumping method is more suitable as the larger flux massifs it identifies are much less dependent on instrument sensitivity (Parnell et al., 2009). For both methods, if the resolution is increased the number

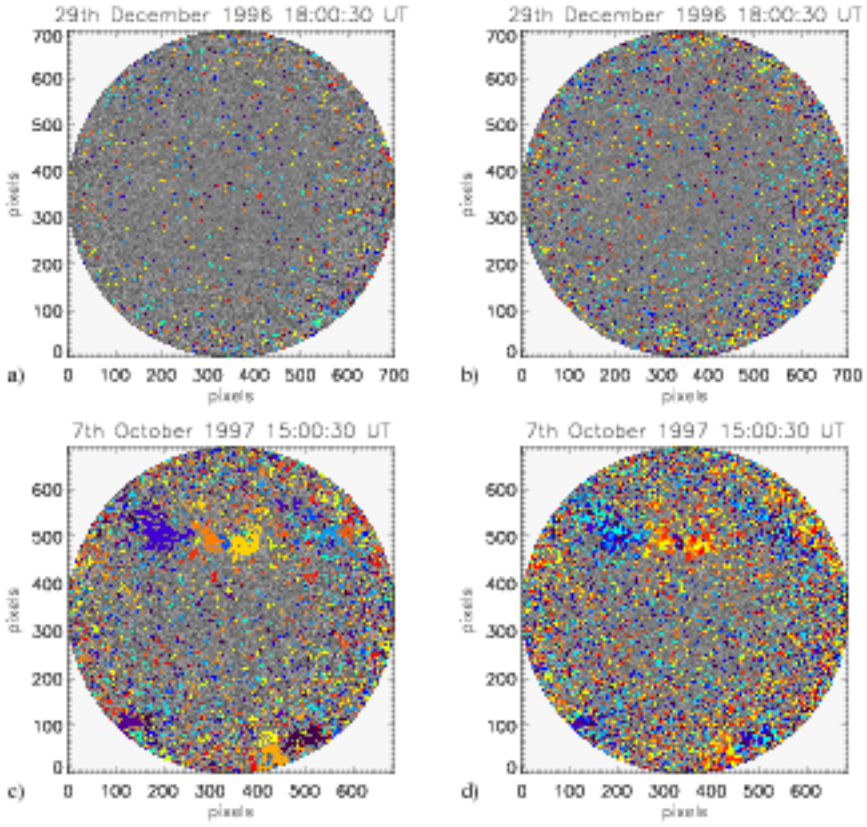

Figure 3.5: Flux massifs identified in full-disk data from December 1996 (a) using the clumping method and (b) the downhill method and from October 1997 (c) using the clumping method and (d) using the downhill method. The blues and magenta colours are the negative features, whilst the reds and yellows are the positive features. The pixel saturation is at $\pm$ 100 Mx cm^{-2}.

of small flux peaks and massifs detected will increase. Parnell et al. (2009) investigated the probability distributions of fluxes of massifs over varying resolutions from Hinode/NFI, MDI high-resolution and MDI full-disk data and found that they follow a single power law, showing that the features found by the clumping method are largely invariant to different instruments and resolutions. Also, for the downhill method, a drawback of identifying the flux peaks is that they are very transient. The fact that downhill identifies local maxima in flux makes it susceptible to flux fluctuations due to noise or solar convection. The bonus of clumping is that the structure of flux massifs identified are not dependent on the transient peaks of flux they contain.

3.2 Feature Tracking

Although a large amount of useful information can be gained about flux features by just identifying them, tracking the features allows for peak flux, peak area and lifetime to be determined. Another benefit of feature tracking is allowing a more accurate determination of when and how a feature is born or dies.

When the preparation of the data was discussed in Chapter 2 it should be noted that whilst derotation was applied to the Hinode/NFI data during the preparation of the data, no derotation was applied to the SOHO/MDI full-disk data. Here I briefly explain why this does not affect the process of feature tracking in the SOHO/MDI full-disk data. Derotation of full-disk data would be done with respect to a reference frame which requires that you reduce the field of view further as pixels will not always be present on the disk. This is not desirable as I have already reduced the field of view as discussed in Chapter 2. Also, it is unlikely that the rotation will have a significant affect on feature association for the following reason. The Sun rotates with a synodic rotation velocity $w = 13.39 - 2.30sin^2\theta_c - 1.62sin^2\theta_c$ deg per day at any co-latitude θ_c, this gives a maximum rotation rate of 565 km in 5 minutes at the equator, which is the cadence of the data. At a maximum speed of 5 km s^{-1} (Harvey and Martin, 1973; Born, 1974; Zirin, 1985; Snodgrass, 1983; Chou and Wang, 1987; Barth and Livi, 1990; Keller et al., 1994; Wang et al., 1995; de Wijn et al., 2008) a feature will move 1500 km in 5 minutes. Thus the combined maximum distance a features could move is 2065 km in 5 minutes. This is a maximum movement of just over 1 pixel of the full-disk data. As the minimum area of a feature is 4 pixels, the rotation is not large enough to prevent features being associated accurately between frames using area overlap, which is the method used, as discussed below.

Feature tracking involves associating a feature in one frame with a feature in the previous frame. This would be simple and straight forward if features tended to typically overlap just one or no other features in the previous frame. However, complications arise because multiple features often overlap. This can occur for several reasons. The processes of fragmentation and merging lead to a 'one to many' overlap and a 'many to one' overlap, respectively. It is also possible to find 'many to many' overlaps of features which may arise through a combination of these processes. Below, we briefly describe how we deal with each case.

3.2.1 Associating Features

I consider each pair of consecutive frames to find the associations between features. In order for two features to be associated between frames they must overlap and have comparable flux. I look at each feature Φ_k^j in frame j and compare with the corresponding pixels in the j-1 frame. Conversely, I also compare each feature Φ_i^{j-1} with the corresponding pixels in frame j. All cases which can occur are discussed below. In Figure 3.6 there is a cartoon picture to illustrate each case.

- **None to one**: If Φ_k^j overlaps no like-polarity features in frame j-1, Φ_k^j is said to have 'appeared' and is given a new unique label.

- **One to none**: If Φ_i^{j-1} overlaps no like-polarity features in frame j, it is said to have 'disappeared' and it is unique label is not used again after frame j-1.

- **One to one**: If there is a unique overlap between like-polarity features Φ_i^{j-1} and Φ_k^j, then Φ_k^j will be given the unique label of Φ_i^{j-1} and the feature is flagged as 'pre-existing'.

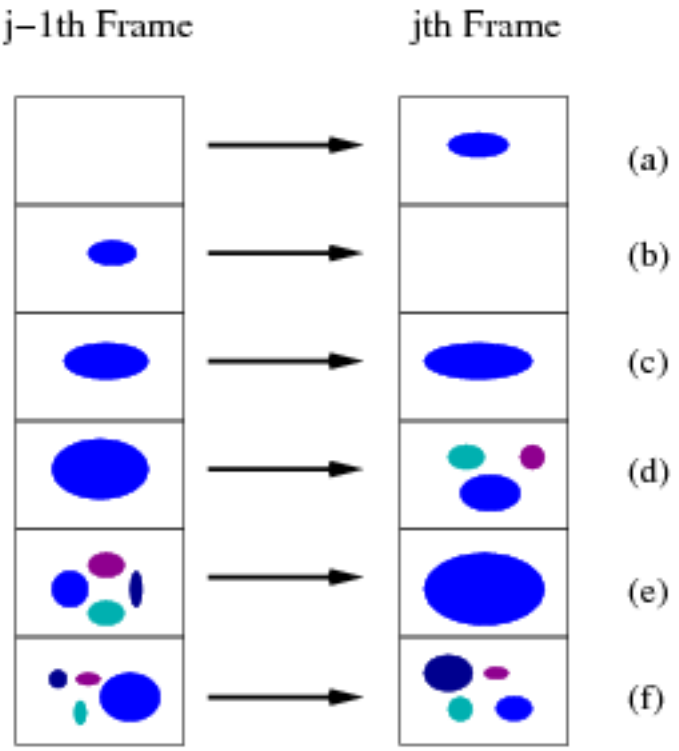

Figure 3.6: An illustration of the various cases which can occur when associating features between frames. (a) None to one (appearance), (b) one to none (disappearance), (c) one to one (direct association), (d) one to many (fragmentation), (e) many to one (merging) and (f) many to many (combination of processes).

- **One to many**: If Φ_i^{j-1} overlaps m like-polarity features in frame j (Φ_{k1}^j,...,Φ_{km}^j), the unique label of Φ_i^{j-1} is passed on to the feature in j which satisfies the following conditions. Let feature $\Phi_{k\alpha}^j$ ($\alpha \in 1, ..., m$) overlap Φ_i^{j-1} with an area of $a_{ik\alpha}^{j-1}$ such that

$$\sum_{\alpha=1}^{m} a_{ik\alpha}^{j-1} \leq A_i^{j-1} ,$$

where A_i^{j-1} is the area of the feature Φ_i^{j-1}. The '$\leq$' is required since it is possible that some of the pixels of Φ_i^{j-1} may overlay nothing in frame j. All features $\Phi_{k\alpha}^j$ with

$$\frac{a_{ik\alpha}^{j-1}}{A_i^{j-1}} \geq \frac{1}{m} ,$$

are potential candidates for taking the unique label of Φ_i^{j-1}. If there is only one feature which satisfies the conditions it automatically takes the Φ_i^{j-1} label. If several features satisfy the criteria then the feature $\Phi_{k\alpha}^j$ with $\Psi_{k\alpha}^j / \Psi_i^{j-1}$ closest to one is taken and the other features are flagged as 'appeared through fragmentation'.

- **Many to one**: If n like-polarity features in j-1 (Φ_{i1}^{j-1},...,Φ_{in}^{j-1}) overlap a single feature Φ_k^j in frame j, then Φ_k^j receives the unique label of the feature which satisfies the following conditions. In a similar manner to the one-to-many case, let feature $\Phi_{i\alpha}^{j-1}$ ($\alpha \in 1,...,n$) overlap Φ_k^j with an area of $a_{ki\alpha}^j$ such that

$$\sum_{\alpha=1}^{n} a_{ki\alpha}^j \leq A_k^j \ ,$$

where A_k^j is the area of the feature Φ_k^j. As above, all features $\Phi_{i\alpha}^{j-1}$ with

$$\frac{a_{ki\alpha}^j}{A_k^j} \geq \frac{1}{n} \ ,$$

are potential candidates for passing on their unique labels to Φ_k^j. If there is only one such feature $\Phi_{i\alpha}^{j-1}$ which satisfies these conditions then this feature gives its unique label to Φ_k^j. If there is more than one feature, then the feature $\Phi_{i\alpha}^{j-1}$ with $\Psi_{i\alpha}^{j-1}/\Psi_k^j$ closest to one is taken. All the other features are then flagged as 'disappeared through merging'

- **Many to many**: If n like-polarity features in frame j-1 (Φ_{i1}^{j-1},...,Φ_{in}^{j-1}) overlap with m features in frame j ($\Phi_{k_1}^j$,...,$\Phi_{k_m}^j$), then we can end up with more than one label being carried forward from j-1 to j. Here, to determine which features are associated between frames, we combine the rules used in the one-to-many and many-to-one cases. All feature pairs $\Phi_{i\alpha}^{j-1}$ ($\alpha \in 1,...,n$) and $\Phi_{k\beta}^j$ ($\beta \in 1,...,m$) which satisfy the following overlapping and flux ratio rules are potential candidates for association

$$\frac{a_{i\alpha k\beta}^{j-1}}{A_{i\alpha}^{j-1}} \geq \frac{1}{m} \quad \text{and} \quad \frac{a_{k\beta i\alpha}^{j}}{A_{k\beta}^{j}} \geq \frac{1}{n} \ .$$

Furthermore, in all situations that the above criteria do not lead to unique associations, the further constraint that $\Psi_{i\alpha}^{j-1}/\Psi_{k\beta}^j$ is closest to one is applied. Once unique associations have been established the labels from the $\Phi_{i\alpha}^{j-1}$ features are transferred to the $\Phi_{k\beta}^j$ features where appropriate. Features from j-1 which are not associated are flagged as 'disappeared through merging' and the features from frame j which are not associated are flagged as 'appeared through fragmentation'.

Further data filtering is applied at this stage, in the form of a lifetime criteria: features must live longer than 4 frames for Hinode/NFI (equivalent to 6 minutes) and 2 frames for the MDI full-disk (equivalent to 10 minutes). Care has to be taken when applying filtering to the downhill data as removing features can result in the *swiss cheese problem* (DeForest et al., 2007). This occurs in larger features that are segmented by the downhill identification method and can result in short lived features that are embedded in a larger feature being removed and producing a hole. To avoid this all features which are single flux massifs in the clumping approach, but are multiple flux peaks in the downhill approach, are identified. This is achieved by finding all flux peaks which have a shared boundary with another like-polarity flux peak, as this can only occur for the case of a large flux massif with multiple flux peaks. Any flux peaks which satisfy this criteria are are tagged as 'worms' and will not be removed by the lifetime filtering algorithm.

Once every pair of frames has been considered the association process is complete and each feature will have a unique label which remains with it for its entire life. This means that the frame of birth and death of each feature can easily be determined by identifying when a feature's unique label appears and disappears, respectively. The approach above also provides information on the nature of each birth and death and in doing so all incidences of fragmenting and coalescing are recorded.

Despite having information about the birth and death of each tracked feature there is still, some ambiguity which needs to be resolved. Tracked features can either be born through 'appearance' (e.g. Figure 3.6a) or 'appear through fragmentation' (e.g. Figure 3.6d). Furthermore, the term 'appearance' covers tracked features being born through genuine emergence, as well as the coalescence of sub-resolution flux of an existing dispersed feature, causing it to appear above the threshold (Lamb et al., 2008). Similarly a feature can either die through 'disappearance' (e.g. Figure 3.6b) or 'disappear through merging' (e.g Figure 3.6e), where 'disappearance' covers both cancellation, due to the interaction with an opposite-polarity feature, and the dispersal of flux causing the peak flux of the feature to fall below the flux threshold. The next chapter describes the algorithms developed to determine which 'appearances' are authentic, whilst the algorithm created to detect genuine cancellation is discussed in Chapter 6.

Chapter 4

Detecting Emergence in Quiet-Sun Magnetograms

Emergence of flux into the quiet-Sun occurs through the emergence of ephemeral regions and IN flux. Ephemeral regions observed in magnetograms have been extensively studied providing information about their characteristics and behaviour (Harvey and Martin, 1973; Martin, 1988; Harvey, 1993; Title, 2000b; Hagenaar, 2001). Ephemeral regions are typically bipoles which initially appear close to supergranular boundaries with a separation of between 1.9 and 8.9 Mm (Wang, 1988; Schrijver et al., 1997; Chae et al., 2001; Hagenaar, 2001). Once emerged, the opposite-polarity components of the ephemeral region separate at a rate of between 2-9 km s^{-1} at approximately 180 degrees from each other (Martin and Harvey, 1979; Chae et al., 2001; Hagenaar, 2001). Flux from the ephemeral regions quickly disperses into the surrounding network, giving lifetimes for ephemeral regions of a few hours to a few days. Ephemeral regions have flux in the range of $10^{18} - 10^{19}$ Mx (Harvey, 1993; Chae et al., 2001; Hagenaar, 2001; Hagenaar et al., 2003), with the lower limit on the flux attributed to instrumental limitations.

The process of IN emerging flux is less clear. Some observations have revealed the emergence of IN features in clusters of mixed-polarity features moving radially from a localized position, whilst others show the emergence of an IN bipolar pair which behaves like an ephemeral region (Zirin, 1985; Martin, 1988; Wang et al., 1995). This has raised the question of whether or not IN features are a continuation of ephemeral regions down to smaller scales. This chapter discusses how to detect these emerging ephemeral region and emerging IN flux in magnetograms.

4.1 Detecting Emerging Events in Magnetograms

In order to develop a detection algorithm for newly emerging flux one must first consider physically how flux might emerge. There are two hypotheses regarding the structure of ephemeral regions as they emerge. The first is that as a flux tube rises from the convection zone into the photosphere a pair of opposite polarity features appears in the photosphere with the same absolute flux and area (Figure 4.1). The second is that as a flux tube rises from the convection zone it is shredded by convective flows. Thus, rather than just a pair of features appearing on the photosphere, a pair of clusters of features appears, one positive cluster of features and one negative cluster of features, as seen in Figure 4.2 (Zwaan, 1987; Wang et al., 1995; Hagenaar, 2001). Theoretically the total absolute flux of each cluster should be the same.

Furthermore, detecting emergence in magnetograms is not straightforward since emergence is not the

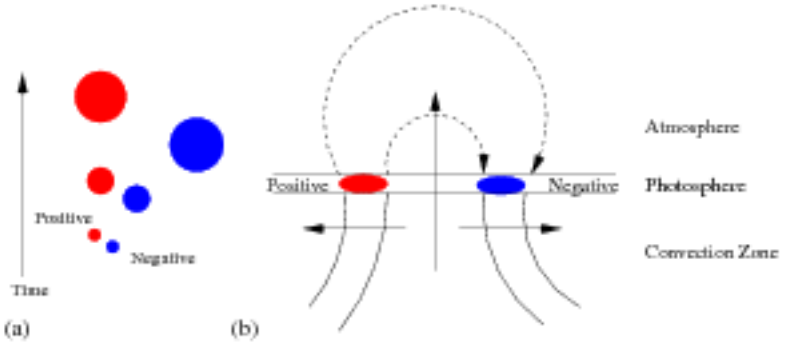

Figure 4.1: An illustration of the bipolar flux emergence hypothesis (a) as seen in the photosphere and (b) as seen in a vertical cut.

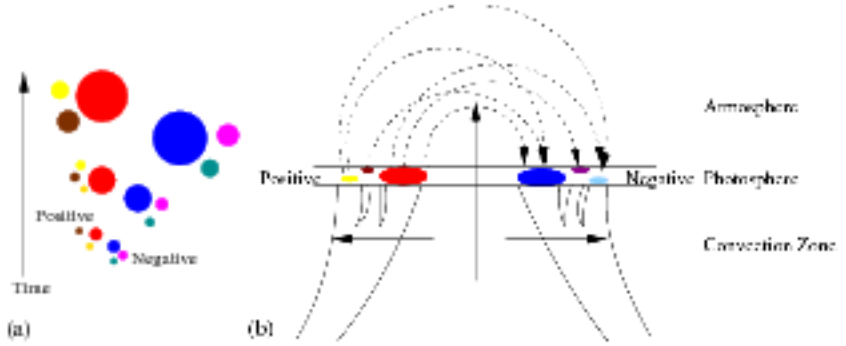

Figure 4.2: An illustration of bipolar cluster flux emergence as seen in (a) the photosphere and (b) a vertical cut.

only process by which new flux features can 'appear' in magnetograms. There are, in fact, three processes of 'appearance' (Lamb et al., 2008): In addition to emergence, new features can appear following fragmentation or when sub-resolution flux merges together to form a feature which can then be identified using a detection algorithm.

Consequently three methods have been developed to find newly emerged flux, which are described below. Two methods assume flux emerges in the form of bipolar pairs of opposite polarity flux (Bipole Comparison and Tracked Bipolar), are discussed. A third method allows for the possibility that flux emerges in the form of opposite-polarity clusters of features (Tracked Cluster). The first method I considered was the bipole comparison method, which is an interpretation of the method used in Hagenaar et al. (1999) and Hagenaar (2001), in order to make a comparison with previous results. This method is applied to the identified features before they are tracked. After analysing the results of this method, it became clear that features were counted multiple times, during emergence, because the features were not tracked over time. Furthermore, when this method was applied to the NFI data, there were a large number of non-unique pairings where features were associated with two or more opposite polarity features, reminiscent of the definition of a how a cluster emergence would appear. Consequently two more flux detection methods were developed. The second flux detection method is the tracked bipolar method, which is applied to the tracked data. This method just deals with the first issue raised by the bipole comparison method and assumes small-scale emergence is bipolar in form. The third method is also applied to the tracked data

and assumes cluster-type emergence as suggested by the non-unique pairings. Below all three emergence methods are described in detail. The results of these methods once applied to the NFI and MDI full-disk data are presented in Chapters 5 and 7, respectively.

4.1.1 Emergence Detection Method 1: Bipole Comparison

The bipole comparison (BC) method assumes that as a flux tube emerges from the convection zone two opposite-polarity features form in the photosphere, with the same absolute flux, i.e they form a bipole. As the flux tube continues to emerge the features grow and move apart, as illustrated in Figure 4.1. Thus, in the BC Method, I divide the identification of flux emergence into 3 steps: (1) finding bipoles in individual frames, (2) determining newly emerged bipoles and then (3) selecting unique bipoles.

4.1.1.1 Bipole Identification

In frame j, the ith opposite-polarity pair of features consists of a positive feature Φ^j_{i+} with flux Ψ^j_{i+} and a negative feature Φ^j_{i-} with flux Ψ^j_{i-}. The shortest distance between the boundaries of Φ^j_{i+} and Φ^j_{i-} is defined as Δ. For this pair of features to be a bipole, Δ must be $\leq$ 7 pixels (812 km) for NFI and 5 pixels (7.0-12.0 Mm depending on the position on the disk) for full-disk MDI. These values were found to give the best results after visual inspection of the data with varying Δ. Furthermore, the fluxes of the opposite-polarity features are expected to be similar, hence:

$$\frac{1}{\rho} \leq \frac{|\Psi_{i+}|}{|\Psi_{i-}|} \leq \rho.$$

A value of 3 was chosen for ρ following trials involving values of ρ from 1-5. Manual inspection of the data, revealed that values of ρ close to 1 led to many bipoles being discounted and ρ too large (near 5) led to the pairing of features which were not connected. Ideally one would expect the pair of features of a true bipole to contain equal amounts of flux, but this is rarely the case since features in a bipole can merge and fragment from birth, which may change their flux significantly (Martin, 1988). Also, instrumental noise can lead to apparent imbalances of flux.

Speculating on the effects on the overall emerging event statistics found due to different values of ρ, it is likely that a reduction in ρ would produce a reduction in bipoles over all fluxes however slightly moreso in bipoles with greater flux as is the features are less likely to have the same absolute flux. Conversly if ρ was increased. It is unlikely that changing the value of ρ would have a measurable impact on the average fluxes and areas of the bipoles identified. Thus, the distribution of bipole fluxes versus number would maintain a similar shape, albeit with the steepness towards the tail varying slightly, but shifting vertically depending on the value of ρ.

4.1.1.2 Finding Emerging Bipoles

The next step is to determine whether the identified bipoles are new emergences. The data array is split into a positive polarity array and a negative polarity array, for each frame j. All features which are deemed to be part of a bipolar pair are then dilated by 3 pixels in each frame, producing new features $\mathrm{D}\Phi^j_{i+}$ and $\mathrm{D}\Phi^j_{i-}$. The process of dilation involves increasing the area of the feature by adding extra pixels around the entire perimeter of the feature. The dilation of 3 pixels used here means that the diameter of thw feature in any direction will increase by 3 pixels. A dilation is applied to each feature to take into account that it can move, fragment or merge between frames. A dilation of three pixels, corresponding to a separation of 2 pixels (232 km for Hinode and ≈2.4-4.8 Mm, depending on the position on the disk, for full-disk MDI), is chosen on the assumption that features move with a velocity ≈2 km s^{-1} (de Wijn et al., 2008), so within the cadence of the data (90 s NFI and ≈5 minutes full-disk MDI) the features move roughly 180 km and ≈600 km, for NFI and MDI full-disk respectively. The pixels of each $\mathrm{D}\Phi^j_i$ are then compared with the corresponding pixels in the $j-1$ frame for the undilated features. Four possible situations arise:

1. Feature $\mathrm{D}\Phi^j_i$ overlaps with no like-polarity features in the $j-1$ frame. In this case Φ^j_i is flagged as **emerging**.

2. If $\mathrm{D}\Phi^j_i$ overlaps with n like-polarity features in the $j-1$ frame, then its flux Ψ^j_i is compared to the fluxes of the n overlapping features. If Ψ^j_i, is significantly bigger than the sum of the fluxes of the features it overlaps, $\sum_{k=0}^{n}\Psi^{j-1}_k$, then the feature Φ^j_i is flagged as **emerging**:

$$\sum_{k=0}^{n}|\Psi^{j-1}_k| < \frac{|\Psi^j_i|}{\rho_k}. \tag{4.1}$$

   The value of ρ_k is chosen to be the same as ρ and hence, $\rho_k = 3$.

3. If $\mathrm{D}\Phi^j_i$ overlaps n like-polarity features in frame $j-1$, but Equation 4.1 does not hold, then the feature Φ^j_i is said to have been present in frame $j-1$ and it must be investigated further. One of two things may have occurred.

   (a) If the flux of Φ^j_i satisfies:

$$\frac{|\Psi^j_i|}{\rho_k} < \sum_{k=0}^{n}|\Psi^{j-1}_k| < |\Psi^j_i|\,,$$

   then the feature is flagged as **increasing**.

   (b) Alternatively, if the flux of Φ^j_i satisfies:

$$\sum_{k=0}^{n}|\Psi^{j-1}_k| > |\Psi^j_i|\,,$$

   then the feature is flagged as **decreasing**.

To be an emerging pair the bipole Φ^j_{i+} and Φ^j_{i-} must comprise of either two features that are flagged as emerging or one emerging feature and one increasing feature.

4.1.1.3 Selecting Unique Bipoles

Once all the emerging bipolar pairs have been identified it needs to be determined which pairs are not part of a unique feature pairing. A non-unique pairing can occur for two main reasons. Firstly, if a true bipole coincidentally emerges close to other appearing features, its features may be paired with one or more of these other features, whether they are genuine emergences or not. Secondly, if a cluster of positive and a cluster of negative features emerge together, due, for instance, to the flux tube being shredded by convection as it rises through the convection zone, then this could also lead to the multiple pairings of features. Thus, the aim of this step is to identify which non-unique pairings are due to coincidental nearby appearances and which are due to cluster-like emergence.

To find out if there are any clusters of same-sign flux appearing together, all the newly emerged features in each frame are dilated by three pixels in turn to find out if they have like-polarity emerging neighbours. If an emerging feature has a like-polarity emerging neighbour these features are said to be associated. The aim here is to find all the third-party like-polarity associations in order that like-polarity clusters of features can be identified. In order to do this an association matrix is utilized (Close et al., 2005).

If there are N like-polarity features in a frame then the initial association matrix, $Assoc_0$, will be an $N \times N$ matrix. If a feature i is associated with a feature k then $Assoc_0(i,k) = 1$, else $Assoc_0(i,k) = 0$. Clearly, the matrix will be symmetric, since association is commutative. Furthermore, all features are assumed to be associated with themselves and so the diagonal elements of the matrix are non-zero, $Assoc_0(i,i) = 1$.

Third-party associations are found simply by repeated multiplication of the matrix by itself,

$$Assoc_n = Assoc_{n-1} \times Assoc_{n-1} \quad n \geq 1 \ ,$$

where all non-zero values of $Assoc_n$ are fixed at each step to 1. This step is repeated until the entries of $Assoc_n$ no longer change, i.e. until

$$\sum_{i,j=1}^{N} Assoc_n(i,k) = \sum_{i,j=1}^{N} Assoc_{n-1}(i,k) \ .$$

The non-zero entries of the i^{th} row of the final matrix can then be simply read off to reveal all the features which belong to the cluster that involves the ith feature.

All non-unique bipoles are considered in turn and the associations of all their like-polarity features investigated. Non-unique bipoles containing features which are deemed to be part of a cluster are kept. For example, if two bipoles have a common negative feature, but different positive features which are associated in the matrix, then the two pairs are deemed to form a cluster emergence.

For the remaining non-unique pairings which are not found to be involved in cluster emergences, the flux ratios of the features in each bipolar pair are considered and the bipole with the ratio closest to unity is regarded as the true emerging bipole and is retained. The other bipoles are removed.

4.1.2 Emergence Detection Method 2: Tracked Bipolar

In the BC method, bipoles are identified in each frame, but they are not associated between frames. Thus, it was not possible to follow the evolution of the identified emergences and also features were multiply counted as being emerging. To address these issues a method was developed, the tracked bipolar method, which used data in which the features have been tracked, in the manner described in Chapter 3. Apart from being applied to tracked data, the tracked bipole method is very similar to the BC method. Indeed, the first and last steps of this method are the same as that used in the BC method, but the second step which involves identifying bipolar emergence is different.

4.1.2.1 Identifying Bipolar Emergence

In order to identify emerging bipoles, bipolar pairs of features Φ_{i+}^{j} and Φ_{i-}^{j} identified in the tracked data are required. These are found using the Bipole Identification the method described in §4.1.1. To find which of these bipoles are actually emerging bipoles, the 'birth' information obtained in Chapter 3 is used. To be classed as an emergence, both features of a bipolar pair must be born within 10 frames (15 minutes) or 3 frames (≈15 minutes) of each other for NFI and full-disk, respectively. To investigate which bipoles are newly emerged, one refers back to the details of the feature tracking in Chapter 3. The birth of a feature is either through 'appearance', which can be a genuine emergence or coalescence of sub-resolution flux, or 'appearance through fragmentation'. For a bipolar pair to be classed as emerging either both features must be flagged as 'appeared' or one feature must have been flagged as 'appeared' and the other flagged as 'appeared through fragmentation'.

As in the previous method, many of these emerging bipoles do not constitute unique pairings, so the Selecting Unique Bipoles approach of §4.1.1 is used to determine which non-unique pairs form cluster emergences and can be retained and which should be removed.

4.1.3 Emergence Detection Method 3: Tracked Cluster

The tracked cluster method is designed to identify emerging clusters of features from a tracked data set (i.e. emerging events that involve more than two features of opposite polarity). The approach applied here is quite different than in the two previous methods, however, it still involves three stages. The tracked cluster is only applied to the NFI data, so all the defined parameters are those used for the NFI.

4.1.3.1 Identifying Feature Emergence

Using the tracked features, features which have 'recently appeared', are flagged in each frame. A feature Φ_{i}^{j} is said to have 'recently appeared' if :

1. It was born by 'appearing' or 'appearing through fragmentation' sometime within the previous 10 frames (15 minutes).

2. Its flux Ψ_i^j is initially small: $|\Psi_i^j| \leq \alpha$, where α is taken to be 2.7×10^{17} Mx ($\frac{1}{3}$ of all feature fluxes are below this value).

3. Its area A_i^j is initially small: $A_i^j \leq \beta$, where β is taken to be 0.3 Mm^2 ($\frac{1}{3}$ of all feature areas are below this value).

4. It is flagged as 'appeared through fragmentation', but the feature Φ_k^s ($j - 10 \leq s \leq j$) from which it fragmented is flagged as 'recently appeared'.

All features that satisfy the above criteria are retained for the next stage of the analysis, which involves finding opposite-polarity associations.

4.1.3.2 Finding Like-Polarity Clusters

To find recently-appeared like-polarity clusters all recently-appeared features within a given frame are dilated by 3 pixels to see if they have any like-polarity neighbours. Any like-polarity neighbours must be born with 5 frames (≈7.5 minutes) of each other before they can be associated. Clusters are then identified by creating an association matrix, as described in §4.1.1. Note, that this stage does not remove any like-polarity features, it simply identifies clusters. If a recently appeared feature does not belong to a cluster it is still retained.

4.1.3.3 Finding Opposite-Polarity Associations

Unlike the other two methods which start off by identifying features which have opposite-polarity neighbours, the opposite-polarity associations are left to the final step of this method. In order to identify if our recently-appeared features are part of an emerging event all 'recently appeared' lone features or all the features in a like-polarity cluster in frame j are dilated by 8 pixels (as used in the BC method §4.1.1). An emerging event is defined as a 'recently appeared' lone tracked feature or like-polarity cluster of tracked features that has at least one association to either an opposite-polarity lone tracked feature or a like-polarity cluster of opposite-polarity features, which are born within 5 frames (≈7.5 minutes) of each other.

Chapter 5

Small-Scale Emergence in Hinode/NFI Data

The emergence of small-scale flux is known to occur through ephemeral regions and IN flux. Whilst the emergence of ephemeral regions has been studied extensively (Harvey, 1971; Harvey et al., 1975; Harvey, 1993; Hagenaar, 2001) the emergence of IN features is less well documented. Even though IN fields are intrinsically weak, their dynamic nature and ubiquitous distribution suggest that they provide a valuable contribution to the total solar magnetic flux budget (Socas-Navarro and Sánchez Almeida, 2002).

There is known to be small-scale emergence occurring with fluxes of $\leq 10^{17}$ Mx (Zirin, 1987) but there is still an ongoing debate as to the process of IN emergence.In § 1.2.2 I discussed in the introduction how the general consensus was that IN features emerged as mixed polarity clusters of features from an emergence centre, inside supergranular cells (Zirin, 1985, 1987; Martin, 1988; Wang et al., 1995). However there have also been suggestions that as observations improve, IN emergence may actually be an extension of ephemeral regions (Zirin, 1985; Wang et al., 1995).

With the launch of instruments like NFI/Hinode, IN emerging features can be observed in detail (Ichimoto et al., 2008; Lites et al., 2008). Martínez González and Bellot Rubio (2009) investigated 69 emerging IN loops in Hinode NFI and BFI data and found IN emerging features have flux typically in the range $2 \times 10^{16} - 2 \times 10^{17}$ Mx, with an average of 9.1×10^{16} Mx. The separation of the emerging event footpoints was found to be between 1-4 km s^{-1} The total flux emergence rate they estimated was 1.1×10^{24} Mx per day over whole solar surface. As only 69 loops were considered, a larger set of emerging events is required to confirm these results.

This chapter aims to investigate the emergence of IN flux in Hinode/NFI magnetograms in which magnetic features can be identified down to just below 10^{16} Mx. I will use both of the feature identification methods and all three of the emergence detection algorithms presented in Chapter 3. This will allow both an investigation into the effectiveness of each method but will also allow a more accurate conclusions to be drawn about the characteristics and nature of IN emergence.

5.1 Data

The data used in this chapter were obtained on the 19th September 2007 between 12:44 UT and 17:43 UT using the Narrowband Filter Imager (NFI) aboard Hinode (Kosugi et al., 2007; Tsuneta et al., 2008). The data and its preparation are described in detail in Chapter 2. The data set has 200 frames with a cadence of 90 seconds and spans 5 hours.

An estimate of the residual noise of the data, after processing, is required for the identification of flux features and is measured by fitting a Gaussian curve to the core of the pixel flux distribution histogram (Figure 2.3), as described in Chapter 2. Here, $\sigma = 4$ Mx cm^{-2}. By defining a pixel value cutoff of 2σ (8 Mx cm^{-2}), the risk of identifying spurious features is reduced.

5.2 Feature Identification and Tracking

Identified Features	Clumping	Downhill
Number of Features Identified ($\times 10^{-16}$ cm^{-2} day^{-1})	369.6	542.8
Mean Features Flux ($\times 10^{17}$ Mx)	1.7	1.2
Mean Feature Area (Mm^2)	0.5	0.3
Total Absolute Flux (Mx cm^{-2} frame^{-1})	6.6	6.7
Tracked Features	Clumping	Downhill
Number of Tracked Flux Features ($\times 10^{-16}$ cm^{-2} day^{-1})	24.3	37.9
Mean Peak Flux of Tracked Features ($\times 10^{17}$ Mx)	1.3	0.9
Mean Tracked Feature Area (Mm^2)	0.5	0.4
Mean Tracked Feature Lifetime (minutes)	15	9
Total Absolute Flux (Mx cm^{-2} frame^{-1})	6.3	6.3

Table 5.1: Characteristics of the identified and tracked features from both the clumping and downhill feature identification programs.

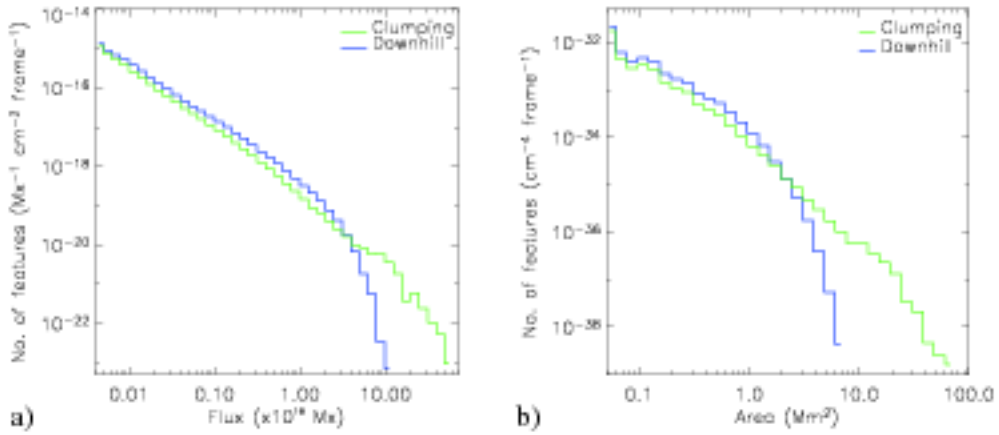

Figure 5.1: Histograms plotted on log-log graphs showing the distribution of (a) flux and (b) area of the features identified by the clumping and downhill algorithms.

For feature identification, I use both the clumping and downhill identification algorithms, as described in Chapter 3. It is clear from Table 5.1(top half) and Figures 5.1a and b that the particular feature identification method does affect the results in some ways. The downhill method identifies approximately 1.5 times as many features as clumping, but the average flux of each feature in downhill is approximately 1.5 times less than the average flux of the clumping features and similarly for feature areas. Hence, downhill and clumping observe more-or-less the same total flux from all features, as one would expect.

In Figure 5.1, histograms of the identified feature fluxes and areas show that at the small-scale end of the

distribution scale (less than 3×10^{18} Mx in flux and 3 Mm^2 in area) downhill identifies more features than clumping. At larger scales, the downhill distribution drops off more rapidly with only clumping identifying features with fluxes above 10^{19} Mx and areas above 7 Mm^2. In light of the discussion in Chapter 3 this is no surprise, as features which are identified as individual flux massifs will often be segmented into multiple flux peaks and this occurs most often for large features. The effect on the downhill flux distribution is an increase in number at small fluxes and a rapid drop off compared to the clumping method at larger fluxes, which is exactly what is seen here.

Two of the emergence detection methods applied to detect emergence events require that the features are tracked throughout the data, as described in Chapter 2. The results of the feature tracking applied to the NFI data, are presented in Table 5.1 (bottom half). The mean values found refer to the mean of all the available results.

The tracked results also highlight the difference in structure between flux massifs and peaks. Again there are about 1.5 times as many downhill features as there are clumping features, with the downhill features having 1.5 times less flux and areas 0.2 times smaller than the clumping ones. The average lifetime of the tracked features in the downhill data is about 0.6 times the lifetime of the tracked features found in the clumping data. This is because flux peaks are more susceptible to local fluctuations in the data due to either granulation or noise, as discussed by Parnell et al. (2009). By removing the short-lived features (lives of less than 4 frames, 6 minutes), the total overall flux that is counted is reduced by 5% for flux massifs and 6% for flux peaks, indicating that short-lived features do not contain a large amount of the surface flux.

The tracked feature characteristics presented in Table 5.1 reveal that there are 93% fewer tracked features in the clumping data and downhill data than there are individual flux massifs or flux peaks, respectively. This is due to the fact that the tracked features have average lifetimes of about 15 and 9 minutes (10 and 6 frames), respectively, for the clumping and downhill data, in comparison to the individual flux massifs and peaks which last just one frame by definition.

Now that the features can be followed over their lifetimes, the average peak flux of the tracked features can be calculated. Interestingly, these peak fluxes are lower, by $\approx 25\%$, than the average flux of the individual flux massifs or peaks. This counter intuitive result arises because large features are typically long lived (Lin and Rimmele, 1999) and, for the mean peak flux, I simply take the mean of a single (the maximum) flux value for each tracked feature rather than the mean of the flux of the feature in every frame. Hence, the number of large fluxes is considerably reduced when calculating the average peak flux of the tracked features, thus lowering the result.

In Table 5.1 and Figures 5.1a and b it can be seen that the features are in the IN range of fluxes and areas. Wang et al. (1995) thought that as much as 10^{23} Mx, which is $\approx 20\%$ of the total flux in quiet-Sun, was in the form of IN features at any given time. By scaling up I estimate that 3.85×10^{23} Mx is present on the solar surface at any one time in the form of tracked IN features, which agrees with Wang et al. (1995). Zirin (1985) andWang et al. (1995) found that to maintain this level of flux, 10^{24} Mx day^{-1} must be emerging (and cancelling) in the photosphere . The next section detects emergence in both the downhill and the clumping data to see if this is the case.

5.3 Detection of Flux Emergence

The results from all three emergence event detection methods applied to both the clumping and downhill Hinode/NFI data are given in Table 5.2. The values for the peak flux and peak area given for the Bipole Comparison (BC) method are found using all the individual identified features in each frame, since the BC method is not applied to the tracked data. This is also the reason the lifetime of the emerging events is not given for the BC method. The values for the peak flux and area for the Tracked Bipolar (TB) and the Tracked Cluster (TC) methods are the maximum values of flux and area the emerging event has during its lifetime. The lifetimes for the TB and TC methods are defined as the time during which the emerging event's opposite-polarity features, $\Phi_{i+/-}$ with flux $\Psi_{i+/-}$, satisfy the condition $\frac{1}{3} \leq \frac{|\Psi_{i+}|}{|\Psi_{i-}|} \leq 3$ and there are no interactions of the emerging event features with any feature not associated with the emerging event.

Bipole Comparison Method	Clumping	Downhill
No. of Emerging Bipoles Identified ($\times 10^{-16}$ cm^{-2} day^{-1})	61.5	79.0
No. of Flux Features Involved in Emergence ($\times 10^{-16}$ cm^{-2} day^{-1})	94.9	116.6
Mean Peak Bipole Flux ($\times 10^{16}$ Mx)	8.8	5.4
Mean Peak Bipole Area (Mm^2)	0.4	0.3
Percentage of Retained Non-Unique Pairings	66	73
Total Absolute Flux (Mx cm^{-2} day^{-1})	470.4	341.4
Percentage of Total Surface Area Where Emergence Occurs	87	89
Tracked Bipolar Method	Clumping	Downhill
No. of Emerging Tracked Bipoles Identified ($\times 10^{-16}$ cm^{-2} day^{-1})	4.2	7.1
No. of Tracked Flux Features Involved in Emergence ($\times 10^{-16}$ cm^{-2} day^{-1})	7.4	11.1
Mean Peak Tracked Bipole Flux ($\times 10^{16}$ Mx)	11.0	7.1
Mean Peak Tracked Bipole Area (Mm^2)	0.7	0.5
Mean Tracked Bipole Life (minutes)	10.7	11.0
Percentage of Retained Non-Unique Pairings	45	55
Total Absolute Flux (Mx cm^{-2} day^{-1})	38.9	50.2
Percentage of Total Surface Area Where Emergence Occurs	19	23
Tracked Cluster Method	Clumping	Downhill
No. of Emerging Tracked Clusters Identified ($\times 10^{-16}$ cm^{-2} day^{-1})	2.3	2.6
No. of Tracked Flux Features Involved in Emergence ($\times 10^{-16}$ cm^{-2} day^{-1})	8.5	10.6
Mean Peak Tracked Cluster Flux ($\times 10^{16}$ Mx)	14.0	14.1
Mean Peak Tracked Cluster Area (Mm^2)	1.0	1.0
Mean Tracked Cluster Life (minutes)	18.8	18.2
Percentage of Retained Cluster Pairings	55	60
Total Absolute Flux (Mx cm^{-2} day^{-1})	32.6	38.8
Percentage of Total Surface Area Where Emergence Occurs	16	17

Table 5.2: Results from all three flux emergence detection methods for both clumping and downhill.

Overall all the emerging events detected were in the flux range of 0.9-3017.8 $\times 10^{16}$ Mx and area range of 0.1-218.9 Mm^2 with the mean peak fluxes and areas being between 5.4-14.1 $\times 10^{16}$ Mx and 0.3-1 Mm^2, respectively, depending on the detection method used. The number of emerging events range from 2.3-79

$\times 10^{-16}$ cm^{-2} day^{-1} which is 1.4 $\times 10^{7} - 4.8 \times 10^{8}$ regions per day assuming the emerge uniformly over the whole surface. This is considerably more than the range of 10^{2} - 10^{4} regions per day determined for ephemeral regions (Harvey, 1993; Chae et al., 2001; Hagenaar, 2001; Hagenaar et al., 2003). I find the flux emergence rate here to be 32.6-116.6 Mx cm^{-2} day^{-1} which is equivalent to 2.0-7.1 $\times 10^{24}$ Mx day^{-1}.

We compare these to the results of Martínez González and Bellot Rubio (2009), who identified 69 emerging loops in Hinode SP, NFI and BFI. Martínez González and Bellot Rubio (2009) found the flux in the foot-points of emerging loops to be in the range $2 - 20 \times 10^{16}$ Mx, which is in good agreement to what I find here. They also found a flux emergence rate of 1.1×10^{24} Mx day^{-1} over the whole solar surface, which is less than the flux emergence rate I find above.

Obviously in Table 5.2 it can be seen that the results of the emerging events depend on both the feature identification method and the emergence detection method applied to the data. The next two sections provide a detailed comparison of which factors have the most impact on the results obtained.

5.4 Comparison Between Methods

This section looks at both the difference between the emerging events detected in the clumping and downhill data, for each method, and it compares the emergence detection methods with each other. The emerging events detected in the clumping and downhill data are compared to assess whether or not an emergence detection method detects the same emerging events regardless of how the features are identified. Also, it allows for an investigation into how the composition of an emerging event, detected both in the downhill and clumping data, varies. Comparing the emergence detection methods themselves will show if the occurrences of emergence detected are independent of the method used.

5.4.1 Comparing the Effects of Different Feature Identification Methods

The results in Table 5.2 demonstrate that fewer emerging events are identified in the clumping data than in the downhill data for each method which is consistent with the feature identification and tracking results from §5.2. In both the BC and the TB results, the flux and area of the emerging events vary between the downhill and clumping data as expected, i.e. the peak flux and area of emerging events detected in the downhill data tends to be smaller than those detected in the clumping data. However, there is little difference in the mean flux and mean area of emerging events if the downhill or clumping data is used when detecting bipoles using the TC method. This suggests that TC method detects basically the same emerging events in both downhill and clumping. This claim will be investigated later in this section. For the tracked emergence detection methods there is no significant difference between the emerging event lifetimes and the feature identification method used.

The total flux emerged per cm^{-2} day^{-1} varies with the feature identification method used. Depending on the emergence detection method used, sometimes more flux is found to emerge in the downhill data and sometimes more in the clumping data, however why this is the case is not clear from the results in Table 5.2.

By directly comparing individual emerging events in the downhill and clumping data for each emergence detection method, later in this section, I am able to gain some insight as to why this is the case.

The results in Table 5.2 highlight that for each method there are more non-unique and cluster pairings when the method is applied to the downhill data than the clumping data. On analysing the non-unique pairings for the BC method further, it is found that, for the downhill data, the mean number of bipoles each feature is associated with is 1.4 bipoles and 2 bipoles for negative and positive features, respectively. For the clumping data these number are 1.4 and 1.7. These numbers are also found for the TB method of emergence detection and the results revealed that each feature, regardless of polarity, was associated with 1.3 bipoles in the clumping data and 1.6 bipoles in the downhill data. For both the TB and TC methods, the number of associated bipoles for each feature is larger for emergence detection methods applied to the downhill data. The increase in multiple pairings for emerging events detected in the downhill data is likely to be a result of the difference in the structure of flux massifs and flux peaks which has already been discussed.

By just looking at the characteristics of the emerging events from each method it is difficult to say conclusively why there is difference between the non-unique and cluster pairings between each method and between the emerging events in clumping and downhill data. A visual comparison is undertaken later in this section to help clarify this issue.

To compare the actual events detected in the downhill data and the clumping data, for each method, each emerging event detected in the clumping data is taken in turn and its pixels determined. These same pixels are then found in the downhill data and the downhill features with which they are associated are determined. The converse of this is also done, where the downhill emerging events are compared to the clumping data. There are four possible outcomes: 1) the emerging event is only detected in one of the data sets, 2) The emerging event is detected in both of them either exactly the same or slightly different, i.e a bipole in one data set matches two positives associated with one negative in the other data set, 3) only the positive component of the emerging event is detected in both data sets and 4) only the negative component of the emerging event is detected in both data sets.

For the BC method it was found for 75% of the emerging events detected in the clumping/downhill data, only the positive feature from the emerging event was identified in both the downhill/clumping data sets. As there was a strong polarity dependence in this result, the identified features themselves were analysed further. It was found in both the clumping and downhill data there were 14% and 24% more negative identified features than positive identified features. The increase in the number of negative features means that the likelihood of a positive feature being associated with the same negative feature in a different data sets is reduced. For the BC method, what is detected as being an emerging event is very dependent on the feature identification data set it is applied to. For the TB method almost 60% of emerging events are identified the same in both the clumping and downhill data, 20% are only identified in one of the data sets and the final 20% have only the positive or negative component identified in both data sets. This again indicates a high level of correlation between the feature identification data used and the emerging events detected. Finally on analysing the difference in the emerging events found by the TC method, in both clumping and downhill data, I find that 80% of the emerging events are identified in both the data sets. The majority of the remaining emerging events detected by the TC method are identified in just one of the data sets. The emerging events found from the TC method are therefore reasonably independent of the feature

identification data used.

5.4.1.1 Visual Examples of Emerging Events

To gain a better understanding of the above results, some visual examples of the emerging events detected in clumping and downhill data, are presented. In all examples only the features of interest are coloured, rather than all the features.

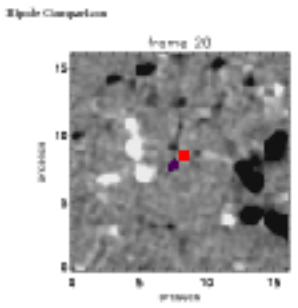

Figure 5.2: Example of a bipole (positive feature red and negative feature purple) identified by the Bipole Comparison in both the clumping and downhill data sets, with pixel saturation ± 30 Mx cm^{-2}.

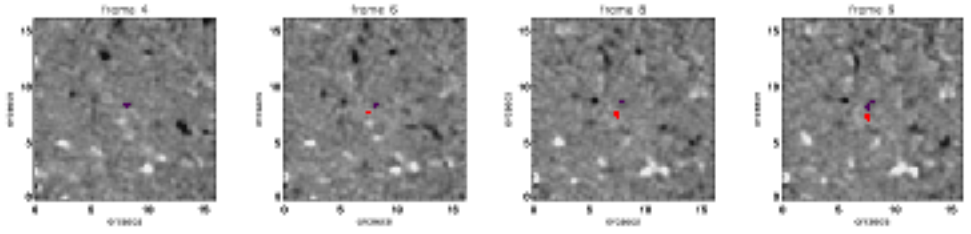

Figure 5.3: Example of a bipole (positive feature red and negative feature purple) identified by the Tracked Bipolar method in both the clumping and downhill data sets, with pixel saturation ± 30 Mx cm^{-2}.

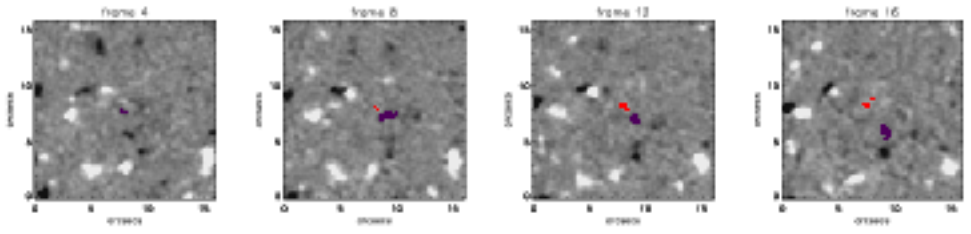

Figure 5.4: Example of a bipole (positive feature red and negative feature purple) identified by the Tracked Cluster method in both the clumping and downhill data sets, with pixel saturation ± 30 Mx cm^{-2}.

The first three examples show a bipole identified in both the clumping and downhill data sets for the BC method (Figure 5.2), the TB method (Figure 5.3) and the TC method (Figure 5.4). As the BC method is applied to un-tracked data the bipole can only be identified for one frame. These figures highlight that emergence often occurs in regions which contain many other features.

The bipole in Figure 5.3 highlights that these small-scale emerging events do not always move apart quickly but often stay in close proximity as the features grow. It also shows that the opposite-polarity components of the bipole do not always appear to be born in the same frame. Figure 5.4, again shows asymmetric emergence, but the overall behaviour of the bipole is more akin to what would be expected of an ephemeral region, namely that the features grow and move apart simultaneously after emergence. Both the bipoles shown in Figures 5.3 and 5.4 detected in the tracked data are examples of emergence events that reach full maturity in the order of 4-6 frames (6-18 minutes), which is found to be the typical time range and is much shorter than the times found for ephemeral regions.

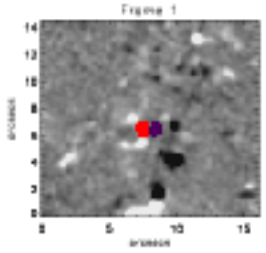

Figure 5.5: Example of a bipole only detected by the BC method in the downhill data (positive feature red and negative feature purple), with pixel saturation ± 30 Mx cm^{-2}.

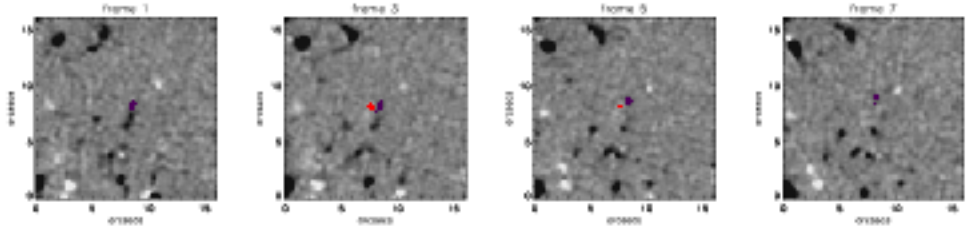

Figure 5.6: Example of a bipole only detected by the TB method in the clumping data (positive feature red and negative feature purple), with pixel saturation ± 30 Mx cm^{-2}.

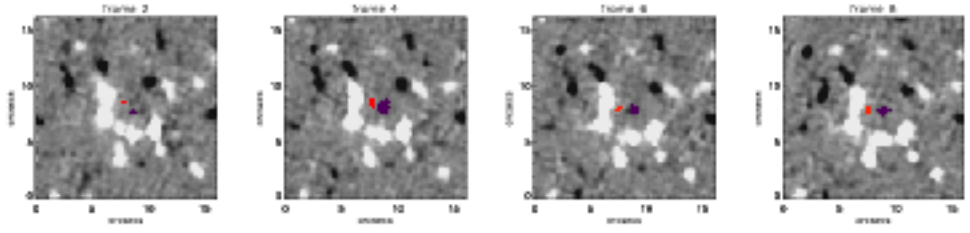

Figure 5.7: Example of a bipole only detected by the TC method in the downhill data (positive feature red and negative feature purple), with pixel saturation ± 30 Mx cm^{-2}.

Of all the emerging events detected by the three methods it was found that 13-15% were only identified in either the clumping or the downhill data. Figures 5.5, 5.6 and 5.7 are all examples of such emerging events. Again there is only one frame for the BC method example (Figure 5.5) as the method is applied to un-tracked data, so the evolution of the bipole cannot be followed. Looking at the figures it is not clear why these emerging events are only detected in one set, as all the emerging events seem to exhibit

characteristic emergence behaviour. However, most of these 13-15% of emerging events appear in regions already containing flux features and it is possible that these pre-existing features impede the ability of the emergence detection methods to (accurately) detect emergence.

One aspect of the detected emerging events this comparison hopes to shed some light on, is why there are so many non-unique and cluster emergence events identified in all three methods. Are cluster emergence events due to localised emergence centers where genuine clusters of mixed-polarity flux emerge, or is a flux tube being shredded by convection as it emerges, as seen in § 4.1. Alternatively, are the methods failing to separate bipoles which are coincidentally emerging close to one another?

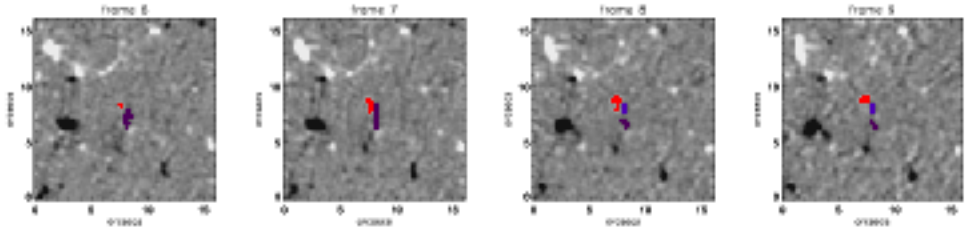

Figure 5.8: Example of a non-unique pairing (positive feature red and negative features blue and purple) identified by the Tracked Bipolar method in the clumping data, with pixel saturation ± 30 Mx cm^{-2}.

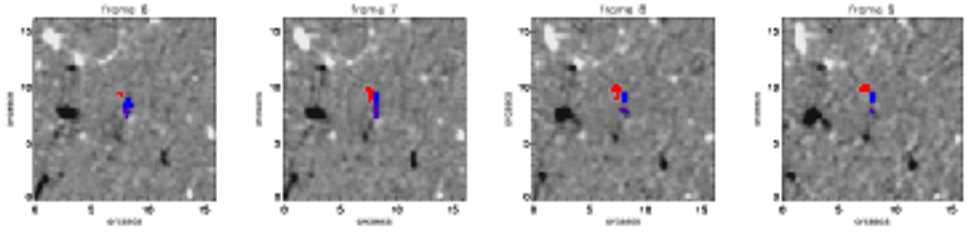

Figure 5.9: Example of the same pairing (positive feature red and negative features blue and purple) as in Figure 5.8 but this time identified by the Tracked Bipolar method in the downhill data, with pixel saturation ± 30 Mx cm^{-2}.

It was found in § 5.3 that more cluster emerging events were found in the downhill data than in the clumping data for each method, which is not surprising since a single feature in clumping data is often identified as two or more features in the downhill data (Parnell et al., 2009). Figures 5.8, 5.9, 5.10 and 5.11 are intended to show visually the differences between non-unique and cluster pairings detected in the clumping and downhill data. The first two examples (Figures 5.8 and 5.9) are a case of a non-unique pairing between bipoles; two negative (purple) features sharing a positive (red) feature. The interesting thing to observe is that in the clumping data the negative feature begins as just one feature which then fragments into two, whereas in the downhill data two negative features are identified from the start of the emergence.

There are two effects to consider due to the segmenting of features into flux peaks by the downhill feature identification method. The first is when there are two opposite-polarity flux massifs identified in clumping and one of the massifs has multiple peaks. In the downhill data then this emergence is likely to be non-unique as the flux massif which is singly peaked will be associated with each of the flux peaks of the multiply peaked feature. The second is where there is a non-unique pairing in the clumping data, for

instance when two positive singly peaked flux massifs are associated with one negative (doubly peaked) massif. In the downhill data the latter case would be detected as two bipoles, as each one of the positive features, has its own negative feature. Many of the non-unique pairings found in downhill data were due to this feature segmenting effect.

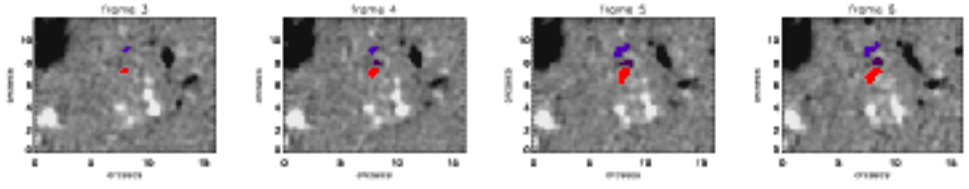

Figure 5.10: Example of a cluster emergence (positive features red and negative features purple) identified by the Tracked Cluster method in the clumping data, with pixel saturation ± 30 Mx cm^{-2}.

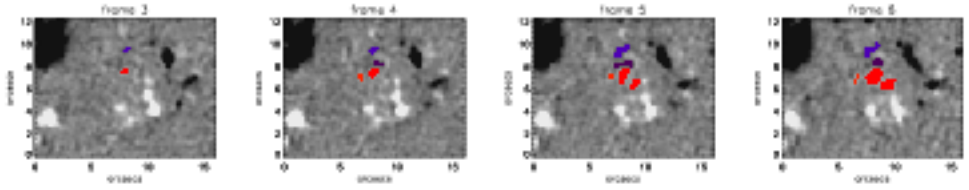

Figure 5.11: Example of the same cluster emergence (positive features red and negative features purple) as in Figure 5.10 but this time identified by the Tracked Cluster method in the downhill data, with pixel saturation ± 30 Mx cm^{-2}.

The second two examples (Figures 5.10 and 5.11) show how a cluster, detected by the TC method, varies when detected in downhill and clumping data. In the clumping data a bipole is seen originally. Then a second negative (purple) feature emerges. As the positive (red) feature grows so do both of the negative features. In the downhill data, however, more features are involved in the emergence, and by frame 5 there are three positive features, as well as the two negative features. It is difficult to determine which, if any, is the correct emergence, as on visual inspection they both behave as an emergence should. One thing to note, from looking at these examples, is that as the emergence progresses the clusters becomes more bipole like. Following the evolution of many of the cluster emergences reveals that most eventually evolve into bipoles, once the features are fully emerged. Indeed, if this emergence was viewed at a lower resolution it is likely it would appear as a bipole not a cluster from the outset.

Figure 5.12 shows a cluster detected by the TC method in both the clumping and downhill data. It draws attention to the question of the source of cluster emerging events. This example appears to contain a complex localised emergence centre, where numerous mixed-polarity features emerge. By eye it is possible to separate many of the features into bipoles. The question is whether or not such examples should be separated or left as clusters? The implications of separating the clusters is to lower the peak flux and area and potentially reduce the lifetime of emerging events, but obviously increases the number of emerging events.

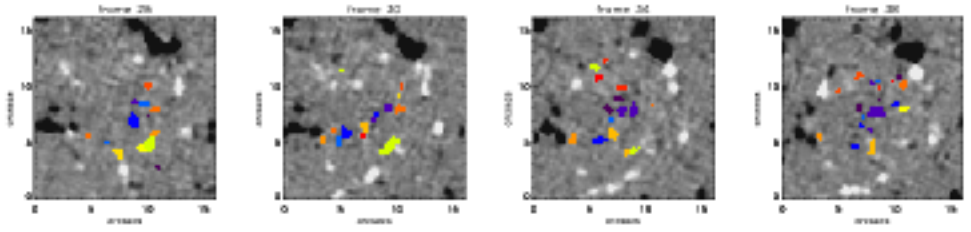

Figure 5.12: Example of a complex cluster emergence (positive features are reds, yellows, greens and oranges whilst the negative features are purples and blues) identified by the Tracked Cluster method in the downhill data, with pixel saturation ± 30 Mx cm^{-2} (This cluster was also detected similarly in the clumping data).

5.4.2 Comparing the Effects of Different Emergence Detection Methods

The differences between the emergence detection methods will now be inspected. A comparison of the number of emerging events detected by each method shows that the BC method detects many more emerging events than the two tracked methods. The BC method is applied to un-tracked data and so identifies bipoles in each frame with no information about their long-term history. As the data has a 90 second cadence, this implies the BC method multiply counts events that last longer than 90 seconds, as I anticipated in §4, would be a problem. Note, however, that multiple counting of events is not the only problem with the BC method. If the number of tracked emerging events, found by the TB and TC methods, is multiplied by the mean number of frames these bipoles live (≈ 7 frames for downhill and ≈ 12 frame for clumping), the result is ≈42-54% and 38-60% fewer events than found using the BC method applied to the clumping and downhill data, respectively. This means that the BC method is not only multiply counting the emerging events found by the two tracked methods, but it is also identifying extra bipoles as emerging events. This result is emphasised when the total number of emerging features are found as a percentage of the total area. The BC method finds that 87-89% of the total observed region has emergence at some point, whereas the TB and TC methods find that emergence occurs in only 16-23% of the observed region. Considering the reduction of the number of tracked features compared to identified features due to lifetime filtering, it is likely some of these extra events involve features that live for less than 4 frames. However, the BC method may also identify emerging bipoles when two opposite-polarity features, which are not newly emerged, move close to one another and happen to satisfy the BC criteria discussed in Chapter 4.

It is clear that there is a dramatic difference in the number of emerging events between the BC method and the tracked emergence detection methods, but what about the characteristics of the emerging events? The peak fluxes and areas of the emerging events found by the TB and TC methods are larger than these of the bipoles found using the BC method, indicating that the BC method is detecting emerging events before they have reached their peak flux. Because the features are tracked for the TB and TC methods, the true peak flux of the emerging events can be found. Not surprisingly, the peak fluxes and areas of the TC events are also larger than those found by the TB method, since a large number of TC events involve more than two features.

The mean lifetime of the emerging events, detected by the TB and TC methods, is the time during which the emerging event can still be recognised as such, without significant interaction with pre-existing features.

The emerging events detected by the TC method tend to be longer lived than those detected in from the TB method as the TC method detects all the features in an emerging events not just bipolar pairs of opposite polarity features, thus there is more chance of the emerging events in the TC method being recognised for longer.

Both the BC and TB methods have a high number of non-unique bipole pairings. The TC method was designed specifically to identify cluster emergence events, in order to better gauge how numerous they are. The numbers of clusters that are identified using the TC method, as opposed to bipoles is 1.28 $\times 10^{-16}$ cm^{-2} day^{-1} and 1.57 $\times 10^{-16}$ cm^{-2} day^{-1} for the clumping and downhill data, respectively. For the BC method there are 40.6 $\times 10^{-16}$ cm^{-2} day^{-1} and 57.8 $\times 10^{-16}$ cm^{-2} day^{-1} events which are non-unique in the clumping and downhill data, respectively. Using these pairing results and assuming that the non-unique pairings consist of one positive feature associated with two negative features or vice-versa, then this would amount to 20.3 $\times 10^{-16}$ cm^{-2} day^{-1} and 28.9 $\times 10^{-16}$ cm^{-2} day^{-1} clusters, in the clumping and downhill data. Similarly for the TB method the number of non-unique events in the clumping and downhill data is 1.8 $\times 10^{-16}$ cm^{-2} day^{-1} and 3.8 $\times 10^{-16}$ cm^{-2} day^{-1}. Using the same assumption as in the BC method as to the nature of the non-unique pairings, then the number of clusters in the TB method would be 0.9 $\times 10^{-16}$ cm^{-2} day^{-1} in the clumping data and 1.9$\times 10^{-16}$ cm^{-2} day^{-1} in the downhill data. The number of TC clusters is less than the estimated number of clusters found in the BC method, even if the lifetimes of the emerging events are taken into account in the TC method. However, comparing the TB and TC methods, it is found that in the clumping data the TC methods detects slightly more clusters than the TB method but in the downhill data the TC method detect slightly less clusters than the TB method.

An algorithm has also been created to automatically investigate the difference between the detection methods. This algorithm is similar to the one for comparing downhill and clumping, discussed in the previous sub-section. To compare the emerging events detected by each method the comparison must be done for the emergence detection methods applied to clumping and downhill data separately since as we have seen the type of identified data used can affect the results. Two methods are compared at a time and there are separate algorithms for comparing the two tracked methods and for comparing a tracked method to the BC method. In the tracked method algorithm, as the methods will be applied to the same data set, only the unique labels of each feature in the emerging event need to be compared. Comparing the BC method to a tracked method is slightly different as they are applied to un-tracked data and tracked respectively, so the unique labels in each data set cannot be compared.

Starting with the emerging events detected by the BC method, I find pixels pertaining to each feature in the emerging event and then find the features that these correspond to in the tracked data. Then I find if those tracked features have been detected as an emerging event by either the TB or TC method in the tracked data. The converse of this is done for comparing pixels from tracked features to the BC method. The possible outcomes of such a comparison are the same four as those discussed in the previous sub-section. For the BC and TC comparison I am comparing bipoles and clusters which I do not necessarily expect to be identical, as the BC and TB methods both detect bipoles a comparison of their emerging events should be more insightful.

Not surprisingly, when the BC method is compared to either of the tracked methods, most of the emerging events found by the BC method are only found by the BC method. Remember the tracked data has had

the minimum lifetime criterian applied to it, so there will be emerging events detected by the BC method which will not be present in the tracked data due to this constraint. Aside from the emerging events only detected by the BC method, it is the TC method which the BC method shares the most emerging events with. On comparing the BC method to both the tracked methods, simultaneously, nearly 50% of bipoles identified by BC are in neither tracked methods and less than 1% of BC bipoles are identified by all three methods. This accounts for 0.6-0.8 $\times 10^{-16}$ cm^{-2} day^{-1} emerging events.

For the TB method, it has more emerging events in common with the TC method, with almost 80% of the TB emerging events also being detected by the TC method, the remaining 20% were not detected at all. In comparison, only 25% of the TB emerging events where detected in the BC method. This implies that a large number of the emerging events detected by the BC method, are not detected as emerging once the features are tracked. Again comparing TB bipoles, simultaneously to the other two methods it can be shown that 10% of emerging events are only found in TB, with 8% of TB bipoles (0.3-0.6 $\times 10^{-16}$ cm^{-2} day^{-1}) found in all.

Finally, examining the TC method in comparison to the other two methods, shows that the TC method has 65% of its emerging events in common with the TB method, however there are also 20% not identifed at all by the TB method, 8% only the positive feature is identified in both and 7% only the negative feature is identifed in both. This is also shown comparing the emerging events found in the TB method to the TC method. Comparing TC bipoles to the other two methods shows that only 4% are found by the TC method alone while, 20% of the TC clusters are also found by both of the other two methods. Again converting this into numbers reveals that 0.5 $\times 10^{-16}$ clusters cm^{-2} day^{-1} are found in all 3 which is in agreement with the TB method but slightly lower than what was found for the BC method.

5.4.2.1 Visual Examples of Emerging Events

A visual comparison again is utilized to provide some insight into the differences between the emergence detection methods. Again only the features of interest are coloured.

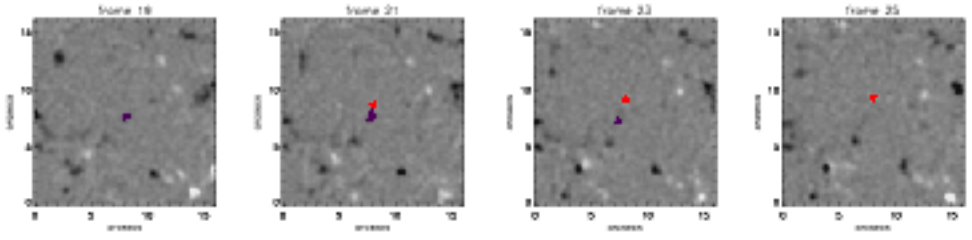

Figure 5.13: Example of a bipole (positive feature red and negative feature purple) identified by all methods in the clumping data, with pixel saturation $\pm$30 Mx cm^{-2}.

Figure 5.13 shows an example of an emerging bipole which is identified identically by all three methods. As mentioned before emerging events are more likely to be identified by more than one method if they occur in a relatively flux free region as shown in the example.

As the results in §5.3 show, the BC method identifies many more emerging features than the two tracked

methods. As the BC method is applied to un-tracked data the history and evolution of features in emerging events cannot be determined. In order to find out how the spurious emerging events arise I relate the events detected by BC to tracked data to determine the history of the features in emerging events. Visual inspection of the emerging events detected reveal that it is often the case that a long-lived feature whose flux is increasing (by, for example, coalescence of sub-resolution flux) is paired with a newly 'appeared' feature of opposite polarity created by an accumulation of sub-resolution flux that raises it above the detection threshold so it can be identified as a feature.

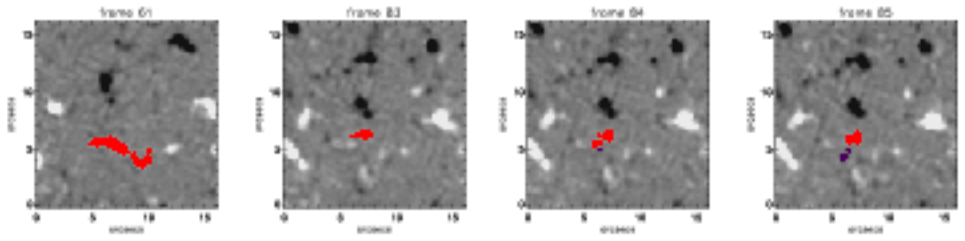

Figure 5.14: Example of where the Bipole Comparison method associates a long-lived (positive - red) feature, which was born in frame 1 (I only show it from 61) with a newly appeared (negative - blue) feature, born in frame 84, to create a false bipole emergence, with pixel saturation ± 30 Mx cm^{-2}.

An example of this type of behaviour is shown in Figure 5.14, where a long lived positive (red) feature which has been in existence since frame 1, becomes paired with a newly appeared negative (purple) feature in frame 84. To identify this so-called emergence, the BC method only considers frames 83 and 84 which alone appear to give reasonable evidence of emergence. It is only apparent after the data has been tracked that this is not really an emergence and that the positive feature has already been in existence for quite sometime.

In a system as dynamic as the small-scale quiet Sun this can often occur. These types of events are not identified by either of the tracked methods since in these methods all the features of an emergence event must be born within 10 frames (15 minutes) of each other. This explains one of the reasons why the BC method produces an over estimate of the rate of flux emergence in the quiet Sun.

It was shown above that the structure of detected emergence events can vary depending on whether they were detected in the clumping or downhill data. Here the structure of cluster emerging events is compared between the three emergence detection methods.

Figures 5.15, 5.16 and 5.17 shows how the same complex emergence event is identified by the three methods. They illustrate that in complex cases of cluster emergence, the three methods often identify different features as being involved. Due to the more stringent constraints of the TB method, it tends to try and simplify all emergences into bipoles no matter how complex they are. On the other hand, the BC and TC methods can connect unlikely features to form a cluster emergence, which needs to be improved on. Again to follow the evolution and find the history of the BC emerging event I related it to the tracked data.

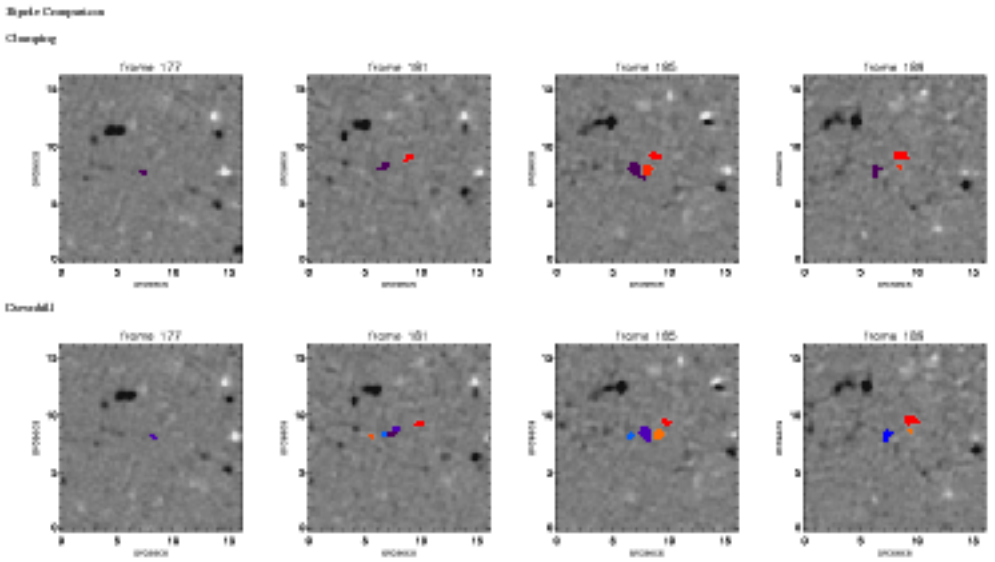

Figure 5.15: A cluster emergence identified by the BC method in frame 181 (negative features - purples/blues and positive features - reds/oranges) in the clumping data (top row) and downhill data (bottom row). Clearly, in the downhill data more and slightly different features are detected than in the clumping data, with pixel saturation ± 30 Mx cm^{-2}.

5.5 Emerging Event Peak Flux Distributions

Figure 5.18 shows a log-log plot of the histogram of fluxes from emergence events found by each emergence detection method, in both the clumping and downhill data sets. As expected, the distributions of the emerging event fluxes found by the BC method, using the clumping and downhill data, are much higher than those found for the TB or TC methods, since, in the former, the events are counted multiple times. It is clear, that the BC method finds not only many more small-scale bipoles, but also in the clumping data set many more large-scale bipoles too, than the two tracked methods. This is in line with what is already known about the distributions of flux massifs and flux peaks (DeForest et al., 2007). This suggests that the extra emerging events found using the BC method involve features with both small and unusually large flux.

The two TC method curves are extremely similar, as expected, since we have seen for both downhill and clumping the TC method identifies many of the same emerging events. The majority of the TC curves are lower than the TB curves, as fewer clusters are identified, than the TB method's bipoles, due to over half of the clusters containing more than two features. Above 5×10^{17} Mx all four tracked curves follow a similar distribution. For the TB method the downhill data finds marginally more events than the method applied to the clumping data. In the clumping data however more large-scale bipoles are identified.

Figure 5.18 suggests that the distribution of emerging event fluxes may follow a power law. However, since these distributions extend over no more than 1.5-2 decades in flux, any conclusive statements will be saved for when the distributions found here are compared with previous results from other authors and the distributions I find for full-disk emergence (Chapter 7), to find if there is a single power law distribution

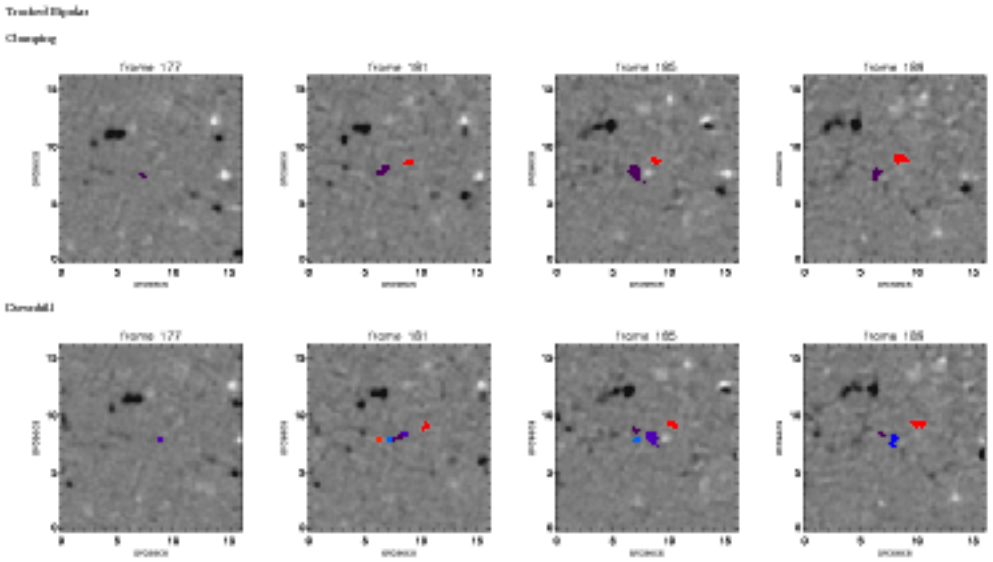

Figure 5.16: As Figure 5.15, but this time the cluster emergence is detected using the TB method. The TB method has a tendency to over simplify emergence events down to bipoles, so finds less features involved in the emergence event than the BC method. Pixel saturation ± 30 Mx cm^{-2} Movie clips available the accompanying DVD.

extending over all small-scale emerging features.

In Figure 5.18 it is noticeable that there is a peak/turnover in all the distributions, below which the number of features drops of rapidly. This is likely to be due to the flux, area and lifetime criteria applied to the data when features are being identified and tracked. By removing pixels with small fluxes, lifetimes or areas, this can remove small features that would possibly have peak emerging flux in the range between the turnover flux and the drop off value. However, it is not possible to tell from the data if this is a true turnover/peak or it is simply due to a combination of the feature identification and tracking criteria.

5.6 Conclusions

The aim of this chapter is to characterise the behaviour of IN emerging flux and examine how the methods and assumptions used to find the emerging events can have an effect on the results obtained. Small-scale features were firstly identified in the Hinode/NFI data using both the clumping and downhill feature identification methods. The clumping method identifies flux massifs above a given lower cutoff and the downhill method divides the flux massifs along saddle points (if there are any) into individual flux peaks. This results in there being more features identified by the downhill method which have a smaller mean area and flux plus a shorter lifetime (as flux peaks are more transient), than those features identified by the clumping method. Despite these differences in the features identified by the clumping and downhill method, there is practically no difference in the total absolute flux detected by both methods.

Three emergence detection methods are used: Bipole Comparison (BC), Tracked Bipolar (TB) and

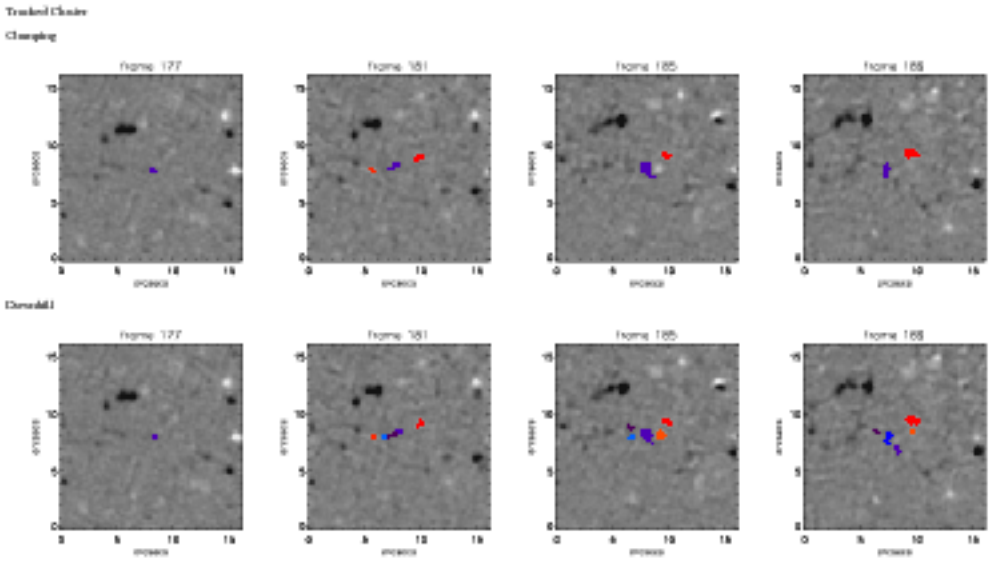

Figure 5.17: As Figure 5.15, but this time the cluster emergence is detected using the TC method, with pixel saturation ± 30 Mx cm^{-2}. Here, the TC method has identified less(more) features in the clumping(downhill) data than the BC method as being involved in the emergence event.

Tracked Cluster (TC). The first method to be considered was the Bipole Comparison method, which is an interpretation of the method used in Hagenaar (2001) (which is fully described in Hagenaar et al. (1999)), in order to make a comparison with previous results. This method assumes that emergence is bipolar in form and is applied to the identified features before they are tracked. After analysing the results of this method, it became clear that features are counted multiple times, as emergence events, because the features are not tracked over time. Furthermore, when this method is applied to the NFI data, there are a large number of non-unique pairings where features are associated with two or more opposite polarity features, reminiscent of the definition of a how a cluster emergence would appear. Consequently two more flux detection methods are used.

The second flux detection method, the tracked bipolar method, is applied to the tracked data. This method just deals with the first issue raised by the bipole comparison method and assumes small-scale emergence is bipolar in form. However, this method identified that there are many non-unique bipolar pairings of IN emerging features. Thus, the third method developed, the tracked cluster method, assumes cluster-type emergence to investigate how numerous cluster-type emergences are. Cluster emergences are found to be common, but is difficult to say if they could be resolved as bipoles at higher resolutions or if they are a single bipole shredded by convection as emerge. I find that the different feature identification methods and the emergence detection methods have a varying effect on the structure and characteristics of the emerging effects detected. Whether or not the features are tracked before emergence is detected seems to be the greatest influencing factor.

Depending on the analysis undertaken, each of the emergence methods has its strengths and weaknesses. The BC identifies the largest volume of emergences in both number and flux input. This is because the method often multiply counted emerging events due to the features not being tracked which meant that no minimum lifetime criteria had been applied yet so there were more features to begin with and older features

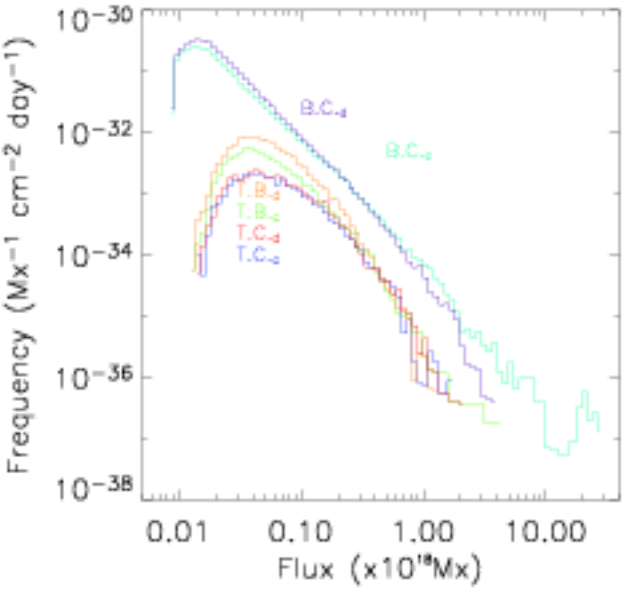

Figure 5.18: Log-log plot of emergence event fluxes against frequency of emergence cm^{-2} day^{-1}.

could be identified as emerging if they fulfilled the criteria of the BC algorithm. The fact that this method is just applied to identified features allows the results to be directly compared with the well known results of This method is computationally faster than either the TB or TC methods because no tracking is applied and is ideal if all that is required is an upper bound estimate on the rate of emerging flux and features.

However if the evolution of features after emergence is the primary focus of a study then it would be recommended that either the TB or TC method is used. If the features are not tracked as in the case of the BC method the the evolution of the emerging events cannot be followed to find the lifetime, peak area and peak flux. The TB and TC methods allow for this. As well as this the TC and TB methods identify if and when the emerging features interact with other features and if so, how soon after they emerge. It is telling that the majority of bipoles in the BC method are identified before their maximum development as the flux and areas were smaller than those of the tracked methods.

The TB and TC methods also have individual advantages. Computationally the tracked bipolar method is less consuming than the TC method although both methods produce similar flux distributions. Thus the TB method is more desirable if the nature of an investigation is simply to find the flux distribution of emerging events. The fact that the TB method identifies bipoles also allows the evolution of emerging events easier to follow.

Despite the TC method being more complicated and computationally more demanding it does allow an insight into the nature of emergence at small scales and whether it is primarily in the form of bipoles or clusters, which is not fully understood. If this method was applied to data of varying resolutions it would help to clarify if the likelihood of cluster emergence is correlated with the resolution of the data.

Generally for the purposes of comparison with other results and as the majority of other research examines bipoles, it is best to use one of the Bipolar methods.

The IN emerging events I find in the Hinode/NFI data have mean peak flux of between 5.4-14.05$\times 10^{18}$ Mx and mean peak area of between 0.3-1 Mm^2. The frequency of emergence is found to be in the range 2.3-79.0 $\times 10^{-16}$ cm^{-2} day-1 (1.4-48.2 $\times 10^{7}$ day^{-1} over the whole surface) and flux emergence rate of between 32.6-470.4 Mx cm^{-2} day^{-1} (2.0-28.7 $\times 10^{24}$ Mx day^{-1} over the whole surface), depending on the features identification and emergence detection method used. Previous estimates of the contribution of IN emerging flux to the total flux budget have found of order 10^{24} Mx day^{-1} over the whole surface (Wang et al., 1995; Martínez González and Bellot Rubio, 2009). I find several times 10^{24} Mx day^{-1} for the tracked emergence detection methods but the Bipole Comparison method detects considerably more flux than this. It is likely that I find a greater rate of flux injection due to the automated detection approaches I used, which are better at detecting very small events than 'by eye' approaches.

In this chapter using three emergence detection methods I have been able to understand the characteristics of IN emerging events more clearly and put a handle on the amount of flux emerging due to small-scale IN emergences. Overall, none of the flux detection methods is perfect, as is apparent on visual inspection of data. There are still emergence events that all three methods miss, although these cases are rare, and also each method identifies some events that are questionable.

Chapter 6

Small-Scale Feature Evolution as Observed by Hinode/NFI

Despite the name, the quiet-Sun magnetic carpet is actually highly dynamic. Magnetic features are continuously undergoing evolution driven by flow patterns in supergranular cells. In photospheric observations, ephemeral regions and IN flux features are seen to emerge inside these cells and are driven to the supergranular vertices and lanes where they form the network. Flow patterns cause features to converge, resulting in coalescence (where two like-polarity features merge to form one large feature) or cancellation (where two opposite-polarity features mutually lose flux, at the same rate, often resulting in the removal of the weakest feature and a significant reduction in the flux of the strongest), respectively. The photospheric flow patterns can also cause features to break up into two or more smaller features: a process known as fragmentation. These processes mean that photospheric flux is continuously changing and results in a so called recycling of the photospheric flux. Previous estimates of the flux recycling time vary from a few hours to a few days (Schrijver et al., 1997, 1998; Hagenaar, 2001; Hagenaar et al., 2003, 2008).

Coalescence, fragmentation and cancellation in small-scale photospheric magnetic features have been observed since the early 70's (Vrabec, 1971; Smithson, 1973; Koemle, 1979; Livi et al., 1985; Lamb et al., 2008). Cancellation of opposite-polarity features occurs between pairs of features that are previously unconnected i.e. features that did not emerge together. Observations of cancelling features show that cancellations are associated with magnetic reconnection occurring at the photospheric level (Priest et al., 1994; Longcope, 1998), with the rate of cancellation being related to the speed of approach of the two opposite-polarity features, in accordance with the Sweet-Parker type reconnection model (Parker, 1984; Lites et al., 1995; Chae et al., 2001, 2002). Chae et al. (2002) used high-resolution MDI data to investigate small-scale cancelling features (with flux of order 10^{18}-10^{19} Mx) and found the flux loss rate per cancelling pair was estimated to be between 1.3-3.5$\times10^{18}$ Mx hr^{-1}, which corresponded to a converging speed of 0.27-0.35 km s^{-1}.

Fragmentation and coalescence have been studied and discussed less than cancellation. It is not clear why this is but it may be because these processes do not obviously appear to be associated with heating or dynamic coronal or chromospheric events. However, understanding these processes, and finding out how numerous they are, would help to provide insight into how flux is dispersed and what the mixed-polarity nature of the photospheric field is. It has already been suggested that the fragmentation of ephemeral regions and the coalescence of IN features supply the large magnetic features that make up the quiet-Sun network (Martin, 1990; Schrijver et al., 1997). The results of Lamb et al. (2008) favour the pile up of IN features as the dominant source, whilst Martin (1990) estimates that ephemeral regions provides the

network with at least 90% of its features. It was also previously found in observations of the behaviour of network elements, that the rate of merging is twice that of fragmentation, which also seems to favour the latter source of network flux (Liu et al., 1994). However, the models of the magnetic carpet presented in Parnell (2001) suggest that fragmentation should be more than 3-5 times that of the rate of merging.

Studying the motions of small-scale magnetic features is also important in order to understand the coupling between the plasma and magnetic field and hence what is driving or hindering the movement of features on the photosphere. Large concentrations tend to move slower than small ones (Hagenaar et al., 1999) and this may be due to the respective depths at which they are anchored: small ones are believed to come from just below the photosphere whilst larger ones may be anchored low down in the convection zone. Also, it seems that the larger the flux concentration the more stable the flows are around it (Hagenaar et al., 1999). Indeed, the mean square velocity of concentrations decreases slowly with increasing flux (Schrijver et al., 1996; Hagenaar et al., 1999).

As found in Chapter 4, Hinode/NFI identifies IN fields and the emergence of these IN features behaves in a similar manner to large ephemeral region emergence. Here I consider whether the other processes that IN fields undergo, are quantitatively similar to the processes larger features undergo. Having found the emergence rates it would be useful to find fragmentation, coalescence and cancellation rates in order to determine what the dominant surface processes are in the quiet-Sun. Knowledge of these processes should hopefully further our understanding of the origin of small-scale fields.

The sections below describe how the Hinode/NFI data is used to evaluate the evolution processes undergone by small-scale fields. Firstly, in § 6.1, I describe how the cancellation detection algorithm works. The cancellation results are then presented and compared to the emergence results from the previous chapter. Secondly, in § 6.2, I explain how, from the birth and death information obtained by feature tracking in Chapter 3, information about the characteristics and rates of fragmenting and coalescence features can be derived. The fragmentation and coalescence results are presented at the end of this section. Finally, § 6.3.1 looks at the evolution of the tracked features detected as emerging in the previous Chapter.

6.1 Detecting Cancellation in NFI/Hinode

When cancellation occurs there are two ways the cancelled flux can be removed: (i) through reconnection in the low atmosphere leading to an Ω-shaped loop which subducts the flux below the surface (Priest et al., 1994; Parnell et al., 1994) (Figure 6.1a) or (ii) when reconnection occurs below the photosphere leading to a U-shaped loop, which transfers the flux into the upper atmosphere, as shown in Figure 6.1b (Zwaan, 1987; Harvey et al., 1999; Kubo and Shimizu, 2007). Harvey et al. (1999) tried to determine which of these possibilities is most common in the quiet-Sun by comparing photospheric and chromospheric observations and found that 44% of cancelling bipoles submerge, 18% of cancellations result in a rising flux tube and for the other 38% they could not tell.

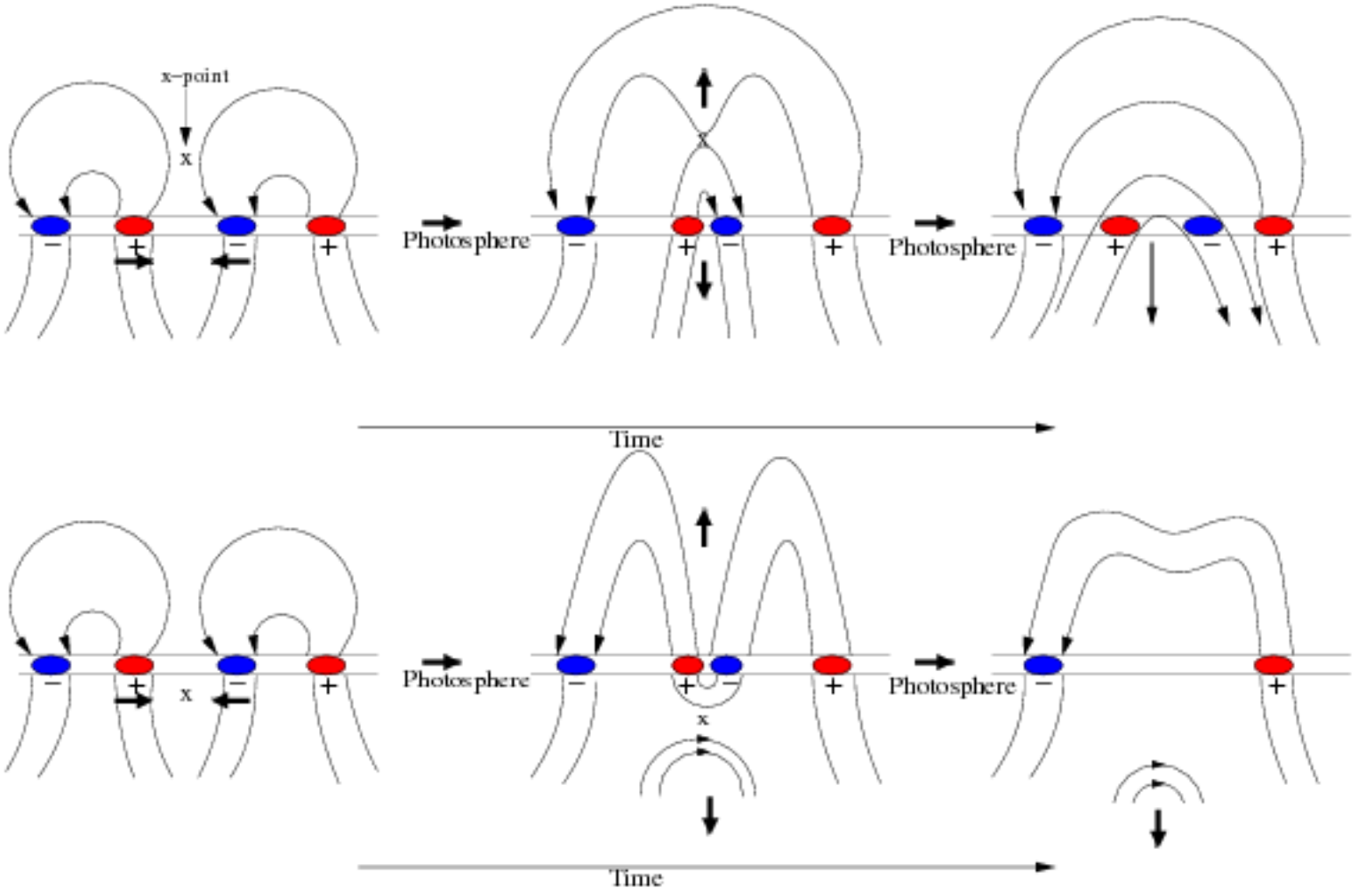

Figure 6.1: Cartoon depicting the two hypotheses for flux removal through cancellation at an x-point through (a) subduction of flux in an Ω-shaped loop below the photosphere or (b) ascension into the upper atmosphere in the form of a U-shaped loop.

In magnetograms, both of these processes are observed as opposite-polarity features in close proximity that mutually lose flux. If the pair of features have a similar absolute flux then they will simultaneously lose equal amounts of flux and reduce in size, often resulting in the disappearance of one or both features. If the two opposite-polarity features are dramatically different in size then both features will lose equal amounts of flux, but the larger feature may often retain its original area and if it loses only a small percentage of its overall flux, whilst the smaller feature can exhibit the typical cancellation behavior, reducing considerably in area and flux and often eventually disappearing.

To detect cancelling events, an algorithm, similar to the initial bipole identification process (§ 4.1.1), is developed. The aim is to identify cancellation by first identifying opposite-polarity pairs of features in each frame and then investigating how the flux in each pair behaves. A bipolar pair of features is identified in each j^{th} frame as the i^{th} opposite-polarity pair of features Φ^j_{i+} and Φ^j_{i-}, with fluxes of Ψ^j_{i+} and Ψ^j_{i-}, respectively. To be a cancelling event each bipolar pair must have a minimum distance between the boundaries of the features of $\leq$ 3 pixels ($\approx$ 0.4 Mm). I choose a smaller distance between the opposite-polarity features, than in the emerging case, as cancelling features move together, rather than apart. The smaller distance also reduces the likelihood of questionable pairings. Note, I do not apply a flux ratio criterian here as cancellation can occur between any two opposite polarity features regardless of the difference in their absolute fluxes. I also leave all non-unique pairings as a large feature can cancel with one or more opposite-polarity feature simultaneously.

When detecting cancellation events it is not just the close opposite-polarity features that go on to die that need to be considered, as features often do not actually lose all their flux following cancellation. However, as I have tracked the features I can investigate the variation of flux of both features in an opposite-polarity pair. I define cancellation as the overall loss of at least 20% of the absolute flux from a pair of tracked opposite-polarity features over a period of 3 or more frames ($\geq$ 4.5 minutes). There is no constraint on the ratio of flux lost in each feature as the cancelling pairs are not always observed to lose a similar amount of flux because features can be cancelling with numerous features at the same time, or larger features may be both cancelling and coalescing or fragmenting at the same time.

The results of the algorithm are presented in Table 6.1. The speed of approach of the cancelling features is found by measuring the rate of change of the edge separation of each pair of opposite-polarity features between each frame. In frame j, the separation d^j_i, of the opposite-polarity features Φ^j_{i+} andΦ^j_{i-}, is defined as the distance between the nearest edges of Φ^j_{i+} andΦ^j_{i-}. The pixels corresponding to the cancelling event features in frame k are found. In frame j, the initial separation of all pixels (x^j_{i-}, y^j_{i-}) associated with the negative features (Φ^j_{i-}) are compared to all the pixels(x^j_{i+}, y^j_{i+}) associated with positive features (Φ^j_{i+}), where the smallest distance between any two opposite-polarity features

$$d^j_i = \sqrt{(x^j_{i-} - x^j_{i+})^2 + (y^j_{i-} - y^j_{i+})^2},$$

is the initial separation of the opposite-polarity components of the cancelling event. The speed of approach is then the rate this separation reduces between frames.

Note, the time of interaction is the time over which both features are decreasing in flux. When counting the total flux lost it is ensured that the flux from non-unique pairings is not multiply counted.

6.1.1 Cancellation Results

Results	Clumping	Downhill
Number of cancelling pairs ($\times 10^{-16}$ cm^{-2} day^{-1})	1.4	2.0
Number of features involved in cancellation ($\times 10^{-16}$ cm^{-2} day^{-1})	2.2	3.1
Mean flux lost per cancelling pair ($\times 10^{17}$ Mx)	3.3	2.0
Mean interaction time (minutes)	10.6	9.7
Mean flux loss rate per cancellation ($\times$ 10^{14} Mx s^{-1})	5.3	3.3
Mean speed of approach (km s^{-1})	0.19	0.10
Surface area where cancellation occurs (%)	32	28
Total flux loss (Mx cm^{-2} day^{-1})	46.9	38.5

Table 6.1: Results for the cancelling events detected in both the downhill and clumping data.

The flux loss rate per cancellation is a few times 10^{14} Mx s^{-1} for the cancelling events, which have mean flux of order 10^{17} Mx. The rate of flux loss is in good agreement with previous results of between $2.8 \times 10^{13} - 2.9 \times 10^{15}$ Mx s^{-1} found from investigating cancellation in features, observed in BBSO and MDI/high-resolution magnetograms, with flux between $10^{17} - 10^{20}$ Mx (Livi et al., 1985; Wang et al., 1988; Harvey, 1993; Chae et al., 2002). However, the cancellations I observe interact, for on average, just 10 minutes compared to 1-36 hours for the cancellations observed by Wang et al. (1988) and Chae et al. (2002). These results show that the rate of flux loss is apparently independent of the flux in the features, but that the duration of cancellation appears to be proportional to the size of the features.

I determine the speed of approach of cancelling features, from the closest edges of the opposite-polarity features moving towards one another when they mutually lose flux. The speed of approach of the cancelling features that I found is between 0.10-0.19 km s^{-1} (for features with pre-cancellation flux of order 10^{17} Mx). Chae et al. (2002) and Litvinenko and Martin (1999) observed cancellations in high-resolution MDI magnetograms and Kitt Peak NSO full-disk daily magnetograms, respectively, and found that features of the order of 10^{18}-10^{19} Mx advance towards one another at between 0.27-0.35 km s^{-1}, which is more than double the speeds that I find. Chae et al. (2002) measure their speed of approach from before the opposite-polarity features begin to cancel, but found that this speed reduced by half when the opposite-polarity features began to cancel. As I measure the speed of approach from when the features begin to cancel, this is likely to be the reason in the differences.

The speed of approach of cancelling features has also been determined theoretically: Chae et al. (2002) used the Sweet-Parker reconnection cancellation model developed by Litvinenko and Martin (1999) to estimate that the converging speed of cancellation giving a flux loss rate (per event) of order 2.8×10^{14} Mx s^{-1} is 0.076 km s^{-1}. This estimate is in much better agreement with the approaching speeds I calculate rather than the previous speed observed.

At the start of this section it was mentioned that finding cancelling features was not simply a case of searching for features which died in subsequent frames, as it was not guaranteed that a feature would lose all of its flux in a single occurrence of cancellation. Here, each cancelling pair is investigated to find what happens to the features. For the cancellations detected in the downhill data it is found that for 50% of cancellations both features die at the end of the flux loss period, for 45% only one feature dies and in 5% none of the features involved die. Similarly for those detected in the clumping data, in 41% of cancellations

both features die, in 51% one feature dies and 8% no features die. Therefore it appears that in the majority of cases of cancellation at least one of the features dies.

In Table 6.1, it can be seen that the number of cancelling pairs detected and the number of features involved in cancellation is a factor of 1.4 times larger in the downhill data compared to the clumping data. However, the flux lost and the flux loss rate per cancelling pair is 1.6 times less in the downhill data in comparison to the clumping data. This is consistent with there being more tracked features in the downhill data which have on average a smaller peak flux. These differences results in the total flux loss detected in the downhill data being lower by a factor of 0.82.

As for the emerging events, I compare the events detected as cancelling in the clumping data and in the downhill data. This is done in the same way as it was for comparing emerging events, i.e. by identifying the pixels of features associated with a cancelling event in the clumping data and finding if the corresponding pixels in the downhill data contain cancelling features and vice versa. For the clumping data 15% of cancellations are detected only in the clumping data. Whilst 60% of cancelling events detected in the clumping data are also detected in the downhill data. In a further 13% and 12% of cases only the positive or negative feature of a cancelling event detected in the clumping data is also detected as cancelling in the downhill data. Comparing those cancellations detected in the downhill data to those detected in the clumping data, I find that 14% are only detected in the downhill data alone. 56% of the downhill cancellations are also wholly detected in the clumping data. For 15% and 14% of the downhill cancellations only the positive or negative feature is also detected in the clumping data, respectively.

Cancellation is naturally thought of as the opposite process to emergence. Since the flux in the quiet-Sun is observed to remain approximately constant over a period of days to weeks, the total flux emerged each day and the total flux which cancels each day in the quiet-Sun should be more-or-less equal. The numbers of cancelling pairs cannot be simply compared to the number of emerging pairs as features may cancel multiple times without losing all of their flux. This is highlighted by the fact that the number of features involved in cancellation is less than double the number of cancelling pairs and indicates that there is cancellation occurring between more than two features, as was hypothesized earlier.

As the cancelling algorithm is applied to tracked data, its results are only compared to the results from the tracked emergence detection methods. It is found that the flux lost in Mx cm^{-2} day^{-1} for cancellation detected in the clumping data is $\approx 30\%$ higher than the rate of flux emergence detected by both the TB and TC methods. For the downhill data, however, the total flux lost is similar to the lower bound of the rate of flux emergence found by the tracked emergence detection methods. If the amount of flux lost through cancellation is greater than the amount detected as gained through emergence and the total flux in the observed area remains approximately constant then this can indicate two things. The first is that flux may be fed into the system from larger-scale features, that break up and move into the network or secondly that there is possibly sub-resolution flux emerging into photosphere, which is not detected by the TB or TC methods, as emerging, in the previous Chapter.

It is believed that cancellation occurs between previously unconnected opposite-polarity features, i.e. pairs of features that do not emerge together (Livi et al., 1985; Schrijver et al., 1997). I investigate if this is true by comparing the cancelling pairs to the pairs of features found to be emerging using the tracked

emergence detection methods. For those bipoles detected by the Tracked Bipolar methods, in both the clumping and downhill data, none of the bipoles cancelled with themselves. However, for those detected by the Tracked Cluster method, just under 6% of clusters underwent some cancellation between their opposite-polarity components, regardless of whether they were detected in the clumping data or the downhill data. Obviously the likelihood of cancellation occurring in a cluster increases as the size of the cluster increases.. Interestingly they indicate that there are possibly U-loop cancellations (Figure 6.1b) occurring between the features in the cluster emergence. This suggests that ephemeral regions and IN emergence occurs in the same way as active region emergence in which U-loop cancellations are regularly seen (van Driel-Gesztelyi et al., 2000). This idea is discussed further in § 6.3.1, where I consider the evolution of emerging events.

6.1.2 Visual Examples of Cancellation In Hinode/NFI

Here, five visual examples of the detected cancellation events are presented, with only the features of interest coloured. The first example (Figure 6.2) shows a negative (turquoise) feature close to a positive (orange) feature. This cancellation event was detected to behave in the same manner in both the clumping and downhill data. As the time progresses, it can be seen that both features reduce in size and flux, leading to the full cancellation of both features. Figure 6.3 shows how the flux varies with time during this cancellation event and indicates that the negative feature loses 1.4 times as much flux as the positive feature. This suggests that there is sub-resolution positive flux that is not observed as being involved in this cancellation event. Interestingly they also appear to rotate as the cancellation progresses. The error size of the flux of the features is given by the area (cm^{-2}) $\times$ cutoff (Mx cm$-$1) of each feature in each frame where the flux is measured.

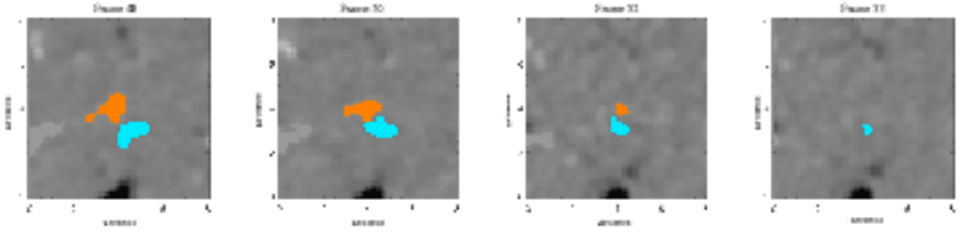

Figure 6.2: An example of a cancellation event detected identically in both the clumping and downhill data. As the time progresses, the negative (turquoise) feature and the positive (orange) feature rotate and reduce in both flux and area.

The second example (Figure 6.4) also had the same structure in both the clumping and the downhill data. This shows a case where only one of the features involved in the cancellation dies. In frame 94 a positive (red) feature can be seen with a negative (blue) feature. Initially the features appear to be of similar size. The features mutually lose flux for 8 frames (12 minutes), after which the negative feature begins to gain flux again and the positive flux continues to fully cancel. During the time when the negative feature is cancelling it loses 60% of its flux, before rising again to just above its initial flux. This situation of only one feature dying is obviously more likely to happen if, like in the instance illustrated here, the features initially have an imbalance of flux.

In the next figure I show a situation where neither of the features die during cancellation. Figure 6.6

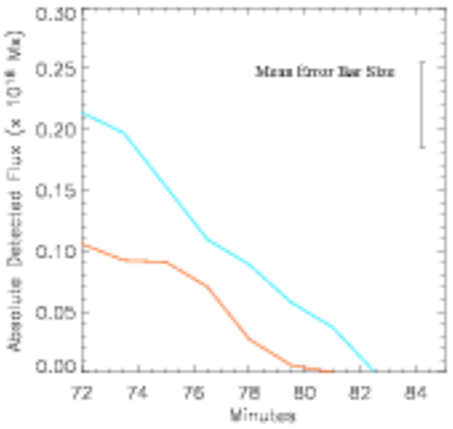

Figure 6.3: The absolute fluxes from the cancelling features detected in Figure 6.2 are plotted against time. The turquoise line and the orange line represent the turquoise and orange features respectively. The average error bar size is plotted in the top right corner.

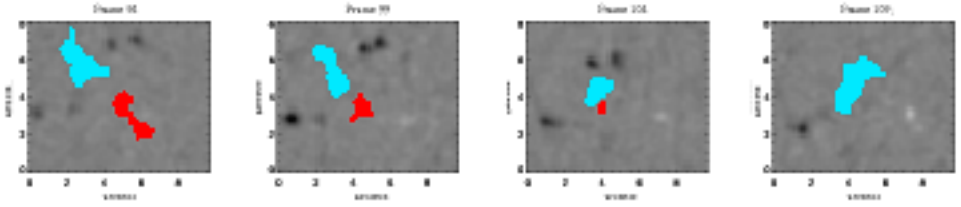

Figure 6.4: Cancellation of a positive (red) feature with a negative (blue) feature in which the positive feature dies, but the negative feature loses just over 40% of its initial flux, before gaining flux again. This is detected the same in both the clumping data and the downhill data

shows a negative (purple) feature alongside a positive (red) feature. Figure 6.7 shows that for the first ≈6 minutes (9 frames) of the interaction, both features mutually lose flux. After this point, the negative feature increases in flux, whilst the red feature continues to lose flux for a few more minutes before gaining flux also. This case of neither feature cancelling fully occurs in only 5% and 8% of the cases of cancellation detected in the downhill and the clumping data, respectively. In most cases they initially start like a typical cancellation, with two opposite-polarity features moving close and losing flux, but for some reason these features begin to gain flux and move apart before they have cancelled fully.

Flux features often appear not to be touching when they are cancelling. This is primarily to do with the threshold constraint applied in the feature identification algorithm. Figure 6.8 shows a cartoon of the Gaussian curves of flux, of a positive (red filled curve) and negative (blue filled curve) feature which are cancelling. The threshold is plotted as a dotted line. After the feature identification algorithm is applied I only observe the flux above the threshold (filled areas of the flux curves). What can be seen is that although the flux curves of the features are overlapping i.e., the features are cancelling, there is a gap between the filled areas of the curves which I observe.

The last visual example (Figure 6.9) shows a complex case of cancellation where multiple opposite-

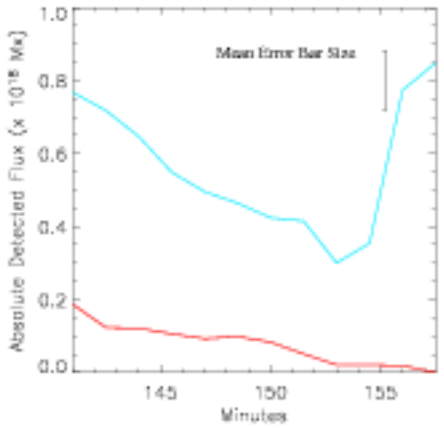

Figure 6.5: The absolute fluxes from the cancelling features detected in Figure 6.4 are plotted against time. The red line and the blue line represent the red and blue features, respectively. The average error bar size is plotted in the top right corner.

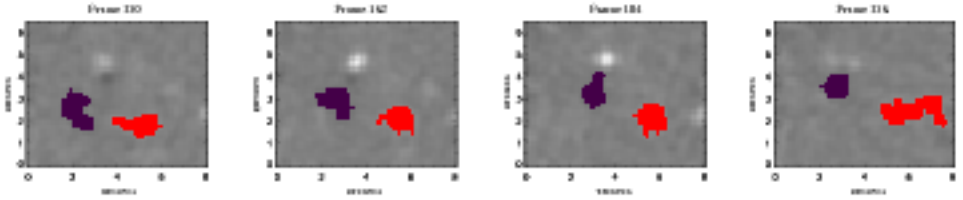

Figure 6.6: An example of a cancelling event where neither of the interacting features die. The negative (purple) feature and positive (red) feature begin to cancel as normal, both mutually losing flux. However, before either feature has fully cancelled they both begin to gain flux and move apart.

polarity features cancel simultaneously. Figure 6.9a shows how this particular cancelling event is detected in the clumping data, the red and yellow features have positive polarity and the purple and blue features have negative polarity. It is obvious that the red, the blue and the purple features reduce in area as flux cancels in these features. This case of complex cancellation is more likely to occur when there is a large flux region, surrounded by smaller features. Figure 6.10 shows how the flux of the features vary over time in the clumping data, again the colour of the lines indicates the flux of the features in Figure 6.9 with the same colour. It can be seen that all the interacting features lose flux for the entire time the interaction occurs.

In the downhill data (Figure 6.9b), cancellation is still detected in this location, but it looks very different and there are now three separate cancellation events. Case 1 is the negative turquoise feature cancelling with the positive orange feature. The turquoise feature was detected in the clumping data as the light blue feature, but the orange feature would have been part of the red feature in the clumping data. Case 2 the positive lime green feature in frame 0 is another portion of the large red feature in the clumping data and is found to be cancelling with the royal blue negative feature (the purple feature in the clumping data). As the features cancel the distribution of flux within the royal blue feature changes as it segments into two flux peaks. Cancelling case 3 is the royal blue and purple negative features cancelling with another positive

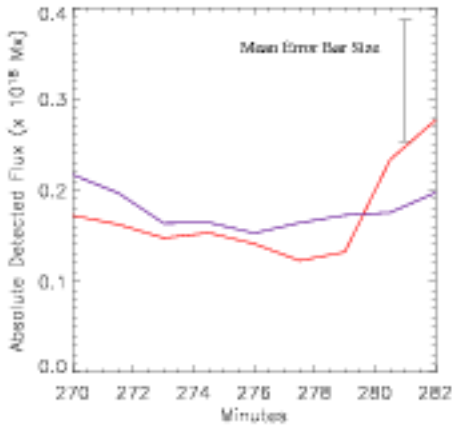

Figure 6.7: This is the flux variation in time for the cancelling features shown in Figure 6.6. The negative (purple) feature and the positive (red) feature initially cancel like normal, both mutually losing flux, before gaining flux and moving apart. The average error bar size is plotted in the top right corner.

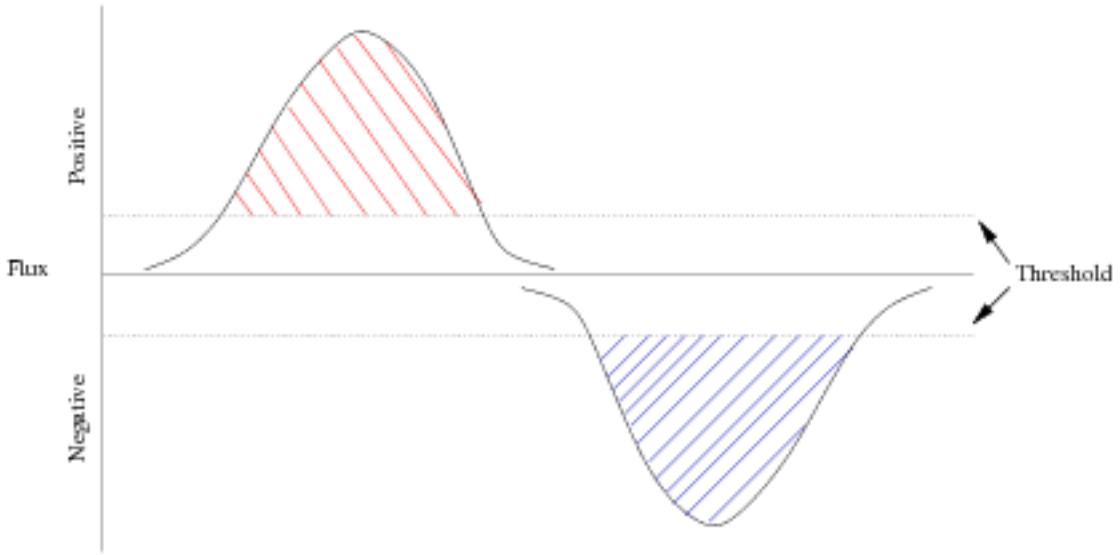

Figure 6.8: Cartoon of the Gaussian flux curves of a positive (red filled curve) and negative (blues filled curve) feature which are cancelling. The dotted line is the flux threshold criteria applied in the identification algorithm.

(red) feature in frame 4 (6 minutes). Comparing case 3 to the clumping data it can be seen this is part of the yellow positive feature, which cancelled for the full time in the clumping data. This example shows that when detecting cancelling events it is not always as straight forward as two opposite-polarity features. That is why the cancellation algorithm allows features to be paired with more than one opposite-polarity feature. The reason only a portion of the original red feature is detected as cancelling is due to the fact that the downhill feature identification method segments large flux regions into single flux peaks and only this particular peak is found to lose flux.

In the clumping case the cancellation was detected as one event. In the downhill data, however, it

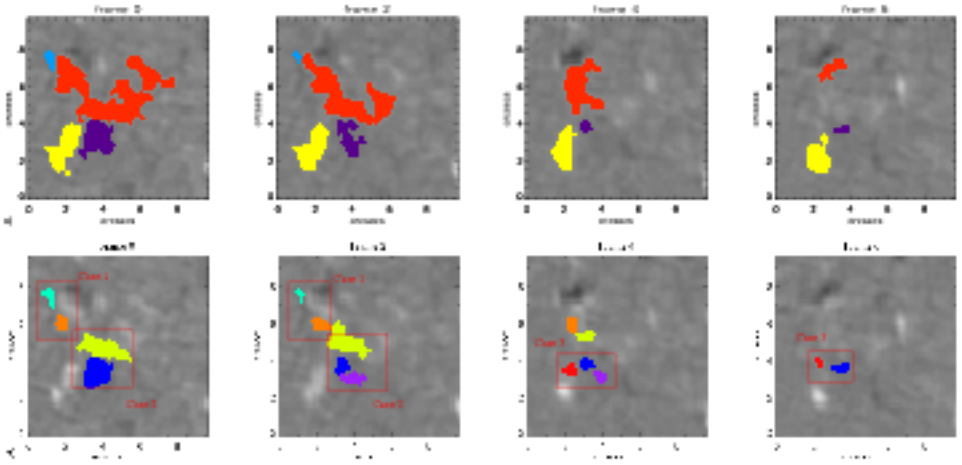

Figure 6.9: In this figure a complex case of cancellation can be seen in a) the clumping data and b) the downhill data. It can be seen that one complex cancelling event in the clumping data is split into three when detected in the downhill data.

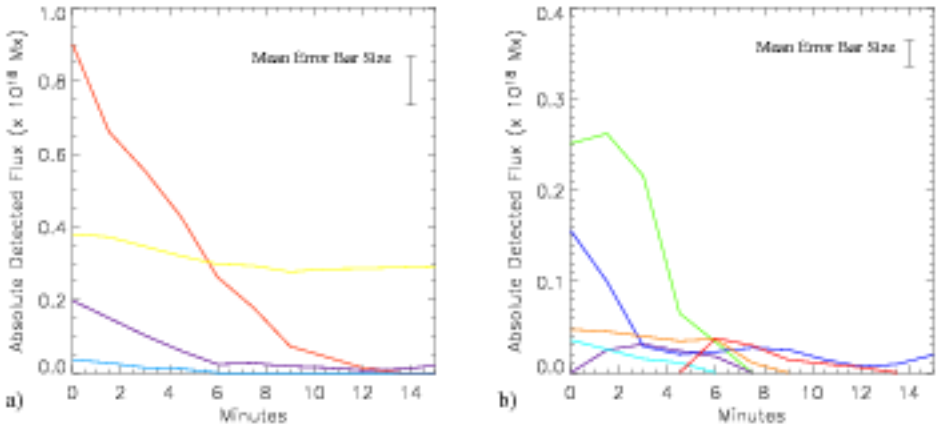

Figure 6.10: A plot of flux versus time for the features observed to be cancelling in a) Figure 6.9a and b) Figure 6.9b. It can be seen that although, the cancellation involves multiple features all of them continually lose flux during the interaction time. The average error bar size is plotted in the top right corner.

appears as three separate events. Figure 6.10b shows the flux versus time in the events in each of the three cancellations that are detected in Figure 6.9b. Unlike the cancellation in the clumping data, the three cases lose flux over different times, rather than all the features losing flux for the entire time.

6.1.3 Distribution of Cancelling Flux

To gauge further how the cancellation and emerging results compare, the distributions of flux lost per cancellation event (Figure 6.11) are plotted alongside the distributions for the peak fluxes of emerging events detected, using the TB and TC methods, in the previous chapter. The cancellation distributions

found actually look similar to the distributions for the tracked methods of emergence detection, which are over plotted as dashed lines. There are more occurrences of cancellations losing less than 10^{18} Mx of flux in the downhill data than in the clumping data. As discussed above, in the majority of cancellations which occur one or both features die. This indicates that in the downhill data the majority of flux features which are cancelling have smaller flux than those detected in the clumping data. Both have a peak in their distributions at about 3×10^{17} Mx, which coincides with the mean peak flux lost for the cancellations as found in Table 6.1, below this value of flux the distribution drops off.

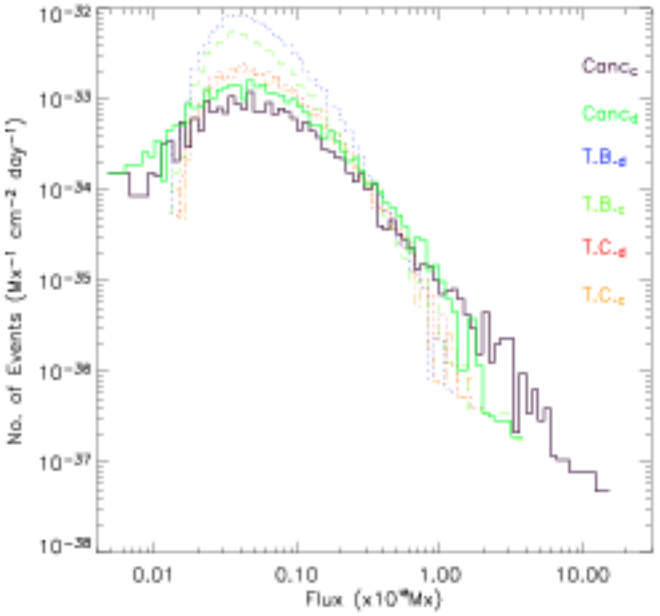

Figure 6.11: Log-log plot of the flux lost per cancelling pair versus number of cancellations compared with the distribution of the flux emerged per event from the previous chapter, where the subscripts c and d refer to clumping and downhill data, respectively.

Not surprisingly I find that distribution for the clumping data has an extended tail and detects cancellations with flux loss of over 10^{19} Mx, whereas the cancellation in the downhill data has a maximum flux loss of 4×10^{18} Mx. Like the emerging features the tails of the cancellation distributions appear to follow a power law. However, due to the small range of fluxes observed not much can be said about this at the moment, but, in Chapter 8, I determine the cancellation of flux in full-disk MDI magnetograms enabling this distribution to be extended. In Chapter 8, I consider whether cancellations follow a power law and, if so, what its slope is.

The cancelling event distributions both extend to larger fluxes than the emerging event distributions. This is not surprising as cancellation can occur between features at any stage in their life and in features of any size, whereas features are only defined as emerging until they interact with other features, during which time their flux is often still relatively small. As in Figure 5.18, it is noticeable in Figure 6.11 that there is a peak/turnover in all the distributions, below which the number of features drops of rapidly. As mentioned in Chapter 5, this is likely to be due to a combination of the feature identification and tracking criteria and not a true peak/turnover for the peak flux lost per cancelling event.

In this section, I have been able to detect small-scale cancellation and investigate its nature. However, my method cannot determine how flux is removed from the photosphere, as we do not compare our observations to chromospheric observations to see if the cancelled flux rises or subducts. This would be the next step to fully understanding the evolution of small-scale features.

6.2 Detecting Fragmentation and Coalescence in NFI/Hinode

In order to find fragmentation and coalescence automatically, I again use the tracked data. In order to track magnetic features it is necessary to flag both fragmenting features and coalescing features. In particular, fragmentation involves the 'birth' of at least one feature whilst coalescence involves the 'death' of at least one feature. The manner by which features can be born or can die is described in detail along with the feature tracking algorithm in Chapter 3. Here, I discuss the assumptions, results and implications of finding fragmenting and coalescing features in the tracked data.

Fragmentation is the splitting of a single magnetic feature into two or more smaller features. In magnetograms, there are three outcomes to this process: (i) the resultant fragmented features will all be above the feature detection threshold; (ii) some of the resultant features will be above the detection threshold, but others may fall below it; and (iii) none of the fragmented features are above the threshold, hence none of the features are detectable with the automated feature identification algorithm.

The tracking algorithm discussed in Chapter 3 only identifies the first two cases as fragmentation. The tracking algorithm works by associating features between frames so each feature has a unique label for its entire lifetime. In the first two cases, the large feature in frame j, before fragmentation, will transfer it is label to the largest of the newly created, smaller, features it overlaps in frame j+1, whilst the other overlapping features in frame j+1 are classed as 'born through fragmentation'. In the third case, if all the resultant features are below the threshold then the feature and its label will disappear between frames and thus will be flagged as 'disappeared'. The number of events which disappeared in this way are estimated in the next section.

The fragmentation algorithm is designed to find all features which are born through fragmentation and associate them to their parent feature. In particular it determines the rate of fragmentation and also finds the number of features involved in each fragmentation. By knowing the frame of fragmentation and the unique label of the features involved, I can find the flux and area of the parent features just before they fragment and I also find the fluxes and areas of the features produced. The fragmentation results are presented in Table 6.2.

Coalescence is the converse process, where two or more like-polarity features coalesce and form a single feature. As for fragmentation, in observations, three cases can occur: (i) two or more tracked features above the threshold may merge to form a single feature, (ii) two or more tracked features, some above and some below the threshold, merge to form a single feature and (iii) two or more features, all below the threshold, form a single feature which appears above the threshold.

As in the case of fragmentation the tracking algorithm only identifies the first two cases as coalescence.

In the first two cases the largest of the initial individual small features before coalescence will transfer its label to the single large feature after coalescence and the others will be flagged as 'disappeared through coalescence'. In the second case, if there are two or more features above the threshold then this will be treated the same as case one. If only one feature is above the threshold which is coalescing with features below threshold features to form a larger feature, then this will seem like a single feature increasing in flux between frames and will not be recognised as coalescence. The third case will not be identified as coalescence at all; as sub-resolution flux coalescing to form a feature above the detection threshold will result in a new feature simply flagged as an 'appearance' (see Chapter 3 for the full definition). These latter cases are discussed in the next section.

A coalescence algorithm was created to find features which die through coalescence and find the parent features. The analysis of the results is similar to that of the fragmentation algorithm and the results are also given alongside the fragmentation results in Table 6.2.

Clearly, after emergence, features can undergo each of the other surface processes multiple times. I find the time of first fragmentation and compare to the time of first coalescence, in order to gain an insight into what happens to features immediately after they emerge.

6.2.1 Fragmentation and Coalescence Characteristics

Table 6.2 shows that there are more cases of fragmentation in the downhill data than in the clumping data. This is not surprising as there are more features identified in the downhill data to start with. The mean flux of the features born through fragmentation is a factor of 3 larger in the clumping data compared to the downhill data. Similarly the mean flux of the features which fragment in the clumping data is almost a factor of 4 larger than in the downhill data . This is due to the differences in mean peak flux of the features identified by the downhill and the clumping data. It can be seen, in both the clumping and the downhill data, that most fragmentation events involve one feature splitting into two, and the fluxes of the features involved reveal that most of the flux is retained in the new features rather being lost in sub-resolution features.

Now looking at the coalescence results in Table 6.2, it can be seen that there are more coalescences detected in the clumping data than in the downhill data. This is not what was expected considering the fragmentation results and with the knowledge that there are more features identified by the downhill method than the clumping method. However on visually inspecting the evolution of the features in both the data sets it is clear that in the downhill data set many of the cases of coalescence found by clumping are not detected by the algorithm, as the merged features retain their identity as individual flux peaks rather than actually coalescing to from a single feature. My algorithm detects coalescences by identifying those features which die (those features whose individual label is no longer in the data set) in the process, so if no feature dies, the coalescence will occur without being detected.

Looking at the fluxes of the features which coalesce and the resulting features reveals again that the fluxes of the features in coalescing events in the downhill data have much smaller fluxes, than those in the clumping data, due to them being singly peaked. This is also the case for the areas of the features. The results also indicate that coalescence is most likely to occur between two features merging to form a

Fragmentation Results	Clumping	Downhill
Number of fragmentations involving above threshold features ($\times 10^{-16}$ sr^{-2} day^{-1})	6.6	14.1
Number of fragmentations involving sub-resolution features ($\times 10^{-16}$ sr^{-2} day^{-1})	11.6	12.8
Number of tracked features involved in fragmentations ($\times 10^{-16}$ sr^{-2} day^{-1})	9.5	19.9
Mean flux of each parent feature before fragmentation ($\times 10^{18}$ Mx)	1.54	0.42
Mean flux of each feature produced through fragmentation ($\times 10^{18}$ Mx)	0.75	0.23
Mean area of each parent feature before fragmentation (Mm^2)	2.96	0.85
Mean area of each feature produced through fragmentation (Mm^2)	1.41	0.47
Mean number of features produced by a feature fragmenting	2.1	2.3
Area where fragmentation occurs (%)	50	56
Mean time until first fragmentation (minutes)	11.9	10.5
Coalescence Results	Clumping	Downhill
Number of coalescences involving above threshold features ($\times 10^{-16}$ sr^{-2}day^{-1})	9.5	6.2
Number of coalescences including sub-resolution features ($\times 10^{-16}$ sr^{-2}day^{-1})	9.1	11.6
Number of tracked features involved in coalescence ($\times 10^{-16}$ sr^{-2}day^{-1})	13.3	11.6
Mean flux of each feature which coalesces ($\times 10^{18}$ Mx)	0.72	0.08
Mean flux of each resulting feature after coalescence ($\times 10^{18}$ Mx)	1.38	0.16
Mean area of each feature which coalesces (Mm^2)	1.33	0.25
Mean area of each resulting feature after coalescence (Mm^2)	2.59	0.45
Mean number features which merge to form a single feature	2.3	2.2
Area where coalescence occurs (%)	52	36
Mean time until first coalescence (minutes)	6.4	6.6

Table 6.2: Results of the algorithms to identify occurrences of fragmentation and coalescence.

single larger feature. The fact that in most cases the flux of the constituent features adds up to that of the newly merged feature reveals that there are not many cases of coalescence detected which involve extra sub-resolution features which are merging with observed features.

In the previous chapter and in the previous section, the emergence and cancellation events detected in the clumping and downhill data, were compared to help gauge the differences in how features are identified and how this affects the various algorithms applied to the data sets. For the fragmentation algorithm applied to the clumping data I find that 85% of the fragmentations detected in the clumping data are not detected in the downhill data. Only 4% are detected completely the same and 11% are detected differently in the downhill data. For the downhill data fragmentations 94% are only detected in the downhill data, 2% are detected the same in both data sets and 4% are detected differently in clumping compared to downhill. Similarly for cases of coalescence, I find that in the clumping data 83% are only detected in the clumping data, 5% are detected the same in both the clumping and downhill data and 12% are detected differently in the different data sets. For coalescence in the downhill data I find that 74% are only found in the downhill data, 10% are detected the same in both data sets and 15% are detected differently in both data sets. It is not surprising that these results are so different considering the difference between the structure of features identified. In the next section we consider visual examples of fragmentations and coalescences and show how the differences in structure can lead to event not being detected in the downhill data. The fact that the downhill data splits large flux regions into individual flux peaks, can lead to extra cases of fragmentation being detected in the downhill data.

In Table 6.2, the percentage of the surface area where fragmentation and coalescence occurs shows that the greater the number of events detected the greater the percentage area they cover, obviously. Visually

observing where fragmentation and coalescence can occur in the data for both clumping and downhill reveals that it is spread over the surface. The higher the concentration of the features the more fragmentation and coalescence occurs. Large features tend to fragment and coalesce frequently, continually destroying and producing small-scale features. If there is some proportion of heating initiated by fragmentation, it would be continuous and well distributed.

Comparing the times of first action of the features following their emergence, indicates that features are more likely to undergo coalescence first. As coalescence is the first surface process that the features undergo after birth, it is not surprising that the fluxes and areas of the features which coalesce are found to be smaller than those features which fragment (Table 6.2). As a large number of clusters were found to emerge in Chapter 5, it is not surprising that coalescence occurs first. This indicates that the small-scale emergence events found in the NFI data also exhibit the same behaviour seen in larger active regions, where clusters of mixed-polarity emerge and coalesce as the region develops (Vrabec, 1974; Solanki, 2003; Handy and Schrijver, 2001).

As discussed in Chapter 3, tracked features can either be born through 'appearance' (Figure 3.6a) or 'appear through fragmentation' (Figure 3.6d). Furthermore, the term 'appearance' covers tracked features being born through genuine emergence with a detected opposite-polarity feature, genuine emergence with a undetected opposite-polarity feature and also the coalescence of sub-resolution flux of an existing dispersed feature, causing it to appear above the threshold (Lamb et al., 2008). Similarly a feature can either die through 'disappearance' (Figure 3.6b) or 'disappear through coalescence' (Figure 3.6e), where 'disappearance' covers the cancellation of a feature with a detected opposite-polarity feature, cancellation with an undetected opposite-polarity feature, and the dispersal of flux causing the peak flux of the feature to fall below the flux threshold. In the previous chapter and in this chapter I have found all cases involving the genuine emergence and cancellation where the features are detected. Furthermore, Lamb et al. (2008) investigated genuine emergence and cancellation in which only one of the features is detected and determined that its occurrence was rare. Here I investigate how many cases of fragmentation result in all the resultant features being sub-resolution and similarly how many cases of coalescence involve only sub-resolution features merging to form a feature above the flux threshold.

The TB and TC emergence detection methods are used plus the fragmentation results to find which features are not identified as appearing through genuine emergence or fragmentation in the downhill and clumping data. Using the TB emergence detection method and the fragmentations I find that 36% and 45% of appearances, for the downhill and the clumping data respectively, are not accounted for and are therefore classed as 'coalescence of sub-resolution flux'. Similarly using the TC emergence detection method I find 30% and 34% (for the downhill and the clumping data, respectively) are classed as 'coalescence of sub-resolution flux'. To find out how common the death of a feature is through the dispersal of sub-resolution flux, I use the results from the cancellation algorithm § 6.1 and the coalescence results from this section. The amount of deaths not accounted for is 50% in the clumping data and 36% in the downhill data. The actual number of events involving sub-resolution features is presented in Table 6.2. They show that the amount of fragmentation and coalescence detected, in features above the flux threshold, by my algorithm is a lower bound on what is actually occurring.

I now compare the number of events I find in Table 6.2 to what I have found for the emerging events

identified by both the tracked emergence detection methods in § 5.3. I take the mean of the number of emerging events found by both the Tracked Bipole and the Tracked Cluster method to get the number of emerging events in the downhill data, 3.3 $\times 10^{-16}$cm^{-2} day^{-1}, and in the clumping data, 4.8 $\times 10^{-16}$cm^{-2} day^{-1}. Comparing the number of fragmentation events to these I find that there is between 1.4-4.2 times more fragmentations than emerging events, in the downhill and clumping data respectively. For the number of coalescences, I find 1.9 times more in the clumping data and 2.0 times more in the downhill data. Remember, however, that in the previous paragraph, I found that it is highly likely that there are in fact extra cases of fragmentation and coalescence which are below resolution. Adding these sub-resolution events to the number of events actually detected would then take the number of fragmentations to between 3.8-8.2 times more in the clumping and downhill data, respectively. The number of coalescences would increase to between 2.7-3.9 times more in the downhill and the clumping data, respectively.

The numbers of sub-resolution fragmentation and coalescence events may look like it accounts for a considerable amount of the evolution events, but how much flux do they actually add or remove from the system? It is found that in the downhill data the sub-resolution fragmentations remove 0.02 Mx cm^{-2} frame^{-1}, whilst exactly the same amount of flux is injected by sub-resolution coalescence events. In the clumping data 0.01 Mx cm^{-2} frame^{-1} is removed through sub-resolution fragmentations, but the same amount of flux is also added by sub-resolution coalescences. The total flux per cm^2 per frame found for the tracked features, in the previous chapter, was 6.3 Mx cm^{-2} frame^{-1} in both the downhill and the clumping data. Thus, these sub-resolution events only account for less than 1% of the flux on the surface at any instant.

As well as just looking at the number of events, to try and get a handle on the behaviour of the features on the surface I also look at the total number of features which take part in fragmentation and coalescence compared to emergence. For the clumping data the number of features taking part in fragmentation and coalescences is ≈3 times less than the total number of features, for both emergence detection methods. Repeating this for the downhill data I find half as many features involved in fragmentation and 4 times less features involved in coalescence compared to emergence. There appears to be a shortfall in the number of features which fragment and coalesce compared to the number of features involved in emergence. This could be due to: (i) the constraint that the fragmentation and coalescence detection algorithm is unable to identify surface processes if they are the result of or results in sub-resolution flux or (ii) simply that not all of the emerged features experience such processes. I have already shown that it is likely that there is a high number of sub-resolution coalescence and fragmentation events which go undetected. If I calculate the percentage of features present that interact I find that 38% of features fragment and 54% of features coalesce in the clumping data and 52% of features fragment and 30% coalesce in the downhill data. These results seem to indicate that most features interact, but a high percentage of interactions are undetected due to the flux being below resolution.

6.2.2 Fragmentation and Coalescence Visual Examples

Here some visual examples are presented of fragmentation events which are detected, with only the features of interest coloured. The first example (Figure 6.12) shows a fragmentation event which is detected

identically in both the clumping and the downhill data.

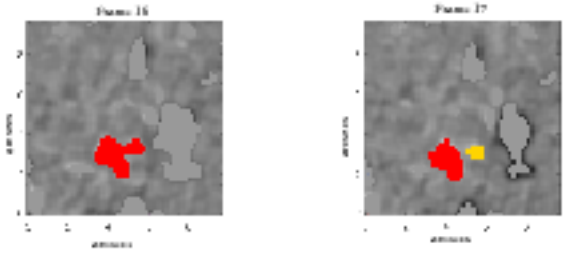

Figure 6.12: An example showing a fragmentation detected identically in both the clumping and downhill data. There is originally one positive (red) feature in frame 16 which has split into two features (red and yellow) by frame 17.

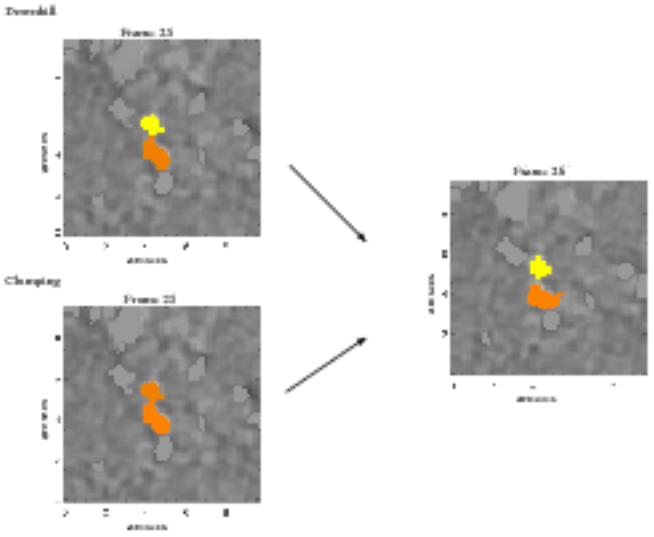

Figure 6.13: This example shows a case of fragmentation identified in the clumping data but not in the downhill data.

Visual inspection of the data revealed that fragmentation events are typically detected differently or only detected in one of the data sets. This is because fragmentation (and coalescence) depends significantly on the feature identification method used. This will be more fully discussed further on in this section once coalescence has also been considered. For now I will present two examples which highlight causes of the differences between the fragmentations detected in clumping and downhill data. Figure 6.13 shows how a case of fragmentation can occur in both the clumping and downhill data but only be detected in the clumping data. Initially in frame 25, in the downhill data two positive features can be seen (orange and yellow), which are the individual flux peaks of a larger flux region. This same flux region is identified as one positive (orange) feature in the clumping data. In frame 26 the flux region splits into two separate regions. This is detected as fragmentation in the clumping data as a new feature is born, however in the downhill data there are the same number of features in both frames and despite them being separated this does not count as a fragmentation as no new feature is born.

The final fragmentation example (Figures 6.14a and 6.14b) shows a large negative flux region in frame

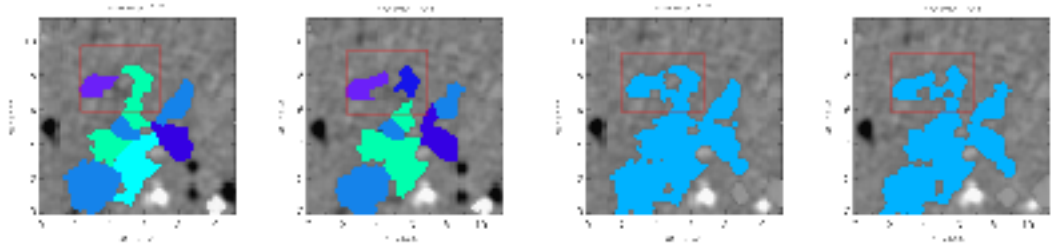

Figure 6.14: An example of a fragmentation which is detected differently in the same large flux feature in downhill and clumping data.

29 detected by downhill as various flux peaks (cyan, blue and purples) and in clumping as a single (light blue) flux massif. Clearly the region has a different structure in the downhill and clumping data. In frame 30 a feature fragments off the top of the flux region in downhill (surrounded by the red square) but in the clumping data the region has only changed shape. Looking at this flux region in the clumping data the difference in the structure is immediately obvious. The flux region is detected as one large feature, which does not fragment between frames.

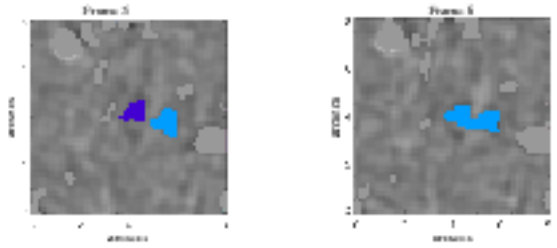

Figure 6.15: This is an example showing a coalescence detected in an identical manner in both the clumping and downhill data.

The first visual coalescence example (Figure 6.15) shows a coalescence event which is detected the same in both the clumping and the downhill data. In frame 5 there are two negative features (light blue and dark blue) which have merged together by frame 6 to form a single larger feature (light blue). This indicates that the label of the light blue feature in frame 5 has been transferred to the feature in frame 6, whilst the dark blue feature is tagged as 'died through coalescence'.

An example of when coalescence is detected differently in the downhill and the clumping data sets is seen in Figure 6.16. In the downhill data, when the two singly peaked features coalesce into a single larger region, this region is still identified as two individual flux peaks. Thus, this is not detected as a coalescence as no feature dies. In the clumping data, however, as it is just flux massifs that are identified the two features merge into a single feature and one of the original flux features dies, so this is detected as coalescence.

A second example of coalescence/fragmentation detected differently is shown in Figure 6.17. In the clumping data there is a large negative flux region detected as a single (turquoise) feature. The three features of interest surrounding the region are coloured. Between frames 6 and 7 it can be seen that the surrounding features all coalesce with the large features to form a single negative feature. In the downhill data however, the large region is separated into individual flux peaks. In the first case of coalescence this

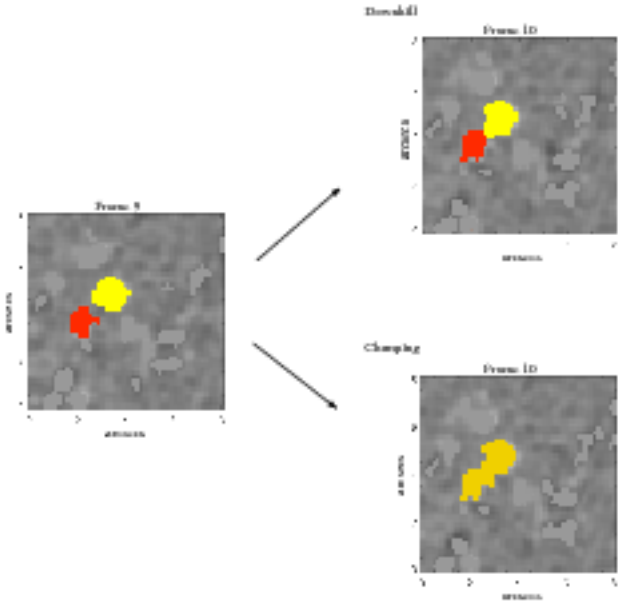

Figure 6.16: This example shows a case of coalescence which is detected by the algorithm in the clumping data but not the downhill data.

is still be detected as a coalescence event between the light blue feature and the turquoise feature, as the turquoise feature dies. However in case 2, it can be seen that despite the region merging together the features retain their individual flux peaks and so in the downhill data this is not be counted as a coalescence event. The example shown in Figure 6.17 also highlights that one of the main causes for differences in the coalescences detected in the two data sets, is the segmentation of large flux regions into individual flux peaks by the downhill data.

6.2.3 Fragmentation and Coalescence Distributions

To help visualize better the differences in the magnetic features undertaking fragmentation and coalescence, I now look at the distributions of the flux (Figure 6.18) and area (Figure 6.19). Before I discuss the results, it is worth recalling that the distribution of feature fluxes (Figure 5.1a) in the clumping data ranges from 5×10^{15} Mx up to 5×10^{19} Mx and 5×10^{15} Mx to only 10^{19} Mx for the downhill data.

From Figures 6.18 it can be seen that in the clumping data features can both fragment or coalesce over the entire range of feature fluxes. However, features have more of a tendency to coalesce up to 10^{17}Mx, after which they are more likely to fragment. For the downhill data features will fragment over the entire range of features fluxes but they will only coalesce up to 6×10^{18}Mx. Again in the downhill data there is a tendency for small features (up to 2×10^{16} Mx this time) to coalesce rather than fragment.

Now comparing fragmentation in the clumping and downhill data (Figure 6.18), it can be seen that there is more fragmentation detected in the downhill data for features with fluxes less than 3×10^{18} Mx. Not surprisingly, though, the downhill distribution drops off before the clumping one does. For fragmentation

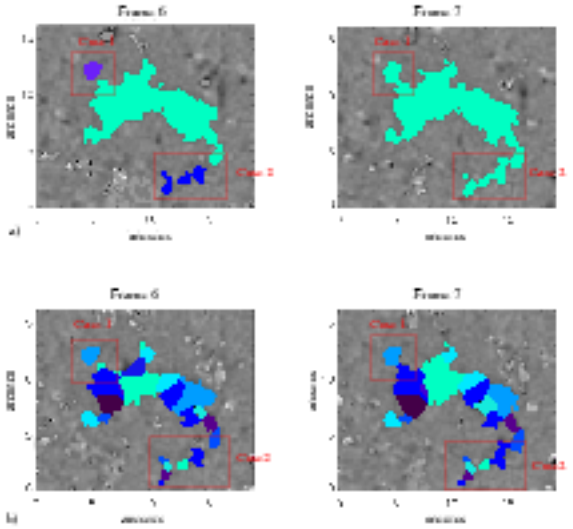

Figure 6.17: This figure illustrates that whether the fragmentation/coalescence algorithm is applied to a) the clumping data or b) the downhill data can affect what is detected as fragmenting and coalescing.

again the distributions reiterate the results found in Table 6.2, namely that there is more coalescence detected in the clumping data than in the downhill data and again the downhill coalescence distribution drops off more quickly. Note that both the coalescence distributions begin the same and only diverge after 10^{16} Mx. This probably signifies the flux above which features can begin to have multiple flux peaks and as I have already discussed in the previous section, this can inhibit the ability to detect coalescence.

Again before looking at the distributions of the areas from fragmenting and coalescing features I refer back to the area probability distribution of areas of all features from the previous Chapter (Figure 5.1b). Figure 5.1b shows that the range of areas for clumping features is 0.06-70 Mm^2 and for the downhill features the range is 0.06-7 Mm^2. With this in mind it can now be seen in Figure 6.19 that for the clumping and the downhill data, coalescence and fragmentation occurs over nearly the whole range of areas. Not surprisingly the area distributions, for coalescing and fragmenting, behave in a very similar manner to the flux distributions and highlight the results given in Table 6.2. In the clumping data features are more likely to coalesce up 0.6 Mm^2, after which they are more likely to fragment. For the downhill data there is a preference for features to coalesce rather than fragment up to 0.2 Mm^2.

Comparing the distributions for the flux of fragmenting and coalescing features found here, to the distributions for the flux of cancelling and emerging events (Figure 6.11), it can be seen that there is more fragmentation and coalescence over all ranges of flux. From the distributions presented here it is difficult to say whether or not the processes of fragmentation and coalescence are scale-free. This will be more thoroughly investigated once coalescence and fragmentation have been detected in SOHO/MDI full-disk data.

To help understand further the process of coalescence and fragmentation I also plot the probability distribution of the ages of the features when they interact (Figure 6.20). This plot shows that the IN features identified here can interact any time after birth, which is consistent with Livi et al. (1985) who have previ-

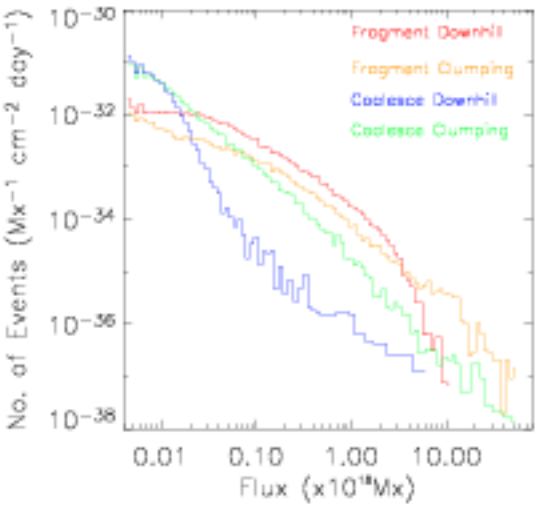

Figure 6.18: A log-log plot of the histograms of the flux of fragmenting features (above the flux threshold) in the downhill (red) and clumping (orange) data sets. Also the histograms of the flux of coalescing features (above the flux threshold) in the downhill (blue) and clumping (green) data sets.

ously considered network features with fluxes over 10^{17} Mx observed in BBSO magnetograms.

6.3 Emerging Region Evolution

This section looks at the evolution of IN emerging regions to examine in more detail the relationship between them and ephemeral regions. It has already been shown that the emergence rate of IN emerging regions is part of a smoothly decreasing distribution of emerging events including ephemeral regions and active regions. Furthermore, IN regions emerge both as bipoles and clusters of flux. This section looks at the evolution of IN emerging regions to examine in more detail the relationship between them and ephemeral regions. In the introduction (§1.2), I have already discussed the emergence evolution results found by other authors for ephemeral regions and active regions. Here I investigate the characteristics of IN emerging regions and compare my results to those found for IN emerging regions and ephemeral regions by other authors. The IN emerging region evolution results are presented in Table 6.3. How these results were determined and their implications are discussed below.

The following methods for determining the emerging region evolution are only applied to the emerging events detected by the Tracked Bipolar and Tracked Cluster methods, as it is not possible to follow the evolution otherwise. The emerging events identified by these methods can be clearly followed through time in the data. The first thing I calculate is the initial and final separation of the opposite-polarity regions of the emergence.

The process of finding the edge separation of two features has already been described in § 6.1. The initial edge separation is measured in the first frame in which the bipole is recognised. This process is then

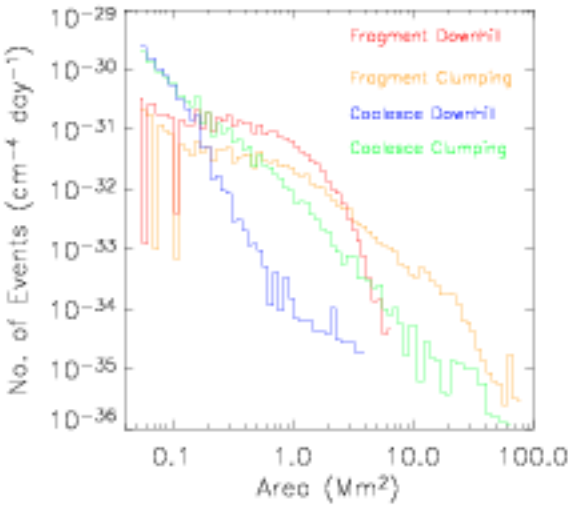

Figure 6.19: A log-log plot of the histograms of the area of fragmenting features (above the flux threshold) in the downhill (red) and clumping (orange) data sets. Also the histograms of the area of coalescing features (above the flux threshold) in the downhill (blue) and clumping (green) data sets.

repeated for successive frames until emergence has been completed. The rate of edge separation, of the opposite-polarity regions relative to one another, is also measured, which is the speed of separation. All the separation results are presented in Table 6.3.

The rate of expansion of area and rate of increase in flux are measured from the time of the emerging event's birth to the time of the first feature interaction. They are determined via a straight forward comparison between the flux and area of the features in consecutive frames. The time of expansion refers to the length of time after the birth of the emerging event during which the emerging event is actively growing in flux or area. To measure the expansion rate of the edges of the emerging event features, I assume the features are circular and compare the feature's radii (found from the area) in consecutive frames. The results are presented in Table 6.3.

In the introduction, it was reported that the initial separation of the opposite-polarity features in ephemeral regions, with fluxes of 10^{19}-10^{20} Mx and areas of 60-100 Mm^2, was in the range of 2-9 Mm (Martin and Harvey, 1979; Chae et al., 2001; Hagenaar, 2001). These results were found using full-disk magnetogram data from Kitt Peak, BBSO and MDI with resolutions of 2-9" arcsecs. The results for the initial separation presented here in Table 6.3 show a mean initial separation of 0.6 Mm, for the IN emerging events which have mean peak flux of order 10^{17} Mx and mean peak area of less than 1 Mm^2. This is despite the fact that the emergence programs can identify an initial separation of up to 0.8 Mm. This reduction in separation between IN emerging events and ephemeral regions is not surprising considering the high resolution of the Hinode/NFI data and the reduction in area and flux of IN emerging events compared to larger ephemeral regions.

The increase in separation, between the initial and final values, for the clumping and downhill emerging events in the TB method is 19% and 10%, respectively. Similarly for the TC method the increase in

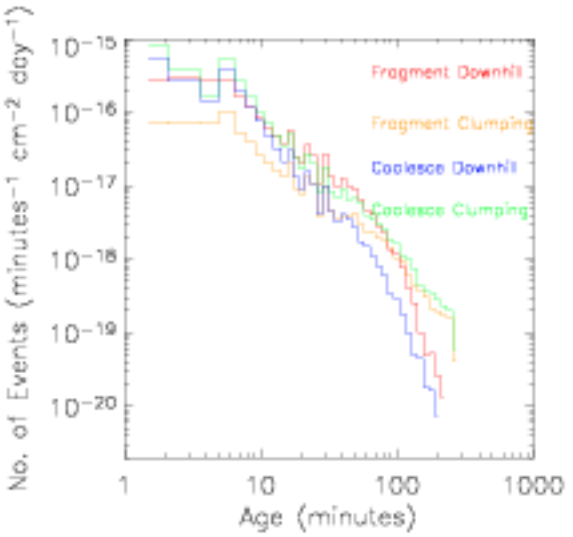

Figure 6.20: A log-log plot of the histograms of the age of features when they fragment and coalesce (for features above the flux threshold) in both the downhill (red and blue) and clumping (orange and green) data sets.

separation is 51% and 33% for clumping and downhill. The difference between the TB and TC methods results is likely to arise from the increased lifetime of the clusters and the increased number of features in the clusters, allowing the features to separate more. The final separation of the emerging events is typically under 1 Mm for both methods. Zirin (1985) has previously found that weak flux emerging events often separated less if at all, as a result of observing ephemeral regions in BBSO magnetograms of 2-3" resolution. On investigating the emerging events, it was found a further ≈2% of emerging events in each case did not have any increase in separation throughout their lifetime.

At a first glance it seems unusual that the initial separation speed should be negative. Looking at the expansion results presented in Table 6.3, it can be seen that in the initial few minutes of the life of an emerging event, the areas of the individual features expand. On further examination, it was discovered that this expansion is initially greater that the speed of separation of the features in the emerging event, thus giving a negative relative initial separation speed of the opposite-polarity components. When the this initial feature area expansion finishes after a couple of minutes then the separation speed becomes positive and the opposite-polarity components start moving away from one another. The speed of separation found here is in the range of what has been previously found for the separation speed of emerging regions with flux ranging from 10^{18}-10^{21} Mx, of between 0.1-5 km s^{-1} (Harvey and Martin, 1973; Born, 1974; Zirin, 1985; Chou and Wang, 1987; Barth and Livi, 1990).

The flux growth rate found here for emerging events detected in NFI ($\approx 2\times10^{14}$ Mx s^{-1}) is 1-2 orders of magnitude less than the flux growth rate of 2-30 $\times10^{18}$ Mx s^{-1} which has been previously found for ephemeral regions with mean peak flux of a few $\times10^{19}$ Mx, detected in MDI full-disk magnetograms (Chae et al., 2001; Hagenaar, 2001). Harvey (1993) found that when investigating the emergence of ephemeral regions in the range of 0.2-33 $\times10^{19}$ Mx using BBSO Kitt Peak full-disk magnetograms, the growth rate of the emerging regions seems to be linked to the peak flux the region attained. What I find here agrees

Tracked Bipolar	Clumping	Downhill
Lifetime (minutes)	10.7	11.0
Mean initial separation (Mm)	0.6	0.6
Mean final separation (Mm)	0.8	0.7
Mean initial edge separation speed (km s^{-1})	-0.2	-0.3
Mean final edge separation speed (km s^{-1})	0.8	0.7
Mean area expansion rate (Mm^2 s^{-1})	0.01	0.01
Mean outer edge expansion rate (km s^{-1})	0.5	0.6
Mean time of spatial expansion (minutes)	1.7	1.8
Mean flux increase rate ($\times 10^{14}$ Mx s^{-1})	2.2	2.1
Mean time of flux increasing (minutes)	2.0	2.1
Tracked Cluster	Clumping	Downhill
Lifetime (minutes)	18.8	18.2
Mean initial separation (Mm)	0.7	0.5
Mean final separation (Mm)	1.0	0.7
Mean initial edge separation speed (km s^{-1})	-0.1	-0.2
Mean final edge separation speed (km s^{-1})	0.9	0.7
Mean area expansion rate (Mm^2 s^{-1})	0.01	0.01
Mean outer edge expansion rate (km s^{-1})	0.5	0.5
Mean time of spatial expansion (minutes)	2.2	1.8
Mean flux increase rate ($\times 10^{14}$ Mx s^{-1})	2.3	2.1
Mean time of flux increasing (minutes)	2.5	2.1

Table 6.3: This table shows the emergence evolution results for emerging events detected by the Tracked Bipolar method (top) and the Tracked Cluster method (bottom).

with this. Comparing the flux increase rate I find here (Table 6.3) to the flux loss rate in Table 6.1, reveals that the increase rate is slightly smaller than the flux cancelling rate of between 3.3-5.3$\times 10^{14}$ Mx s^{-1}. The cancellations I observe interact, for on average, just over 10 minutes, compared to between 11-19 minutes for emerging events.

The expansion of the borders for the emerging events is of the order of 0.5 km s^{-1} in all cases which is less than the border expansion rates of between 1-3 km s^{-1} found for ephemeral regions with fluxes of 10^{18}-10^{20} Mx (Harvey, 1993; Hagenaar, 2001). Contrasting the times for the full flux increase and outer edge expansion to occur shows that it takes slightly longer for the emerging events to reach their maximum flux, at just $\approx$ 2.2 minutes, than the outer edge expansion which takes $\approx$ 1.9 minutes. The time of flux expansion is considerably less than those found by Zirin (1985) for ephemeral regions of order 10^{19} Mx, using BBSO full-disk daily magnetograms, who estimated an initial faster expansion rate up to 30 minutes after birth and a reduced expansion rate for up to a few hours.

6.3.1 Emerging Region Lifetime

Here I investigate IN emerging regions as they evolve and integrate into the magnetic network. The main aim is to better understand the processes these events undergo following emergence and what determines that they are no longer emerging events. The IN emerging region evolution results are presented in Table 6.3. The first thing I calculate is the initial and final separation of the opposite-polarity regions of the emergence. Regardless of whether they are applied to downhill or clumping, $\approx$ 1/4 of emerging events had

no growth in flux or area after birth. A further ≈2% had only area expansion and ≈6% only increased in flux.

In Table 6.3.1 I present the results, in terms of the percentage of overall emerging events, of what factors determine the end of the emerging phase of IN features. The end of the emerging phase is deemed to be when the emerging opposite-polarity components are no longer associated with one another through the flux ratio test (Equation 4.1), or when the features of the emergence have interacted with other features which are not part of the emerging event.

Each emerging event is taken in turn and, in the frame subsequent to its birth, each feature associated with the event is examined to see if it has fragmented, coalesced or cancelled with any other feature. The interaction of these is only significant if it involves another feature not associated with the emerging event. The total flux ratio is also found (Chapter 4), as part of the criteria for being an emerging event involves the total flux of the positive features of an emerging event being within 1/3-3 of the total flux of the negative features. If one of the emerging event features dies and it cannot be related to either coalescence or cancellation, then it is defined as an unexplained feature death.

Cause of deaths of as a percentage of number of newly emerged events	Tracked Bipolar		Tracked Cluster	
	Downhill	Clumping	Downhill	Clumping
Fragmentation:				
Positive feature	10.7	10.2	4.6	2.1
Negative feature	11.3	12.1	1.5	1.0
Coalescence:				
Positive feature	21.9	37.7	21.2	37.0
Negative feature	19.5	32.4	18.9	32.1
Cancellation:				
Positive feature	5.8	4.5	5.4	4.9
Negative feature	6.5	5.6	4.0	4.0
Flux Ratio Outside Range:	0	0	48.0	41.6
Unexplained death:				
Positive feature	19.1	4.6	14.6	3.8
Negative feature	18.1	6.6	14.0	5.3

Table 6.4: This table shows the possible reasons for an emerging event to no longer be recognised. For each method the cause of loss of identity is given as a % of the total number of emerging events. Note that each emerging event can undergo more than one case of death.

The results of applying these criteria to the TB and TC emergence detection method are now discussed. Looking at Table 6.3.1, it can be seen that the total percentages are greater than 100% for all cases. This indicates that in many of the emerging events there is more than one reason for them coming to the end of their emerging phase. For the TB method the most common cause for the end of the emerging phase is that one or more of the features in the emerging event coalescences. This is also the second most common cause for the TC method. In § 6.2, we have already seen that, after birth, features are most likely to undergo coalescence first, so these results are not surprising. For both methods, those emerging events which are detected in downhill are less likely to fragment or coalesce. This has again been discussed in § 6.2, and is due to the structure of the downhill feature.

For the TB emergence detection method none of the emerging events have a flux ratio which is outside

the 1/3-3 range during the time they are defined as emerging. For the TC method, however, almost half of the clusters detected, have a large flux imbalance of the positive and negative components. This results from the emerging events in the TC method often containing more than two opposite-polarity features. The greater number of features associated with an emerging event in these cases increases the chances of the emerging event losing flux balance as it emerges, due to these emerging features interacting with other features.

The emergence of small-scale IN flux can be shown to have both similarities and differences to ephemeral regions. They both have a characteristic growth in flux and area and move apart. However, the timescales for these actions is much less for the IN emerging events I have found than for the larger ephemeral regions. The flux and area growth rates are also an order of magnitude less than those found for ephemeral regions. By comparing the evolution of IN ephemeral regions after initial emergence to traditional ephemeral regions, it can be seen that whilst the traditional end of the ephemeral region emerging phase was when the features fragmented and joined the network, here it is found that the IN emerging event features are most likely to coalesce than fragment. The picture given by my results is that the majority of the features survive for a time after being part of an emerging event and interact with preexisting magnetic features, coalescing to form larger features which may then go on to form part of the network. These results are consistent with what is known about IN features and agrees with the suggestion by Martin (1990) that the network is built up in part from IN features.

6.4 Conclusions

In this chapter I investigated the surface processes features under go after emergence including evolution after emergence, fragmentation, coalescence and cancellation. Emerging region evolution was analysed for the emerging events found by the tracked emergence detection methods: Tracked Bipolar and Tracked Cluster. It is found that the IN emerging events exhibit similar behaviour to larger ephemeral regions, but on smaller scales. The opposite-polarity components are typically between 0.5-0.7 Mm apart upon detection and generally move less than 0.3 Mm apart during their growth. The flux growth rate of the emerging events is of the order 2×10^{14} Mx s^{-1}, the outer edge expansion rate is typically 0.5 km s^{-1} and the time over which this spatial and flux growth occurs is only of the order of 2 minutes. The initial edge separation speed is negative (-0.3- -0.1km s^{-1}) as the outer edge expansion rate is greater than the rate of separation, but as the growth of features abated, the separation speed increased to between 0.7-0.9 km s^{-1}. The feature identification method or the emergence detection method applied had little effect on the overall emerging evolution results.

After emergence it is found that features are more likely to undergo coalescence first indicating that the small-scale emergence events found in the NFI data also exhibit the same behaviour seen in larger active regions, where clusters of mixed-polarity emerge and coalesce as the region develops (Vrabec, 1974; Solanki, 2003; Handy and Schrijver, 2001). The rate of fragmentation is found to be 1.6-3.4 $\times10^{-16}$ cm^{-2} day^{-1} (9.8-20.7 $\times10^{6}$ day^{-1} over the whole surface) with most fragmentations involving one feature splitting into two and the mean flux of parent fragmentation feature being 0.42-1.54 $\times10^{18}$ Mx. The rate of coalescences is similar to the rate of fragmentations at 1.5-2.3 $\times10^{-16}$ cm^{-2} day^{-1} (9.2-14.0 $\times10^{6}$

day^{-1} over the whole surface). Like fragmentations, most coalescences involve two features that merge into a single feature. The mean flux of coalescing features is smaller than fragmenting features at between 0.08-0.72 $\times 10^{18}$ Mx. The fragmentation and coalescence detected is found to depend significantly on the feature identification method used, with the processes being more difficult to detect in downhill data due to the transient nature of the flux peaks. From the histograms presented in this chapter it is difficult to say whether or not the processes of fragmentation and coalescence follow a single distribution over all flux scales. This is more thoroughly investigated once coalescence and fragmentation have been detected in SOHO/MDI full-disk data.

The cancellations detected in the Hinode/NFI data are found to exhibit the behaviour seen in cancellation events in the network. Namely, the opposite-polarity features move together as they cancel and mutually lose flux. The speed of approach is found to be between 0.10-0.19 km s^{-1}, whilst the mean flux loss rate per event being between 3.3-5.3 $\times$ 10^{14} Mx s^{-1}. This is in good agreement with previous results of between $2.8 \times 10^{13} - 2.9 \times 10^{15}$ Mx s^{-1}, found from investigating cancellation in features observed in BBSO and MDI/high-resolution magnetograms, with flux between $10^{17} - 10^{20}$ Mx (Livi et al., 1985; Wang et al., 1988; Harvey, 1993; Chae et al., 2002). The mean rate of cancellation events is found to be between 1.4-2.0 $\times 10^{-16}$ cm^{-2} day^{-1} (8.6-12.1 $\times 10^{6}$ cancellations per day over the whole surface), similar to both the rate of fragmentation and coalescence. The total flux loss rate at between 38.5-46.9 Mx cm^{2} day^{-1} (2.3-2.9 $\times 10^{24}$ Mx day^{-1} over the whole surface). The distribution of flux lost per cancelling event versus number of events appears to follow a power law but this is investigated further once cancellation has been found in SOHO/MDI full-disk, as a larger scale of fluxes will give a more conclusive result. Unfortunately using the Hinode/NFI data I was unable to ascertain the flux removal in a cancelling event is due to an Ω-loop or U-loop.

This chapter has emphasised the extremely dynamic nature of IN features and hinted at a relationship to larger network features. This possible relationship is investigated in the chapters that follow.

Chapter 7

Variation of Small-Scale Emerging Flux Over the Solar Cycle As Observed in SOHO/MDI

The large-scale global magnetic field follows a well documented cycle which lasts on average 22 years (Hale and Nicholson, 1925; Friis-Christensen and Lassen, 1991; Fligge et al., 1999). This variation in magnetic activity has many consequences for large-scale features on the Sun. At solar maximum there is a rise in the number of sunspots and in the frequency of CME's and flares. Active regions also experience a shift in their latitude of emergence as the magnetic cycle progresses from minimum to maximum, emerging initially at high latitudes then migrating toward the equator as the cycle progresses.

Studies of the variation of quiet-Sun magnetic fields reveal both differences and similarities in their behaviour, to large scale fields, over the solar cycle. Meunier (2003) and Hagenaar et al. (2003) both investigated network features in MDI full-disk magnetograms over the period 1996 until 2002. Hagenaar et al. (2003) found that the number density of network features decreased in anti-phase with the solar cycle by a factor of $\approx 1/5$. Meunier (2003) found that over the same period there was an increase in-phase by a factor of 3 of network features per frame. Foukal et al. (1991) also find that, in Kitt Peak magnetograms, the number of network features increases in-phase with the solar cycle by a factor of 1.5. Hagenaar et al. (2003) and Meunier (2003) both found that the mean flux density per small-scale feature increased from solar minimum to maximum and Meunier (2003) calculated this increase to be 26%. Although the flux per feature is increased from minimum to maximum, the total flux contained in the quiet-Sun network is found to be changing only weakly throughout the solar cycle (Labonte and Howard, 1982; Hagenaar et al., 2003). On plotting the distributions of the number of network features versus area, Meunier (2003), noticed that they followed a power law which was steeper at the solar minimum and shallower at the solar maximum, with the distributions continuing to larger fluxes at solar maximum.

One of the most obvious changes in the large-scale solar cycle is the emergence rate of sunspots throughout the cycle which increases by a factor of ≈ 8 at solar maximum. Unlike active regions, ephemeral regions were previously found to vary weakly in anti-phase with the solar cycle by a factor of 1.5 (Martin and Harvey, 1979; Martin, 1988; Meunier, 2003). There also appears to be no distinct orientation of the ephemeral region bipoles and no preferred latitude of emergence, especially with respect to the solar cycle (Hagenaar, 2001; Hagenaar et al., 2003).

For the first time there is a satellite in a unique position to have observed the Sun for a complete solar cycle. SOHO was launched in 1996 and has continued to provide observations of the photospheric magnetic field, using MDI, up to the present day. Using high cadence SOHO/MDI full-disk data sets from between

December 1996 to December 2008, I investigate the emergence of small-scale magnetic fields over an entire solar cycle. The aims are (1) to resolve the uncertainties in the behaviour of network features throughout the solar cycle and (2) to investigate the relationship between the features in the intranetwork and the network.

7.1 Data, Feature Identification and Feature Tracking

I study 17 SOHO/MDI full-disk magnetogram sequences spanning a complete solar cycle from the cycle 22/23 minimum up to the present cycle 23/24 minimum. The preparation of the data is detailed in Chapter 2. The sequences have a cadence of 4-6 minutes and are more than 8.5 hours in duration. An estimate of the residual noise of each data set is required for the identification of flux features as described in Chapter 2. I choose a cutoff of 2σ, for each data set which ranges between 10.98-12.99 Mx cm^{-2}. This cutoff is sufficiently low so that small-scale flux is still identified but that noise effects are significantly reduced.

In Chapter 5, the results of applying both the clumping and downhill methods of identifying features in NFI magnetogram data were compared. Here, again, magnetic features must be identified in the prepared SOHO/MDI full-disk magnetograms. However, I choose to apply only the clumping method of identification because the focus of this study is the overall variation of small-scale surface flux, not the transient variation in the structure of the flux within flux regions, as detected by the downhill method. Indeed Parnell et al. (2009) found that clumping method was more suitable for comparing Hinode/NFI and SOHO/MDI as the flux massifs it identifies are much less dependent on instrument sensitivity. I also wish to analyse the nature of the evolution of features and, as seen in Chapter 6, it is difficult to detect fragmentation and coalescence accurately using the downhill data. Furthermore, Chapters 5 and 6 highlighted that the differences in the features identified by clumping and downhill did not drastically affect the total flux observed to have emerged or cancelled. Thus, the conclusions we draw on the nature of emergence, should not be biased by just using the clumping data. The identified features are associated between frames using the feature tracking approach detailed in Chapter 3, after which the peak flux, peak area and lifetime of each of the tracked features is found. The characteristics of the tracked features are presented in Table 7.1. The definition of small-scale features applies to those features with peak flux of $\leq 10^{20}$ Mx. This value is chosen since Parnell et al. (2009) found, from a comparison of flux distributions at solar minimum and maximum, that features with fluxes above this value tail off during solar minimum.

Tracked Features ($> 10^{20}$ Mx):	Dec 96	Mar 97	Jul 97	Oct 97	Feb 98	Dec 99	Dec 00	Dec 01	Jun 03	Jun 04	Nov 04	Nov 05	Feb 07	Dec 07	Mar 08	Oct 08	Dec 08
No. features (sec^{-2} $\times 10^{-19}$ day^{-1})	0.2	0.6	0.6	1.1	2.0	3.2	3.0	3.3	2.4	2.3	1.4	1.0	0.8	0.2	0.4	0.2	0.1
Mean peak flux ($10^{1.8}$ Mx)	12.8.3	27.8.0	41.3.3	4.8.4	4.8.3	6.2.9	14.9.3	8.8.9	1.8.6.7	3.9.6	4.8.3	3.3.9	3.2.3.1	2.1.2.1	3.1.6.0	1.4.3.8	1.3.8.7
Mean peak field strength all features (Mx sec^{-2})	1.7.9.1.9	2.2.9.9.8	1.6.8.4.8	3.1.3.3.1	4.1.8.2.1.9	2.2.8.8.8.1	2.4.1.3.4.1.9	2.0.4.8.6.8	1.9.2.3.4.0.3	6.1.9.6.6.1	3.2.8.7.0.2	6.2.6.7.1.0	1.3.1.2.4.0	3.1.2.3.1.7	1.1.9.0.0.8	2.7.2.3.8	2.1.4.7.3
Mean peak area (Mm^2)	2.6.2.3	3.4.4.3	4.9.0.1	5.1.7.4	5.4.0.0	3.6.7.8	9.7.0.9	1.1.3.9.1	1.8.6.2.	4.8.1.0	4.1.0.7	3.2.7.3	4.0.4.3	3.0.1.1	5.4.6.7	3.6.1.9	2.7.1.2
Av. lifetime (minutes)	2.3.2.	8.3	1.7.0	1.4.3	1.3.8	1.1.3	1.2.0	1.1.0	1.4.3	1.4.6	1.3.6	2.2.0	1.4.8	3.6.4	1.7.7	2.7.2.	3.2.8
Total flux (10^{21} Mx sec^{-2} per day)	1.9	3.6.7	2.4.3	4.9.8	8.9.6	2.1.3.4	4.3.2.3	9.9.9.6	4.3.1.6	5.8.3	3.1.3	1.4.2	2.4.3	1.3	2.1.3	2.4	2.0
Surface area covered by features (% frame^{-1})	0.1	1.6	1.3	3.2	4.9	1.4.4	1.3.1	1.4.7	1.1.8	6.7	4.3	3.2	1.4	0.6	1.0	0.2	0.1
Mean Number density of features ($\times 10^{-21}$ sec^{-2} frame^{-1})	0.1	1.1	1.6	3.8	3.4	10.4	8.7	9.3	7.1	7.4	4.3	2.3	1.6	0.6	0.4	0.2	0.1
Tracked Features ($\leq 10^{20}$ Mx):																	
No. features (sec^{-2})($10^{-1.9}$ day^{-1})	1.1.0	9.0	7.7	7.9	8.6	7.0	6.6	6.4	7.4	8.3	9.1	9.3	1.1.0	1.1.7	1.0.1	1.1.1	1.1.0
Mean peak flux ($10^{1.8}$ Mx)	8.9	9.8	1.0.0	9.7	1.0.4	1.1.8	1.2.3	1.2.3	1.2.1	1.1.3	9.9	1.0.1	9.2	9.1	9.4	8.7	8.9
Mean peak field strength (Mx sec^{-2})	3.0.6	3.0.6	3.1.3	3.1.3	3.1.9	3.5.8	3.8.0	3.6.6	3.8.6	3.5.7	3.1.7	3.1.3	3.1.3	3.1.2	3.1.2	3.1.6	3.1.1
Mean peak area (Mm^2)	2.7.7	3.0.1	3.0.0	2.8.7	2.8.3	2.9.0	2.9.1	3.0.6	2.8.4	2.8.6	2.7.3	2.8.2	2.6.2	2.6.2	2.6.8	2.6.3	2.5.9
Av. lifetime (minutes)	3.0	3.1	3.2	3.2	3.0	3.2	3.2	3.2	3.3	3.1	3.1	3.2	3.0	2.9	3.1	3.0	3.0
Total flux (10^{21} Mx sec^{-2} per day)	9.8.0	8.8.0	7.6.7	7.7.3	8.9.8	8.2.3	8.1.8	7.9.2	8.9.8	9.8.7	9.3.3	9.8.9	1.0.6.9	1.0.6.6	9.6.2	9.6.7	9.8.4
Surface area covered by features (% frame^{-1})	7.2	7.1	6.3	6.4	6.3	5.6	5.6	5.4	6.2	6.3	6.8	7.2	6.9	6.9	6.6	6.8	6.4
Number density of small-scale features ($\times 10^{-13}$ sec^{-2} frame^{-1})	3.4	3.4	3.4	3.3	3.3	3.9	3.9	3.9	3.8	3.6	3.3	3.3	3.4	3.4	3.4	3.4	3.4

Table 7.1: Characteristics of the large-scale tracked features ($> 10^{20}$ Mx, top) and the small-scale tracked features ($\leq 10^{20}$ Mx, bottom).

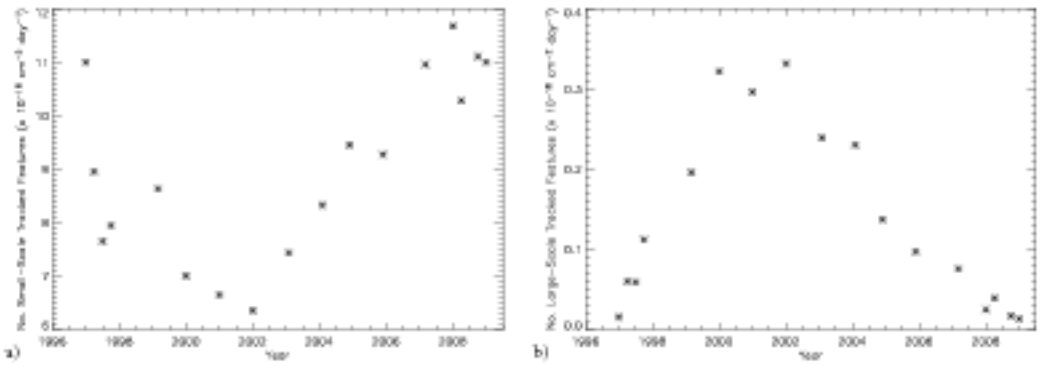

Figure 7.1: Plots of the number of a) small-scale tracked features (flux $\leq 10^{20}$ Mx) and b) active regions (flux $> 10^{20}$ Mx) versus year.

Firstly I look at the variation in the number of small-scale features detected throughout the cycle (Figure 7.1a). There is an anti-phase variation in the number of small-scale features over the solar cycle by a factor of at most 1.9. This is in agreement with Hagenaar et al. (2003), rather than with Foukal et al. (1991) and Meunier (2003) who found an in-phase variation.

By comparison Figure 7.1b shows how the number of features with fluxes $> 10^{20}$ Mx vary over the cycle. The number of large-scale features increases by a factor of ≈ 22 from minimum to maximum. The decrease in the number of network features in anti-phase with the number of sunspots suggests a connection between small and large-scale features.

However, these numbers are meaningless without some indication of the accuracy of these numbers and the errors associated with the methods used to indentify and track the features. Various instrumental factors can affect the number of features identified, such as the cadence which tend to affect short-lived low-flux features more accutely as does the resolution of the images. By varying the cadence of my images and the imposed flux cutoff (σ) I can give a rough estimate of these effects on the numbers. Removing every second image in each sequence gave a cadence of rougly 10 minutes. The number large-scale features ($> 10^{20}$ Mx) changed minimally. However the number of small-scale features ($\leq 10^{20}$ Mx) reuced by a factor of 1.4. Increasing the cadence resulted again in little change in the large-scale features but an increase in the number of small-scale features by a factor of 1.6. Changing the cutoff between 1σ and 3σ, again had little effect on the large-scale features but varied the number of small-scale features by $\pm$ a factor 1.3. It is clear then that there will be a uncertainty up to factor of $\approx$3 in the number of small-scale features. However this will be consitent throughout the cycle.

Investigating the mean peak flux of the tracked small-scale features (Figure 7.2a), shows that there appears to be an in-phase relationship with the solar cycle by a factor of 1.4. Throughout most of the solar cycle there will be some fraction of the network features which originate from the decay of active regions. It is known that the field strength of active regions are higher than quiet-Sun fields due to restricted flows and pressure. I next investigate if there are increases in network field strengths during active periods on the Sun due to features from decaying active regions retaining their higher field strength when they migrate into the network. Or are dispersed active regions indistinguishable from the network?

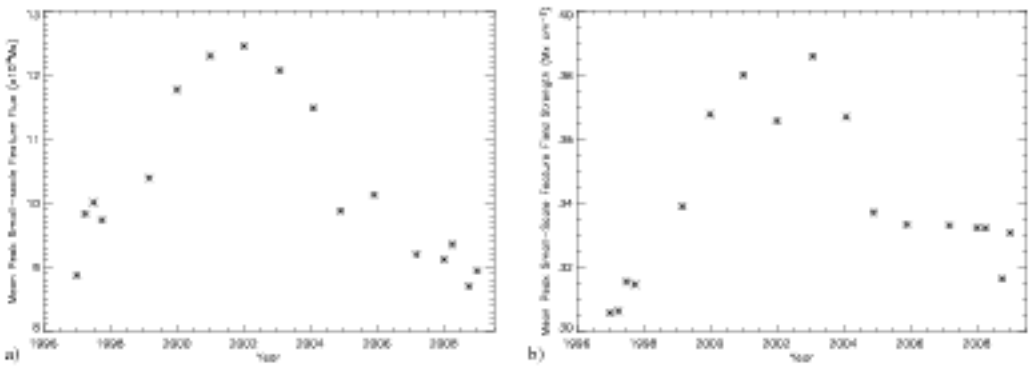

Figure 7.2: Plots showing the mean peak feature a) flux and b) field strength versus year for small-scale features ($\leq 10^{20}$ Mx)

Figure 7.2b shows that the variation of the feature field strengths is similar to what is seen for the mean peak flux (Figure 7.2a), namely an in-phase increase in the mean peak field strength by a factor of 1.3. If decaying active regions are responsible for a consequential number of high field-strength, small-scale features, then one would expect the mean peak field strength of small-scale features to be higher throughout the period of maximum activity. This what is seen here. However it is unclear whether this is solely due to the network features from dispersal of active regions retaining their high field strength characteristic of active regions or whether larger and stronger flux tubes are being emerged into the photosphere at solar maximum. Once the flux of ephemeral regions has been investigated in § 7.2 this question can be answered in more detail.

Again I give a quick estimate as to the accuaracy of these numbers. As the flux and field strength plotted for each year is the mean, I take the standard deviation to represent the possible variation in these numbers. For the flux I find that the average standard deviation is $\pm 9.2 \times 10^{18}$ Mx and for the field strength it is ± 8 Mx cm^{-2}. These values did not vary drastically throughout the cycle.

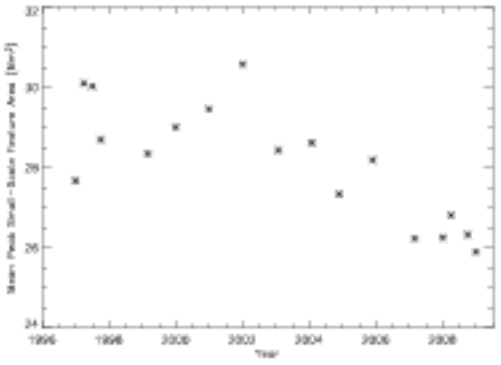

Figure 7.3: This plot shows the variation in the mean peak area of small-scale features ($\leq 10^{20}$ Mx) throughout cycle 23.

Like the mean peak flux and the mean peak field strength, the mean peak area of small-scale tracked features (Figure 7.3) varies in-phase (by at most a factor of 1.2) with cycle 23, although this variation is

less obvious than for the previous two properties. Again I calculate the standard deviation in the area and find an that the area on average has a standard devation of ± 15 Mm^2. Like the flux and field strength this does not vary drastically throughout the solar cycle.

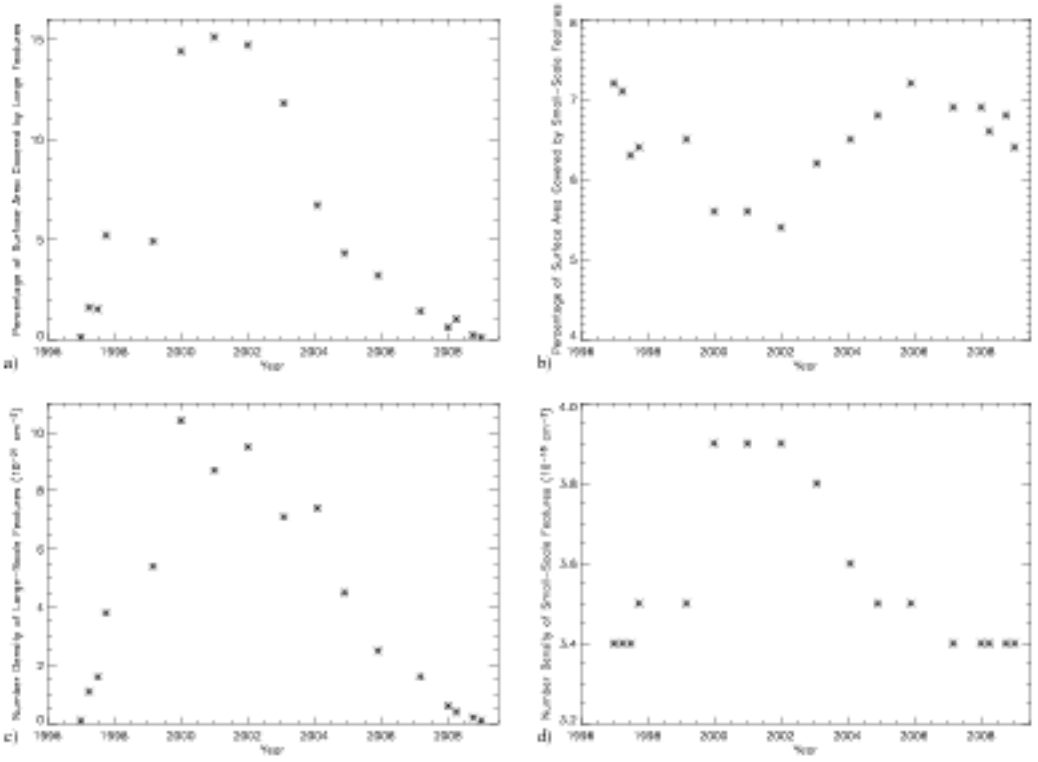

Figure 7.4: The percentage of surface area covered by a) large-scale features ($> 10^{20}$ Mx), b) small-scale features ($\leq 10^{20}$ Mx) and the variation in number density of c) large-scale features and d) small-scale features throughout cycle 23.

As expected the percentage of the total surface area of the Sun that is covered by large-scale features, varies in-phase with the solar cycle by a factor of ≈116 (Figure 7.4a). The percentage area taken up by the small-scale features (Figure 7.4b) has a variation which in anti-phase to the solar cycle but only by a factor of 1.3.

The accuracy of these is influenced by the size of the features, the possible variation in the number of flux features and the area of those features. Large-scale features are less susceptible to sytematic biases and therefore counting them and measuring their flux is more accurate. By measuring a standard deviation on the active region flux and including the possible variation in the numbers (Figure 7.1) I find a maximum of ≈ 3% variation. For the small-scale features, although the numbers are susceptible to change, the area associated with these features is very small and results in the surface area and density having a variation of ≈ 10%.

Thinking about how the density of small-scale features could change throughout the cycle there are three possibilities as the number of active regions increases: i) if there is not a lot of flux-free space on the photosphere then the area which can be inhabited by small-scale features is reduced and the density is

increased, ii) if all the features present on the photosphere only take up a small percentage of the surface area and there are areas with practically no (or very weak) fields then as the number of small-scale features and sunspots increase, there is plenty of space for them to both take up more area. This will lead to either iii) a steady density of small-scale features throughout the cycle or iv) a decrease in density may be found if the increase in the area taken up by small-scale features increases by a larger factor than the increase in the number of features.

Figure 7.4c shows that as expected the number density of large-scale regions increases in-phase with the solar cycle. Figure 7.4d shows a slight in-phase variation in the number density of small-scale features from 2000-2006, by a factor of 1.1. This is not wholly surprising as we have seen in this section that both the number of features in the network and the mean area of the features increases, whilst the percentage of the surface area decreases in anti-phase with the cycle. Obviously these hypotheses also do not take into account that the network is bound to the lanes and vertices of supergranular cells. It is likely that there are also features, outwith those identified, which are below resolution, removed by lifetime or size criteria, and it is not known how these will affect the dispersal of network features.

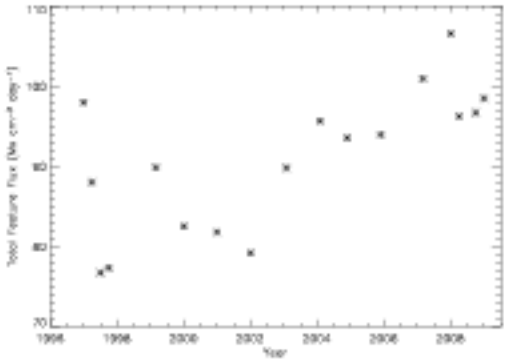

Figure 7.5: The total feature flux of features $< 10^{20}$ Mx versus year for all the full-disk data sets.

The final aspect to be looked at is the overall flux contribution from small-scale features. The graph of the variation in total flux (Figure 7.5) for all small-scale features with fluxes $< 10^{20}$ Mx most closely resembles Figure 7.1, which depicts the change in the number of features with the cycle. The variation in the total flux is in anti-phase with the solar cycle by a factor of at most 1.4, the same factor that the number of small-scale tracked features varies by. By using the uncertainty on the number of small-scale features and the flux associated with these I find that total flux on average will have an uncertainty of $\approx$ 15 Mx cm^{-2} day^{-1}. This is failry large and is due to the various factors which contribute to the uncertainty in the numbers of small-scale features.

7.1.1 Flux and Area Distributions of Tracked Features

Looking closely at the distributions of peak flux versus number of features, it can be seen that there are two patterns within them. For the period October 1997-November 2005 these distributions contain fewer features up to just above 2×10^{19}Mx than the distributions from December 1996-July 1997 and February

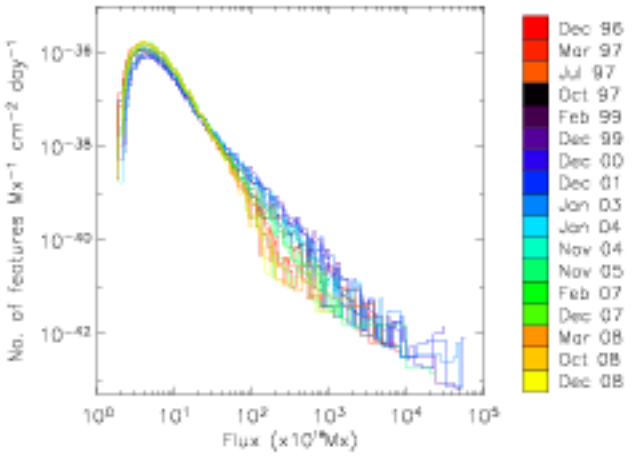

Figure 7.6: Log-log plots of the histograms of the fluxes of all the tracked features identified in the SOHO/MDI full-disk data sets.

2007-December 2008. However above this flux value the opposite is true. It is likely that the reason for this is that December 1996-July 1997 and February 2007-December 2008 have significantly fewer large-scale features, whilst the number of small-scale features increases due to the dispersal of decaying active region fields and possibly increased emergence rate of ephemeral region, which is to be discussed in the next section.

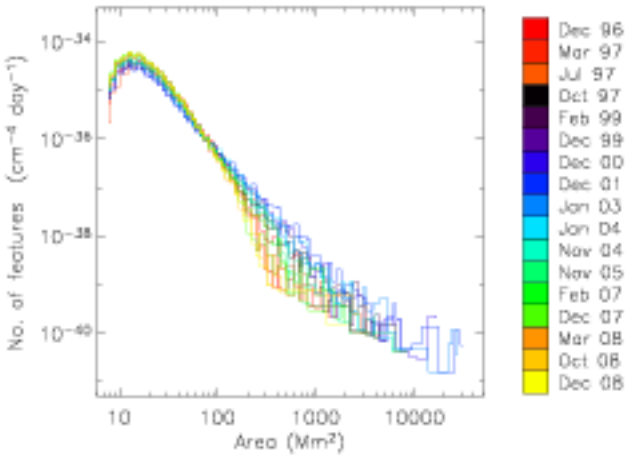

Figure 7.7: Log-log plots of the histograms of the areas of all the tracked features identified in the SOHO/MDI full-disk data sets.

The internal pattern which was apparent in the tracked feature flux distributions in Figure 7.6, is also apparent for the area distribution (Figure 7.7). For the period February 1999-November 2004 these distributions contain fewer features up to just above 100Mm^2 than the distribution from December 1996-October 1997 and November 2005-December 2008 and above this area value the opposite is true.

It is apparent from Figures 7.6 and 7.7 that the distributions for area and flux are marginally steeper during the periods of the solar cycle which contain less active regions, than those during the active periods of the cycle. Also the distributions during active periods have extended tails to higher values of flux/area. Meunier (2003), has already observed this variation in the slope between maximum and minimum for the distributions of number of network features versus area.

At this stage it is unclear what is the cause of the extra injection of small-scale features in the distributions between December 1996- October 1997 and November 2005-December 2008. The increase in the number of features could be due to: an increased emergence rate of flux on all scales, the dispersal of small-scale flux features from decaying active regions or an increase in frequency of surface processes. To properly answer this question the emergence and evolution of small-scale flux over the solar cycle needs to be investigated.

Both the flux and area histograms appear to follow a power-law relationship. This is investigated in more detail in § 7.4 where the tracked features identified in the SOHO/MDI full-disk data are compared to those identified in the Hinode/NFI data.

7.2 Variation in Small-Scale Emergence Over Cycle 23

In order to detect emergence in magnetograms, we use the Tracked Bipolar (TB) method detailed in Chapter 4. This method was chosen rather than the Bipole Comparison and Tracked Cluster methods for two main reasons. The first is that the magnetic features are tracked, which allows us to follow feature evolution after emergence. The second reason is that on visual inspection of SOHO/MDI full-disk magnetograms, the emergence of new quiet-Sun flux is primarily bipolar in nature as opposed to cluster-type. The results are presented in Table 7.2 and Figures 7.8a, b, c and d. The results in this section are for all the emerging bipoles which are detected, no flux limit is imposed, as on inspection of all the results overall there are only a few cases of ephemeral regions whose total absolute flux exceeded 10^{20} Mx.

Emerging Events Results	Dec 96	Mar 97	Jul 97	Oct 97	Feb 98	Dec 98	Dec 00	Dec 01	Jan 03	Jan 04	Nov 04	Nov 05	Feb 07	Dec 07	Mar 08	Oct 08	Dec 08
No. emerging events ($\times 10^{-10}$ sec^{2} day^{-1})	3.0	3.7	2.9	3.3	3.3	2.3	2.3	1.9	2.6	3.3	4.6	3.9	3.9	6.6	3.3	6.1	6.4
Mean peak emerging event flux ($\times 10^{18}$ Mx)	17.8	18.2	19.0	16.6	18.7	19.1	20.1	18.7	19.7	19.1	18.3	17.8	17.7	18.3	18.3	17.2	18.3
Mean peak emerging event area (Mm^{2})	11.8	11.7	11.3	11.8	11.9	12.2	12.7	11.8	10.1	11.1	12.3	12.6	11.2	12.9	11.0	12.3	12.9
Total Flux Emerged (Mx cm^{2} day^{-1})	8.9	6.7	5.1	5.3	6.1	4.3	4.7	3.3	5.1	6.3	8.4	6.9	10.4	12.0	10.1	10.3	11.6
Mean emerging event life (minutes)	16	16	16	17	13	17	17	16	17	17	17	17	17	17	17	17	17
Statistical uncertainty in emergence rates (%)	0.8	0.3	0.5	0.3	0.5	0.5	0.4	0.3	0.4	0.3	0.7	0.6	0.8	0.9	0.8	0.9	0.9
Number density of emerging features ($\times 10^{-21}$ sec^{-2} frame^{-1})	2.6	3.0	2.3	2.9	2.6	2.9	2.7	2.8	2.9	3.0	2.8	2.8	2.9	2.8	2.7	2.8	2.7
Percentage of non-unique pairings	21	20	13	20	20	19	20	17	20	23	29	23	34	37	33	32	35

Table 7.2: Emergence detection results.

Firstly looking at how the number of emerging events varies through the solar cycle (Figure 7.8a), it can be seen that there is a variation in anti-phase by a factor of 3.4. By comparison, it is known that the emergence rate of active regions varies by a factor of 8 in-phase with the solar cycle (Harvey and Zwaan, 1993).

Can the ephemeral region emergence rate tell us anything about the variation in the number of tracked features over cycle 23? The variation in the number of emerging events is a factor of 3.4 compared to a factor of 1.9 for the number of tracked features. The differences in the magnitude of the changes of two graphs highlight that the variation in the number of small-scale tracked features in the photosphere must not just be solely due to the how the emergence varies but also due to changes in the frequency of surface processes and due to the decay of active regions. In the next chapter I consider the behaviour of the surface processes over the solar cycle, thus enabling me to assess the importance of ephemeral regions, surface processes and decaying active regions in the production of network features.

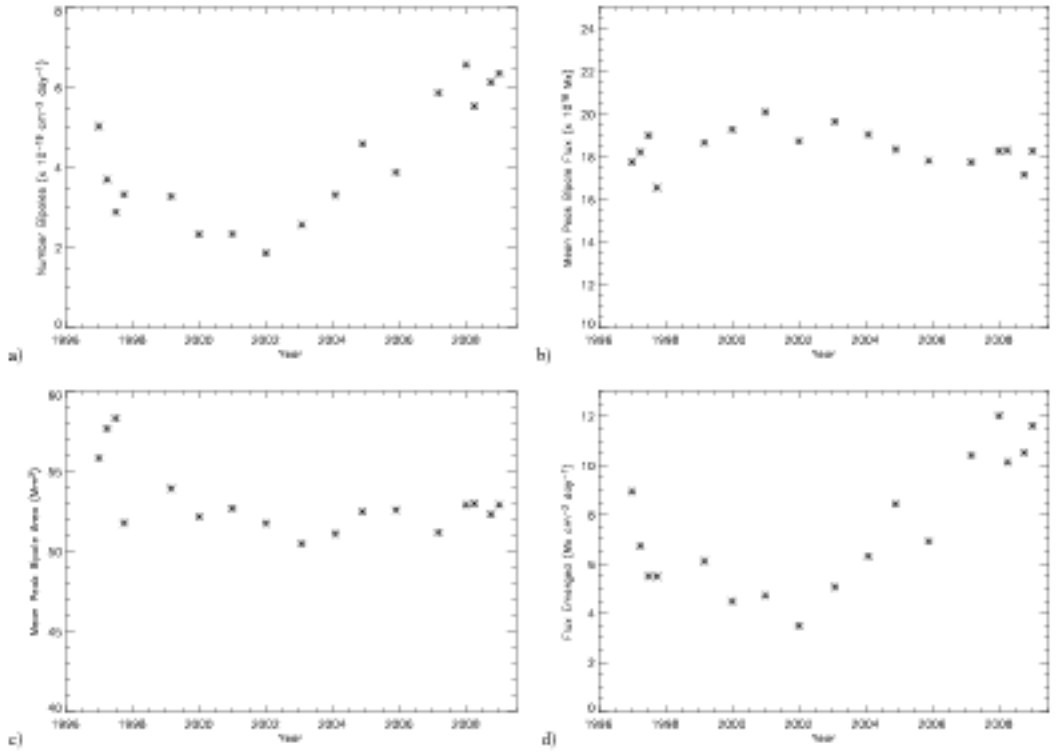

Figure 7.8: Plots showing the variation throughout solar cycle 23 of a) number of emerging bipoles, b) mean peak emerging event flux , c) mean peak emerging event area and d) total flux emerged.

Figures 7.8b and 7.8c show that there is little change in the mean peak flux and area in the emerging events over the cycle. Neither follow the anti-phase variation witnessed in the number of emerging events.

As the number of emerging events seems to be the dominant variation over the cycle so far, it is then no surprise that the flux emerged follows a similar evolution to the number of emerging events, also altering by a factor of 3.4 in anti-phase with the solar cycle.

Again to gauge the uncertainty in the number (Figure 7.8a) I vary the cadence and flux cutoff (σ). What I find here is that the total mean variation is of the order of a factor of 2. It is likely that the method of emergence detection would also play a role in the number of bipoles identified, as was seen in Chapter 5. Thus, like the feature numbers, it is likely that the bipole numbers could vary by up to a factor of 3. However, I did not observe this to behave in a cyclic manner.

Again I use a standard deviation to give an insight into the accuracy of the flux and area of the bipoles. The standard deviation of the bipole flux was on average 4.1×10^{18} Mx whilst for the area it was 3 Mm^2. Combining the uncertainty for the number of bipoles and the flux gives an uncertainty in the total flux of $\pm \approx 2$ Mx cm^{-2} day^{-1}.

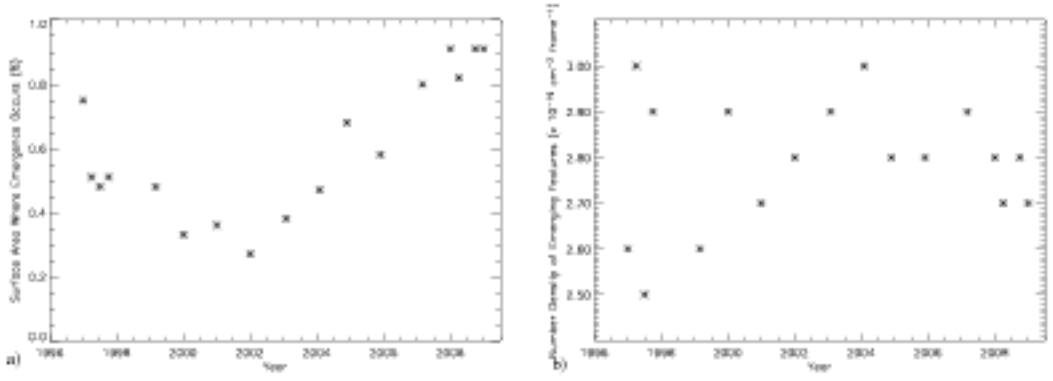

Figure 7.9: These two plots show a) the percentage of the surface area where emergence occurs and b) the number density of emerging features.

From the results so far, it appears that the presence of active regions at the cycle maximum acts to inhibit the emergence of ephemeral regions. Here I investigate this further. Firstly, I find the percentage surface area where emergence is found to occur, in all the data sets (Figure 7.9a). The percentage area inhabited by emerging events varies in anti-phase with the solar cycle by a factor of 1.3. However, the number density (Figure 7.9b) of emerging events does not vary significantly in a meaningful way throughout the cycle at all. These results suggest that active regions inhibit the emergence of ephemeral regions by reducing the free space available for small-scale emergence to occur.

Like the other cyclic variation graphs in this chapter I attempt to put a handle of the accuracy of the results to help put the results in perspective. Here this is achieved by referring to the liley inaccuracies in the number of bipoles but also in the uncertainty in the areas of these bipoles. The fact that the standard deviation in the are of the bipoles is relatively small reduces the uncertainty in Figures 7.9a and 7.9b toa factor of ≈ 1.5.

The percentage of non-unique pairings increases in phase with the cycle, So either there are more clusters emerging during active periods or it is more difficult for my algorithm to distinguish unique-pairings. From Chapter 5 I already know that non-unique pairings in emerging events are more likely to occur in regions with more flux features. Visually looking at the full-disk data, it is apparent that the majority of non-unique pairings occur closer to the limb although it is still the case that when emergence occurs in a region already containing flux features there are more likely to be non-unique pairings. The problem with detecting

emergence closer to the limb is that the separation criterian applied in the Tracked Bipolar method is a uniform number of pixels for the whole surface, even though the distance across a pixel increases as the limb is approached. Thus, there are more likely to be non-unique parings the closer to the limb you get.

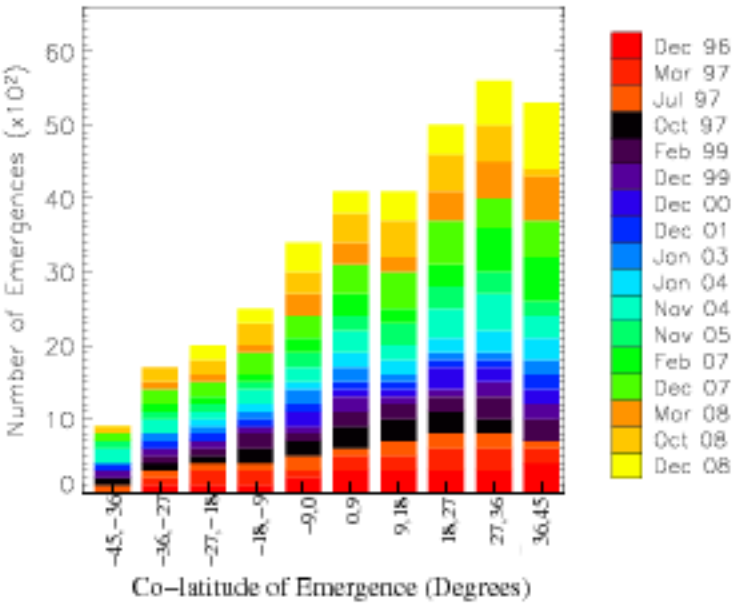

Figure 7.10: Bar plot showing the number of features for each year in latitude bands of emergence location, where -45° (North) is the top of my calibrated data and 45° (South) is the bottom.

I now consider the latitude of emergence of all emerging events throughout the cycle (Figure 7.10). This is plotted in the form of a stacked bar chart, with the x-axis being divided into co-latitude bands (10 in total) and the y-axis gives the number of emerging regions. Each data set is represented by a colour (the same colours for each data set which have been used throughout this section) and the height of that colour, in each bar, gives the respective number of emerging events emerged in that latitude band, for that particular data set.

From this it is evident that during the solar cycle, for the majority of the data sets, there is an asymmetry in the preferred latitude of emerging events, with more occurring in the southern hemisphere. During the more active periods, it would be expected that the latitude bands with the smallest amount of emergence would coincide with the presence of active regions. However, looking back at the original MDI/full-disk data in Figure 2.1 it is difficult to discern any relation between the active regions present and the latitude bands where the ephemeral regions emerge. The ephemeral regions detected here do not follow the butterfly diagram exhibited by active region emergence latitude.

Another effect which could be responsible for asymmetry in Figure 7.10 is the changing rotation axis of the Sun (B angle).Throughout the year this changes the tilt of the Sun relative to the Earth, so that the Sun is sometimes tilted towards us and sometimes tilted away from us. However, as the asymmetry in Figure 7.10 is consistently biased to the south, this suggest that the asymmetry is not related to the B angle.

Figures 7.11a and 7.11b show log-log plots of the distributions of the mean peak flux and mean peak

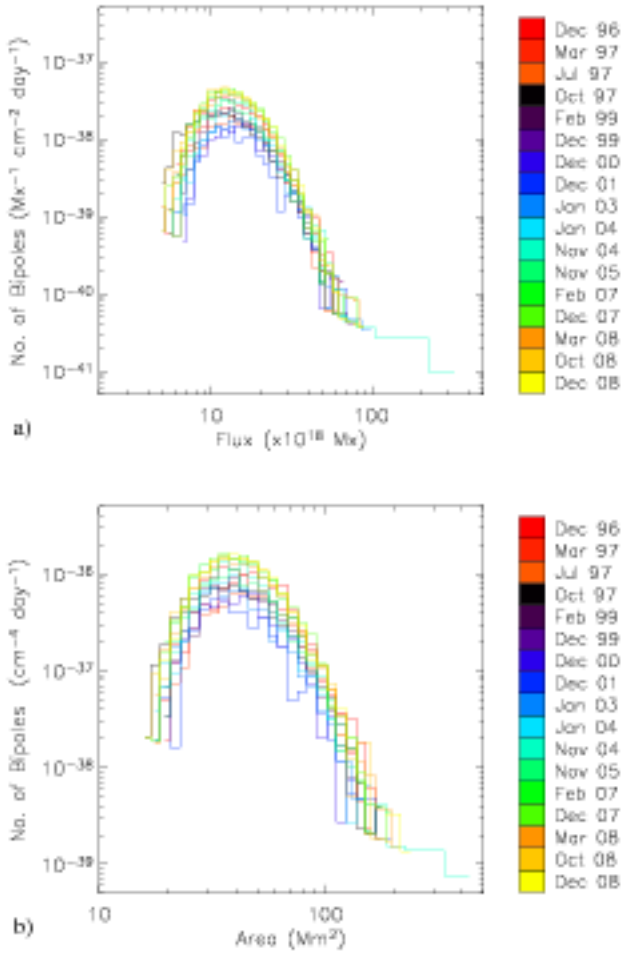

Figure 7.11: Log-log plot of the histograms of the (a) mean peak fluxes and (b) the mean peak areas of emerging events identified in each data set.

area of all emerging events. There appears to be another power-law relationship between the number of emerging events and the mean peak flux of the emerging events, however, in this case, the range of fluxes is too small to make any solid conclusions. In § 7.4 I compare the results I obtained from the Tracked Bipolar method (applied to the clumping data) for the emergence of small-scale ephemeral regions in Hinode (§ 5.3) to the results here to see if a single power-law can be formed.

7.2.1 Visual Examples of Detected Emerging Events

As in Chapter 5, I present some examples of the emerging events detected by the Tracked Bipolar method in the SOHO/MDI full-disk data.

Figure 7.12 shows a typical emerging event detected from the December 1996 (cycle 22/23 minimum) data set. The emerging event appears in frame 4 in an area which is quiet. The positive (red) and negative

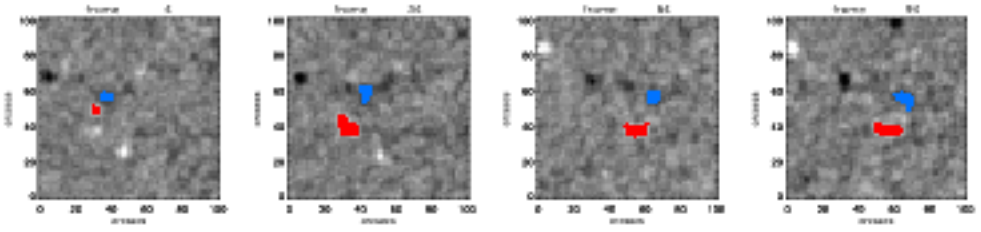

Figure 7.12: Example emerging event from the December 1996 data set.

(blue) features grow in time and move apart. By frame 34 they have reached their maximum separation and remain at this distance for the duration of the data set.

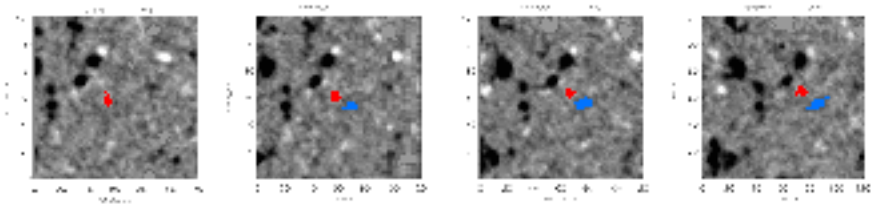

Figure 7.13: Example emerging event from the December 2001 data set in a quiet region.

Figure 7.13 is an example emerging event taken from an active data set in December 2001. It shows a bipole emerging in a relatively quiet region in this data set, however it can be seen that there are still a number of features close by. This example shows asymmetric emergence, with the positive (red) features emerging first in frame 49. It is closely followed by the negative (blue) feature and both features grow in flux. The separation in this case does not increase significantly throughout the lifetime of the emerging event.

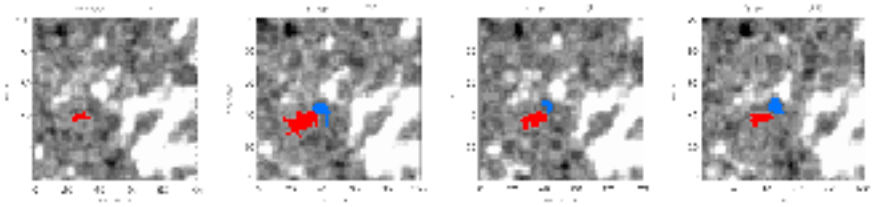

Figure 7.14: Example emerging event from the December 2001 data set emerging in an active region.

The final example (Figure 7.14) shows a bipole emerging in an active region in the December 2001 data set. Ephemeral region emergence is less likely to be detected in active regions. This bipole emerges in a region predominantly covered in positive (white) flux. Again the emergence is asymmetric with the positive (red) features appearing first in frame 74, closely followed by the negative (blue) feature. The emerging event appears to initially expand quickly before reducing slightly. Again there is no marked increase in the separation. On visually viewing the data sets at both the minimum and active periods, it can be seen that when emerging events emerge in regions already containing flux they tend to separate less, if at all, when they are emerging.

7.3 Investigating The Relationship Between Flux and Area of Ephemeral Regions

When investigating bipolar active regions and their associated plage regions, in the range $0.8 - 651.3 \times 10^{20}$ Mx observed in NSO/KP full-disk daily magnetograms, Harvey (1993) found that there was a linear relationship between the peak flux and peak area of the plage regions:

$$\Phi_p(A) = (-1.8 \pm 0.8) + (153 \pm 4)A,$$

where A is the peak area (10^{20}cm^2) and Φ_p is the peak flux (10^{20}Mx). Here I wish to find the relationship between the peak flux and peak area of all the ephemeral regions which are detected in the SOHO/MDI full-disk data.

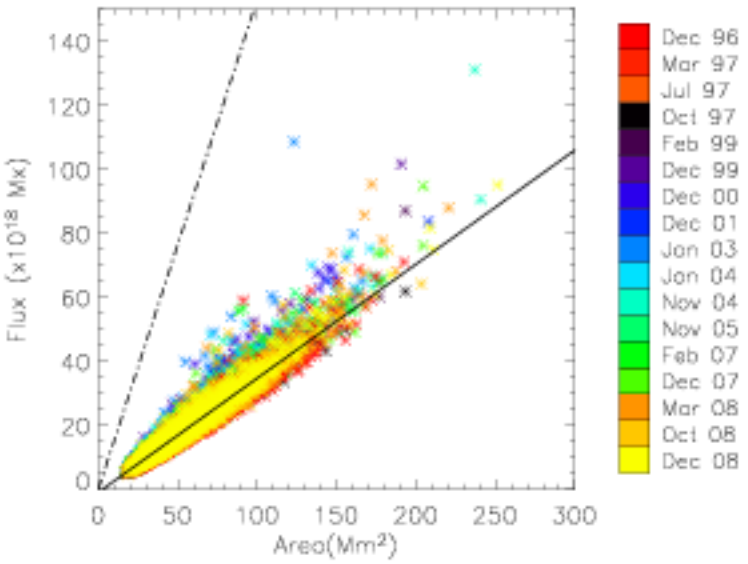

Figure 7.15: This is a plot of the mean peak flux versus mean peak area of all the emerging bipoles detected in this chapter. The solid line shows the slope calculated using LADFIT, the dot-dashed line is the slope Harvey (1993) predicted for flux versus area.

Figure 7.15 shows a plot of the mean peak flux versus mean peak area of all the ephemeral regions detected by the Tracked Bipolar method in this chapter. The range of fluxes of the emerging events detected in this chapter is $2.8 - 3306.0 \times 10^{18}$ Mx, with the mean being 13.9×10^{18} Mx. Using LADFIT a slope is plotted (solid line) through the results I find, the resulting line has the equation F=-0.89 +22.32A, with F being the peak flux (Mx) and A the peak area (Mm) of a feature. This has a much shallower slope than Harvey (1993) (dot-dash line).

Why could this be the case? It could be due to convective collapse making flux tubes more concentrated in larger magnetic features (Spruit, 1979; Rajaguru et al., 2002). Also when looking at pixels containing small-scale features there is a higher likelihood of single pixels containing mixed polarities and thus re-

ducing the total flux detected in that pixel. Finally, when finding the flux through an element of area it is assumed that the magnetic field is perpendicular to the surface i.e. that it is vertical. The flux is then given by the product of the magnetic field and the area element. It is less likely that small-scale features, especially those which are emerging, have vertical field lines associated with them, which could reduce the flux detected in them.

7.4 Comparison of MDI/Full-disk to Hinode/NFI

Now I have applied the clumping feature identification and the Tracked Bipolar emergence detection method to both Hinode/NFI and SOHO/MDI full-disk, I compare the results to discover if the IN tracked features and emerging events are effectively the same as the events found in this chapter, just at lower fluxes. It is clear from the results in this chapter that the SOHO/MDI full-disk results are dependent on the time of the magnetic cycle. As I only have one data set of Hinode/NFI data I am unable to say if the features identified in that data vary in the same way. The easiest way to compare the results between SOHO/MDI full-disk and Hinode/NFI is by plotting distributions of the flux and area of the all the tracked features and emerging events found. Firstly I will look at the distributions of the tracked features mean peak flux (Figure 7.16a) and mean peak area (Figure 7.16b).

Figure 7.16a shows that the histogram of mean peak flux ($10^{16} - 10^{23}$ Mx) of the tracked features indicates a power-law relationship. The dashed line through the histograms shows the power-law relationship found using LADFIT with the Hinode data, SOHO/MDI full-disk December 1996 data and the SOHO/MDI full-disk December 2001 data.

LADFIT is an IDL procedure which fits the paired data (x_i, y_i) to the linear model, y = A + Bx, using a least absolute deviation method. The least absolute deviation is a mathematical optimization technique similar to the least squares technique that attempts to find a function which closely approximates a set of data. The method minimizes the sum of absolute errors between points generated by the function and corresponding points in the data.

The power-law found by LADFIT is of the form:

$$P(\Phi) = \frac{N_p}{\Phi_\circ}\left(\frac{\Phi}{\Phi_\circ}\right)^{\alpha}, \tag{7.1}$$

$N_p = 7.5 \times 10^{-15}$ is the number of tracked features with units of cm^{-2} day^{-1}. $\Phi_\circ$ is the lower bound of the flux values such that $\Phi_\circ \leq \Phi_1 < \Phi_2$, in this case I choose $\Phi_\circ = 5 \times 10^{18}$ Mx. α is the slope of the power-law fit and I find $\alpha = -2.03$

This flux distribution is steeper than that found by Parnell et al. (2009), however, I am plotting the peak fluxes of the tracked features during their entire life as opposed to the flux in each feature at any one instant.

The distributions for the area of the tracked features (Figure 7.16b) again appear to follow a power-law.

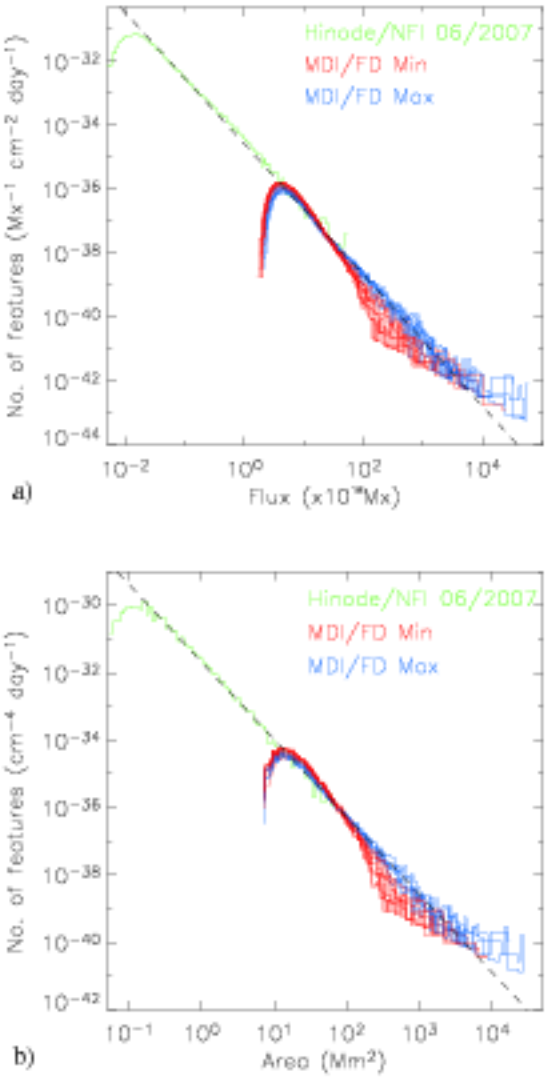

Figure 7.16: Log-log plots of the histograms of a) the mean peak flux and b) the mean peak area of tracked features found by the clumping feature identification method in the Hinode/NFI (green), SOHO/MDI full-disk December 1996-October 1997, November 2005-December 2008 (red) and SOHO/MDI full-disk February 1999-November 2004 (blue). The dashed lines are power-law fits to the data for the mean peak flux with $\alpha = -2.03$ and for the mean peak area with $\gamma = -2.21$

The dashed line through the area distribution (Figure 7.16b) shows the power-law relationship found using LADFIT with the Hinode data, SOHO/MDI full-disk December 1996 data and the MDI full-disk December 2001 data. The power law is of the form:

$$F(A) = \frac{N_f}{A_o}\left(\frac{A}{A_o}\right)^{\gamma}, \tag{7.2}$$

N_f is the number of tracked features in units of cm^{-2} day^{-1}, with a value of $N_f = 4.0 \times 10^{-18}$ cm^{-2} day^{-1} being found here. A_o is the lower bound of the flux values such that $A_o \leq A_1 < A_2$,where

$A_{\odot} = 5 \times 10^{14}\text{cm}^2$ and γ is the slope of the power-law fit and I find $\gamma = -2.21$

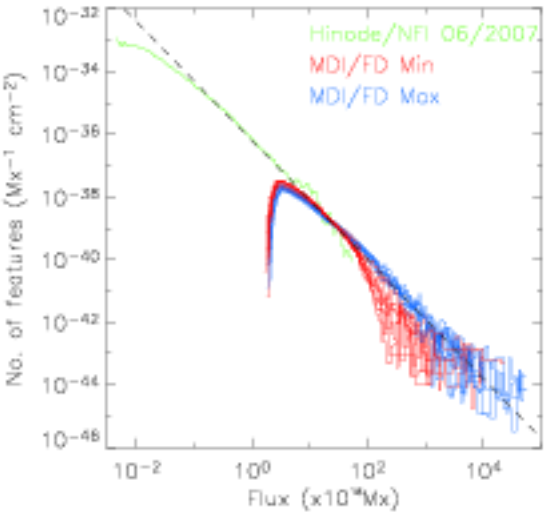

Figure 7.17: Log-log plot of the histograms of features fluxes, identified at any instant in the Hinode/NFI (green), SOHO/MDI full-disk December 1996-October 1997, November 2005-December 2008 (red) and SOHO/MDI full-disk February 1999-November 2004 (blue). The power-law (dashed line), with $\alpha = -1.90$ is computed using the Hinode/NFI data, SOHO/MDI full-disk December 1996 data and December 2001 data.

Parnell et al. (2009) previously looked at the distributions of all features fluxes, at any given time, using Hinode/NFI and SOHO/MDI full-disk data. They found that the distribution of all photospheric feature fluxes at any instant, from small-scale intranetwork features right up to sunspots, follows a single power law with $\alpha = -1.87$ and $N_p = 3.8 \times 10^{-17}$ cm^{-2} frame^{-1}. To compare to the plot in Parnell et al. (2009), I also plot the distributions for the flux in features at any instant (Figure 7.17). I find a slope of $\alpha = -1.90$ and $N_p = 7.8 \times 10^{-17}$ cm^{-2} frame^{-1}, which is in good agreement with the findings of Parnell et al. (2009).

Now I want to see if the log-log plots of the histograms of the peak flux and area of the emerging events detected in both the SOHO/MDI full-disk and Hinode/NFI also follow power-law relationships. As I have only used the Tracked Bipolar method applied to the clumping data in this chapter I will only use the equivalent data set from Chapter 5 for the Hinode/NFI data. I also include the results from Harvey et al. (1975), Howard (1989), Harvey (1993), Title (2000a), Chae et al. (2001), Hagenaar (2001), Hagenaar et al. (2003) and Hagenaar et al. (2008) for ephemeral and active region emergence. Table 7.3 shows the previous results found by other authors for the frequency of emergence of ephemeral regions, including the instrument used for the observations, the cadence of the data used and the average flux of the ephemeral regions detected.

Howard (1989) only gives the flux for their emerging active region results and Harvey (1993) only gives the areas for their emerging active region results. However, Harvey (1993) found a linear relationship between flux and area

$$\Phi_p(A) = (-1.8 \pm 0.8) + (153 \pm 4)A,$$

Paper	Instrument	Cadence	Av. Emerging Event Flux ($\times 10^{18}$)	Frequency of Emergence $\mathrm{sr}^{-2}\,\mathrm{day}^{-1}\,(\times 10^{-23})$
HHM75	KP/NSO fd	2-6 hrs	100	2.95-6.08*
$H93_{er}$	KP/NSO fd	24 hrs	30	14.3 *
T00	MDI hr	1 min	13	88.7 *
C01	BBSO hr	2.5 mins	28.9	169.5 *
HJH01	MDI fd	96 mins	11.3	722.8*
HST03	MDI fd	96 mins	10.3*	198.3-390
HDS08	MDI fd	5 mins	9.6*	1200-1610
†HRF89	Mt.Wilson fd	24 hrs	11000*	9.85-18.3* $\times 10^{-8}$
†$H93_{ar}$	KP/NSO fd	24 hrs	13413*	0.16-1640* $\times 10^{-8}$

Table 7.3: Frequency of emergence and flux emergence rate results for both ephemeral regions and active regions from various authors: HHM75 - Harvey et al. (1975), HRF89 - Howard (1989), $H93_{er}$/$H93_{ar}$ - Harvey (1993), T00 - Title (2000a), C01 - Chae et al. (2001), HJH01 - Hagenaar (2001), HST03 - Hagenaar et al. (2003), HDS08 - Hagenaar et al. (2008). * These results were not directly given in the paper but have been determined from the presented results. † These are the active region results.

of active regions, which I will use to get an estimate of the areas of the emerging active regions found by Howard (1989) and the flux for the emerging active regions found by Harvey (1993).

It can be seen that Figures 7.18a and 7.18b both show continuous distributions. To find the power-law fits (dashed lines) I use LADFIT with the Hinode data, SOHO/MDI full-disk December 1996, SOHO/MDI full-disk December 2001, Howard (1989) results and Harvey (1993) results. I find that the distribution for the mean peak flux of emerging events follows a power law of the form expressed in Equation 7.1, with $\alpha = -2.50$, $\Phi_\circ = 5 \times 10^{18}$ Mx and $N_p = 3.2 \times 10^{-18}$ cm^{-2} day^{-1}. Whilst the distribution of the areas have a power law relationship in the form of Equation 7.2, with $\gamma = -2.90$, $A_\circ = 5 \times 10^{14}$ cm^2 and $N_f = 7.3 \times 10^{-17}$ cm^{-2} day^{-1}.

At this point I estimate the error in the slope α. The error from the line fitting itself is estimated to be small, due to the method applied. The choice of $\Phi_\circ$ can introduce systematic errors. A choice of $\Phi_\circ$ which is too low would result in too many features, with flux near the observational limit, being identified. Conversely allowing $\Phi_\circ$ to be too high would discount many of the low-flux features. The value of $\Phi_\circ$ is chosen so that a balance is attained between maximizing the numbers of feature fluxes included whilst time maintaining a power-law distribution (Parnell et al., 2009). The feature identification and tracking algorithms also introduce systematic errors due to the assumptions made and constraints applied throughout the algorithms. Systematic errors may also be attributed to instrumental biases such as pixel degradation and B-angle. As well as this observational effects play a role in introducing systematic errors through area, duration and cadence of the data sets. The effects of these errors on flux features varies significantly depending on the flux of the feature. Indeed, as small-scale flux features often lie just above the detection limit, their frequency of occurrence is influenced more by by errors that occur. Parnell et al. (2009) found that these systematic biases introduced an uncertainty in the slope of frequency versus flux of ± 0.14. As a similar analysis is undertaken here I assume this error in the slopes to be valid here.

Hagenaar et al. (2003) previously used quiet-Sun SOHO/MDI high resolution data to determine the distribution of ephemeral regions with fluxes between 5×10^{18} and 10^{20} Mx. They compared their quiet-

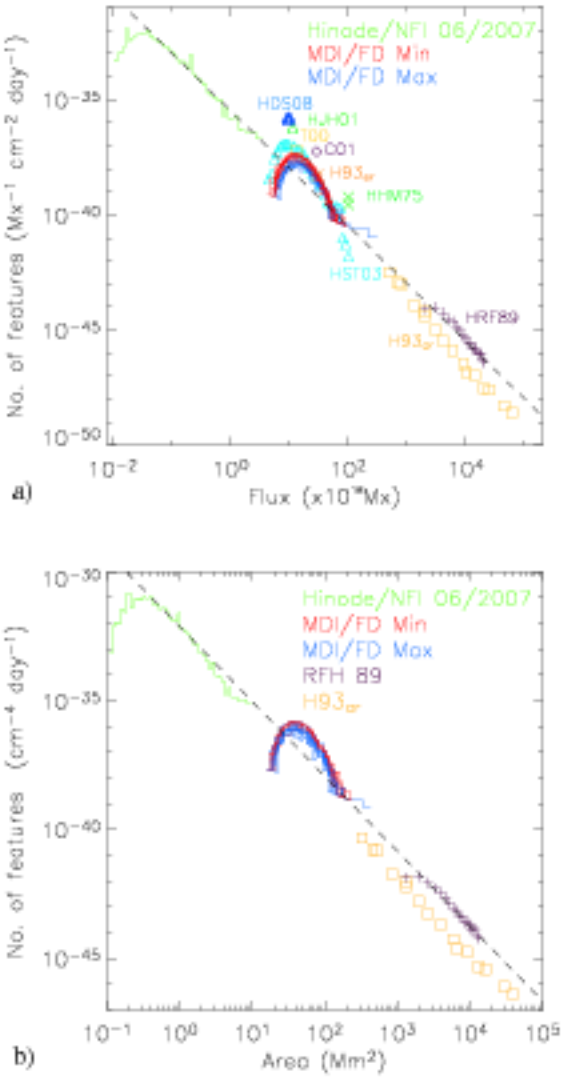

Figure 7.18: Log-log plot of emergence event a) mean peak fluxes and b) mean peak areas against frequency of emergence. The flux distribution includes results for both ephemeral regions from Hinode (green), SOHO/MDI full-disk (reds and blues as before) and results from the following papers HRF89 - Howard 1989 (purple crosses) and ephemeral regions and active regions from various authors shown in Table 7.3. The power laws (dashed lines) are the lines N_p against Φ and N_f against A, which have a power law index of a) α= -2.50 and b) $\gamma = -2.90$.

Sun ephemeral region results with emergence results from Harvey (1993) for active regions and concluded that bipolar emergence follows a smoothly decreasing distribution over nearly 5 orders of magnitude in flux and 8 orders of magnitude in frequency. In Figure 7.18a, the results from §5.3 are compared to, not only theirs, but also results from other papers (listed in Table 7.3). It can be seen that the emerged fluxes follow the same distribution over nearly 7 orders of magnitude in flux and nearly 18 orders of magnitude in frequency, in line with Hagenaar et al. (2003).

Integrating just over the distribution relationship (Equation 7.1), I find the total emergence rate of emerg-

ing events from $10^{16} - 10^{23}$ Mx in flux to be $2.2{\times}10^{-15}$ cm^{-2} day^{-1} (1.3×10^{8} regions per day on the Sun assuming uniform emergence over the whole surface). The majority of emergences are small-scale and have fluxes $< 10^{20}$ Mx with only 2.2×10^{-21} cm^{-2} day^{-1} (131 events per day over the whole surface) having fluxes above 10^{20} Mx.

The flux emergence rate, Φ_{emer}, of small-scale features over the range $\Phi_1 (\geq \Phi_0)$ Mx and $\Phi_2 > \Phi_1$ Mx is then given by:

$$\Phi_{emer} = \int_{\Phi_1}^{\Phi_2} P_e(\Phi)\Phi d\Phi = \frac{N_e \Phi_0}{2+\alpha_e}\left[(\Phi/\Phi_0)^{2+\alpha_e}\right]_{\Phi_1}^{\Phi_2} \tag{7.3}$$

Substituting the equation for emergence-event frequency P_e (Mx^{-1} cm^{-2} day^{-1}), given in Equation 7.1, into Equation 7.3 allows us to determine the typical total amount of flux emerged per unit area per day into the photosphere. Integrating Equation 7.3 from $\Phi_1 = 10^{16}$ Mx to $\Phi_2 = 10^{23}$ Mx, I find a total of 64.7 Mx cm^{-2} day^{-1} (3.9×10^{24} Mx day^{-1} over the whole solar surface) is found to emerge.

Since the power-law index of the emerging flux distribution is greater than -2 this suggests that most of the flux on the Sun does not come from large-scale features, but rather small-scale features. The flux emergence rate of small-scale features with fluxes in the range $10^{16} - 10^{20}$ Mx is 63.9 Mx cm^{-2} day^{-1}, or $3.9{\times}10^{24}$ Mx day^{-1} over the whole solar surface. Those events with peak fluxes greater than 10^{20} Mx produce just 0.7 Mx cm^{-2} day^{-1} or $4.2{\times}10^{22}$ Mx day^{-1} over the whole solar surface. An upper bound of 10^{20} Mx is used as the maximum for small-scale flux for two reasons: firstly, Hagenaar et al. (2003) defined ephemeral regions as bipoles with a total absolute flux below 3×10^{20} Mx and, secondly, because Parnell et al. (2009) found that, from a comparison of flux distributions at solar minimum and solar maximum, it was fluxes above this value that tailed off during solar minimum.

The flux which has been estimated to emerge from ephemeral regions has increased over the years as observations have improved. Harvey et al. (1975) investigated ephemeral regions with flux $\approx 10^{20}$ Mx and found a flux emergence rate of 1.8-3.7 $\times 10^{22}$ Mx day^{-1} over the whole surface. As observations improved the size of ephemeral regions decreased and the flux emergence frequency increased. Chae et al. (2001) and Hagenaar (2001) both investigated ephemeral regions of the order of 10^{19} Mx in flux and found flux emergence rates of between 2.9-5 $\times 10^{23}$ Mx day^{-1} over the whole surface. Previous estimates of the contribution of IN emerging flux (of order of 10^{16} Mx per emerging event) to the total flux budget have found a rate of order 10^{24} Mx day^{-1} over the whole surface (Wang et al., 1995; Martínez González and Bellot Rubio, 2009). The rate of flux emergence I find for small-scale emerging events (mean peak emerging event flux of 10^{16}-10^{20} Mx) is in line with what has previously been found for IN emerging events, highlighting that the majority of flux that is injected into the quiet-Sun is done so through the smallest-scales.

7.4.1 Estimating the Lifetimes of Features from Flux Distributions

It is obvious that there is a decrease in slope between the distribution of emerging bipole fluxes (Figures 7.18a) and the flux of the features at any instant present on the Sun (Figure 7.17). I wish to investigate if this decrease in slope is just through the features having a lifetimes of more than one frame, or if it is due to surface processes. To do this I estimate the distribution of lifetimes required to enable the emergence slope of mean peak fluxes (Mx^{-1} cm^{-2} day^{-1}) to reduce to the slope of all features at any instant (Mx^{-1} cm^{-2}). The distribution of emerging event flux ($P_e(\Phi)$) is given by:

$$P_e(\Phi) = \frac{N_e}{\Phi_\circ}\Big(\frac{\Phi}{\Phi_\circ}\Big)^{\alpha_e},$$

with N_e being the number of emerging events (cm^{-2} day^{-1}) which I previously found to be 3.2×10^{-16} cm^{-2} day^{-1}. $\Phi_\circ$ is the lower bound of the flux values such that $\Phi_\circ \leq \Phi_1 < \Phi_2$, in this case I choose $\Phi_\circ = 5 \times 10^{15}$Mx. α_e is the slope of the power-law fit and I find $\alpha_e = -2.50$

The power law for the flux present at any instant is given by the relationship:

$$P_i(\Phi) = \frac{N_i}{\Phi_\circ}\Big(\frac{\Phi}{\Phi_\circ}\Big)^{\alpha_i},$$

with N_i being the number of tracked features at any instant (cm^{-2}) which I previously found to be 7.8×10^{-17} cm^{-2} day^{-1}. $\Phi_\circ$ again is the minimum flux value which here I define as 10^{16} Mx, so it matches that of emerging events. α_i is the slope of the power-law fit and I find $\alpha_i = -1.90$.

I define the $L(\Phi)$ as the lifetime of features with flux Φ,

$$L(\Phi) = \ell\Big(\frac{\Phi}{\Phi_\circ}\Big)^{\delta},$$

where ℓ is the lifetime in days, δ is the slope of the lifetime distribution, Φ is the emerging event flux (Mx) and $\Phi_\circ$ is flux cutoff (5×10^{15} Mx).

The three distributions are associated as follows:

$$P_i(\Phi) = P_e(\Phi)L(\Phi) = \frac{N_e}{\Phi_\circ}\ell\Big(\frac{\Phi}{\Phi_\circ}\Big)^{\alpha_e+\delta} = \frac{N_i}{\Phi_\circ}\Big(\frac{\Phi}{\Phi_\circ}\Big)^{\alpha_i},$$

therefore $\gamma = \alpha_i - \alpha_e = 0.6$ and $\ell = \frac{N_i}{N_e} = 0.02$ day. Now by putting any value of flux into the lifetime distribution $L(\Phi)$, I will get the lifetime associated with that value of flux, which would be required to get $P_i(\Phi)$ from the emerging fluxes. In the Hinode data the mean peak flux of the features is 10^{17} Mx. Using the lifetime distribution calculated here gives a lifetime of ≈173 minutes for features of this size. However in Chapter 5 it was found that the mean lifetime of features in the Hinode data set (Table 5.1) is 9 minutes for features identified in the downhill data and 15 minutes for features identified in the clumping data. Repeating this for the MDI full-disk data, where I find the mean peak flux of the small-scale features is $\approx 6 \times 10^{18}$ Mx (Table 7.1), I calculate a lifetime of 627 minutes using the lifetime distribution. The

actual values for the small-scale tracked features lifetimes in MDI full-disk data sets is between 21-30 minutes (Table 7.1). Thus the lifetimes of features would be higher if not for surface processes. The lifetime distribution calculated here indicates a linearly increasing relationship between lifetime and flux of a feature, which is clearly not the case.

7.5 Discussion and Conclusions

The aim of this chapter was to investigate the characteristics of ephemeral regions over a complete solar cycle to see if a) there is any variation in ephemeral region emergence over a solar cycle and b) to try and determine a relationship (if any) between ephemeral regions and active region emergence.

Firstly I look at the variation in the small-scale tracked (network) features. The number detected throughout the cycle (Figure 7.1) exhibited an anti-phase variation over the solar cycle is by a factor of at most 1.9 at solar maximum. Investigating the mean peak flux of the tracked small-scale features (Figure 7.2a), showed that they appear to be in-phase with the solar cycle by a factor of 1.4. Figure 7.2b shows that the variation of the feature field strengths is similar to what is seen for the mean peak flux (Figure 7.2a), namely an in-phase increase in the mean peak field strength by a factor of 1.3. The mean peak area (Figure 7.3) varies in-phase (by at most a factor of 1.2) with cycle 23. The variation in the total flux is in anti-phase with the solar cycle by a factor of at most a factor of 1.4 and it appears that the total flux on the Sun associated with features is correlated with the number of features present, rather than the flux contained in the features.

The variation in the number of emerging events (Figure 7.8a) is similar to what is seen for the variation in small-scale features throughout the solar cycle i.e. a variation in anti-phase, although by a larger factor of 3.4. However, there is little change in the mean peak flux and area in the emerging events over the cycle. As the number of emerging events seems to be the dominant variation over the cycle so far, it is then no surprise that the flux emerged follows a similar evolution to the number of emerging events, also altering by a factor of 3.4 in anti-phase with the solar cycle. The percentage area inhabited by emerging events varies in anti-phase with the solar cycle by a factor of 1.3.

What can these results reveal about the dynamic nature of the magnetic carpet? If there were no fragmentation and coalescence and no influence from decaying active regions it would be expected that the variation in the number of tracked features present on the surface at any time over the solar cycle would be the same as the variation in the number of emerging regions. It can be seen that the number of tracked features present varies by a much smaller factor than the number of emerging events throughout the solar cycle. The reason is likely to be due to the fact that the variation in the number of active regions increases in-phase with the solar cycle, thus increasing the number of tracked features due to the dispersal of active regions adding to the small-scale feature population. However it may also be due to changing surface processes during the solar cycle. Once the evolution of the features has been investigated in the following chapter, I will be able to answer this more clearly.

The second aim of this chapter was to investigate if there is a relationship between the smallest scales of flux features up to active regions. It is found that the number of tracked features followed a single

power law distribution with a power-law index -2.03, i.e. which increases in frequency as the value of flux decreases over 7 orders of magnitude in flux and 14 orders of magnitude in frequency. Furthermore, the mean peak areas of tracked features also reveals a single power law distribution with power-law index -2.21 over 6 orders of magnitude in area and 13 orders of magnitude in frequency. Similarly the peak flux of the emerging events follows a distribution with a power-law relationship with index $\alpha = -2.50$ over nearly 7 orders of magnitude in flux and nearly 18 orders of magnitude in frequency, in line with Hagenaar et al. (2003). Whilst the distribution of the areas have a power-law index of $\gamma = -2.90$.

From the emerging event distribution I estimated the flux injected through the entire range (10^{16}-10^{23} Mx) of emerging events. I find a total of 64.7 Mx cm^{-2} day^{-1} (3.9×10^{24} Mx day^{-1} over the whole solar surface) is found to emerge. Since the power-law index of the emerging flux distribution is greater than -2 this suggests that most of the flux on the Sun does not come from large-scale features, but rather small-scale features. Indeed, the flux emergence rate of small-scale features with fluxes in the range $10^{16} - 10^{20}$ Mx is 63.9 Mx cm^{-2} day^{-1}, or 3.9×10^{24} Mx day^{-1} over the whole solar surface. Those events with peak fluxes greater than 10^{20} Mx produce just 0.7 Mx cm^{-2} day^{-1} or 4.2×10^{22} Mx day^{-1} over the whole solar surface.

7.5.1 Implications for the Generation of Magnetic Flux

Physically a power-law distribution of, for instance, flux implies that the fluxes are produced by a mechanism that is scale free. That is the physical process(es) that produce the smallest magnetic features are the same as the process(es) that produce all other features, including the largest features. Parnell et al. (2009) speculated that the distribution of magnetic feature fluxes was produced by one of two mechanisms. Either (i) all magnetic features are created by a solar dynamo that acts in the same way on all scales or (ii) magnetic features are created by dynamo action that is not the same on all scales but, after emergence into the solar atmosphere, surface processes (e.g. fragmentation, coalescence and cancellation) dominate and create a single distribution of feature fluxes. In order to distinguish between these two mechanisms, it is obviously essential to determine whether the distribution of fluxes of newly emerged features follows a power law or not. The work that we have presented, here, strongly suggests that the distribution of fluxes from newly emerged features follows a power law with a slope of -2.50. This provides considerable support for the first mechanism, namely that all magnetic features are created by a solar dynamo that acts in the same way on all scales.

For more than five decades it has been known that the Sun's magnetic field is created by dynamo action (Parker, 1955; Moffat, 1978; Choudhuri et al., 1995; Dikpati and Gilman, 2006; Weiss and Thompson, 2009) which must occur in or just below the convection zone. Theoretical modelling has established that a dynamo acting throughout the convection zone cannot produce sunspots, since magnetic buoyancy causes these strong magnetic fields to rise too rapidly (Parker, 1984; Choudhuri and Gilman, 1987). Instead, the generally accepted view is that these features are most likely created by a dynamo situated around the base of the convection zone (Spiegel and Weiss, 1980; Parker, 1993). This idea was strengthened by the discovery of the tachocline, a shear layer just below the base of the convection zone (Schou et al., 1998). Also, it has been suggested that small-scale emerging magnetic features are generated by a second (local)

dynamo just below the photosphere (Cattaneo, 1999; Cattaneo and Hughes, 2001; Hagenaar et al., 2003). In this scenario, dynamo action is predominantly driven by turbulent convection flows, although the tachocline may play a role (Corbard and Thompson, 2002).

This picture of two separate dynamos dominating the flux distribution, one in the tachocline and one at the surface, is however inconsistent with our discovery of a single power-law over all emerging flux scales. Instead, it suggests that, in addition to the solar-cycle dynamo at the tachocline, turbulent dynamo action occurs continuously over a range of scales throughout the convection zone, from the tachocline right up to the surface. As already noted, Parnell et al. (2009) found from their distributions of all photospheric feature fluxes that the numbers of the largest-scale flux features ($> 10^{20}$ Mx) fall off at solar minimum. So we suspect that these large magnetic features are created in the tachocline, whereas we speculate that smaller features ($< 10^{20}$ Mx) would continue to be produced in the convection zone throughout solar maximum and solar minimum. This idea has some support from the recent numerical convection simulations of Stein et al. (2008) and Nordlund (2008), which show that convection does not occur at two discrete scales (granulation and supergranulation), but rather that it occurs at a continuum of scales whose scale-length increases with depth.

The emerging flux results that we present in this thesis are not conclusive proof of a scale-free dynamo, but are highly suggested of it. Clearly, the results plotted in Figure 7.18a have a reasonable spread and do not lie perfectly on a single line. The reasons for this are that the results plotted are from different data sets with different spatial and temporal resolutions. Furthermore, large-scale, and therefore invariably long-lived, emergence is relatively simple to detect and quantify, whilst small-scale, short-lived emergence is much more difficult to quantify, as discussed in this paper. In order to firmly establish the existence of a scale-free dynamo requires further work on both the theoretical and observational fronts. In particular, to find the slope of the resulting flux distribution to a high degree of accuracy from observations requires an approach that determines the fluxes of all newly emerged features on all scales in a consistent manner.

Chapter 8

Variation of Magnetic Feature Evolution, Over the Solar Cycle, as Observed in SOHO/MDI

Much work has been done on the variation of the network features (in terms of numbers and density) and the emergence of flux in the photosphere, throughout a solar cycle (Foukal et al., 1991; Meunier, 2003; Hagenaar et al., 2003). However, no work has been done on examining the variation of feature evolution over the solar cycle. In the previous chapter it was seen that the number of tracked features and emerging events varied in anti-phase with the solar cycle by factors of 1.9 and 3.4, respectively. Here I see whether these results are reflected in the surface processes throughout the cycle. This will provide insight into the development of the mixed polarity network and whether it is influenced by the magnetic cycle.

This chapter is an extension to the analysis of the data prepared for the previous section. Using the methods developed and discussed in Chapter 6, for analysing feature evolution in Hinode/NFI, I analyse feature evolution of the tracked features and emerging events detected in the previous chapter. The methods are described in Chapter 6, however a few parameters are changed here such that the algorithms are compatible with the full-disk data and these are discussed in the appropriate sections which follow. The aim is to determine the change, if any, in feature evolution throughout the solar cycle and also to provide an insight into what is driving feature evolution in the photosphere.

8.1 Variation of Emerging Event Evolution Over Cycle 23

Table 8.1 shows the mean results of the emerging event evolution characteristics for each of the 17 SOHO/MDI full-disk data sets. For each data set I have plotted the mean initial (stars) and final (triangles) separation of the detected emerging events (Figure 8.1a) from the results in Table 8.1. The mean separation of each emerging event is the closest-edge separation, of the opposite-polarity components. The initial separation is found upon first detection of the emerging event and the final separation at the end of the emerging event lifetime. As expected the final separation is greater then the initial separation, confirming that features move apart as they emerge. The initial separation varies only slightly between 6.61-7.59 Mm ($\pm$2.21 Mm using standard deviation) but not with any apparent relation to the solar cycle. The final separation (triangles) ranges from 7.58-14.98 Mm ($\pm$5.34 using standard deviation) . In the introduction, it was reported that the initial separation of the opposite-polarity features in ephemeral regions, with flux in the range 10^{19}-10^{20} Mx and area 60-100 Mm^2, was in the range of 2-9 Mm (Martin and Harvey, 1979; Chae et al., 2001; Hagenaar, 2001), which is in agreement with my findings here.

	Dec 96	Mar 97	Jun 97	Oct 97	Feb 99	Dec 99	Dec 00	Dec 01	Jan 03	Jan 04	Nov 04	Nov 05	Feb 07	Dec 07	Mar 08	Oct 08	Dec 08
Mean coupling event life (minutes)	1316	17.9	17.8	17.3	13.2	16.9	16.3	13.6	17.1	17.0	17.0	16.6	16.7	16.6	16.6	17.3	16.3
Mean initial separation (Mm)	7.0	7.2	7.6	7.3	6.9	6.9	7.1	6.8	6.9	6.8	6.7	6.9	6.7	6.6	6.8	6.8	6.6
Mean final separation (Mm)	10.7	12.2	13.0	10.0	10.6	14.6	10.3	14.4	13.1	11.7	7.8	10.7	8.2	10.7	10.2	8.6	8.0
Mean initial edge separation speed (km s^{-1})	9.4	11.3	14.1	6.0	10.9	10.0	8.9	19.1	22.6	13.3	1.9	8.1	2.0	11.9	9.6	3.9	2.3
Mean final edge separation speed (km s^{-1})	2.6	1.9	4.0	2.8	1.3	3.7	2.7	1.1	4.3	2.7	1.4	4.3	2.8	2.1	0.3	1.7	1.4
Mean area expansion rate (Mm^2 s^{-1})	0.7	0.7	0.7	0.6	0.6	0.6	0.6	0.8	0.3	0.6	0.6	0.6	0.6	0.7	0.7	0.7	0.7
Mean outer edge expansion rate (km s^{-1})	3.0	3.1	2.9	2.7	2.9	2.3	2.9	2.4	2.4	2.9	3.0	2.8	3.0	3.3	3.0	3.3	3.2
Mean time of spatial expansion (minutes)	6	6	6	7	6	6	6	6	6	6	6	6	6	6	6	6	6
Mean flux increase rate ($\times 10^{18}$ Mx s^{-1})	22.3	23.2	23.4	20.9	22.9	21.6	24.9	21.3	20.3	22.8	22.1	21.6	22.1	24.3	23.8	23.0	24.2
Mean time of flux increase (minutes)	7	7	7	7	7	7	7	7	7	7	7	7	7	7	7	7	7

Table 8.1: Emerging event evolution results from all SOHO/MDI/full-disk data sets.

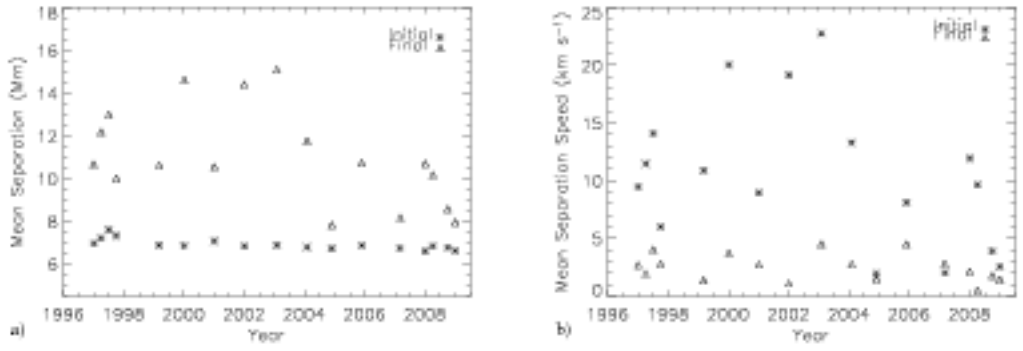

Figure 8.1: Plots of (a) mean emerging event separation and (b) mean emerging event separation speed throughout cycle 23

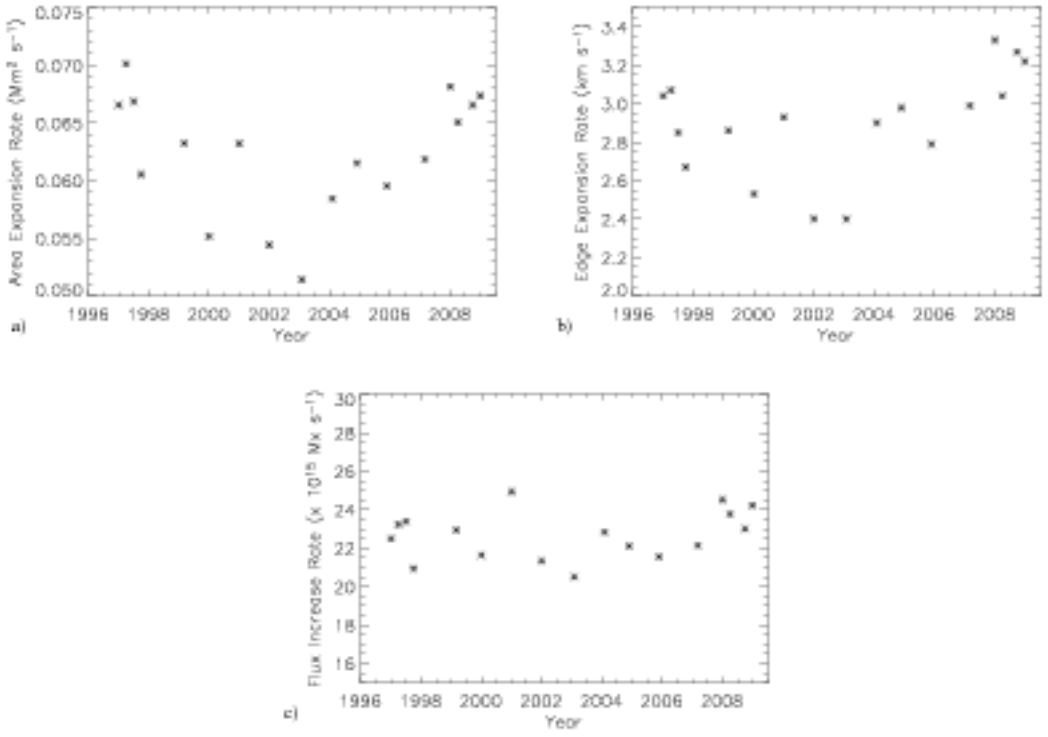

Figure 8.2: Plots showing the a) mean area expansion rate, b) mean edge expansion rate and c) mean flux increase rate versus year , throughout cycle 23

In the majority of cases the initial speed of separation of the emerging events, presented in Table 8.1 and Figure 8.1b, is greater than the final speed, which agrees with previous findings for ephemeral regions (Harvey and Martin, 1973; Born, 1974; Zirin, 1985; Chou and Wang, 1987; Barth and Livi, 1990). There is also a significant difference between the results here and those found for Hinode/NFI data. For IN ephemeral regions it was found that the initial separation speed was negative as the border expansion was initially greater than the movement apart. Once the feature has expanded then the separation speed became positive and the features appeared to move apart. This behaviour is not observed at all here, which suggests

these events are not being properly resolved in the full-disk data. On the whole it is difficult to see any sort of pattern relating to the solar cycle for the speed of separation. The range of initial speeds of 2.52-22.75 km s^{-1} ($\pm$2.57 km s^{-1} found using standard deviation) that are found here overlap with the rates of between 0.1-5 km s^{-1} which has been found previously for ephemeral regions in Kitt Peak magnetograms and Big Bear video magnetographs (Harvey and Martin, 1973; Zirin, 1985; Chou and Wang, 1987), but they reach a considerably higher upper limit.

In Figures 8.2a-c I consider the growth of features they are emerging. The spatial expansion rates both show a slight variation in anti-phase with the solar cycle, however the flux increase rate shows no significant difference over the cycle. To help uncover whether or not the slight variations are anything meaningful, I calculate the mean standard deviation for each plot. I find 0.003$\pm$ Mm^2 s^{-1} Figure 8.2a, $\pm$0.2 km s^{-1} for Figure 8.2b and $\pm 2 \times 10^{18}$ Mx s^{-1}. For Figures 8.2a and d these will still allow for a subtle cyclic variation.

How do the spatial expansion and flux increase rates found here compare to previous results? For ephemeral regions detected in SOHO/MDI full-disk with flux or order 10^{19} Mx, a flux growth rate of 2-30 $\times 10^{18}$ Mx s^{-1} was found (Chae et al., 2001; Hagenaar, 2001). All the flux increase rate results in Table 8.1 fall in this range. As for spatial expansion only the border expansion rates have been previously investigated and were found to lie between 1-3 km s^{-1} for ephemeral regions between 10^{18}-10^{20}Mx, observed in BBSO Kitt Peak and SOHO/MDI full-disk magnetograms (Harvey, 1993; Hagenaar, 2001). The higher bound of this range coincides with the edge expansion rates I find.

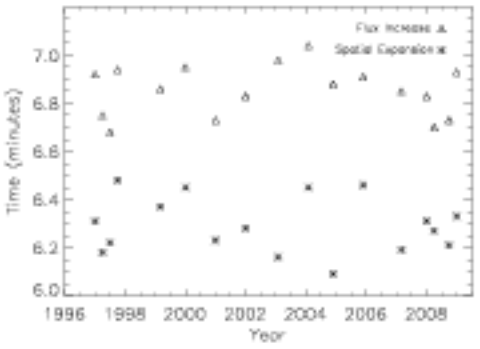

Figure 8.3: Plots showing the duration of spatial expansion and flux increase versus year, throughout cycle 23.

The final plot, Figure 8.3, shows the mean duration of flux increase (triangles) and spatial increase (stars) plotted throughout cycle 23. What is immediately obvious is that the mean time for flux increase is greater, than for area, in all cases. There is no obvious cyclic behaviour for either the flux growth times or the spatial expansion times. It is difficult to draw any solid conclusions from these results as the overall variation in time of the flux increase and spatial increase is only at most 0.6 minutes and 0.4 minutes, respectively, whilst the cadence of the data is 5 minutes. The standard deviation of the both the time of flux increase and spatial expansion is $\pm$0.3minutes. To measure evolution on such time-scales, it is clear that data with a significantly higher cadence would be required to do it accurately. It is also interesting to note that the time of flux increase and spatial expansion is always less than the ephemeral region lifetime.

8.2 Variation of Cancelling Events Over Solar Cycle 23

In this section the cancellation algorithm is applied to all the tracked features found in the full-disk data sets, using the clumping feature identification method. The algorithm is described in detail in Chapter 6, for the detection of cancellation events in Hinode/NFI. However, when the algorithm is applied to SOHO/MDI full-disk data here, some of the parameters must be changed. In the SOHO/MDI full-disk data, to be a cancelling event, each bipolar opposite-polarity pair must have a minimum distance between the boundaries of the features of ≤ 4 pixels ($\approx$ 5.6-9.6 Mm depending on the position on the disk) and both tracked opposite-polarity features must have an overall loss of at least 20% of their initial flux over a period of 3 or more frames ($\geq$ 15 minutes). For this section, I wish to know how small-scale features behave, throughout cycle 23, independently of the large-scale field. This requires a flux criterian to be added to the detection algorithm which separates cancellation events into those in which both opposite-polarity features have flux, upon the initiation cancellation, of $\leq 10^{20}$ Mx (small-scale cancellations). Those cancelling events which occur between opposite-polarity features where at least one of them is considered a large-scale feature (flux on the initiation of cancelling being $> 10^{20}$ Mx).The results of the large-scale and small-scale cancellation events are presented in Table 8.2 top and bottom, respectively.

Again the impetus of this section is to find if there is any variation in the process of cancellation throughout cycle 23 and whether there is any distinct difference in the cancellation that occurs at the previous and current solar minimums. I also want to find the relationship, if any, between the processes of cancellation and emergence throughout the solar cycle.

8.2.1 Characteristics of Cancellation Events

Not surprisingly the variation in the number of large-scale cancelling pairs (Figure 8.4a) varies in-phase with the solar cycle by a factor of 10.6. The variation in the number of small-scale cancelling pairs (Figure 8.5a) is similar in shape to that already been seen for the variation in the number of tracked features (Figure 7.1a) and the variation in the number of bipoles emerging (Figure 7.8a) , i.e. an anti-phase relationship to the cycle (by a factor of at most 3.1). Again to give a rough estimate on the accuracy of these numbers, I vary the cadence of the data and flux cutoff (σ) when identifying the features. This helps me to simulate how the cadence and resolution of data can impact the number of features identified and in turn those features which are found to be cancelling. I found that the upper bound for the variation for large-scale cancellations, taking both these factors into account, was a factor of 1.2. For the small-scale cancellations I found that the number of cancellations can vary by as much as a factor of 2.

Now looking at the mean peak flux lost per cancellation, for large-scale cancellations (Figure 8.4b), there is a variation loosely in phase with the solar cycle. Between 2000 and 2004 where there is a dramatic increase in the mean flux lost per cancellation increasing by a factor of almost 5 around the time of the cycle 23 maximum. Either side of the maximum the flux lost per interaction drops off steeply. Calculating the mean standard deviation gives $\pm 450 \times 10^{18}$ Mx. The mean flux lost per cancelling event in small-scale features (Figure 8.5b) also appears to vary in-phase with cycle 23 by a factor of 1.2. This is not surprising considering the variation of the mean peak small-scale tracked feature flux in Figure 7.2a is a factor of

1.4, and in-phase with the solar cycle.The standard deviation for small-scale cancellations is considerably smaller at $\pm 1 \times 10^{18}$ Mx.

Large-Scale Cancellations ($\Phi > 10^{20}$ Mx)	Dec 96	Mar 97	Jul 97	Oct 97	Feb 98	Dec 98	Dec 00	Dec 01	Jun 03	Jan 04	Nov 04	Nov 05	Feb 07	Dec 07	Mar 08	Oct 08	Dec 08
No. cancellations ($\times 10^{-21}$ sec^2 day^{-1})	3.0	8.3	8.3	10.8	17.3	30.3	26.4	32.1	31.8	27.1	23.2	17.1	16.3	8.0	7.1	3.8	3.7
Mean peak flux lost per cancellation ($\times 10^{18}$ Mx)	32.2	118.0	233.3	316.9	208.6	474.4	223.4	251.23	175.33	230.6	408.3	121.9	168.0	121.0	870.9	78.9	78.2
Total flux cancelled (Mx sec^{-2} day^{-1})	0.2	1.0	2.0	3.6	3.3	14.4	61.2	80.6	55.8	6.2	9.4	2.1	2.7	1.0	6.2	0.4	0.4
Mean intervention time (minutes)	64	41	69	61	67	33	60	48	64	41	47	53	39	72	40	91	38
Small-Scale Cancellations ($\Phi \leq 10^{20}$ Mx)																	
No. cancellations ($\times 10^{-19}$ sec^2 day^{-1})	3.2	2.0	1.7	1.7	1.9	1.3	1.1	1.0	1.7	1.7	2.2	2.1	2.9	3.3	2.8	3.0	3.1
Mean peak flux lost per cancellation ($\times 10^{16}$ Mx)	21.8	23.7	22.8	23.9	24.4	24.4	24.0	23.3	23.3	24.8	22.3	23.8	24.3	22.3	22.4	20.7	22.0
Total flux cancelled (Mx sec^{-2} day^{-1})	7.1	4.6	3.9	4.1	4.5	3.1	2.6	2.6	4.2	4.2	4.9	5.0	6.2	7.8	6.3	6.2	6.9
Mean intervention time (minutes)	46	49	30	31	30	44	47	40	49	41	43	30	42	41	40	43	43

Table 8.2: Cancellation detection results for large-scale cancellations (top) and small-scale cancellations (bottom) detected in the SOHO/MDI full-disk data sets.

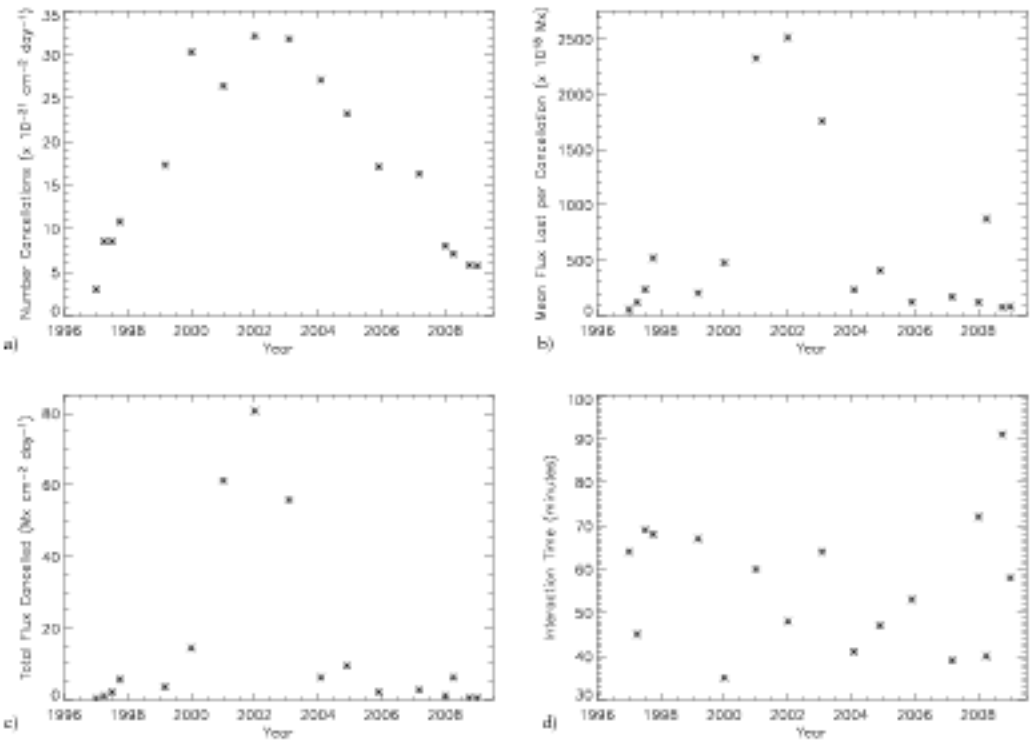

Figure 8.4: Plots of the a) number of cancellations, b) mean cancelled flux per interaction, c) total flux lost in all interactions and d) interaction time of cancellations, for large-scale cancellations.

For the large-scale cancelling events the total flux cancelled for all cancellation events (Figure 8.4c) varies in the same way as the flux lost per cancellation for large-scale features (Figure 8.4b), with a drastic increase in-phase with the cycle between 2000 and 2004 and little variation out with. Considering also how the total flux cancelled per event, changes throughout cycle 23, for all events, it is not surprising that there is such a sharp peak in the total flux cancelled. Again the peak seems to line up exactly with the peak in the sunspot numbers (Figure 7.1b). To give a bound on how accurate this is I once more use a variation of cadence and flux cutoff of the data. What I find is that the total flux emerged can vary by a factor of 1.2.

For the small-scale features the total flux cancelled (Figure 8.5c) is much more dependent on the number of cancellation events occurring, which in turn varies largely in anti-phase with the number of active regions present. The variation here is by a factor of 3.2. Again I give a bound on this using the same method as the previous paragraph. The total flux cancelled in small-scale cancellations can vary by a factor of 1.8. Remember that Figure 7.8d showed that the total flux emerged in small-scale emergences varies in this way too, but by a reduced factor of 1.9. There is a larger variation in the total cancelling flux lost for small-scale cancelling events, compared to the total flux emerging, as in the network the mean peak flux of the features increases in-phase with the cycle, whilst there is no variation in the mean peak flux of emerging events.

The final aspect to look at from Table 8.2 is the mean interaction time of the opposite-polarity features whilst they cancel (Figures 8.4d and 8.5d). Both Figures 8.4d and 8.5 show no relationship to the solar cycle. Finding the mean standard deviation in both these figures yields ± 20 minutes for the large-scale

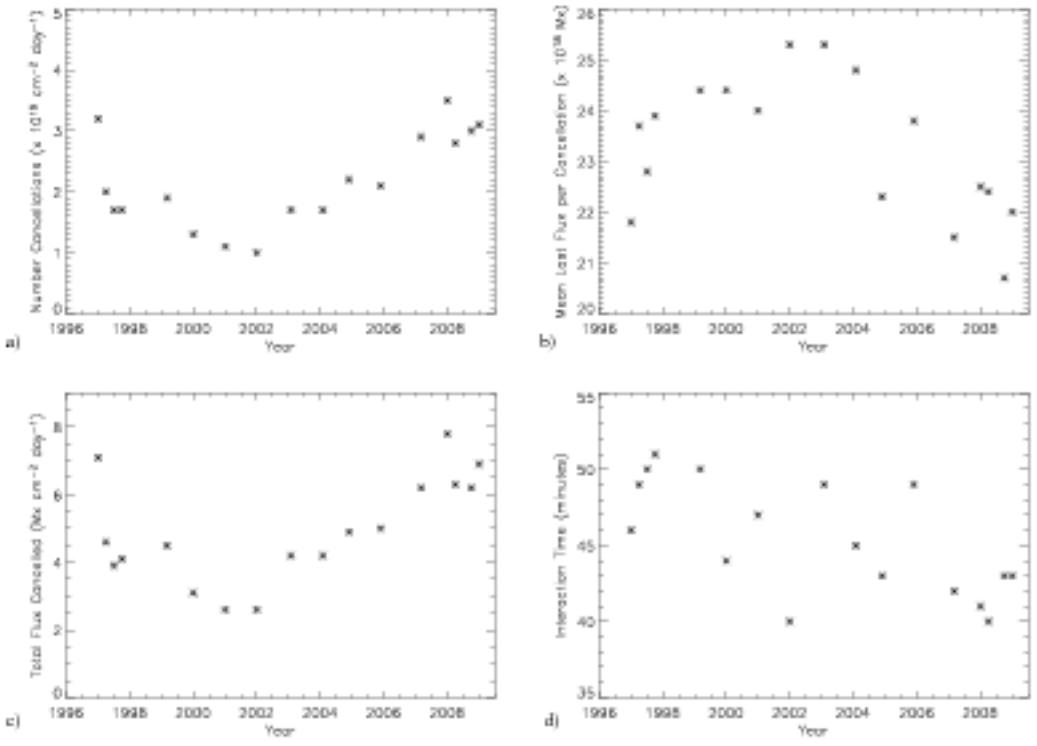

Figure 8.5: Plots of the a) number of cancellations, b) mean cancelled flux per interaction, c) total flux lost in all interactions and d) interaction time of cancellations, for small-scale cancellations.

cancellations and ±5 minutes for the small-scale cancellations. It is obvious from these that is difficult to accurately measure the time of interaction. This is likely to be due to the fact that multiple features can interact which makes it difficult to define a single interaction time. Also features can partially, as well as, full cancel which will also have effect on the interaction time.

Figure 8.6 shows that the total flux lost per interaction is directly proportional to the total peak flux of the features which are involved in the cancellation. The bottom boundary of the fan distribution is a result of the fact that the opposite polarity features must mutually lose at least 20% of their flux to be defined as a cancellation. Thus the lower slope of this curve is 0.2. The upper bound of the fan has a slope of 1 and is a consequence of the fact that the maximum flux lost occurs when both features lose all their flux whilst cancelling. Plotting the mean slope on this distribution using LADFIT (dashed line) gives a slope of 0.50, which reveals that the mean flux lost during a cancelling event is 50% of the total initial flux of the interacting opposite-polarity features.

Here I present an example of a cancelling event detected in the SOHO/MDI full-disk data, with this particular case being taken from the December 1996 data set (Figure 8.7).

In frame 9 of the data a positive (orange) and negative (purple) feature, with similar absolute flux, begin to cancel. The features slowly cancel over a prolonged period (77 frames/≈ 385 minutes), which is much longer than the interaction time observed for cancelling events in Hinode/NFI. During the cancellation there

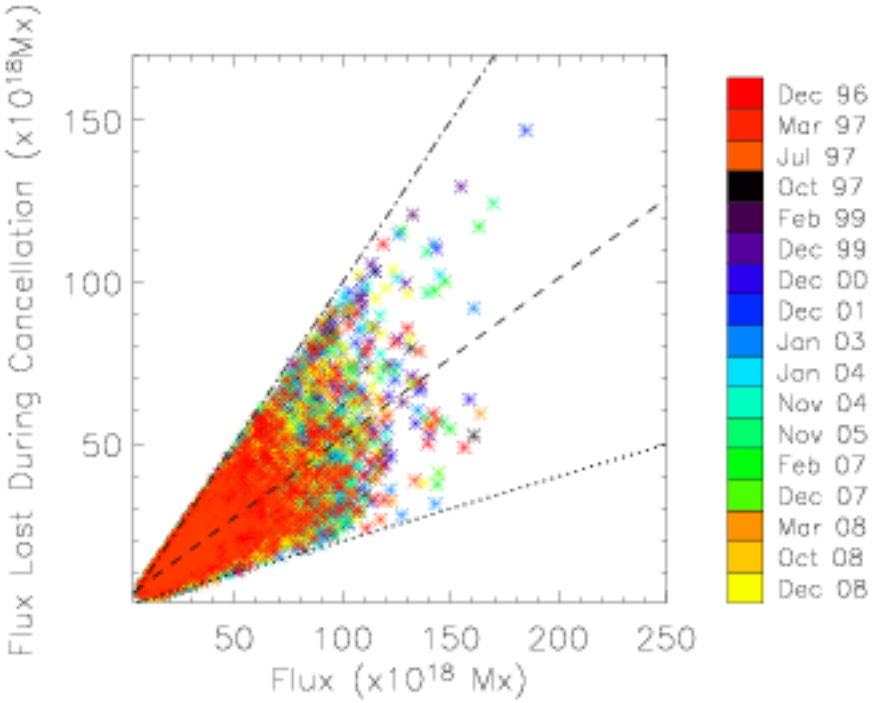

Figure 8.6: This plot shows the flux lost during cancellations versus the total absolute initial flux in the cancelling features. The dashed line is the mean flux lost per cancellation (slope of 0.50), the dot-dash line is the maximum flux lost per cancellation (slope=1) and the dot-line is the self-imposed minimum flux lost per cancellation (slope =0.2).

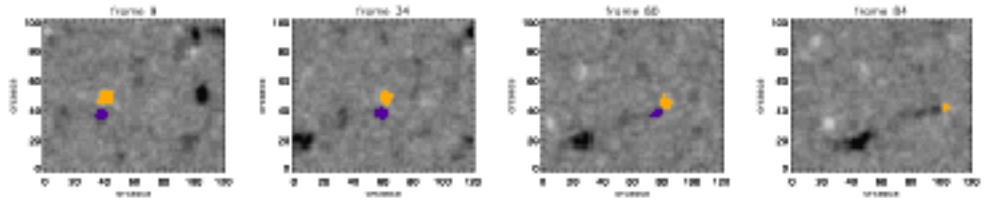

Figure 8.7: A visual example of a cancelling event from the December 1996 data set. In frame 9 of the data a positive (orange) and negative (purple) feature begin to cancel. Throughout their interaction time the flux and area reduce slowly, with the negative/positive features eventually dying after 360 and 380 minutes, respectively.

is no drastic decrease in distance between the cancelling features, but they reduce gradually in area. The flux of the features is plotted versus time in Figure 8.8, which shows that even though the overall trend is that the features are losing flux, it is a very erratic process. The error size of the flux of the features is given by the area (cm^{-2}) $\times$ cutoff (Mx cm$-$1) of each feature in each frame where the flux is measured. In this particular example both the cancelling features eventually die.

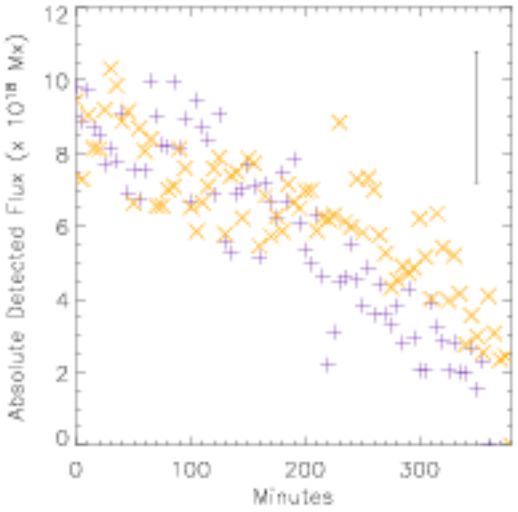

Figure 8.8: A plot of absolute flux against time for the cancelling features in Figure 8.7. The purple plus signs correspond to the purple (negative) feature flux and similarly the orange crosses correspond to the orange (positive) feature flux. The average error bar size is plotted in the top right corner. The overall trend is that the features are losing flux, but it is a very erratic process.

8.2.2 Distributions of Cancelling Events

In the previous chapter I illustrated that the distribution of mean peak fluxes of the tracked features and the distribution of mean peak fluxes of emerging events detected in both Hinode/NFI and SOHO/MDI full-disk data follow power-law distributions, indicating that there is a scale-free mechanism producing flux on the Sun. A log-log plot of the histograms of the flux lost per interaction is presented in Figure 8.9. Again it can be seen that there are two distinct patterns for the SOHO/MDI full-disk data sets: a steeper slope during quiet times and a shallower slope when the Sun is more active, with an extended tail. This is not surprising considering the distributions of tracked feature peak flux, tracked features peak area and emerging event flux (Figures 7.6, 7.7 and 7.11, respectively), which were presented in the previous chapter and taking into account the results from Table 8.2.

I also do a log-log plot of the flux lost per interaction against number of cancellation events from this section, along with the Hinode/NFI results from Chapter 6 (Figure 8.10). I only compare it to results from the cancellation algorithm applied to the Hinode/NFI clumping data as the features in the SOHO/MDI/full-disk data have been identified using the clumping method. It is clear there is a power-law relationship, which is of the form seen in Equation 7.1. Using LADFIT with the Hinode/NFI data set and the SOHO/MDI full-disk December 1996 and December 2001 data sets, I find the power-law index $\alpha = -2.10$, with $\Phi_o = 5 \times 10^{18}$ Mx and $N_p = 1.8 \times 10^{-15}$ cm^{-2} day^{-1}. This slope indicates that small-scale cancellations remove more flux from the photosphere than large-scale cancellation events.

As in the previous chapter, I use the cancellation flux distributions to calculate the total flux lost (Equation 7.3). The total flux loss through cancellation over the range $10^{16} - 10^{23}$ Mx is 67.2 Mx cm^{-2} day^{-1} which is 4.1 $\times 10^{24}$ Mx day^{-1} over the whole solar surface. The flux cancellation rate of small-scale fea-

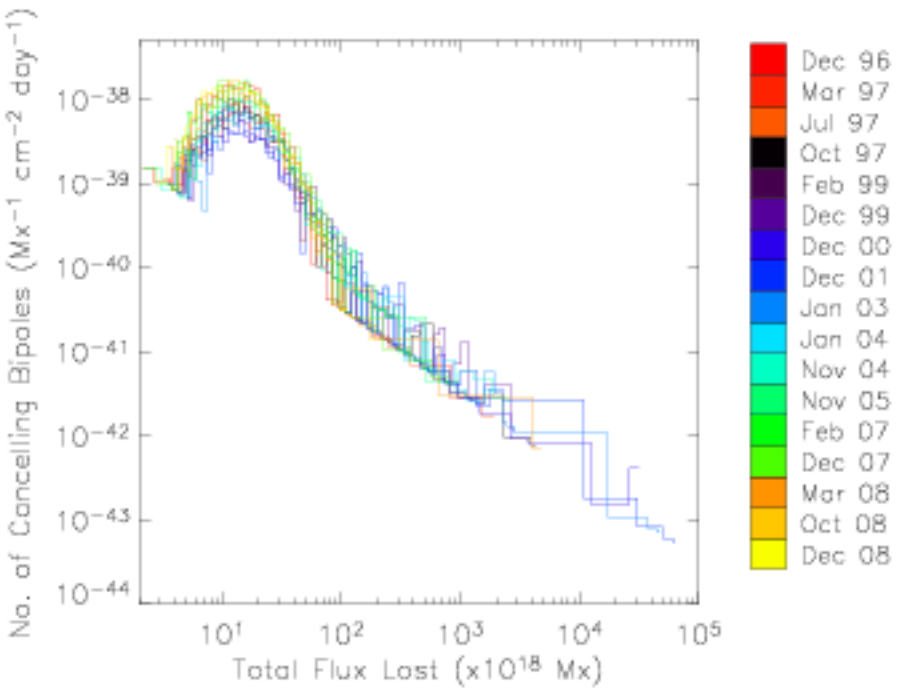

Figure 8.9: Log-log plot of the number of all the cancelling events versus the total flux lost per cancelling event, for all the SOHO/MDI/full-disk data sets.

tures with flux loss in the range $10^{16} - 10^{20}$ Mx is 50.5 Mx cm^{-2} day^{-1} (3.1×10^{24} Mx day^{-1} over the whole solar surface). Those events with peak flux loss in the range $10^{20} - 10^{23}$ Mx lose a total 16.7 Mx cm^{-2} day^{-1} (during active periods) (1.0×10^{24} Mx day^{-1} over the whole solar surface). This highlights that the numerous small-scale cancellations are removing the majority of flux from the photosphere. Comparing these results to what was found for all emergence in the previous chapter; the total emergence was 64.7 Mx cm^{-2} day^{-1} (4.0×10^{24} Mx day^{-1}), with 63.9 Mx cm^{-2} day^{-1} (3.9×10^{24} Mx day^{-1} over the whole surface) and 0.7 Mx cm^{-2} day^{-1} (4.3×10^{22} Mx day^{-1}) being associated with features in the ranges $10^{16} - 10^{20}$ Mx and $10^{20} - 10^{23}$ Mx, respectively. These show that emergence and cancellation are injecting and removing similar amounts of flux, although there is more emergence of flux at smaller scales.

Integrating over the distribution also gives the total number of cancellation events over the entire range of cancellations with flux loss between $10^{16} - 10^{23}$Mx. I find the total number of cancellations to be 7.6 $\times 10^{-16}$ cm^{-2} day^{-1}, which is 4.5×10^{7} cancellations per day over the whole surface. Only 3.0×10^{-20} cm^{-2} day^{-1} ($\approx$ 1856 cancelling events) of the cancellations is there more than 10^{20} Mx of flux lost, i.e., numerous small-scale/low flux loss cancellations make up the majority of the cancelling events which occur.

Now I wish to compare the cancelling flux lost distributions (Figure 8.10) to the distributions for tracked features (Figure 7.16) and the emerging events (Figure 7.18a) in the previous chapter. For all tracked features detected in both Hinode/NFI and SOHO/MDI there was a power-law relationship between the peak flux and event frequency with index $\alpha = -2.03$ similarly the emerging events distribution followed a power-law with $\alpha = -2.49$. The slope of the cancellation distribution is much closer to that of the tracked

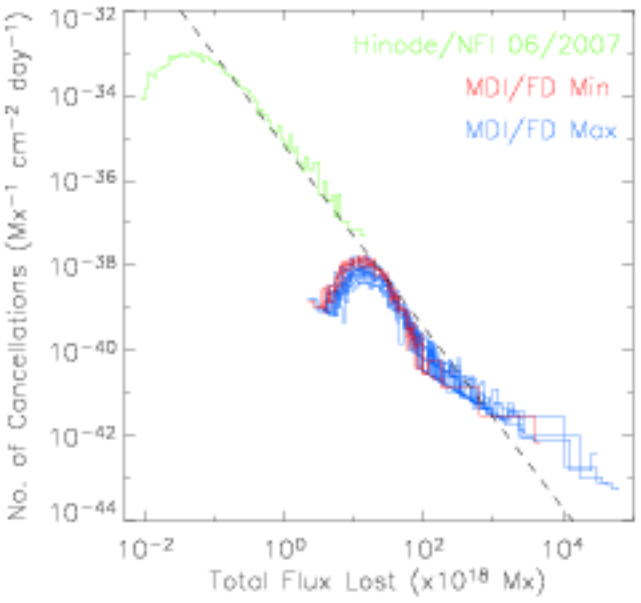

Figure 8.10: Log-log plot of the histograms of flux lost per cancelling event versus number from the Hinode/NFI clumping data (green),SOHO/MDI full-disk minimums (red),SOHO/MDI full-disk maximums (blues). The power law (dashed line) has index α= -2.10

feature distributions. This is not surprising considering that cancellation can occur between features at any time throughout their lifetime.

8.3 Variation Fragmentation and Coalescence Events Over Cycle 23

The final aspects of the feature evolution to be covered in this chapter are the processes of fragmentation and coalescence. The cases of fragmentation and coalescence are determined during the tracking of the features (Chapter 3) and the implications and assumptions I apply when investigation fragmentation and coalescence are discussed in Chapter 6 when the evolution of Hinode/NFI features is investigated. The impetus of this section is to gauge the importance of each process throughout the solar cycle and how this compares to the variation in emergence and cancellation. The fragmentation results are given in Tables 8.3 and 8.4 and the coalescence results are given in Tables 8.5 and 8.6. Tables 8.3 and 8.5 present the results found for large-scale (the parent feature has flux $> 10^{20}$ Mx for fragmentation and the total flux of the merging features is $> 10^{20}$ Mx for coalescence) and Tables 8.4 and 8.6 present the results for small-scale (the parent feature has flux $\leq 10^{20}$ Mx for fragmentation and the total flux of the merging features is $\leq 10^{20}$ Mx for coalescence).

Firstly looking at how the number of cases of large-scale fragmentations and coalescences vary throughout the cycle, (Figures 8.11a and 8.13a). The mean number fragmentations and coalescences occurring is remarkably similar: for both processes the number of events varies in-phase with the solar cycle. Looking

at Figures 8.12a and 8.14a and Tables 8.4 and 8.6 shows that the number of cases of fragmentations and coalescences occurring in only small-scale features both have an anti-phase variation by factors of 2.4 and 2.2, respectively. Again to gauge how accurate these results are I follow I've done this for the number of emerging bipoles (Figure 7.8) and cancelling features (Figure 8.5). I vary both the cadence between 1, 5 and 10 minutes and the flux cutoff ($m\sigma$) between m=1,2 and 3, to simulate varying cadence and resolution of the observations. This can help to show how robust the results are here. I find that by a combination of these factors, the number of cases of small-scale fragmentations and coalescences identified in each data set can vary by as much as a factor of 2.6. The large-scale fragmentations and coalescences identified each year vary by at most 1.7.

Fragmentation Results	Dec 96	Mar 97	Jul 97	Oct 97	Feb 98	Dec 98	Dec 00	Dec 01	Jan 03	Jan 04	Nov 04	Nov 05	Feb 07	Dec 07	Mar 08	Oct 08	Dec 08
Number of fragmentations ($\times 10^{-1.5}$ sec^{-2} day^{-1})	0.1	0.2	0.1	0.4	0.6	1.0	0.9	1.0	0.9	0.8	0.3	0.4	0.2	0.1	0.1	0.1	0.1
Mean flux of each feature produced																	
through fragmentation ($\times 10^{1.5}$ Mx)	31.17	3 15.3	44.34	947.8	2 59.0	4134.3	2768.7	2 59.2	4 11.73	473.9	474.9	1484.6	2 00.3	131.0	5 48.2	66.0	38.9
Mean flux of each feature which																	
fragments ($\times 1.0^{1.5}$ Mx)	12 4.8	102.08	90 3.3	188 3.6	64 .0	81 2.0	38 7.3	63 4.1	1 58 3.6	97 4.0	96 2.9	292 .9	43 4.3	27 .1	10 2.2	14 .2	18 .0
Mean number of emb features produced																	
by fragmentation (Mm^{-2})	30 .6	3 .9	9 .0	7 .0	3 .1	19 .2	14 .0	1 .07	2 .18	4 .0	3 .7	3 .9	2 .0	1 .4	6 .2	1 .2	1 .2
Mean number of emb features																	
which fragments (Mm^{-2})	2 .2	7 .2	1 .1	1 .3	6 .3	9 .9	1 .3	1 .3	4 .7	8 .2	7 .0	10 .6	4 .9	3 .6	12 .7	2 .2	2 .1
Mean number of frames produced																	
by a feature fragmenting	2.1	2.1	2.1	2.2	2.2	2.2	2.2	2.2	2.2	2.2	2.2	2.2	2.2	2.2	2.2	2.2	2.2
Mean time of first fragmentation (minutes)	13	14	16	16	13	13	14	14	13	13	13	13	14	14	13	16	14

Table 8.3: Results of large-scale fragmentation events (parent features with flux $> 10^{20}$ Mx).

Fragmentation Results	Dec 96	Mar 97	Jul 97	Oct 97	Feb 98	Dec 98	Dec 00	Dec 01	Jan 03	Jan 04	Nov 04	Nov 05	Feb 07	Dec 07	Mar 08	Oct 08	Dec 08
Number of fragmentations ($\times 10^{-13}$ cm^{-2} day^{-1})	2.3	2.0	1.8	1.7	1.8	1.7	1.4	1.2	1.6	1.8	2.1	2.2	2.6	2.8	2.3	2.6	2.3
Mean flux of each feature produced																	
through fragmentation ($\times 10^{1.3}$ Mx)	8.8	10.9	10.9	10.6	12.6	14.4	14.1	15.3	19.2	13.3	11.7	12.3	10.1	9.1	10.4	9.1	8.6
Mean flux of each feature																	
which fragments ($\times 10^{1.8}$ Mx)	19.0	23.1	23.1	22.6	26.1	29.8	29.8	31.2	30.3	28.3	24.7	26.2	21.2	19.3	21.1	19.3	18.3
Mean area of each feature produced																	
by fragmentation (Mm^2)	21.3	28.0	27.3	27.1	28.4	29.2	28.9	31.3	30.9	27.9	26.2	28.2	23.3	22.4	24.1	22.9	21.3
Mean area of each feature																	
which fragments (Mm^2)	51.3	60.1	59.6	58.6	60.2	62.3	61.9	60.8	60.7	59.8	56.4	60.3	50.3	48.0	51.2	49.1	46.2
Mean number of fragments produced																	
by a feature fragmenting	2.1	2.1	2.1	2.1	2.2	2.2	2.2	2.2	2.2	2.2	2.2	2.2	2.2	2.2	2.2	2.2	2.1
Mean time of first fragmentation (minutes)	15	14	16	16	13	13	14	14	13	13	15	13	14	14	15	16	14
Percentage of deaths which																	
are fragmentation to below resolution	33	33	60	52	30	43	41	41	43	46	49	30	33	33	34	34	34

Table 8.4: Results of small-scale fragmentation events (parent features with flux $\leq 10^{20}$ Mx).

Coalescence Results	Dec 96	Mar 97	Jul 97	Oct 97	Feb 98	Dec 98	Dec 00	Dec 01	Jan 03	Jan 04	Nov 04	Nov 05	Feb 07	Dec 07	Mar 08	Oct 08	Dec 08
Number of coalescences ($\times 10^{-15}$ sec^{-2} day^{-1})	0	0.1	0.1	0.4	0.4	1.0	0.9	0.9	0.7	0.6	0.4	0.2	0.2	0.1	0.1	0.1	0.1
Mean flux of each feature																	
which coalesces ($\times 10^{15}$ Mx)	0	1123.9	719.3	1259.6	461.6	4893.1	2768.7	4236.3	6884.7	7000.3	7351.6	3304.0	3044.3	2316.1	3159.0	1271.1	1099.2
Mean flux of each resulting																	
feature ($\times 10^{15}$ Mx)	0	2198.8	1548.4	3425.0	816.1	9390.3	5887.3	8422.3	12478.0	13293.3	14320.3	6776.2	5534.4	5065.9	5851.4	2227.3	2123.9
Mean area of each feature																	
which coalesces (Mm^2)	0	649.9	379.6	1033.3	471.0	2297.3	1486.0	2267.3	3308.8	3592.4	3731.8	1324.9	1166.6	967.1	1106.9	784.6	593
Mean area of each																	
resulting feature (Mm^2)	0	1249.1	1981.4	1981.0	1100	4393.6	3149.3	4189.4	6674.3	7156.1	5950.0	2776.3	1850.1	1910.7	2082.2	1112	1971.8
Mean number features which merge																	
to form a single feature	0	2.3	2.3	2.3	2.4	2.3	2.2	2.6	2.3	2.3	2.4	2.3	2.4	2.4	2.3	2.7	2.1
Mean time of first and last sensor (minutes)	0	12	13	13	12	14	14	13	13	12	12	12	10	10	11	11	10

Table 8.5: Results of large-scale coalescence events (total flux of the merging features is $> 10^{20}$ Mx).

Coalescence Results	Dec 96	Mar 97	Jul 97	Oct 97	Feb 98	Dec 98	Dec 00	Dec 01	Jan 03	Jan 04	Nov 04	Nov 05	Feb 07	Dec 07	Mar 08	Oct 08	Dec 08
Number of coalescences ($\times 10^{-13}$ sec^{-2} day^{-1})	4.3	3.3	2.3	2.7	3.2	2.3	2.3	2.3	2.9	3.3	3.9	3.9	4.6	4.9	4.0	4.3	4.4
Mean flux of each feature which coalesces ($\times 10^{18}$ Mx)	9.9	13.3	12.8	13.3	17.9	22.2	21.6	23.9	22.1	20.2	15.9	16.8	12.4	10.8	11.8	10.6	10.0
Mean flux of each resulting feature ($\times 10^{18}$ Mx)	17.7	24.9	24.3	30.3	37.1	47.4	48.3	50.3	139.6	39.7	30.4	31.4	23.8	19.3	22.7	18.7	18.3
Mean area of each feature which coalesces (Mm^2)	26.3	32.8	31.7	34.6	36.1	40.0	38.3	42.6	38.1	37.3	32.4	33.4	27.6	23.7	27.1	26.0	24.3
Mean area of each resulting feature (Mm^2)	46.1	59.7	57.7	60.9	70.2	80.0	68.3	81.3	136.8	71.1	59.2	64.3	49.2	41.4	48.7	44.6	42.8
Mean number features which merge to form a single feature	2.3	2.3	2.3	2.3	2.4	2.6	2.4	2.7	2.3	2.4	2.4	2.3	2.4	2.3	2.3	2.3	2.4
Mean time of first coalescence (minutes)	10	12	13	11	12	14	14	11	13	12	12	12	10	10	11	11	10
Percentage of births which are due to coalescence of sub-resolution flux	62	60	64	60	59	54	54	53	53	54	57	58	59	59	60	60	60

Table 8.6: Results of small-scale coalescence events (total flux of the merging features is $\leq 10^{20}$ Mx).

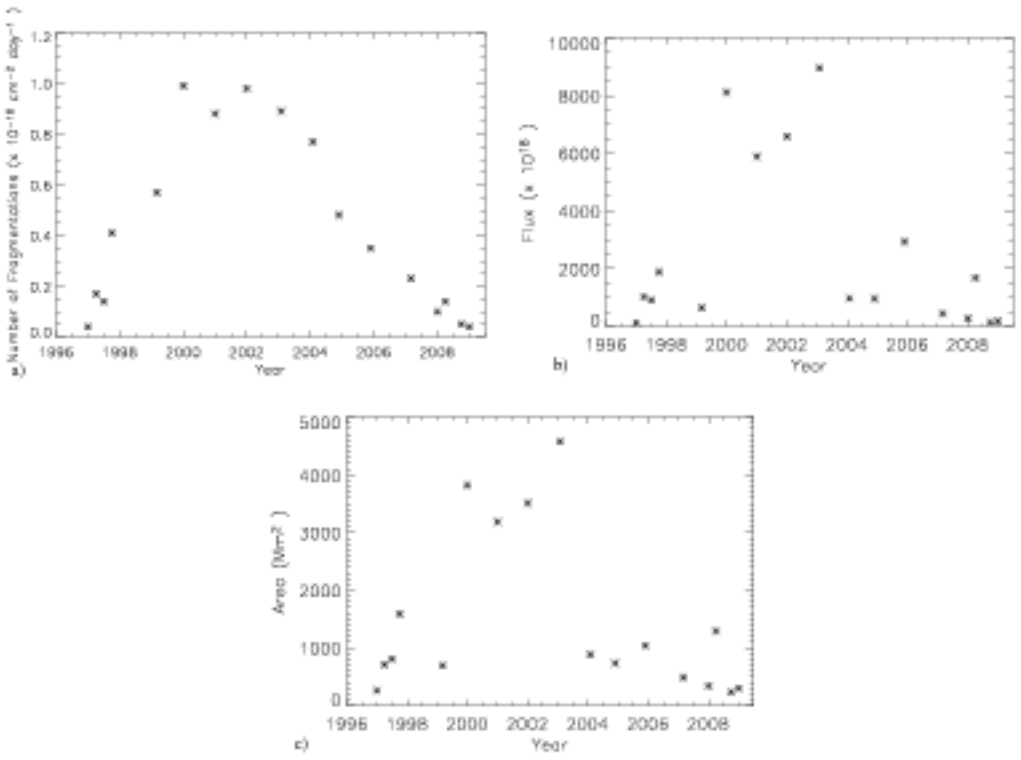

Figure 8.11: Plots showing the variation over cycle 23 in the a) mean number of fragmentations, b) mean flux of each fragmenting feature and c) mean area of each fragmenting feature for large-scale fragmenting features.

The flux and area of fragmenting features for the large-scale cases varies in phase with the solar cycle by a factor of ≈ 72 and ≈ 20, respectively, whilst the flux and area of coalescing features varies by factors of ≈ 60 and ≈ 36, respectively. The flux and area for small-scale features which fragment varies in-phase by factors of 1.7 and 1.4. The flux for small-scale coalescing features varies in phase with the solar cycle by factor of 2.4 . For the area of small-scale coalescing features, it can be seen that the variation is in-phase with the solar cycle by a factor of at most 1.7. To estimate the accuracy of these results here I take the standard deviation over the fluxes of the fragmenting and coalescing features in each year. What I find is that the large-scale fragmenting features have a mean standard deviation of $\pm 1.5 \times 10^{21}$Mx and ± 750Mm^2 for the flux and area respectively, whilst for the large-scale coalescing features I find $\pm 7.7 \times 10^{21}$Mx for the flux and ± 630Mm^2 for the area. The small-scale fragmenting features have a mean standard deviation of $\pm 5 \times 10^{18}$Mx for flux and ± 4Mm^2 for area and for small-scale coalescing features I find a $\pm 4 \times 10^{18}$Mx and ± 5Mm^2 for flux and area respectively.

The first time of fragmentation and coalescence is also calculated for all the features (Figure 8.15) which undergo these processes regardless of flux. Comparing the time for first fragmentation and coalescence we see that features are slightly more likely to coalesce first, which is the same result as that was found in Chapter 6 for IN features detected in Hinode/NFI. As in Chapter 6 this result is consistent with the fact that throughout cycle 23 the features that coalesce have smaller values of mean flux and area than those which fragment. Finding the standard deviation on these results for each year will help to show how robust this conclusion is. The mean standard deviation for the first time of fragmentation and coalescence is ± 1minute.

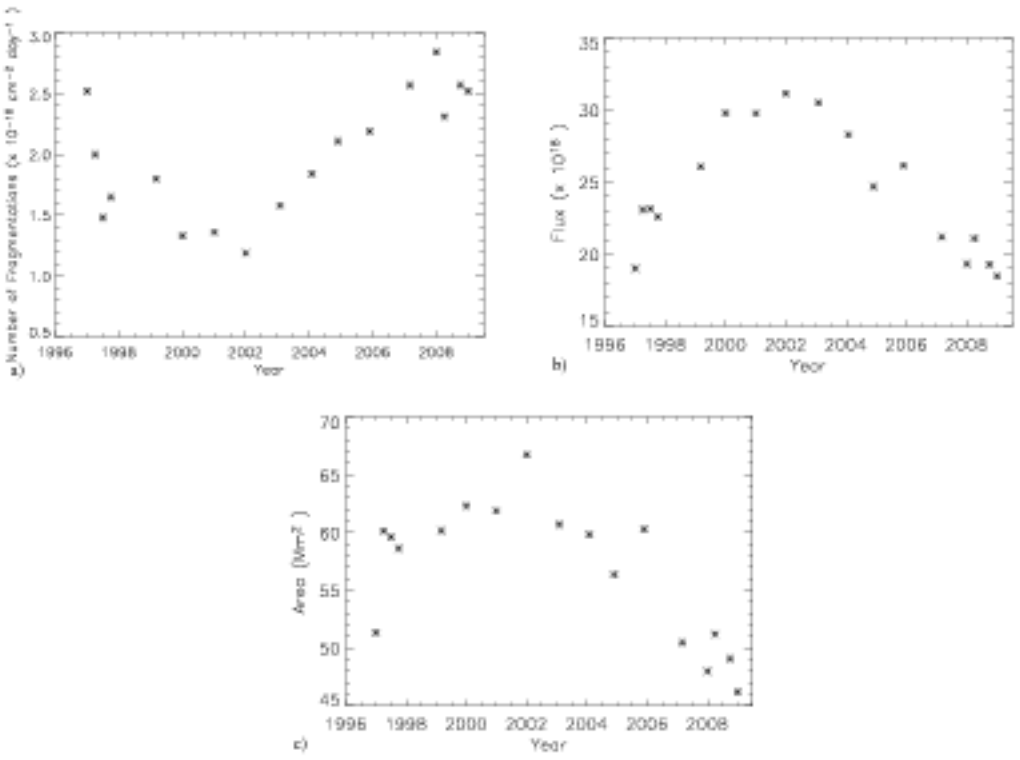

Figure 8.12: Plots showing the variation over cycle 23 in the a) mean number of fragmentations, b) mean flux of each fragmenting feature and c) mean area of each fragmenting feature for only the small-scale fragmenting features.

This shows further analysis would need to be undertaking to fully conclude the results stated.

Comparing the results in this section to those of emerging events (Table 7.2) also provides some insight into these processes. The mean lifetimes of emerging events, in all data sets, is always longer than the mean time of first coalescence or first fragmentation, indicating that surface processes are an integral part of many of the emerging events which occur. The flux and area of coalescing events are always slightly larger than the peak flux of emerging events. The mean flux and area of all fragmenting events are also larger than the mean peak flux and area of the tracked features (Table 7.1), in each respective data set. This could indicate that features are more inclined to fragment and coalesce once over some critical flux/area value but it could also suggest that there are fragmentations and coalescences missed due to their parent components being below resolution.

In Chapter 6 when analysing the evolution of IN features in Hinode/NFI data, it was discovered that many births could not be accounted for by visible emergence or fragmentation, and many deaths cannot be accounted for through coalescence and cancellation. There were two reasons for this, either that genuine emergence and cancellation events were occurring but for some reason only one of the polarities was being detected or that sub-resolution flux could gather and merge and cause a feature to suddenly appear above resolution, or the converse of this where a feature fragments into pieces all of which are below resolution. Lamb et al. (2008) have already investigated genuine emergence and cancellation in which only one of the

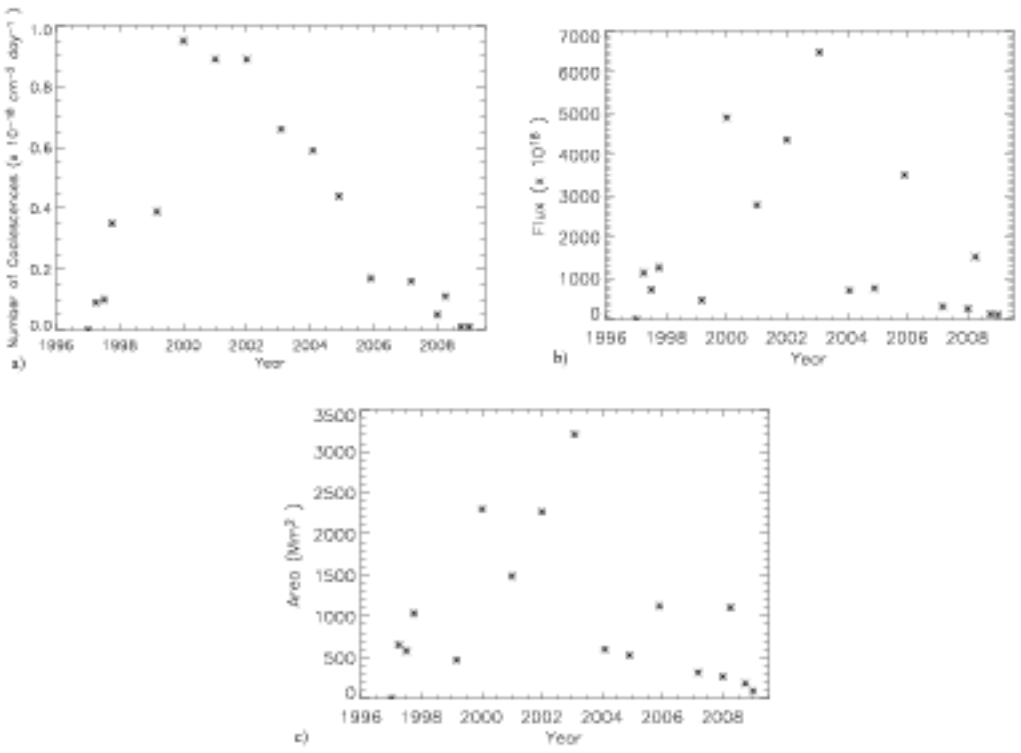

Figure 8.13: Plots showing the variation over cycle 23 in the a) mean number of coalescences, b) mean flux of each coalescing feature and c) mean area of each coalescing feature for large-scale coalescing features.

features is detected and found that its occurrence was rare. In Chapter 6 for Hinode/NFI data using the Tracked Bipolar emergence detection method I found that 45% of appearances in the clumping data are not attributed for and therefore are classed as 'coalescence of sub-resolution flux'. The amount of deaths not attributed for (i.e. flagged as death of a feature through dispersal below the resolution) is 50% in the clumping data. For the SOHO/MDI full-disk data I find that there consistently more sub-resolution births than there are deaths which is the opposite to what was found for the Hinode/NFI data.

Here I find, interestingly, that both the percentage of births which are due to the gathering of sub-resolution flux and deaths through the dispersal of flux below resolution, have an anti-phase variation, with the number of unaccountable births and deaths reducing during the active periods of the solar cycle. This along with the fact that the mean flux and area of the features varies in-phase with the solar cycle highlights that there are likely to be less features being removed by my flux and area criteria at the tracking stage during active periods of the cycle. The accuracy of these results can be estimated through seeing how their value changes as the cadence and flux cutoff (σ) change in a similar analysis to Figure 8.11. What can be seen is that the number of deaths through sub-resolution fragmentation can varying by at most $\pm 7\%$ whilst the number of births through sub-resolution coalescences can vary by up to $\pm 4\%$.

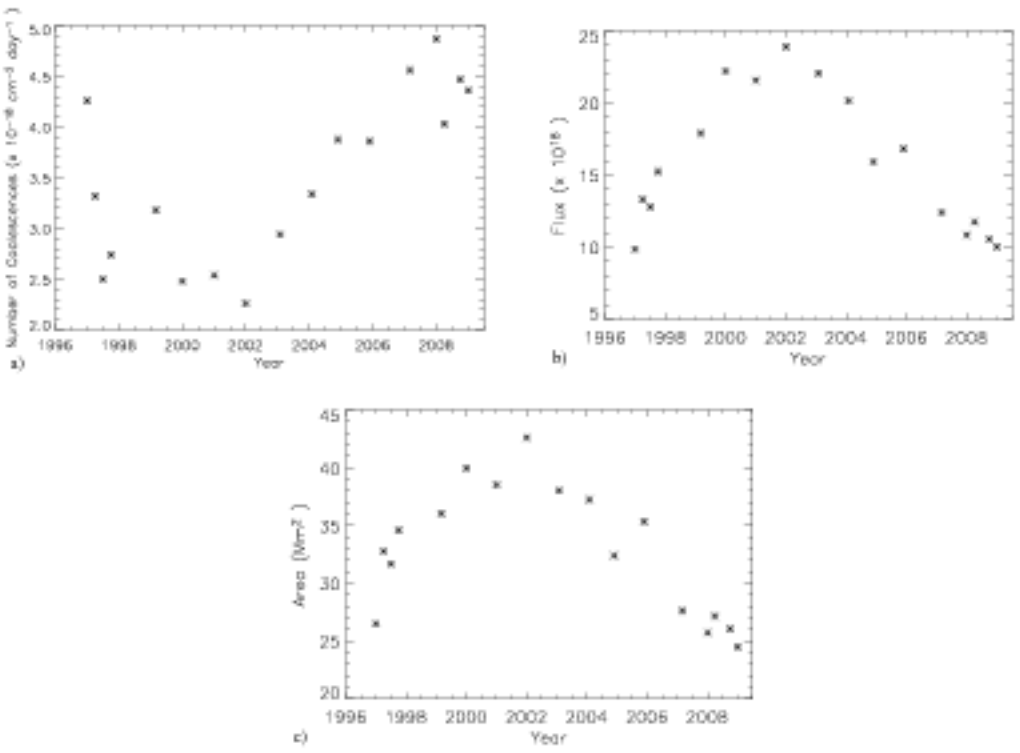

Figure 8.14: Plots showing the variation over cycle 23 in the a) mean number of coalescences, b) mean flux of each coalescing feature and c) mean area of each coalescing feature for only the small-scale coalescing features.

8.3.1 Visual Examples of Fragmentation and Coalescence in SOHO/MDI Full-disk Data

To complement the results I have found in this section I present a few examples of fragmenting and coalescing events observed in the December 1996 data set.

Figures 8.17 and 8.18 show examples of fragmenting and coalescing, which just involve two features. The fragmenting example in Figure 8.17 shows a single large positive (orange) feature in frame 2, which has split into two features (orange and red) by the following frame. One of the features produced by the fragmentation retains the label of the original features, in this case it is the orange feature, whilst the other is tagged as born through fragmentation. Figure 8.18 shows essentially the opposite process, where there are two positive features (red and yellow) in frame 55, which coalesce to form a single larger (red) feature in frame 56. The coalesced feature will take the label of the red feature in frame 55, whilst the yellow feature is tagged as died through coalescing.

Comparing the flux and area of coalescing features and their first interaction time to the flux, area and lifetime of emerging events indicated that coalescing events were occurring within an emergence before its full development. Figure 8.19 shows an example of this. An emerging event, consisting of a positive (red) and negative (blue), appears in frame 48. As the bipole is developing another negative (purple) feature

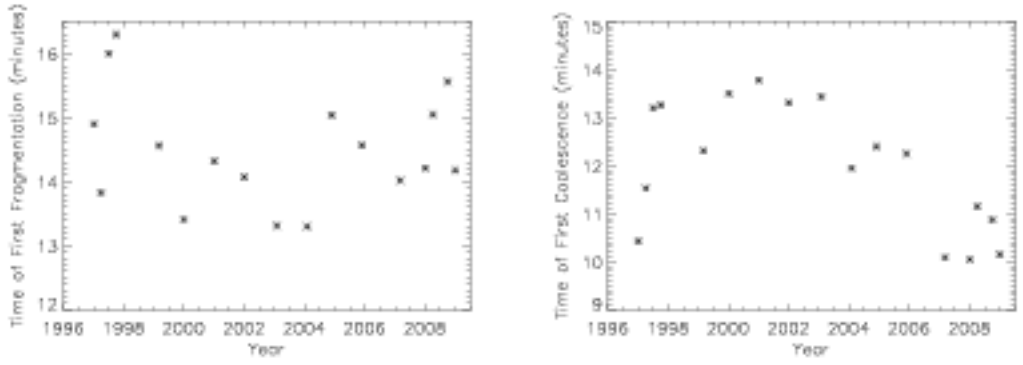

Figure 8.15: Plot showing how the mean time of first a) fragmentation and b) coalescence varies throughout solar cycle 23.

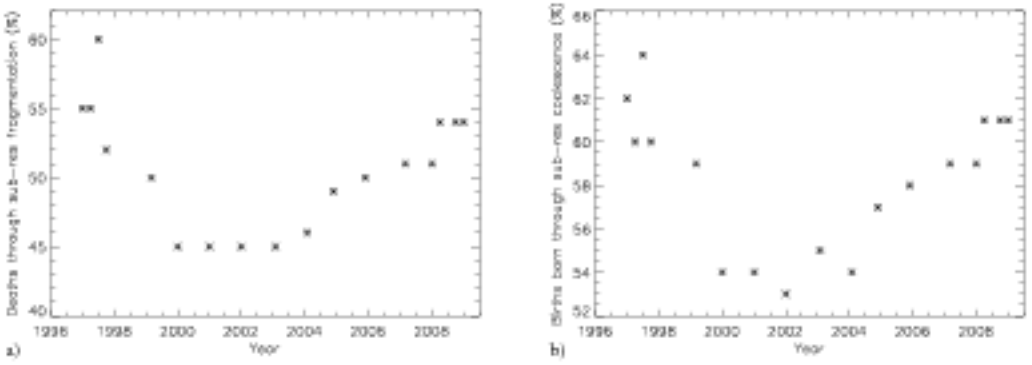

Figure 8.16: These two plots show the variation over cycle 23 of a) the percentage of deaths deemed to be a result of fragmentation resulting in features below the resolution and b) the percentage of births deemed to be a result of the collection of sub-resolution flux such that a feature appears above resolution.

appears along side it in frame 60. By the following frame the two negative features have coalesced to form a single negative feature.

It is clear from the results in Tables 8.3, 8.4, 8.5 and 8.6 that fragmentation and coalescence can occur between more than two features at a time. Figure 8.20 shows an example of this for a fragmentation event. A positive (orange) feature in frame 19 is seen to have fragmented into three parts by the following frame.

8.3.2 Fragmentation and Coalescence Distributions

Here I present log-log plots of the histograms for the flux, area and age versus frequency of the features which fragment (Figures 8.21a-c) and coalesce (Figures 8.22a-c). I combine data from both the fragmenting and coalescing events detected in this section and in Chapter 6 in the Hinode/NFI data to provide better statistics. The Hinode/NFI results I use here are only those for the fragmentation and coalescence events detected in the clumping tracked data as this is the data that is used for the SOHO/MDI full-disk.

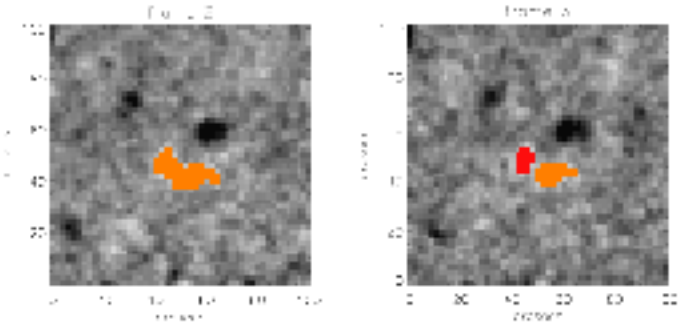

Figure 8.17: This figure shows a single large positive (orange) feature in frame 2, which has split into two features (orange and red) by the following frame.

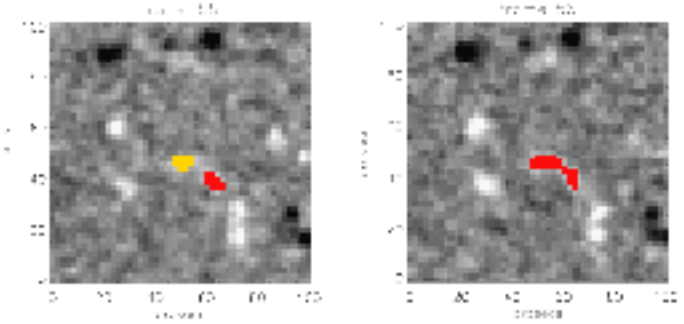

Figure 8.18: This figure shows two positive features (red and yellow) in frame 55, which coalesce to form a single larger (red) feature in frame 56. This a typical example of coalescing event, which just involves two features.

Figure 8.21a and 8.21b show the log-log plots of histograms of the fragmenting feature fluxes and areas for both the SOHO/MDI full-disk data, with those data sets between December 1996-October 1997 and November 2005-December 2008 (quieter periods) being coloured red and those between February 1999-November 2004 (active periods) being coloured blue, and the Hinode/NFI results being green. The fragmenting feature fluxes and areas do not follow distributions with a power-law relationship. Comparing the SOHO/MDI full-disk and the Hinode/NFI results there are clearly not enough small-scale fragmentations detected in the full-disk data for there to be a continuous relationship. This may be because the smallest scale features fragmenting in the SOHO/MDI data go below the resolution, so are not detected. The shapes of the Hinode/NFI and SOHO/MDI full-disk are similar, so if this was the case for SOHO/MDI data then it is likely that some of the fragmentation occurring at the smallest-scale in Hinode/NFI also goes undetected. I still provide an estimate of the fragmentation frequency using the Hinode/NFI clumping data results, from features with fluxes in the range $5 \times 10^{18} - 5 \times 10^{19}$ Mx. The shape of the fragmentation histogram indicates that the majority of fragmentations occur in features with fluxes $10^{18} - 10^{20}$Mx. The frequency of fragmentation is 1.6×10^{-10} cm^{-2} day^{-1}, which is 9.7×10^{6} fragmentations day^{-1} over the whole surface. I assume that the number of fragmentations above this flux range is fairly insignificant.

The histogram for the age of the features when they fragment (Figure 8.21c) shows a completely different relationship between Hinode/NFI and SOHO/MDI full-disk. There is a very large overlap in the age of the

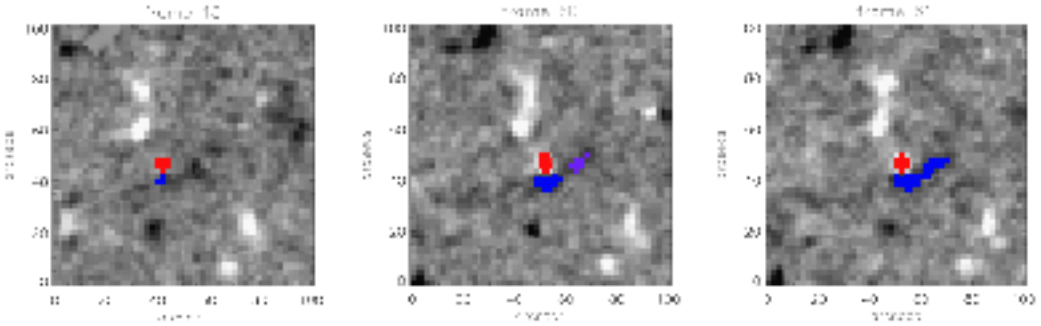

Figure 8.19: This figure shows an emerging event, consisting of a positive (red) and negative (blue), appears in frame 48.As the bipole is developing another negative (purple) feature appears along side it in frame 60. By the following frame the two negative features have coalesced to form a single negative feature.

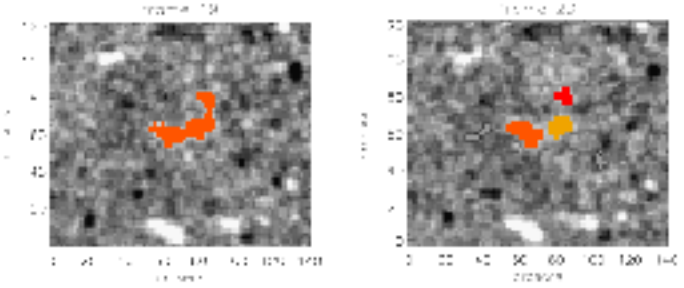

Figure 8.20: In many cases fragmentation and coalescence can occur between more than two features at a time. This example shows a positive (orange) feature in frame 19 that fragments into three features in the following frame.

features when they interact, with there obviously being more events in the Hinode/NFI data. It is clear that, in both data sets, events can occur any time after birth. The first possible chance for fragmentation to take place being the frame after birth, is 90 seconds for Hinode/NFI and ≈5 minutes for the SOHO/MDI data. Figure 8.21c shows that fragmentation occurs in features of all ages.

The log-log plots of histograms for the flux and area of coalescing features (Figures 8.22a and 8.22b) in Hinode/NFI (green) and SOHO/MDI full-disk (red and blue), do show power-law relationships (dashed lines) in the form of Equations 7.1 and 7.2. For the flux distributions, using LADFIT with the Hinode/NFI (green), December 1996 (red) and December 2007(blue) results to fit a power-law (dashed line) I find α = -1.92 and $N_p = 2.1 \times 10^{-16}$ cm^{-2} day^{-1} (with $\Phi_\circ = 4 \times 10^{15}$ Mx). Similarly for the area distributions I find $\gamma = -2.20$ and $N_f = 1.2 \times 10^{-18}$ cm^{-2} day^{-1} (with $A_\circ = 5 \times 10^{14}$ cm^2).

Integrating over the flux distribution I find a total of 5.8×10^{-17} coalescences cm^{-2} day^{-1} (3.6×10^6 day^{-1} over the whole surface) occurring in all identified features with flux between $10^{16} - 10^{23}$ Mx. Only 9.2×10^{-22} coalescences cm^{-2} day^{-1} (≈ 60 per day over the whole surface) occur in features with flux above 10^{20} Mx.

For the tracked feature distributions for Hinode and SOHO/MDI data (§ 7.4) I found power-law rela-

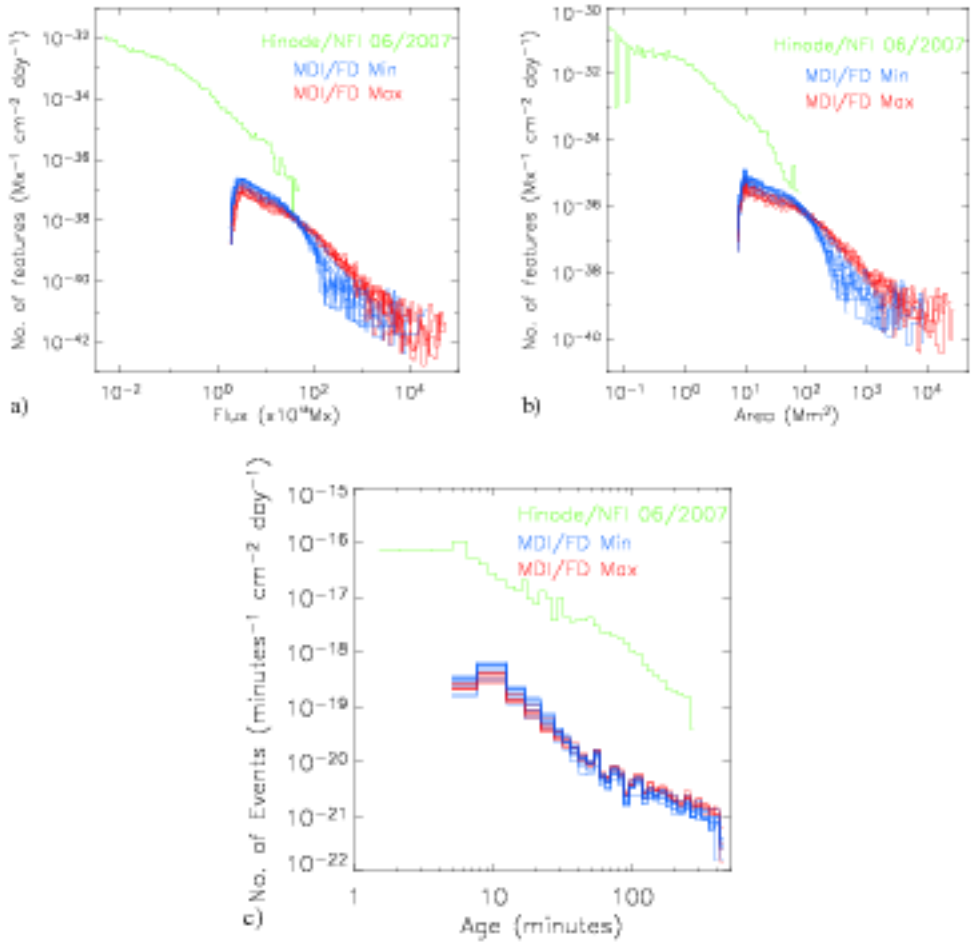

Figure 8.21: Log-log plot of histograms of a) mean peak fluxes, b) mean peak area and c) age of features when they interact, against frequency of fragmentation events from Hinode/NFI (green), SOHO/MDI full-disk minimum (red) and SOHO/MDI full-disk maximum (blues).

tionships with $\alpha = -2.05$ for mean peak flux and $\gamma = -2.30$ for the mean peak area. Similarly for the emerging events I found $\alpha = -2.50$ for the flux distribution and $\gamma = -2.90$ for the area distribution. The power-laws found for the coalescence events are shallower, this is not surprising as coalescence makes larger features and thus enhances the distribution at larger scales reducing the slope.

The age distributions for coalescing features (Figure 8.22c) are remarkably similar to those for the fragmenting features (Figure 8.21c), with the only obvious difference being the number of Hinode coalescences at small-scale being larger than the respective number of fragmentations.

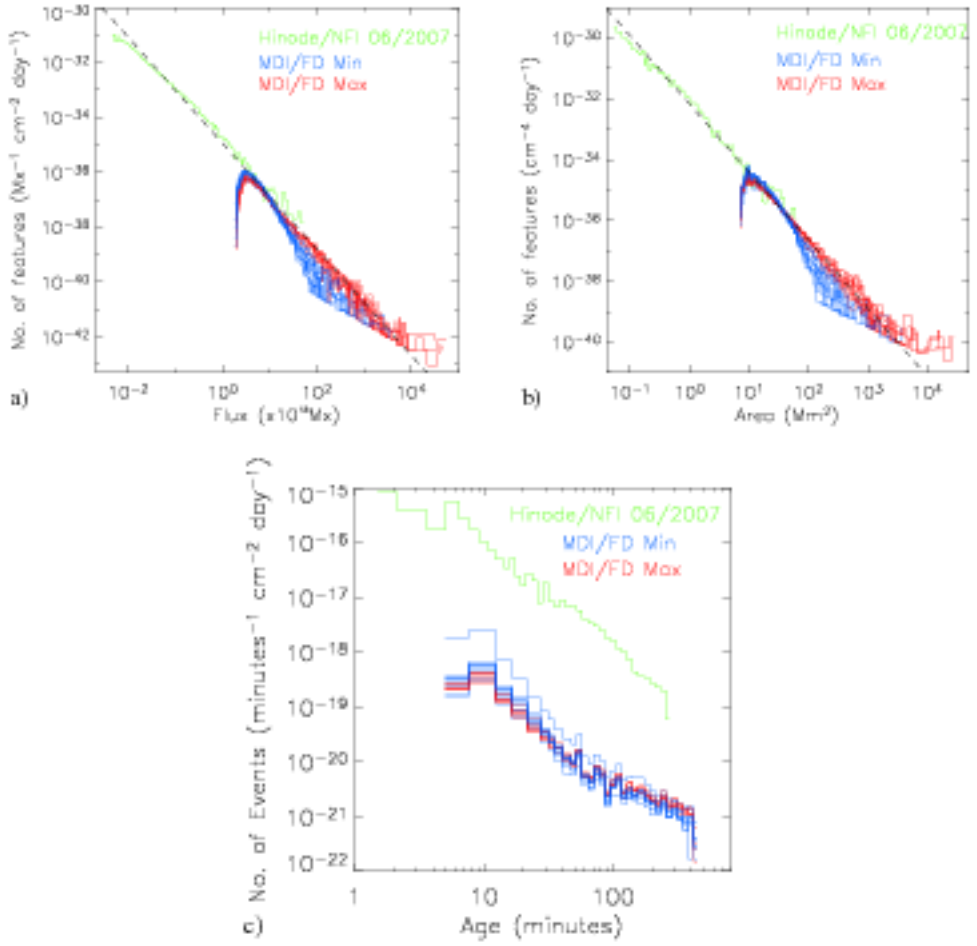

Figure 8.22: Log-log plot of a) mean peak fluxes, b) mean peak areas and c) age of features when they interact, against frequency of coalescence events from those detected Hinode/NFI (green), SOHO/MDI full-disk minimums (red) and SOHO/MDI full-disk (maximums). The power laws in a) and b) (dashed line) have an index of α= -1.92 and $\gamma = -2.24$, respectively.

8.4 Conclusions

This chapter aims to investigate how dynamic the network is and how the surface processes vary over the solar cycle. Firstly in this chapter I investigated the process of the evolution of emerging events. It was found that the emerging events detected exhibited typical behaviour, i.e., the opposite polarity features move apart during the emergence and simultaneously increase in flux and area. This behaviour, however, did not exhibit any significant cyclic behaviour.

The process of cancellation, however, did show some relation to the solar cycle. The variation in the number of small-scale cancelling events was similar in shape what was seen in the previous chapter for the variation in the number of tracked features and the variation in the number of bipoles emerging, i.e., an anti-phase relationship to the cycle (by a factor of at most 3.1). The mean flux lost per cancelling event in

small-scale features varies in-phase with cycle 23 by a factor of 1.2. This is not surprising considering the variation of the mean peak small-scale tracked feature flux. The features involved in cancellation did not always die, indeed it was found that the mean flux lost per cancellation is 50% of the total initial flux of the opposite-polarity pair. The total flux cancelled, by small-scale cancelling events, is much more dependent on the number of cancellation events occurring, which in turn largely varies in anti-phase with the number of active regions present. The variation here is by a factor of 3.2. Remember that the total flux emerged in small-scale emergences varies in this way too, but by a reduced factor of 1.9.

A log-log plot of the histograms for the flux lost per cancelling events (detected in both Hinode/NFI and SOHO/MDI full-disk) versus frequency, showed a power-law relationship with a power law index $\alpha = -2.10$. As in the case of emergence the process of cancellation appears to be scale free and the slope is greater than 2 indicating that numerous small-scale features are cancelling the majority of flux on the Sun. The cancellation slope is much closer to the power-law index that was find for all the tracked features peak flux as opposed to the emerging events peak flux. This is not surprising as the process of cancellation can occur at any point in a feature's life once it has been subjected to numerous surface processes.

Using the cancellation flux distributions I calculate the total flux lost through cancellation over the range $10^{16} - 10^{23}$Mx. I found a value of 67.2 Mx cm^{-2} day^{-1} which is 4.1 $\times 10^{24}$ Mx day^{-1} over the whole solar surface. The flux cancellation rate of small-scale features with flux loss in the range $10^{16} - 10^{20}$ Mx is 50.5 Mx cm^{-2} day^{-1} (3.1 $\times 10^{24}$ Mx day^{-1} over the whole solar surface). Those events with peak flux loss in the range $10^{20} - 10^{23}$ Mx lose a total 16.7 Mx cm^{-2} day^{-1} (during active periods) (1.0 $\times 10^{24}$ Mx day^{-1} over the whole solar surface). Comparing these results to those found for all emergences in the previous chapter; the total emergence is 64.7 Mx cm^{-2} day^{-1}, with 63.9 Mx cm^{-2} day^{-1} and 0.7 Mx cm^{-2} day^{-1} being associated with features in the ranges $10^{16} - 10^{20}$ Mx and $10^{20} - 10^{23}$ Mx, respectively.

Integrating over the cancellation flux distribution also gives the total cancellation rate over the entire range of cancellations with flux loss between $10^{16} - 10^{23}$Mx. I find the total cancellation rate to be 7.6 $\times 10^{-16}$ cm^{-2} day^{-1}, which is 4.5×10^{7} cancellations per day over the whole surface. In only 2.35×10^{-20} cm^{-2} day^{-1} ($\approx$ 1986 cancelling events) of the cancellations is there more than 10^{20} Mx of flux lost, i.e., numerous small-scale/low flux loss cancellations make up the majority of the cancelling events which occur.

The final aspect of evolution to be investigated is the processes of fragmentation and coalescence. The number of cases of fragmentations and coalescences occurring in small-scale features both have an anti-phase variation by factors of 2.4 and 2.2, respectively. The flux and area for small-scale features which fragment varies in-phase by factors of 1.7 and 1.4. The flux for small-scale coalescing features varies in phase with the solar cycle by factor of 2.4 . For the area of small-scale coalescing features, it can be seen that the variation is in-phase with the solar cycle by a factor of at most 1.7. Comparing the time for first fragmentation and coalescence we see that features are more likely to coalesce first, which is the same result as that was found in Chapter 6 for IN features detected in Hinode/NFI. As in Chapter 6 this result is consistent with the fact that throughout cycle 23 the features that coalesce have smaller values of mean flux and area than those which fragment.

Once more I refer to the log-log plots of histograms to provide more detail on the variation throughout the solar cycle and to relate the results found from Hinode/NFI and SOHO/MDI full-disk. The log-log

plots of histograms for the flux and area of coalescing features in Hinode/NFI and SOHO/MDI full-disk, show single distributions with power-law relationships, with the flux distribution power-law index being α = -1.92 and the area distribution power-law index being $\gamma = -2.20$. As for emergence and cancellation, coalescence also appears to be a scale-free process. The fact that there is no size dependence for coalescence indicates that the process is driven by plasma flows. Integrating over the coalescence flux distribution I find a total of 5.8×10^{-17} coalescences cm^{-2} day^{-1} (3.6×10^{6} day^{-1} over the whole surface) occurring in all identified features with flux between $10^{16} - 10^{23}$ Mx. Only 9.2×10^{-22} coalescences cm^{-2} day^{-1} ($\approx$ 60 per day over the whole surface) from features with flux above 10^{20} Mx.

For the fragmenting features flux and area histograms I do not find a single distribution with a power-law relationship. Comparing the SOHO/MDI full-disk and the Hinode/NFI results there are clearly not enough small-scale fragmentations detected in the full-disk data for there to be a continuous relationship. This may be because the smallest scale features fragmenting in the SOHO/MDI data go below the resolution, so are not detected. The shapes of the Hinode/NFI and SOHO/MDI full-disk are similar, so if this is the case for SOHO/MDI data then it is likely that some of the fragmentation occurring at the smallest-scale in Hinode/NFI also goes undetected. As there is no power-law distribution I estimate the frequency of fragmentation from the Hinode/NFI data. I find 1.6×10^{-16} fragmentations cm^{-2} day^{-1}, which is 9.7×10^{6} fragmentations day^{-1} over the whole surface.

Both the fragmentation and coalescence histograms for flux, area and age versus frequency show that small, young features are more likely to interact. As the features get older they interact less, most likely because they are trapped by strong plasma flows in intergranular lanes and vertices.

These results show that the large-scale solar cycle plays a complex role in the surface processes features undergo. The fact that the number of ephemeral region emergences has an anti-phase variation has a knock on effect in the number of features which are available to undergo surface processes. Also the contribution of decaying active regions injecting features, with higher flux density, into the network has been clearly seen to have an effect on the surface processes.

It was speculated in the previous chapter as to the reason for the decrease in slope between the distribution of emerging bipole fluxes (slope = -2.49) and the flux of the features at any instant present on the Sun (slope = -1.90). I investigated if this decrease in slope was just through the features having a lifetimes of more than one frame, or if it was due to surface processes. The conclusion is that if it was not for surface processes then tracked features would have significantly longer lifetimes. Also the decrease in slope indicates an increase in the number of features at larger fluxes. This is consistent with the results found in this chapter showing that small-scale features are continually being influenced by surface processes. The fact that coalescence is the most numerous process, helps to reduce the slope by producing features with larger fluxes.

Chapter 9

The Quiet-Sun As a Source For Coronal Heating

Approximately 70 years ago it was discovered that the outer atmosphere, namely the chromosphere and corona, were much hotter than the photosphere below them. Rather than being a gradual decrease in temperature from the photosphere to the corona, as one might expect, there is a steep temperature increase from the top of the chromosphere, through a region known as the transition region, up to the base of the corona. In the years that have followed, scientists have proposed numerous mechanisms which could provide the vast amount of energy required to produce this steep temperature gradient and maintain the chromospheric and coronal temperatures of between ≈10000 K and ≈ million K. Any proposed mechanism needs to provide sufficient energy to balance the losses from both the chromosphere and corona, as well as drive the solar wind. To keep the outer atmosphere in the quiet-Sun heated it is estimated that a power of the order 10^5 ergs s^{-1} cm^{-2} is needed uniformly over the surface of the Sun (Athay, 1976; Withbroe and Noyes, 1977).

There have been many mechanisms investigated over the years including waves, either acoustic or MHD, and current dissipation through magnetic reconnection (Narain and Ulmschneider, 1990, 1996; Browning, 1991; Narain and Kumar, 1993; Narain and Agarwal, 1994; Galsgaard and Nordlund, 1996; Hood et al., 1997; Sturrock, 1999; Sakai et al., 2001). It is likely, however, that rather than a single process being responsible for all the heating, many processes are acting simultaneously both globally and locally. This chapter is primarily interested in heating through magnetic reconnection at small-scale levels as this will be induced by the emergence and cancellation which has been detected in the previous chapters.

Levine (1974) was the first to introduce the idea that the reconnection and reconfiguration of magnetic fields could be the mechanism for heating the upper atmosphere. This idea became popular following a series of papers by Parker in the early 80's (Parker, 1981, 1983a,b, 1988a, 1989). The discovery of the dynamic nature of the magnetic carpet further promoted this idea (Schrijver et al., 1997; Title and Schrijver, 1998; Tarbell et al., 1999; Moore et al., 1999).

Energy release in the quiet-Sun is believed to be predominantly through small-scale impulsive events known as nano-flares which are instigated by magnetic reconnection (Porter et al., 1987; Parker, 1988b; Hudson, 1991). Each micro-flare event has energy in the range $10^{26} - 10^{27}$ ergs and nano-flares have energy in the range $10^{23} - 10^{25}$ ergs (Parker, 1991).

A topic of interest regarding micro and nano-flares is their frequency of occurrence as a function of energy. For quiet-Sun events to be a major contributor to the heating of the quiet-corona their power law

exponent, of the distribution of events, needs to be greater than 2 (Hudson, 1991). In the last 10 years various estimates have been done over various energy ranges. Initially the results seemed to conclude that slope of the distribution of events was between 1.5-1.6, over the energy range $10^{27} - 10^{31}$ ergs, indicating that micro-flares could only be contributing to 1/5 of the total power required to heat the quiet upper atmosphere (Crosby et al., 1993; Shimizu, 1995). For small-scale nano-flares to have any significance for quiet-coronal heating their frequency would need to drastically increase as the energy decreased. When observations of events were extended down to the nano-flare range of energies ($10^{23} - 10^{26}$ ergs), it was found that the distribution followed a power law with exponent of between 2-2.6 (Krucker and Benz, 1998; Parnell and Jupp, 2000). This is highly suggestive that the power released in nano-flare events is a large contributor to quiet-Sun coronal heating.

Following the work of Priest et al. (1994), Parnell et al. (1994) and Longcope (1996) which indicate that the cancellation or emergence of new flux can lead to reconnection and a release of magnetic energy in the corona, in this chapter, I estimate a lower bound on the amount of energy injected into the quiet-Sun atmosphere as a result of emerging and cancelling events causing reconnection and reconfiguration in the surrounding magnetic field. Using the emerging and cancelling events already found in both the Hinode/NFI (clumping data) and the SOHO/MDI full-disk data I estimate an amount of energy associated with each emergence and cancellation and plot the distribution. Some fraction of this energy could be used to heat the corona. Here the exact details of the heating mechanism is not considered, only that there will be an amount of energy coming from emerging and cancelling features in some way.

9.1 Estimating Energy From Small-Scale Emerging and Cancelling Events

To estimate how much energy each small-scale emergence contains, I use a simple model. First I find the absolute flux and area of each feature in the emerging event, at the time of the peak emerging event flux, and use this to determine a mean peak flux and mean peak area of the emerging event features. Then I find the mean magnetic field strength by dividing the mean peak flux of all the features by the mean peak area of all the features. The separation of the bipole at the time when the peak flux occurs is also determined. If there are more than two opposite-polarity features in an emerging event then I take the mean distance between the all the opposite-polarity components. The peak flux and area of the emerging and cancelling events are already known in Chapter 5 and 6 for the Hinode/NFI data and in Chapter 7 for the SOHO/MDI full-disk data. Here, I only use the Hinode/NFI clumping data and use only the emergences detected by the Tracked Bipolar method (§ 4.1.2) in the clumping data as this is the way emergences were detected in the SOHO/MDI data, in order to compare the distributions of the energy.

Similar characteristics are found for the cancelling events, except the total flux lost and the combined mean area of the opposite-polarity features (during cancellation) is used for cancelling events, rather than the peak flux and peak area. In the case of cancellation events, the separation is defined as the separation which the opposite-polarity features have when they begin to mutually lose flux.

To estimate an energy associated with emerging or cancelling events, it is assumed that the loops have

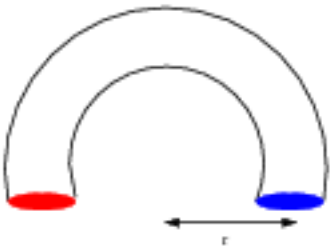

Figure 9.1: Illustration showing the semi-circular loop geometry that emerging and cancelling features are assumed to have, with r being half the separation of the features.

semi-circular geometry with the radius of the magnetic loop being half the mean separation between the opposite-polarity features (Figure 9.1). Therefore the loop length is given by πr. The magnetic energy contained in this loop, connecting the opposite-polarity features, is defined as

$$\int_V B^2 dV = < B >^2 < A > \pi r,$$

with the energy given in ergs assuming the field strength is in Gauss (Mx cm^{-2}), the area in cm^2 and the radius in cm. Once the peak energies of emergence and cancellations are found for all data sets, I plot the resulting distributions.

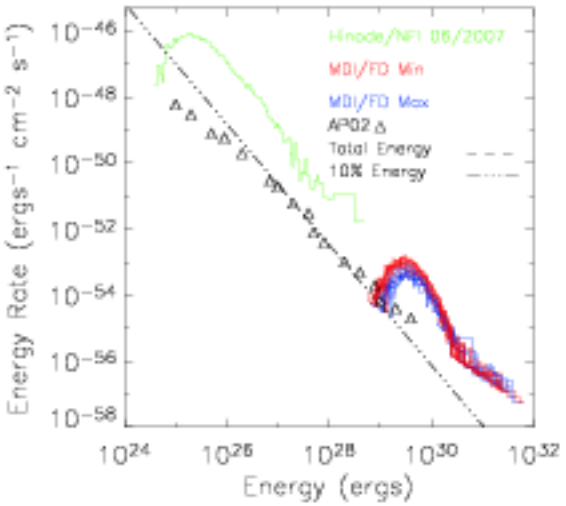

Figure 9.2: Log-log plot of histograms of peak energy of emerging events from Hinode/NFI (green), SOHO/MDI full-disk minimum (red, December 1996-October 1997 and November 2005-December 2008) and SOHO/MDI full-disk maximum (blue, February 1999-November 2004). The power law (dashed line) has a power law index of ζ= -1.83. Over-plotted is the nano-flare distribution (triangles) found by Aschwanden and Parnell (2002). The dot-dashed line shows the distribution of 10% of the energy due to emergence.

Figure 9.2 shows the distributions of the peak energies associated with all emerging events detected by the Tracked Bipolar method in the clumping data in both Hinode/NFI (green) and SOHO/MDI full-disk

December 1996-October 1997 and November 2005-December 2008 (red) and SOHO/MDI full-disk February 1999-November 2004 (blues). Using LADFIT with the Hinode/NFI, SOHO/MDI full-disk December 1996 and SOHO/MDI full-disk December 2001 results, it can be seen that the peak energy of emergences detected by the Tracked Bipolar method and features identified by the clumping method in Hinode/NFI and SOHO/MDI full-disk follow a single power law (dashed-line in Figure 9.2) of the form:

$$P(E) = \frac{N}{E_\circ}\left(\frac{E}{E_\circ}\right)^\zeta,$$

where E is the energy of the event in ergs, $E_\circ$ is the lower bound of energy = 4×10^{24} ergs, N is the number of events with $N = 1.55 \times 10^{-20}$ cm^{-2} s^{-1} and the power-law index being $\zeta = -1.83$. The values of N and ζ are found using the December 1996, December 2001 and Hinode data sets.

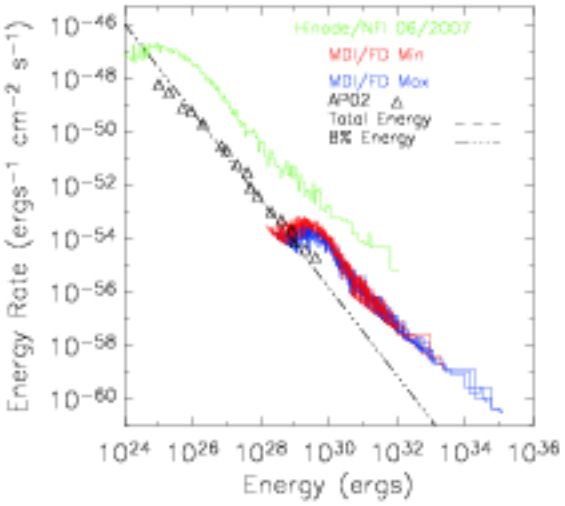

Figure 9.3: Log-log plot of peak energy per cancellation from Hinode/NFI (green), SOHO/MDI full-disk minimum (red, December 1996-October 1997 and November 2005-December 2008) and SOHO/MDI full-disk maximum (blues, February 1999-November 2004). The power law (dashed line) as power law index of ζ= -1.65. Over-plotted is the nano-flares distribution (triangles) found by Aschwanden and Parnell (2002). The dot-dashed line shows the distribution of 8% of the energy due to cancellation.

Despite being previously suggested that the energy distribution would have a slope greater than 2 (Krucker and Benz, 1998; Parnell and Jupp, 2000) I have found a slope less than 2. This, in part, is likely to be due to the method of estimating the amount of energy in emerging events. Comparing my distribution in Figure 9.2, to one associated with nano-flares, allows me to estimate the percentage of free magnetic energy required from emerging events to be converted to heat to produce the required nano-flare distributions power-law. The distribution I choose to make the comparison is the nano-flare distribution found by Aschwanden and Parnell (2002), which has a power-law with index ζ= -1.54. This is plotted as the triangles in Figure 9.2. It can be seen that in the paper by Aschwanden and Parnell (2002), other results found for flares over various energy ranges share similar distributions, I chose the Aschwanden and Parnell (2002) results as they covered the energy range associated with small-scale emergence energy. The dot-dashed line plotted in Figure 9.2 shows the best fit to the nano-flare distribution which I estimate manually by taking

a percentage of the emergence energies distribution. By trial and error I find the best fit to the nano-flare distribution occurs when just 10% of the peak emerging energy is assumed as being free energy to go into heating.

It is also worth bearing in mind that emergence is not the only source of energy and that also cancellation and surface reconfiguration of the field will contribute. We will see shortly how incorporating cancelling together with emerging events affects the energy distribution found (Figure 9.4). What it highlights, though, is that even if the mechanisms to convert this magnetic energy into heat are not efficient, only a small fraction is required to satisfy the energy needs of the quiet-Sun corona.

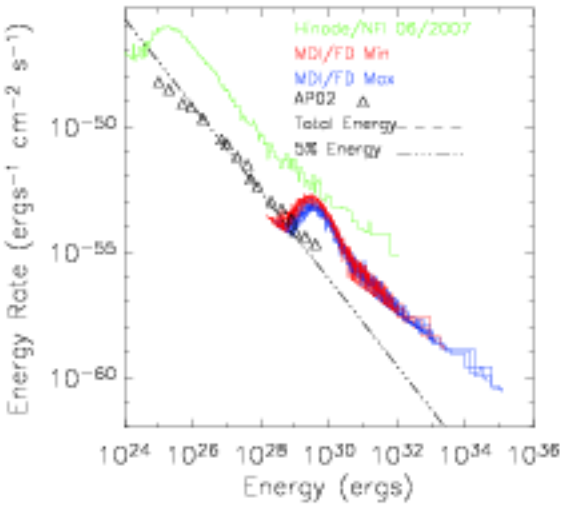

Figure 9.4: Log-log plot for both the peak flux emerging events and the flux lost during cancelling events from Hinode/NFI (green), SOHO/MDI full-disk minimum (red, December 1996-October 1997 and November 2005-December 2008) and SOHO/MDI full-disk maximum (blues, February 1999-November 2004). The power law (dashed line, found using LADFIT with the Hinode/NFI, December 1996 and December 2001 results) has a power law index of ζ= -1.73. The dot-dashed line shows the distribution of 5% of the energy due to emergence and cancellation events combined.

Similarly Figure 9.3 shows a log-log plot of the histograms of cancelling event energies from cancelling events detected in both the Hinode/NFI data and the SOHO/MDI full-disk data. The cancelling energy distributions also follow a single power law (dashed line). Using LADFIT with the Hinode/NFI, SOHO/MDI full-disk December 1996 and SOHO/MDI full-disk December 2001, I find the power law index to be ζ= -1.65, E_0 is now 6×10^{23} ergs and $N = 1.03 \times 10^{-20}$ cm^{-2} s^{-1}. Again the nano-flare distribution (triangles) found by Aschwanden and Parnell (2002) is over-plotted as triangles. Again I find that the energy distribution has a slope of less than 2, even more so than the energy distribution from just the emerging events. The dot-dashed line plotted in Figure 9.3 shows the best fit to the nano-flare distribution which I estimate manually if 8% of the energy from cancellation was free for heating.

Finally, as both emergence and cancellation are occurring simultaneously on the surface, I combine the emergence distribution (Figure 9.2) with the cancelling distribution in Figure 9.3, to find an estimate of the total energy (Figure 9.4). I find the power law relationship using using LADFIT with the Hinode/NFI,

SOHO/MDI December 1996 and December 2001. The combined distribution of emergence and cancellation has a power law index ζ = -1.73, $E_\circ = 6 \times 10^{23}$ ergs and N =5.1 $\times 10^{-20}$ cm^{-2} s^{-1}, which is plotted as the dashed line in Figure 9.4. The nano-flare distribution found by Aschwanden and Parnell (2002) is once more plotted as triangles. I find that just 5% of the energy from the combined energies of the emergence and cancelling would need to be free for heating to fit the nano-flare distributions (dot-dashed line), respectively. Not surprisingly the combined distribution slope for both emerging and cancelling events is still less than 2. In order for the quiet-Sun to be heated by mostly small-scale events it is clear there would need to be injection of energy at the smallest flux scales. Possibly the energy due to surface processes reconfiguring the fields could provide this, but obviously this will need to be investigated further.

To find the total energy produced due to all cancellations and emergences I use the distribution $P(E)$ from above, multiplied by energy then integrated across the energy range of interest:

$$E_{\rm tot} = \int_{E_1}^{E_2} P(E) E dE = \frac{N E_0}{2+\zeta} \left[(E/E_0)^{2+\zeta} \right]_{E_1}^{E_2}.$$

Substituting in the values of $E_\circ$, N and ζ from above, I find that emergence and cancellation events individually producing energy of between 10^{24}-10^{35} ergs contribute a total of 1.21×10^{6} ergs cm^{-2} s^{-1}. This is considerably larger than the 10^{5} ergs s^{-1} cm^{-2} that Athay (1976); Withbroe and Noyes (1977) estimated is needed uniformly over the surface to heat the quiet-Sun outer atmosphere.

I have shown that only a small percentage of energy from small-scale emerging events and cancellations, would be required to account for the nano-flare distribution found by Aschwanden and Parnell (2002). The energy found here is likely to be a lower bound on what the quiet-Sun can produce, as the continual movement of features will also drive reconnection and energy release (Close et al., 2004, 2005).

Chapter 10

Summary and Future Work

10.1 Summary

The quiet-Sun is comprised of two types of features: network fields and intranetwork (IN) fields. The network fields reside in intergranular lanes and vertices with fluxes of a few times $10^{18} - 10^{19}$ Mx. It is sustained by ephemeral regions, decaying active regions and the coalescence of IN fields (Schrijver et al. 1997). Within supergranular cells there exist IN fields, observed as mixed-polarity magnetic features with a typical size of $10^{16} - 10^{18}$ Mx (Livingston and Harvey, 1975; Zirin, 1985, 1987; Keller et al., 1994; Wang et al., 1995). There are four key processes that can effect flux features: emergence; fragmentation; merging and cancellation (Livi et al., 1985; Schrijver et al., 1997; Parnell, 2001).

In this thesis I have examined the details of these four key processes for small-scale magnetic features identified in Hinode/NFI and SOHO/MDI full-disk. In particular, I examined emergence, fragmentation, coalescence and cancellation in features with fluxes down to just below 10^{16} Mx and over an entire solar cycle.

Features are identified and tracked in the Hinode/NFI and SOHO/MDI data sets. I applied two feature identification methods to the Hinode/NFI data which define features in different ways, in order to gauge the differences between the methods. The clumping identification method identifies features as groups of same-sign contiguous pixels that have absolute flux above a given lower cutoff (2σ) (Parnell, 2002; Parnell et al., 2009). The downhill identification method, defines features as groups of contiguous same-sign pixels with flux above a lower cutoff (also equal to 2σ) that are singly peaked, i.e., they are formed by dividing the features found using the clumping method along saddle lines (Welsch and Longcope, 2003).

Although the characteristics such as mean peak flux and area of features are different between the methods the overall flux detected is the same. When deciding which feature identification method to use the impetus should be on what is going to be studied. The downhill method identifies the structure of flux within flux regions, however these tend to be transient, making it difficult to follow feature evolution. Applying the downhill method to data with increased resolution has the effect of identifying more structure (flux peaks) within larger flux features (i.e., there will be a reduction in the number of larger features identified). This is ideal if the aim of the feature identification is to gain insight into the complex structure of large flux features, such as sunspots. However, if the aim is to compare features from different instruments with different resolution, then the clumping method is more suitable as the larger flux massifs it identifies are much less dependent on instrument sensitivity. With this in mind only the clumping feature identification method was applied to the SOHO/MDI full-disk data sets, as I wished to compare the features identified in

both the Hinode/NFI and SOHO/MDI full-disk data sets.

In the Hinode/NFI and SOHO/MDI full-disk data I identified tracked features over the range of peak fluxes $4 \times 10^{18} - 10^{23}$ Mx and the range of areas 0.04-10^3 Mm^2. It is found that the fluxes of all tracked features at any instant, identified by the clumping method in both Hinode/NFI and SOHO/MDI full-disk, are part of a continuously decreasing distribution with a power-law index of -1.90.

Three emergence detection methods were developed in this thesis: the Bipole Comparison (BC) method, the Tracked Bipolar (TB) method and the Tracked Cluster (TC) method. The BC method is applied to untracked data, whilst the TB and TC methods are applied to tracked features. Both the BC and TB methods were designed to detect bipoles but the TC method was designed to detect clusters.

All three were applied to the Hinode/NFI data on both the downhill and the clumping data sets. For the IN features, cluster emergences are found to be common, but it is difficult to say if they could be resolved as bipoles at higher resolutions or if they are a single bipole shredded by convection as they emerge. I find that the different feature identification methods and the emergence detection methods have a varying effect on the structure and characteristics of the emerging events detected. Whether or not the features are tracked before emergence is detected seems to be the greatest influencing factor. Overall, none of the flux detection methods are perfect, as is apparent on visual inspection of data. There are still emergence events that all three methods miss, although these cases are rare, and also each method identifies some events that are questionable. Clearly more work needs to be done to determine which of the emergence detection methods most accurately detect emerging events.

Only the Tracked Bipolar emergence detection method was applied to the SOHO/MDI full-disk data. In both data sets I detect bipoles over the range $5.4 \times 10^{18} - 10^{23}$ Mx in flux and 0.3- 10^3Mm^2 in area. When a log-log plot of the histograms of all emerging event peak fluxes for those events detected here plus active regions found by Harvey (1993) and Howard (1989) is plotted, it is found that all emerging events are part of a smoothly decreasing distribution that spans almost 7 orders of magnitude in flux and 18 orders of magnitude in frequency. This distribution has a power-law relationship with index -2.50.

Since the power-law index of the emerging flux distribution is greater than -2 this suggests that most of the flux on the Sun does not come from large-scale features, but rather small-scale features. The flux emergence rate of small-scale features with fluxes in the range $10^{18} - 10^{20}$ Mx is 63.9 Mx cm^{-2} day^{-1}, or 3.9×10^{24} Mx day^{-1} over the whole solar surface. Those events with peak fluxes from $10^{20} - 10^{23}$ Mx produce just 0.7 Mx cm^{-2} day^{-1} or 4.2×10^{22} Mx day^{-1} over the whole solar surface. I find the total emergence rate of emerging events from $10^{18} - 10^{23}$ Mx in flux to be 2.2×10^{-18} cm^{-2} day^{-1} (1.3×10^{8} regions per day assuming uniform emergence over the whole surface). Again the majority of emergences come from the lower end of the scale with only 2.2×10^{-21} cm^{-2} day^{-1} (131 events per day over the whole surface) occurring above 10^{20} Mx.

Physically a power-law distribution of, for instance, flux implies that the fluxes are produced by a mechanism that is scale free. That is the physical process(es) that produce the smallest magnetic features are the same as the process(es) that produce all other features, including the largest features. Parnell et al. (2009) speculated that the distribution of magnetic feature fluxes was produced by one of two mechanisms. Either (i) all magnetic features are created by a solar dynamo that acts in the same way on all scales or

(ii) magnetic features are created by dynamo action that is not the same on all scales but, after emergence into the solar atmosphere, surface processes (e.g. fragmentation, coalescence and cancellation) dominate and create a single distribution of feature fluxes. In order to distinguish between these two mechanisms, it is obviously essential to determine whether the distribution of fluxes of newly emerged features follows a power law or not. The work that we have presented, here, strongly suggests that both the distribution of fluxes from all features present at any instant follows a power law with slope -1.90 and the distribution of fluxes from newly emerged features follows a power law with a slope of -2.50. This provides considerable support for the first mechanism, namely that all magnetic features are created by a solar dynamo that acts in the same way on all scales.

It is obvious that there is a decrease in slope between the distribution of emerging bipole fluxes and the flux of all features at any instant present on the Sun. Indeed it was found that this reduction in slope was due to both features having lifetimes of more than one frame and the effects of fragmentation, coalescence and cancellation occurring on practically all the features in the magnetic carpet anytime after they are born.

In both the Hinode/NFI and the SOHO/MDI full-disk data sets, fragmentation, coalescence and cancellation were investigated. When investigating the surface processes it was found that features are more likely to undergo coalescence first after emergence. This is thought to be due to the fact that the flux tubes which emerge are composed of a number of thin flux tubes. For some reason in the convection zone a large flux tube splits into smaller bundles of flux which rise separately but coalesce back into the large flux tubes once they are on the surface. This behaviour has also been seen in active regions (Vrabec, 1974; Solanki, 2003).

The behaviour of fragmenting and coalescing features in both the Hinode/NFI and SOHO/MDI data is similar, despite being on different size scales of flux. The mean flux and area of the features that coalesce are found to be smaller than those features which fragment. Most fragmentations involve one feature splitting into two, likewise most coalescences involve two features merging into a single feature.

The distribution relating frequency of coalescing events versus the original flux of coalescing parent features, follows a power-law distribution with slope -1.92. From this I estimate a total of 5.8×10^{-17} coalescences cm^{-2} day^{-1} (3.6×10^{6} day^{-1} over the whole surface) occurring in all identified features with flux between $10^{16} - 10^{23}$ Mx. Only 9.2×10^{-22} coalescences cm^{-2} day^{-1} (≈ 60 per day over the whole surface) occur in features with flux above 10^{20} Mx.

There is not a clear power law distribution relationship between the flux of the parent fragmenting feature and the frequency of the fragmentation. Comparing the SOHO/MDI full-disk and the Hinode/NFI results there are clearly not enough fragmentations detected at the smallest observable flux scales (10^{17} Mx) in the full-disk data, for there to be a power-law distribution. This may be because the smallest scale features fragmenting in the SOHO/MDI data go below the resolution, so are not detected. The shapes of the Hinode/NFI and SOHO/MDI full-disk are similar, so if this is the case for SOHO/MDI data then it is likely that some of the fragmentation occurring at the smallest-scale in Hinode/NFI also goes undetected. I still provide an estimate of the fragmentation frequency using the Hinode/NFI results from features with fluxes in the range $5 \times 10^{18} - 5 \times 10^{19}$ Mx. The frequency of fragmentation is 6.6×10^{-16} cm^{-2} day^{-1}, which is 4.0×10^{7} fragmentations per day over the whole surface.

The final surface process to be investigated was cancellation. It is found that the cancellation events

detected in Hinode/NFI and SOHO/MDI full-disk data behave in a similar manner just on different flux scales. Cancellation is found to occur any time after birth. It can be seen that the mean flux loss per cancellation event is dependent on the original flux of the features.

A log-log plot of the histograms for the flux lost per cancelling events (detected in both Hinode/NFI and SOHO/MDI full-disk), shows a power-law relationship with slope -2.10. As in the case of emergence, the process of cancellation appears to be scale free and the slope is greater than 2 indicating that numerous small-scale features are cancelling the majority of flux on the Sun. The cancellation slope is much closer to the power-law index that is found for all the tracked feature's peak flux as opposed to the emerging event's peak flux. This is not surprising as the process of cancellation can occur at any point in a feature's life once it has been subjected to numerous surface processes.

I find the total cancellation rate, for features with flux between $10^{18} - 10^{23}$ Mx, to be 7.6×10^{-16} cm^{-2} day^{-1}, which is 4.5×10^{7} cancellations per day over the whole surface. Only in 3.0×10^{-20} cm^{-2} day^{-1} ($\approx$ 1856 cancelling events) cases of cancellations is there more than 10^{20} Mx of flux lost per event, i.e., numerous small-scale/low flux loss cancellations make up the majority of the cancelling events which occur. Indeed on analysing the average flux loss per event it is found that when features cancel they typically only lose 50% of their original flux. The flux cancellation rate of small-scale features with flux loss in the range $10^{18} - 10^{20}$ Mx is 50.5 Mx cm^{-2} day^{-1} (3.1×10^{24} Mx day^{-1} over the whole solar surface). Those events with peak flux loss in the range $10^{20} - 10^{23}$ Mx lose a total 16.7 Mx cm^{-2} day^{-1} (during active periods) (1.0×10^{24} Mx day^{-1} over the whole solar surface).

The distribution relationships for the surface processes indicate that young features are more likely to interact. As the features get older they interact less probably because they are trapped by strong plasma flows in intergranular lanes and vertices.

In this thesis I also investigated how the four key surface processes vary throughout cycle 23 using SOHO/MDI full-disk. It is found that the emergence rate of bipoles varied in anti-phase with the solar cycle by a factor of 3.4. The variation in the number of small-scale cancelling events also shows an anti-phase relationship varying by a factor of 3.1 over the cycle. The number of cases fragmentations and coalescences occurring in small-scale features both have an anti-phase variation, decreasing by factors of 2.4 and 2.2, respectively over the cycle. Not surprisingly therefore the number of network features detected throughout the cycle also exhibits an anti-phase variation over the solar cycle by a factor of 1.9. The variation in the number of network features is a results of both the fact that the number of fragmentations and coalescences do not vary in anti-phase by as much as emergence does and because there is an increase in the number of active regions. Thus the number of network features due to the dispersal of decaying active regions will increase in-phase with the solar cycle

When investigating the variation of feature flux over cycle 23 it is found that the flux of emerging bipoles showed no cyclic variation. However, investigating the mean peak flux of the tracked small-scale features showed that there appears to be an in-phase relationship with the solar cycle by a factor of 1.4 (the mean peak field strength also showed an in-phase variation by a factor of 1.3). The flux for small-scale features which fragment vary in-phase by factors of 1.7, whilst the flux for small-scale coalescing features vary in phase with the solar cycle by factor of 2.4. Finally the mean flux lost per cancelling event in small-scale

features varies in-phase with cycle 23 by a factor of 1.2.

Earlier in this thesis the question was asked whether decaying active regions retained the higher field strength when they migrated into the network or are the dispersed active regions indistinguishable from the network? The fact that the mean flux and the field strength of the network features varies in-phase with the solar cycle, whilst the mean bipole flux does not change, and the processes of fragmentation and coalescence retain their relationship with respect to one another, indicates that there is an increases in network features whose origin is from the decay of active regions throughout the solar cycle. This increase in flux of network features obviously has a knock on effect for the fluxes of features undergoing surface processes.

Obviously these results reveal two different aspects of the behaviour of small-scale features throughout the solar cycle. The final aspect to be looked at is the total flux emergence and cancellation rates. It is not surprising that the total flux emergence rate varies in anti-phase with the solar cycle (by a factor of 1.9), considering the number of events varies in this way and there is no cyclic variation in the mean flux of emerging events. The variation in the total flux lost through cancellation is in anti-phase by a factor of 3.2. This is clearly most dependent on the number of cancelling events taking place.

The results in this thesis show that the large-scale solar cycle plays a complex role in the surface processes features undergo. The fact that the number of ephemeral region emergences has an anti-phase variation to the solar cycle has a knock on effect in the number of features which are available to undergo surface processes. Also the contribution of decaying active regions, during more active periods, injecting features, with higher flux density, into the network has been seen to have an effect on the surface processes.

The final aspect of this thesis estimated a lower bound on the amount of energy injected into the quiet-Sun atmosphere as a result of emerging and cancelling events causing reconnection and reconfiguration in the surrounding magnetic field. Using the emerging and cancelling events already found in both the Hinode/NFI (clumping data) and the SOHO/MDI full-disk data I estimate the amount of energy associated with each emergence and cancellation and plot the distribution assuming some fraction of this energy could be used to heat the corona. Here the exact details of the heating mechanism is not considered, only that there will be an amount of energy coming from emerging and cancelling features in some form. I found that the energies from both emerging and cancellation events versus frequency follows a power law relationship with slope -1.73. Comparing this to the distribution for nano-flares Aschwanden and Parnell (2002) found, I find that just 5% of the energy from emergence and cancellation events would be needed to fulfill the nano-flare energy requirements.I find that emergence and cancellation events individually producing energy of between 10^{24}-10^{36} ergs contribute a total of 1.21×10^{8} ergs cm^{-2} s^{-1}. Considering that there are many other actions in the magnetic carpet, such as fragmentation and coalescence which are capable of generating energy in the magnetic field it is likely that there is a large amount of energy in the magnetic carpet free for heating.

This thesis has provided an insight into many aspects of the small-scale carpet which were previously unknown. However, there are still many questions to be investigated and much work to be done before we are even close to fully understanding the complex behaviour of magnetic features in the photosphere. The next section briefly discusses some suggested directions to develop this work and the understanding of the

magnetic carpet, further.

10.2 Future Work

The work presented here has provided an insight into the behaviour of small-scale features observed in Hinode/NFI and SOHO/MDI. Throughout this thesis I have had to make assumptions regarding parameters used. For the feature identification and tracking I specify a flux cutoff, area cutoff, data cadence and minimum lifetime criteria. Obviously varying any of these parameters will have some effect of the results. It would be interesting to fully investigate the influence each of these parameters has on the features identified, their characteristics and the knock on effect when further algorithms are used. Each of the algorithms for examining emergence, emergence evolution, fragmentation, coalescence, cancellation and energy also have various criteria that are specified by me, usually after trial and error. Again varying the various criteria will influence the results but to what degree is unknown. It would be useful to document the differences in the results as the parameters varied, to see if any of the parameters is dominant as a guideline for others who wish to analyse characteristics of features in magnetograms.

For the Hinode/NFI data only one data set was available for analysis, so I was unable to investigate the behaviour of the current smallest observable features throughout the solar cycle. It would be interesting to find if the features of order 10^{16}-10^{19} Mx, in Hinode/NFI, exhibit a similar variation to the features of order 10^{18}-10^{23} Mx, identified in SOHO/MDI.

At the moment I draw my conclusions on the emergence evolution and origin of small-scale features from comparing data from two instruments: Hinode/NFI and SOHO/MDI. In February this year Solar Dynamics Observatory (SDO) was launched which has the instrument Helioseismic and Magnetic Imager (HMI) aboard. One of the main aims for HMI is further understanding of magnetic field generation and its role in structuring the atmosphere of the Sun. The HMI instrument will extend the capabilities of the SOHO/MDI instrument with continual full-disk coverage at higher spatial resolution by producing: i) 1 arc-second resolution full-disk Doppler velocity image and line-of-sight magnetic flux image at least every 50 seconds and ii) 1 arc-second resolution full-disk vector-magnetic images of the longitudinal solar magnetic field at least every 90 seconds. Using magnetograms from this instrument in comparison to Hinode/NFI and SOHO/MDI, would help to further validate the results and conclusions of this work as we should be able to cover this range of fluxes using just a single telescope.

An obvious next step for the work presented here would be to provide a similar examination of a large number of active regions throughout the solar cycle. It is clear there is some sort of relationship between small-scale features and active regions, but to fully understand it more work needs to be done.

Bibliography

T. E. Abdelatif. Heating of coronal loops by phase-mixid shear Alfven waves. *Astrophys. J.*, 322:494–502, November 1987. doi: 10.1086/165745.

M. J. Aschwanden and C. E. Parnell. Nanoflare Statistics from First Principles: Fractal Geometry and Temperature Synthesis. *Astrophys. J.*, 572:1048–1071, June 2002. doi: 10.1086/340385.

A. S. Assis and J. Busnardo-Neto. Cherenkov damping of surface waves. *Astrophys. J.*, 323:399–405, December 1987. doi: 10.1086/165837.

R. G. Athay, editor. *The solar chromosphere and corona: Quiet sun*, volume 53 of *Astrophysics and Space Science Library*, 1976.

R. G. Athay and O. R. White. Chromospheric and coronal heating by sound waves. *Astrophys. J.*, 226: 1135–1139, December 1978. doi: 10.1086/156690.

H. W. Babcock. The Solar Magnetograph. *Astrophys. J.*, 118:387–+, November 1953. doi: 10.1086/145767.

J. Bahng and M. Schwarzschild. Lifetime of Solar Granules. *Astrophys. J.*, 134:312–+, September 1961. doi: 10.1086/147160.

C. S. Barth and S. H. B. Livi. Magnetic Bipoles in Emerging Flux Regions on the Sun. *Revista Mexicana de Astronomia y Astrofisica, vol. 21*, 21:549–+, November 1990.

J. M. Beckers and E. H. Schröter. The Intensity, Velocity and Magnetic Structure of a Sunspot Region. I: Observational Technique; Properties of Magnetic Knots. *Solar Phys.*, 4:142–164, June 1968. doi: 10.1007/BF00148076.

R. Born. First phase of active regions and their relation to the chromospheric network. *Solar Phys.*, 38: 127–131, September 1974. doi: 10.1007/BF00161830.

N. S. Brickhouse and B. J. Labonte. Mass and energy flow near sunspots. I - Observations of moat properties. *Solar Phys.*, 115:43–60, March 1988. doi: 10.1007/BF00146229.

M. P. Brouwer and C. Zwaan. Sunspot nests as traced by a cluster analysis. *Solar Phys.*, 129:221–246, October 1990. doi: 10.1007/BF00159038.

P. K. Browning. Mechanisms of solar coronal heating. *Plasma Physics and Controlled Fusion*, 33:539–571, June 1991. doi: 10.1088/0741-3335/33/6/001.

V. Bumba and R. Howard. Large-Scale Distribution of Solar Magnetic Fields. *Astrophys. J.*, 141:1502–+, May 1965. doi: 10.1086/148238.

F. Cattaneo. On the Origin of Magnetic Fields in the Quiet Photosphere. *Astrophys. J. Letts.*, 515:L39–L42, April 1999. doi: 10.1086/311962.

F. Cattaneo and D. W. Hughes. Solar dynamo theory : Solar dynamo theory: a new look at the origin of small-scale magnetic fields. *Astronomy and Geophysics*, 42(3):030000–3, June 2001. doi: 10.1046/j.1468-4004.2001.42318.x.

J. Chae, S. F. Martin, H. S. Yun, J. Kim, S. Lee, P. R. Goode, T. Spirock, and H. Wang. Small Mag-

netic Bipoles Emerging in a Filament Channel. *Astrophys. J.*, 548:497–507, February 2001. doi: 10.1086/318661.

J. Chae, Y.-J. Moon, H. Wang, and H. S. Yun. Flux Cancellation Rates and Converging Speeds of Canceling Magnetic Features. *Solar Phys.*, 207:73–85, May 2002.

D.-Y. Chou and H. Wang. The separation velocity of emerging magnetic flux. *Solar Phys.*, 110:81–99, March 1987. doi: 10.1007/BF00148204.

A. R. Choudhuri and P. A. Gilman. The influence of the Coriolis force on flux tubes rising through the solar convection zone. *Astrophys. J.*, 316:788–800, May 1987. doi: 10.1086/165243.

A. R. Choudhuri, M. Schussler, and M. Dikpati. The solar dynamo with meridional circulation. *Astron. Astrophys.*, 303:L29+, November 1995.

R. M. Close, C. E. Parnell, D. W. Longcope, and E. R. Priest. Recycling of the Solar Corona's Magnetic Field. *Astrophys. J. Letts.*, 612:L81–L84, September 2004. doi: 10.1086/424659.

R. M. Close, C. E. Parnell, D. W. Longcope, and E. R. Priest. Coronal Flux Recycling Times. *Solar Phys.*, 231:45–70, September 2005. doi: 10.1007/s11207-005-6878-1.

T. Corbard and M. J. Thompson. The subsurface radial gradient of solar angular velocity from MDI f-mode observations. *Solar Phys.*, 205:211–229, February 2002.

N. B. Crosby, M. J. Aschwanden, and B. R. Dennis. Frequency distributions and correlations of solar X-ray flare parameters. *Solar Phys.*, 143:275–299, February 1993. doi: 10.1007/BF00646488.

J. M. Davila. Heating of the solar corona by the resonant absorption of Alfven waves. *Astrophys. J.*, 317: 514–521, June 1987. doi: 10.1086/165295.

M. L. De Rosa and J. Toomre. Evolution of Solar Supergranulation. *Astrophys. J.*, 616:1242–1260, December 2004. doi: 10.1086/424920.

A. G. de Wijn, B. W. Lites, T. E. Berger, Z. A. Frank, T. D. Tarbell, and R. Ishikawa. Hinode Observations of Magnetic Elements in Internetwork Areas. *Astrophys. J.*, 684:1469–1476, September 2008. doi: 10.1086/590237.

C. E. Deforest. On Re-sampling of Solar Images. *Solar Phys.*, 219:3–23, January 2004. doi: 10.1023/B:SOLA.0000021743.24248.b0.

C. E. DeForest, H. J. Hagenaar, D. A. Lamb, C. E. Parnell, and B. T. Welsch. Solar Magnetic Tracking. I. Software Comparison and Recommended Practices. *Astrophys. J.*, 666:576–587, September 2007. doi: 10.1086/518994.

C. E. DeForest, Y. Katsukawa, T. Berger, T. Tarbell, H. J. Hagenaar, D. A. Lamb, C. E. Parnell, and B. T. Welsch. in preparation. *Solar Phys.*, 2009.

M. Dikpati and P. A. Gilman. Simulating and Predicting Solar Cycles Using a Flux-Transport Dynamo. *Astrophys. J.*, 649:498–514, September 2006. doi: 10.1086/506314.

V. Domingo, B. Fleck, and A. I. Poland. The SOHO Mission: an Overview. *Solar Phys.*, 162:1–37, December 1995. doi: 10.1007/BF00733425.

I. Domínguez Cerdeña, F. Kneer, and J. Sánchez Almeida. Quiet-Sun Magnetic Fields at High Spatial Resolution. *Astrophys. J. Letts.*, 582:L55–L58, January 2003. doi: 10.1086/346199.

I. Domínguez Cerdeña, J. Sánchez Almeida, and F. Kneer. The Distribution of Quiet Sun Magnetic Field Strengths from 0 to 1800 G. *Astrophys. J.*, 636:496–509, January 2006a. doi: 10.1086/497955.

I. Domínguez Cerdeña, J. Sánchez Almeida, and F. Kneer. Quiet Sun Magnetic Fields from Simultaneous Inversions of Visible and Infrared Spectropolarimetric Observations. *Astrophys. J.*, 646:1421–1435, August 2006b. doi: 10.1086/505129.

R. B. Dunn and J. B. Zirker. The Solar Filigree. *Solar Phys.*, 33:281–304, December 1973. doi: 10.1007/BF00152419.

B. R. Durney, D. S. De Young, and I. W. Roxburgh. On the generation of the large-scale and turbulent magnetic fields in solar-type stars. *Solar Phys.*, 145:207–225, June 1993. doi: 10.1007/BF00690652.

G. Einaudi and Y. Mok. Alfven wave dissipation in the solar atmosphere. *Astrophys. J.*, 319:520–530, August 1987. doi: 10.1086/165475.

M. Fligge, S. K. Solanki, and J. Beer. Determination of solar cycle length variations using the continuous wavelet transform. *Astron. Astrophys.*, 346:313–321, June 1999.

P. Foukal, K. Harvey, and F. Hill. Do changes in the photospheric magnetic network cause the 11 year variation of total solar irradiance? *Astrophys. J. Letts.*, 383:L89–L92, December 1991. doi: 10.1086/186249.

E. Friis-Christensen and K. Lassen. Length of the Solar Cycle: An Indicator of Solar Activity Closely Associated with Climate. *Science*, 254:698–700, November 1991. doi: 10.1126/science.254.5032.698.

K. Galsgaard and Å. Nordlund. Heating and activity of the solar corona 1. Boundary shearing of an initially homogeneous magnetic field. *J. Geophys.Res.*, 101:13445–13460, June 1996. doi: 10.1029/96JA00428.

H. J. Hagenaar. Ephemeral Regions on a Sequence of Full-Disk Michelson Doppler Imager Magnetograms. *Astrophys. J.*, 555:448–461, July 2001. doi: 10.1086/321448.

H. J. Hagenaar, C. J. Schrijver, A. M. Title, and R. A. Shine. Dispersal of Magnetic Flux in the Quiet Solar Photosphere. *Astrophys. J.*, 511:932–944, February 1999. doi: 10.1086/306691.

H. J. Hagenaar, C. J. Schrijver, and A. M. Title. The Properties of Small Magnetic Regions on the Solar Surface and the Implications for the Solar Dynamo(s). *Astrophys. J.*, 584:1107–1119, February 2003. doi: 10.1086/345792.

H. J. Hagenaar, M. L. De Rosa, and C. J. Schrijver. The Dependence of Ephemeral Region Emergence on Local Flux Imbalance. *Astrophys. J.*, 678:541–548, May 2008. doi: 10.1086/533497.

G. E. Hale. On the Probable Existence of a Magnetic Field in Sun-Spots. *Astrophys. J.*, 28:315–+, November 1908. doi: 10.1086/141602.

G. E. Hale and S. B. Nicholson. The Law of Sun-Spot Polarity. *Astrophys. J.*, 62:270–+, November 1925. doi: 10.1086/142933.

B. N. Handy and C. J. Schrijver. On the Evolution of the Solar Photospheric and Coronal Magnetic Field. *Astrophys. J.*, 547:1100–1108, February 2001. doi: 10.1086/318429.

J. Harvey. Solar Magnetic Fields - Small Scale. *Publications of the Astronomical Society of the Pacific*, 83: 539–+, October 1971. doi: 10.1086/129171.

J. W. Harvey. Observations of Small-Scale Photospheric Magnetic Fields. *Highlights of Astronomy*, 4: B223+, 1977.

J. W. Harvey, D. Branston, C. J. Henney, C. U. Keller, and SOLIS and GONG Teams. Seething Horizontal Magnetic Fields in the Quiet Solar Photosphere. *Astrophys. J. Letts.*, 659:L177–L180, April 2007. doi: 10.1086/518036.

K. L. Harvey. *Magnetic Bipoles on the Sun*. PhD thesis, Univ. Utrecht, 1993.

K. L. Harvey and S. F. Martin. Ephemeral Active Regions. *Solar Phys.*, 32:389–402, October 1973. doi: 10.1007/BF00154951.

K. L. Harvey and C. Zwaan. Properties and emergence of bipolar active regions. *Solar Phys.*, 148:85–118, November 1993. doi: 10.1007/BF00675537.

K. L. Harvey, J. W. Harvey, and S. F. Martin. Ephemeral active regions in 1970 and 1973. *Solar Phys.*, 40: 87–102, January 1975. doi: 10.1007/BF00183154.

K. L. Harvey, H. P. Jones, C. J. Schrijver, and M. J. Penn. Does Magnetic Flux Submerge at Flux Cancelation Sites? *Solar Phys.*, 190:35–44, December 1999. doi: 10.1023/A:1005237719407.

A. W. Hood, J. Ireland, and E. R. Priest. Heating of coronal holes by phase mixing. *Astron. Astrophys.*, 318:957–962, February 1997.

R. Howard. Magnetic Field of the Sun (observational). *Annual review of astronomy and astrophysics*, 5: 1–+, 1967. doi: 10.1146/annurev.aa.05.090167.000245.

R. F. Howard. The magnetic fields of active regions. I - Data and first results. *Solar Phys.*, 123:271–284, September 1989. doi: 10.1007/BF00149106.

H. S. Hudson. Solar flares, microflares, nanoflares, and coronal heating. *Solar Phys.*, 133:357–369, June 1991. doi: 10.1007/BF00149894.

K. Ichimoto, B. Lites, D. Elmore, Y. Suematsu, S. Tsuneta, Y. Katsukawa, T. Shimizu, R. Shine, T. Tarbell, A. Title, J. Kiyohara, K. Shinoda, G. Card, A. Lecinski, K. Streander, M. Nakagiri, M. Miyashita, M. Noguchi, C. Hoffmann, and T. Cruz. Polarization Calibration of the Solar Optical Telescope onboard Hinode. *Solar Phys.*, 249:233–261, June 2008. doi: 10.1007/s11207-008-9169-9.

C. U. Keller, F.-L. Deubner, U. Egger, B. Fleck, and H. P. Povel. On the strength of solar intra-network fields. *Astron. Astrophys.*, 286:626–634, June 1994.

E. V. Khomenko, M. J. Martínez González, M. Collados, A. Vögler, S. K. Solanki, B. Ruiz Cobo, and C. Beck. Magnetic flux in the internetwork quiet Sun. *Astron. Astrophys.*, 436:L27–L30, June 2005. doi: 10.1051/0004-6361:200500114.

N. Koemle. Structure and evolution of magnetic network features. *Solar Phys.*, 64:213–221, December 1979. doi: 10.1007/BF00151432.

T. Kosugi, K. Matsuzaki, T. Sakao, T. Shimizu, Y. Sone, S. Tachikawa, T. Hashimoto, K. Minesugi, A. Ohnishi, T. Yamada, S. Tsuneta, H. Hara, K. Ichimoto, Y. Suematsu, M. Shimojo, T. Watanabe, S. Shimada, J. M. Davis, L. D. Hill, J. K. Owens, A. M. Title, J. L. Culhane, L. K. Harra, G. A. Doschek, and L. Golub. The Hinode (Solar-B) Mission: An Overview. *Solar Phys.*, 243:3–17, June 2007. doi: 10.1007/s11207-007-9014-6.

S. Krucker and A. O. Benz. Energy Distribution of Heating Processes in the Quiet Solar Corona. *Astrophys. J. Letts.*, 501:L213+, July 1998. doi: 10.1086/311474.

M. Kubo and T. Shimizu. Magnetic Field Properties of Flux Cancellation Sites. *Astrophys. J.*, 671:990–1004, December 2007. doi: 10.1086/523080.

B. J. Labonte and R. Howard. The magnetic flux in the quiet sun network. *Solar Phys.*, 80:15–19, September 1982. doi: 10.1007/BF00153420.

D. A. Lamb, C. E. DeForest, H. J. Hagenaar, C. E. Parnell, and B. T. Welsch. Solar Magnetic Tracking. II. The Apparent Unipolar Origin of Quiet-Sun Flux. *Astrophys. J.*, 674:520–529, February 2008. doi: 10.1086/524372.

K. R. Lang. *The Cambridge Encyclopedia of the Sun*. Cambridge University Press, 2001.

R. H. Levine. A New Theory of Coronal Heating. *Astrophys. J.*, 190:457–466, June 1974. doi: 10.1086/152898.

H. Lin. On the Distribution of the Solar Magnetic Fields. *Astrophys. J.*, 446:421–+, June 1995. doi: 10.1086/175800.

H. Lin and T. Rimmele. The Granular Magnetic Fields of the Quiet Sun. *Astrophys. J.*, 514:448–455, March 1999. doi: 10.1086/306925.

B. W. Lites, B. C. Low, V. Martinez Pillet, P. Seagraves, A. Skumanich, Z. A. Frank, R. A. Shine, and

S. Tsuneta. The Possible Ascent of a Closed Magnetic System through the Photosphere. *Astrophys. J.*, 446:877–+, June 1995. doi: 10.1086/175845.

B. W. Lites, M. Kubo, H. Socas-Navarro, T. Berger, Z. Frank, R. Shine, T. Tarbell, A. Title, K. Ichimoto, Y. Katsukawa, S. Tsuneta, Y. Suematsu, T. Shimizu, and S. Nagata. The Horizontal Magnetic Flux of the Quiet-Sun Internetwork as Observed with the Hinode Spectro-Polarimeter. *Astrophys. J.*, 672: 1237–1253, January 2008. doi: 10.1086/522922.

Y. E. Litvinenko and S. F. Martin. Magnetic reconnection as the cause of a photospheric canceling feature and mass flows in a filament. *Solar Phys.*, 190:45–58, December 1999. doi: 10.1023/A:1005284116353.

Y. Liu, H. Zhang, G. Ai, H. Wang, and H. Zirin. The evolution of magnetic network elements in the quiet Sun. *Astron. Astrophys.*, 283:215–220, March 1994.

S. H. B. Livi, J. Wang, and S. F. Martin. The cancellation of magnetic flux. I - On the quiet sun. *Australian Journal of Physics*, 38:855–873, 1985.

W. Livingston and J. Harvey. Observational Evidence for Quantization in Photospheric Magnetic Flux. *Solar Phys.*, 10:294–296, December 1969. doi: 10.1007/BF00145516.

W. Livingston and J. Harvey. The Kitt Peak magnetograph. I. Principles of the instrument. *Contributions from the Kitt Peak National Observatory*, 558, 1971.

W. C. Livingston and J. Harvey. A New Component of Solar Magnetism - The Inner Network Fields. In *Bulletin of the American Astronomical Society*, volume 7 of *Bulletin of the American Astronomical Society*, pages 346–+, March 1975.

W. C. Livingston and F. Q. Orrall. Magnetic pukas and the lifetime of the supergranulation. *Solar Phys.*, 39:301–304, December 1974. doi: 10.1007/BF00162421.

D. W. Longcope. Topology and Current Ribbons: A Model for Current, Reconnection and Flaring in a Complex, Evolving Corona. *Solar Phys.*, 169:91–121, November 1996. doi: 10.1007/BF00153836.

D. W. Longcope. A Model for Current Sheets and Reconnection in X-Ray Bright Points. *Astrophys. J.*, 507:433–442, November 1998. doi: 10.1086/306319.

R. Manso Sainz, E. Landi Degl'Innocenti, and J. Trujillo Bueno. Concerning the Existence of a "Turbulent" Magnetic Field in the Quiet Sun. *Astrophys. J. Letts.*, 614:L89–L91, October 2004. doi: 10.1086/425176.

S. F. Martin. The identification and interaction of network, intranetwork, and ephemeral-region magnetic fields. *Solar Phys.*, 117:243–259, September 1988. doi: 10.1007/BF00147246.

S. F. Martin. Small-Scale Magnetic Features Observed in the Photosphere. In J. O. Stenflo, editor, *Solar Photosphere: Structure, Convection, and Magnetic Fields*, volume 138 of *IAU Symposium*, pages 129–+, 1990.

S. F. Martin and K. H. Harvey. Ephemeral active regions during solar minimum. *Solar Phys.*, 64:93–108, November 1979. doi: 10.1007/BF00151118.

M. J. Martínez González and L. R. Bellot Rubio. Emergence of Small-scale Magnetic Loops Through the Quiet Solar Atmosphere. *Astrophys. J.*, 700:1391–1403, August 2009. doi: 10.1088/0004-637X/700/2/1391.

P. S. McIntosh. The birth and evolution of sunspots - Observations. In L. E. Cram & J. H. Thomas, editor, *The Physics of Sunspots*, pages 7–54, 1981.

M. Meneguzzi and A. Pouquet. Turbulent dynamos driven by convection. *Journal of Fluid Mechanics*, 205:297–318, 1989. doi: 10.1017/S0022112089002041.

N. Meunier. Statistical properties of magnetic structures: Their dependence on scale and solar activity. *Astron. Astrophys.*, 405:1107–1120, July 2003. doi: 10.1051/0004-6361:20030713.

H. K. Moffat. *Magnetic Field Generation in Electrically Conducting Fluids*. Cambridge University Press, 1978.

R. L. Moore, D. A. Falconer, J. G. Porter, and S. T. Suess. On Heating the Sun's Corona by Magnetic Explosions: Feasibility in Active Regions and Prospects for Quiet Regions and Coronal Holes. *Astrophys. J.*, 526:505–522, November 1999. doi: 10.1086/307969.

U. Narain and P. Agarwal. On heating of stellar (solar) chromospheres and coronae by magnetoacoustic waves: A review. *Bulletin of the Astronomical Society of India*, 22:111–131, June 1994.

U. Narain and S. Kumar. On the electric circuit approach of coronal heating: a review. *Bulletin of the Astronomical Society of India*, 21:85–102, June 1993.

U. Narain and P. Ulmschneider. Chromospheric and coronal heating mechanisms. *Space Science Reviews*, 54:377–445, December 1990. doi: 10.1007/BF00177801.

U. Narain and P. Ulmschneider. Chromospheric and Coronal Heating Mechanisms II. *Space Science Reviews*, 75:453–509, February 1996. doi: 10.1007/BF00833341.

Å. Nordlund. Stellar (magneto-)convection. *Physica Scripta Volume T*, 133(1):014002–+, December 2008. doi: 10.1088/0031-8949/2008/T133/014002.

D. Orozco Suárez, L. R. Bellot Rubio, J. C. del Toro Iniesta, and S. Tsuneta. Magnetic field emergence in quiet Sun granules. *Astron. Astrophys.*, 481:L33–L36, April 2008. doi: 10.1051/0004-6361:20079032.

E. N. Parker. The Dissipation of Inhomogeneous Magnetic Fields and the Problem of Coronae - Part Two - the Dynamics of Dislocated Flux. *Astrophys. J.*, 244:644–+, March 1981. doi: 10.1086/158743.

E. N. Parker. Magnetic neutral sheets in evolving fields. I - General theory. *Astrophys. J.*, 264:635–647, January 1983a. doi: 10.1086/160636.

E. N. Parker. Magnetic Neutral Sheets in Evolving Fields - Part Two - Formation of the Solar Corona. *Astrophys. J.*, 264:642–+, January 1983b. doi: 10.1086/160637.

E. N. Parker. Nanoflares and the solar X-ray corona. *Astrophys. J. Letts.*, 330:474–479, July 1988a. doi: 10.1086/166485.

E. N. Parker. Solar and stellar magnetic fields and atmospheric structures - Theory. *Solar Phys.*, 121: 271–288, March 1989. doi: 10.1007/BF00161700.

E. N. Parker. Hydromagnetic Dynamo Models. *Astrophys. J.*, 122:293–+, September 1955. doi: 10.1086/146087.

E. N. Parker. Kinematical Hydromagnetic Theory and its Application to the Low Solar Photosphere. *Astrophys. J.*, 138:552–+, August 1963. doi: 10.1086/147663.

E. N. Parker. Magnetic buoyancy and the escape of magnetic fields from stars. *Astrophys. J.*, 281:839–845, June 1984. doi: 10.1086/162163.

E. N. Parker. Nanoflares and the solar X-ray corona. *Astrophys. J.*, 330:474–479, July 1988b. doi: 10.1086/166485.

E. N. Parker. Micro/Nanoflare Coronal Heating (With 8 Figures). In P. Ulmschneider, E. R. Priest, & R. Rosner, editor, *Mechanisms of Chromospheric and Coronal Heating*, pages 615–+, January 1991.

E. N. Parker. A solar dynamo surface wave at the interface between convection and nonuniform rotation. *Astrophys. J.*, 408:707–719, May 1993. doi: 10.1086/172631.

C. E. Parnell. A model of the Solar Magnetic Carpet. *Solar Phys.*, 200:23–45, May 2001.

C. E. Parnell. Nature of the magnetic carpet - I. Distribution of magnetic fluxes. *Mon. Not. Roy. Astron.Soc.*, 335:389–398, September 2002. doi: 10.1046/j.1365-8711.2002.05618.x.

C. E. Parnell and P. E. Jupp. Statistical Analysis of the Energy Distribution of Nanoflares in the Quiet Sun.

Astrophys. J., 529:554–569, January 2000. doi: 10.1086/308271.

C. E. Parnell, E. R. Priest, and L. Golub. The three-dimensional structures of X-ray bright points. *Solar Phys.*, 151:57–74, April 1994. doi: 10.1007/BF00654082.

C. E. Parnell, C. E. DeForest, H. J. Hagenaar, B. A. Johnston, D. A. Lamb, and B. T. Welsch. A Power-Law Distribution of Solar Magnetic Fields Over More Than Five Decades in Flux. *Astrophys. J.*, 698:75–82, June 2009. doi: 10.1088/0004-637X/698/1/75.

H. H. Plaskett. Motions in the Sun at the photospheric level. V. Velocities of granules and of other localized regions. *Mon. Not. Roy. Astron.Soc.*, 114:251–+, 1954.

J. G. Porter, R. L. Moore, E. J. Reichmann, O. Engvold, and K. L. Harvey. Microflares in the solar magnetic network. *Astrophys. J.*, 323:380–390, December 1987. doi: 10.1086/165835.

H. E. Potts and D. A. Diver. Post-hoc derivation of SOHO Michelson doppler imager flat fields. *aa*, 492: 863–871, December 2008. doi: 10.1051/0004-6361:200810606.

E. Priest and T. Forbes. *Magnetic Reconnection*. June 2000.

E. R. Priest, C. E. Parnell, and S. F. Martin. A converging flux model of an X-ray bright point and an associated canceling magnetic feature. *Astrophys. J.*, 427:459–474, May 1994. doi: 10.1086/174157.

S. P. Rajaguru, R. L. Kurucz, and S. S. Hasan. Convective Intensification of Magnetic Flux Tubes in Stellar Photospheres. *"Astrophys. J. Letts."*, 565:L101–L104, February 2002. doi: 10.1086/339417.

H. E. Ramsey, S. A. Schoolman, and A. M. Title. On the size, structure, and strength of the small-scale solar magnetic field. *Astrophys. J. Letts.*, 215:L41+, July 1977. doi: 10.1086/182472.

J.-I. Sakai, A. Takahata, and I. V. Sokolov. Heating of Coronal Loop Footpoints by Magnetic Reconnection Resulting from Surface Alfvén Waves and Colliding Plasma Flows in Chromospheric Current Sheets. *Astrophys. J.*, 556:905–911, August 2001. doi: 10.1086/321622.

J. Sánchez Almeida. A Simple Model for the Distribution of Quiet-Sun Magnetic Field Strengths. *Astrophys. J.*, 657:1150–1156, March 2007. doi: 10.1086/511146.

J. Sánchez Almeida, I. Domínguez Cerdeña, and F. Kneer. Simultaneous Visible and Infrared Spectropolarimetry of a Solar Internetwork Region. *Astrophys. J. Letts.*, 597:L177–L180, November 2003. doi: 10.1086/379969.

P. H. Scherrer, R. S. Bogart, R. I. Bush, J. T. Hoeksema, A. G. Kosovichev, J. Schou, W. Rosenberg, L. Springer, T. D. Tarbell, A. Title, C. J. Wolfson, I. Zayer, and MDI Engineering Team. The Solar Oscillations Investigation - Michelson Doppler Imager. *Solar Phys.*, 162:129–188, December 1995. doi: 10.1007/BF00733429.

J. Schou, H. M. Antia, S. Basu, R. S. Bogart, R. I. Bush, S. M. Chitre, J. Christensen-Dalsgaard, M. P. di Mauro, W. A. Dziembowski, A. Eff-Darwich, D. O. Gough, D. A. Haber, J. T. Hoeksema, R. Howe, S. G. Korzennik, A. G. Kosovichev, R. M. Larsen, F. P. Pijpers, P. H. Scherrer, T. Sekii, T. D. Tarbell, A. M. Title, M. J. Thompson, and J. Toomre. Helioseismic Studies of Differential Rotation in the Solar Envelope by the Solar Oscillations Investigation Using the Michelson Doppler Imager. *Astrophys. J.*, 505:390–417, September 1998. doi: 10.1086/306146.

C. J. Schrijver, R. A. Shine, H. J. Hagenaar, N. E. Hurlburt, A. M. Title, L. H. Strous, S. M. Jefferies, A. R. Jones, J. W. Harvey, and T. L. Duvall, Jr. Dynamics of the Chromospheric Network: Mobility, Dispersal, and Diffusion Coefficients. *Astrophys. J.*, 468:921–+, September 1996. doi: 10.1086/177747.

C. J. Schrijver, A. M. Title, A. A. van Ballegooijen, H. J. Hagenaar, and R. A. Shine. Sustaining the Quiet Photospheric Network: The Balance of Flux Emergence, Fragmentation, Merging, and Cancellation. *Astrophys. J.*, 487:424–+, September 1997. doi: 10.1086/304581.

C. J. Schrijver, A. M. Title, K. L. Harvey, N. R. Sheeley, Y.-M. Wang, G. H. J. van den Oord, R. A. Shine, T. D. Tarbell, and N. E. Hurlburt. Large-scale coronal heating by the small-scale magnetic field of the Sun. *Nature*, 394:152–154, July 1998. doi: 10.1038/28108.

M. Schwabe. Die Sonne. Von Herrn Hofrath Schwabe. *Astronomische Nachrichten*, 20:283–+, March 1843. doi: 10.1002/asna.18430201706.

N. R. Sheeley, Jr. Measurements of Solar Magnetic Fields. *Astrophys. J.*, 144:723–+, May 1966. doi: 10.1086/148651.

N. R. Sheeley, Jr. The Evolution of the Photospheric Network. *Solar Phys.*, 9:347–357, October 1969. doi: 10.1007/BF02391657.

T. Shimizu. Energetics and Occurrence Rate of Active-Region Transient Brightenings and Implications for the Heating of the Active-Region Corona. *Publ. of the Astronomical Society of Japan*, 47:251–263, April 1995.

G. W. Simon and R. B. Leighton. Velocity Fields in the Solar Atmosphere. III. Large-Scale Motions, the Chromospheric Network, and Magnetic Fields. *Astrophys. J.*, 140:1120–+, October 1964. doi: 10.1086/148010.

G. W. Simon, A. M. Title, and N. O. Weiss. Sustaining the Sun's Magnetic Network with Emerging Bipoles. *Astrophys. J.*, 561:427–434, November 2001. doi: 10.1086/322243.

R. C. Smithson. Videomagnetograph Studies of Solar Magnetic Fields. I: Magnetic Field Diffusion in Waek Plage Regions. *Solar Phys.*, 29:365–382, April 1973. doi: 10.1007/BF00150814.

R. C. Smithson. Observations of Weak Solar Magnetic Fields with the Lockheed Diode Array Magnetograph. In *Bulletin of the American Astronomical Society*, volume 7 of *Bulletin of the American Astronomical Society*, pages 346–+, March 1975.

H. B. Snodgrass. Magnetic rotation of the solar photosphere. *Astrophys. J.*, 270:288–299, July 1983. doi: 10.1086/161121.

H. Socas-Navarro and J. Sánchez Almeida. Magnetic Properties of Photospheric Regions with Very Low Magnetic Flux. *Astrophys. J.*, 565:1323–1334, February 2002. doi: 10.1086/324688.

H. Socas-Navarro, V. Martínez Pillet, and B. W. Lites. Magnetic Properties of the Solar Internetwork. *Astrophys. J.*, 611:1139–1148, August 2004. doi: 10.1086/422379.

S. K. Solanki. Sunspots: An overview. *Astronomy and Astrophysics Review*, 11:153–286, 2003. doi: 10.1007/s00159-003-0018-4.

E. A. Spiegel and N. O. Weiss. Magnetic activity and variations in solar luminosity. *Nature*, 287:616–+, October 1980. doi: 10.1038/287616a0.

H. C. Spruit. Convective collapse of flux tubes. *"Solar Phys."*, 61:363–378, March 1979. doi: 10.1007/BF00150420.

R. F. Stein, A. Nordlund, D. Georgobiani, D. Benson, and W. Schaffenberger. Supergranulation Scale Connection Simulations. *ArXiv e-prints*, November 2008.

J. O. Stenflo. Magnetic-Field Structure of the Photospheric Network. *Solar Phys.*, 32:41–63, September 1973. doi: 10.1007/BF00152728.

P. A. Sturrock. Chromospheric Magnetic Reconnection and Its Possible Relationship to Coronal Heating. *Astrophys. J.*, 521:451–459, August 1999. doi: 10.1086/307544.

T. Tarbell, M. Ryutova, J. Covington, and A. Fludra. Heating and Jet Formation by Hydrodynamic Cumulation in the Solar Atmosphere. *Astrophys. J. Letts.*, 514:L47–L51, March 1999. doi: 10.1086/311929.

A. Title. Magnetic fields below, on and above the solar surface. In *Astronomy, physics and chemistry of H_3^+*,

volume 358 of *Royal Society of London Philosophical Transactions Series A*, pages 657–668, February 2000a. doi: 10.1098/rsta.2000.0551.

A. Title. Magnetic fields below, on and above the solar surface. In *Astronomy, physics and chemistry of H_3^+*, volume 358 of *Royal Society of London Philosophical Transactions Series A*, pages 657–668, February 2000b. doi: 10.1098/rsta.2000.0551.

A. M. Title and C. J. Schrijver. The Sun's Magnetic Carpet. In R. A. Donahue & J. A. Bookbinder, editor, *Cool Stars, Stellar Systems, and the Sun*, volume 154 of *Astronomical Society of the Pacific Conference Series*, pages 345–+, 1998.

S. M. Tobias. The solar dynamo. *Royal Society of London Philosophical Transactions Series A*, 360: 2741–2756, December 2002. doi: 10.1098/rsta.2002.1090.

S. Tsuneta, K. Ichimoto, Y. Katsukawa, S. Nagata, M. Otsubo, T. Shimizu, Y. Suematsu, M. Nakagiri, M. Noguchi, T. Tarbell, A. Title, R. Shine, W. Rosenberg, C. Hoffmann, B. Jurcevich, G. Kushner, M. Levay, B. Lites, D. Elmore, T. Matsushita, N. Kawaguchi, H. Saito, I. Mikami, L. D. Hill, and J. K. Owens. The Solar Optical Telescope for the Hinode Mission: An Overview. *Solar Phys.*, 249:167–196, June 2008. doi: 10.1007/s11207-008-9174-z.

L. van Driel-Gesztelyi, E. B. J. van der Zalm, and C. Zwaan. Active Nests on the Sun. In K. L. Harvey, editor, *The Solar Cycle*, volume 27 of *Astronomical Society of the Pacific Conference Series*, pages 89–+, 1992.

L. van Driel-Gesztelyi, J.-M. Malherbe, and P. Démoulin. Emergence of a U-loop - sub-photospheric link between solar active regions. *Astron. Astrophys.*, 364:845–852, December 2000.

D. Vrabec. Magnetic Fields Spectroheliograms from the San Fernando Observatory. In R. Howard, editor, *Solar Magnetic Fields*, volume 43 of *IAU Symposium*, pages 329–+, 1971.

D. Vrabec. Streaming Magnetic Features Near Sunspots. In R. G. Athay, editor, *Chromospheric Fine Structure*, volume 56 of *IAU Symposium*, pages 201–+, 1974.

H. Wang. Structure of magnetic fields on the quiet sun. *Solar Phys.*, 116:1–16, 1988. doi: 10.1007/BF00171711.

H. Wang and H. Zirin. Flows around sunspots and pores. *Solar Phys.*, 140:41–54, July 1992. doi: 10.1007/BF00148428.

J. Wang, Z. Shi, S. F. Martin, and S. H. B. Livi. The cancellation of magnetic flux on the quiet sun. *Vistas in Astronomy*, 31:79–83, 1988. doi: 10.1016/0083-6656(88)90179-1.

J. Wang, H. Wang, F. Tang, J. W. Lee, and H. Zirin. Flux distribution of solar intranetwork magnetic fields. *Solar Phys.*, 160:277–288, September 1995. doi: 10.1007/BF00732808.

J.-X. Wang, Z.-X. Shi, J.-Q. Liu, H. Feng, and G.-L. Liu. The observed size, flux spectrum of small-scale magnetic features. *Publications of the Beijing Astronomical Observatory*, 14:44–61, December 1989.

N. O. Weiss and M. J. Thompson. The Solar Dynamo. *Space Science Reviews*, 144:53–66, April 2009. doi: 10.1007/s11214-008-9435-z.

B. T. Welsch and D. W. Longcope. Magnetic Helicity Injection by Horizontal Flows in the Quiet Sun. I. Mutual-Helicity Flux. *Astrophys. J.*, 588:620–629, May 2003. doi: 10.1086/368408.

G. L. Withbroe and R. W. Noyes. Mass and energy flow in the solar chromosphere and corona. *Annual review of astronomy and astrophysics*, 15:363–387, 1977. doi: 10.1146/annurev.aa.15.090177.002051.

J. Zhang, G. Lin, J. Wang, H. Wang, and H. Zirin. The evolution of intranetwork magnetic elements. *Astron. Astrophys.*, 338:322–328, October 1998a.

J. Zhang, J. Wang, H. Wang, and H. Zirin. The motion patterns of intranetwork magnetic elements. *Astron.*

Astrophys., 335:341–350, July 1998b.

H. Zirin. Evolution of weak solar magnetic fields. *Australian Journal of Physics*, 38:961–969, 1985.

H. Zirin. Weak solar fields and their connection to the solar cycle. *Solar Phys.*, 110:101–107, March 1987. doi: 10.1007/BF00148205.

C. Zwaan. On the Relation Between Moving Magnetic Features and the Decay Rates of Sunspots. In R. G. Athay, editor, *Chromospheric Fine Structure*, volume 56 of *IAU Symposium*, pages 233–+, 1974.

C. Zwaan. On the Appearance of Magnetic Flux in the Solar Photosphere. *Solar Phys.*, 60:213–240, December 1978. doi: 10.1007/BF00156523.

C. Zwaan. Elements and patterns in the solar magnetic field. *Annual review of astronomy and astrophysics*, 25:83–111, 1987. doi: 10.1146/annurev.aa.25.090187.000503.